UNIVERSITÄT BONN
Physikalisches Institut

Production of Heavy Flavours with Associated Jets at HERA

von
Oliver Maria Kind

Inclusive cross–sections for the production of open beauty and charm in ep collisions at HERA recorded with the ZEUS detector in the years 1996—2000 are measured. The data is restricted to photoproduction processes, *i. e.* collision events with small four–momentum transfers squared, $Q^2 \approx 0$. Two associated jets with transverse energies $E_t > 7(6)$ GeV and pseudo–rapidities $|\eta| < 2.5$ are required. The flavour is tagged by the identification of electrons and positrons from semi–leptonic decays of the heavy quark. For this a likelihood method is developed, mainly consisting of energy loss measurements in the central drift chamber of the detector and some other discriminant variables. The fractions of beauty and charm production are determined by a fit of Monte Carlo templates to the data. The total measured production cross–section for $b\bar{b}$ production is $820 \pm 150^{+20}_{-30}$ pb for centre–of–mass energies $\sqrt{s_{ep}} = 300$ GeV and $1170 \pm 130^{+30}_{-100}$ pb for $\sqrt{s_{ep}} = 318$ GeV. The total cross–section for charm production is given as well as differential cross–sections for $b\bar{b}$ and $c\bar{c}$ production.

Post address:
Nußallee 12
53115 Bonn
Germany

BONN-IR-2007-04
Bonn University
December 2006
ISSN-0172-8741

UNIVERSITÄT BONN
Physikalisches Institut

Production of Heavy Flavours with Associated Jets at HERA

von
Oliver Maria Kind

Dieser Forschungsbericht wurde als Dissertation von der Mathematisch - Naturwissenschaftlichen Fakultät der Universität Bonn angenommen und ist auf dem Hochschulschriftenserver der ULB Bonn `http://hss.ulb.uni-bonn.de/diss_online` elektronisch publiziert.

Angenommen am:	18. Dezember 2006
Kolloquium:	26. Februar 2007
Referent:	Prof. Dr. Ian C. Brock
Korreferent:	Prof. Dr. Klaus Desch

Preface

Studying the strong force is one of the most fascinating subjects in particle physics. Described by the theory of Quantum Chromodynamics (QCD), the combination of a strong coupling and the non-Abelian SU(3) symmetry leads to a multi–faceted appearance in nature, such as asymptotic freedom or confinement. However, the very same structure makes any prediction quite difficult — even in times of almost unlimited computing power. Various techniques have been developed in order to cope with the problem. The most precise predictions so far are achieved with the help of perturbation theory. The scope of this approach is however limited to very high energies.

The HERA electron–proton collider provides such energies. A multitude of experimental tests of Quantum Chromodynamics are possible: the running of the strong coupling constant, scaling violations in deep inelastic scattering, measurements of jets and event–shapes, and the production of vector mesons or heavy quarks. In particular the latter is of some interest, since the heavy quark masses provide a hard scale which should make perturbative calculations more reliable. The beam energies of the machine allow for the production of beauty and charm quarks.

The objective of this thesis is the measurement of beauty and charm production cross–sections in ep collision data at HERA recorded with the ZEUS detector. Since this will be an inclusive measurement, the flavour quantum number for beauty or charm must be non-zero. This is often referred to as “naked” or “open” beauty and charm. An essential tool for the analysis are QCD jets. They are needed to ascertain the event and parton kinematics, as well as to tag the beauty and charm flavours. The latter is done with the help of semi–leptonic decays of the beauty and charm hadrons originating from the hadronisation of the heavy quarks. Here, the electron channel of the semi–leptonic decays is studied. Since no life–time information of the beauty and charm hadrons is available, the heavy flavour tagging is based upon the electron identification and the kinematics of the semi–leptonic decays with respect to the heavy quark jets. A new procedure has been developed in order to combine all the information and test the beauty or charm flavour hypothesis for each candidate. It should be mentioned, however,

that the focus of this analysis lies on the measurement of beauty production. The charm measurements came as a by-product of the beauty analysis and thus are not as precise as those for beauty.

For experimental reasons this analysis is restricted to photoproduction. The physics of hard photoproduction with two jets and the production of heavy quarks is the subject of Chapter 1. In Chapter 2 the experimental context, *i. e.* the HERA machine and the ZEUS detector, is presented. The event samples used, their selection and the event reconstruction are described in Chapter 3. As already mentioned, the identification of electrons and positrons plays a major role for the flavour tagging. For this a general particle identification tool was developed, which relies mainly on energy loss measurements in the central drift chamber of the ZEUS detector, but also calorimeter information. Details of the energy loss measurements and its calibration are given in Chapter 4. Chapter 5 outlines the particle identification procedure. The actual flavour tagging method and the extraction of the beauty and charm signals are the subject of Chapter 6. Finally, the measured beauty and charm production cross–sections and their comparison with predictions from theory are presented in Chapter 7. Chapter 8 then concludes the thesis.

Beside the physical aspects, the technical side of this analysis is also noteworthy. Part of this work was the development of a new analysis framework, which, in principle, can be used for any type of analysis at ZEUS. The emphasis of this framework was put on a more efficient and rapid development of physics analyses, on robust and error–resistant code. A more detailed description of the framework can be found in Appendix F. The framework is closely related to an earlier project, the new ZEUS event display, which is described in Appendix E.

Contents

Chapter 1

Heavy Quark Production at HERA

1.1 Short Review of QCD

Quantum Chromodynamics is the present theory of the strong interaction. It is a local gauge theory and thus fits into the common picture of the fundamental forces in nature, which describes interactions by gauge fields caused by local changes in the phase of the quantum fields. In QCD the interacting spinors, the "quarks" possess an internal degree of freedom called colour. The force between the quarks is mediated by a set of massless gauge bosons, the "gluons". The quarks come in three colours and the gluons in eight colour combinations. The underlying symmetry of the QCD Lagrangian is of type SU(3) which is known to be of non–Abelian nature. This is exhibited in the fact that the gluons carry colour charge and hence interact not only with the coloured quarks, but also with each other.

Once the Lagrangian is given, physical observables, such as decay rates or scattering cross–sections, can be calculated by the help of the S–matrix element for the process in question. Generally S cannot be computed exactly and must be approximated via a perturbative calculation (pQCD). Usually the kinetic part of the Lagrangian is taken as unperturbed and the interacting part as the perturbation, so that S is given as a power series in the coupling constant of the strong force. The actual evaluation of the terms in the series is done using FEYNMAN diagram techniques.

The S–matrix elements depend on parameters of the bare fields, like the bare mass and bare coupling constant. If the parameters are regarded as *fixed numbers*, then it is found that in the evaluation of many S–matrix elements by perturbation theory the integrals involved in certain FEYNMAN diagrams diverge[1] giving

[1]There are three types of divergences: (1) *Ultraviolet divergences*, which appear when the momenta in the FEYNMAN loop integrals go to infinity. (2) *Infrared divergences* show up in the calculation when in real and virtual gluon amplitudes the gluon momenta go to zero. However, the

rise to nonsensical results. The problem is solved by introducing a *renormalisation scheme* which renders results finite. It is based on the idea of allowing the parameters mentioned above to depend on some cut–off parameters (*scales*), μ_R. Since no physical observable may depend on these artificially introduced scales, the bare parameters (*e. g.* couplings) are replaced by effective ones. They are related via the renormalisation group equation. In particular the dependency of the strong coupling constant ("running coupling"), α_s, is given in first order of QCD perturbation theory by [LP82]

$$\alpha_s(\alpha_s^0, \mu_R) \quad = \quad \frac{12\pi}{\beta_0 \ln\left(\frac{\mu_R}{\Lambda^2_{QCD}}\right)}, \tag{1.1}$$

with

$$\beta_0 = 33 - 2n_f \qquad \text{and} \qquad \Lambda^2_{QCD} = {\mu_R}^2 \, e^{-\frac{12\pi}{\beta_0 \alpha_s^0}}.$$

The bare coupling is denoted by α_s^0. It is noteworthy that for deriving this equation parts of the perturbation expansion are already summed to *all* orders. Experimentally the value of Λ_{QCD} in leading order is determined to 200 MeV. The dependence on the normalisation scale μ_R is shown in Fig. 1.1. In contrast to QED, α_s *decreases* with increasing μ_R, which results in asymptotic freedom for small distances and confinement for long distances, the latter being the reason for the non–existence of free quarks. In the figure the masses of the charm and beauty quark are indicated showing that the heavy quarks provide a *hard* scale making perturbative QCD applicable.

The ep collider HERA provides an opportunity for tests of pQCD, for example through studying the production of jets above a certain energy threshold and heavy quarks.

1.2 Electron Proton Scattering

The fundamental, lowest order process in lepton proton scattering is mediated by the electroweak force either by the exchange of a neutral boson, γ or Z, or a $W^{\pm}$ as shown in Fig. 1.2. For obvious reasons the former case is called *neutral current* (NC) and the latter *charged current* (CC). The result of the scattering process can be a high multiplicity hadronic final–state, X. Using the four–momenta of

infrared singularities cancel between real and virtual gluon graphs. In an inclusive measurement, which implies that one integrates over all momenta in the final–state, the infrared divergence is no longer present. (3) *Collinear* or mass singularities appear whenever the momenta of quarks or gluons become parallel to each other, which is only possible for coupling between massless particles.

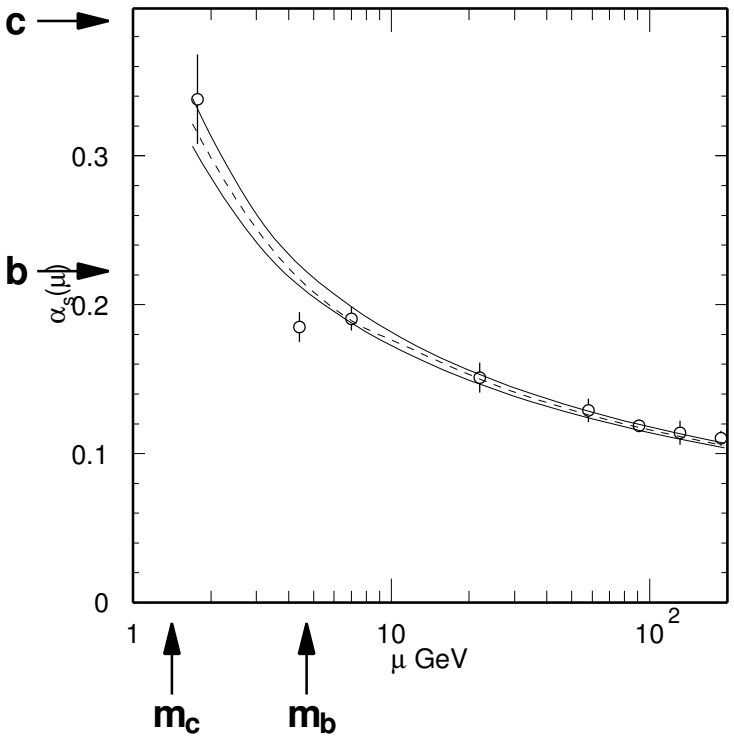

Figure 1.1: Running of the strong coupling constant α_s (courtesy of [Y+06]). If the renormalisation scale is defined by the mass of the charm or the beauty quark, α_s is small enough to perform perturbative QCD computations: $\alpha_s(m_c) \approx 0.39, \alpha_s(m_b) \approx 0.22$.

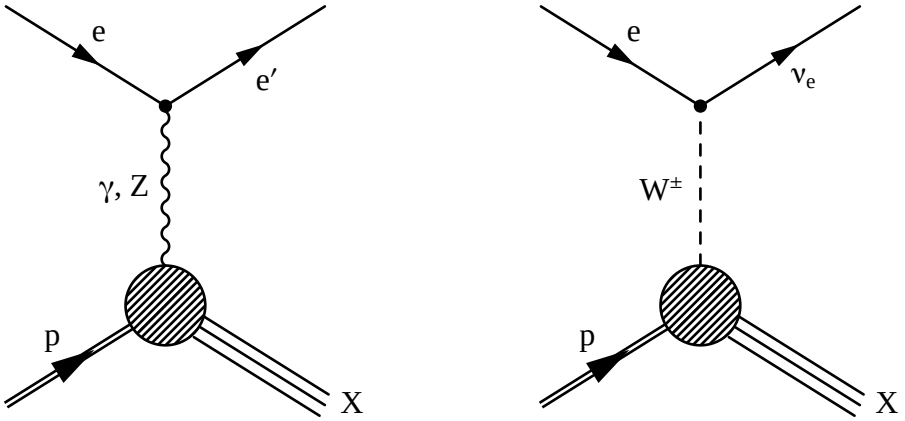

(a) Neutral Current (b) Charged Current

Figure 1.2: Electron proton scattering in lowest order. In (a) a neutral vector boson is mediated (γ or Z) while in (b) a charged $W^{\pm}$ is exchanged with an undetectable neutrino in the final state. The hadronic final–state is denoted by X.

the incoming and scattered lepton, $k = (E, \vec{k})$ and $k' = (E', \vec{k}')$, and the four-momenta of the proton and the photon (or Z and W resp.), $p = (E_p, \vec{p})$ and $q = (E_\gamma, \vec{q})$, the kinematics of the process is defined by a set of four LORENTZ–invariant quantities:

$$s = (k + p)^2 , \tag{1.2}$$

$$Q^2 \equiv -q^2 = -(k - k')^2 , \tag{1.3}$$

$$y = \frac{q \cdot p}{k \cdot p} , \tag{1.4}$$

$$x_p = \frac{-q^2}{2p \cdot q} . \tag{1.5}$$

The centre–of–mass energy, $\sqrt{s}$, is given by the incoming lepton and proton beam energies and is thus fixed. All other quantities vary. Q^2 is the negative square of the four–momentum transfer of the exchanged boson, which defines its virtuality and can vary from 0 to s. In the proton rest frame the inelasticity, y, denotes the fraction of the energy from the lepton taking part in the scattering process. In the parton model x_p is the fraction of momentum carried by the struck quark. It is referred to as the Björken scaling variable. One can easily show that x_p and y vary between 0 and 1 as expected. Neglecting all masses the above four quantities are related by

$$Q^2 = s\, x_p\, y . \tag{1.6}$$

In the exchange of a photon,the cross–section falls rapidly as a function of Q^2. At low Q^2, the photon dominates the cross–section over the weak bosons. Only when Q^2 is sufficiently large are the contributions from the Z and $W^\pm$ bosons significant. When $Q^2 \gtrsim M^2_{Z,W}$ the neutral and charged cross–sections are found to be of comparable size. The convergence of the NC and CC cross–sections as seen in Fig. 1.3 is a very nice demonstration of the electroweak theory [Wei67, Sal68, Gla61]. The high Q^2 region is, however, not subject of this thesis so will not be discussed further.

For large Q^2, the scale is provided by this variable and allows perturbative calculations to be performed. This is applicable down to $\sim \Lambda_{QCD}$. For $Q^2 \gg \Lambda_{QCD}$, the events are referred to as *deep inelastic scattering* (DIS). For very low Q^2, there is an exchange of an almost real photon and the process is referred to as *photoproduction*. Here Q^2 is not a hard scale: however, the transverse momentum of jets or the mass of the heavy quarks produced may define a hard scale in the event.

In the case of photoproduction the exchanged photon is quasi–real and thus almost completely transversely polarised. The inelastic electron proton scattering cross–section can be calculated in the equivalent photon approximation (EPA),

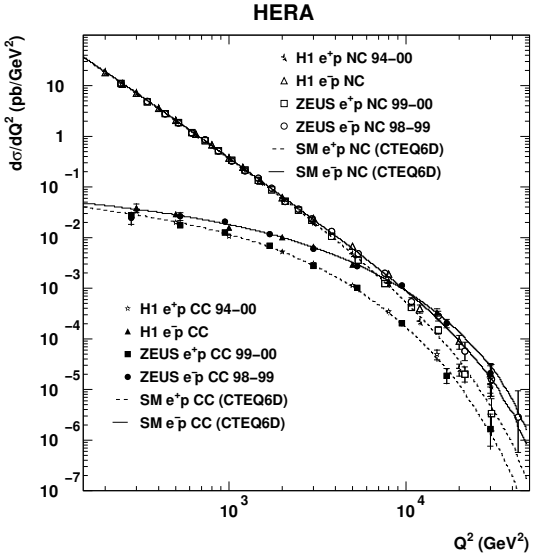

Figure 1.3: Measurement of the NC and CC cross–sections at HERA (from [ZEU04]). At low Q^2 the cross–section is dominated by photon exchange, only at $Q^2 \gtrsim M^2_{Z,W}$ are contributions from Z and W significant.

which is often, neglecting the longitudinal photon polarisation and its virtuality, referred to as the Weizsäcker–Williams approximation (WWA) [vW34, Wil35]. Here, the field of a fast charged particle moving past another particle is similar to electromagnetic radiation and can be interpreted as a flux of photons with energy distribution $n(y)$ with y defined as above. The cross–sections can therefore be reduced to photon proton interactions:

$$\mathrm{d}\sigma_{\mathrm{ep}}(y, Q^2) = \sigma_{\gamma\mathrm{p}}\, \mathrm{d}n(y, Q^2)\,, \tag{1.7}$$

where $\sigma_{\gamma\mathrm{p}}$ denotes the total photo–absorption cross–section. Integrating the emission of quasi–real photons in an interval $Q^2_{\mathrm{min}} < Q^2 < Q^2_{\mathrm{max}}$ and in a small energy bin dy, the equivalent number of photons is

$$\mathrm{d}n(y, Q^2_{\mathrm{min}}, Q^2_{\mathrm{max}}) = f_{\gamma/\mathrm{e}}(y, Q^2)\,\mathrm{d}y \tag{1.8}$$

with the photon spectrum[2]

$$f_{\gamma/\mathrm{e}} = \frac{\alpha_{\mathrm{em}}}{2\pi}\left\{\frac{1+(1-y)^2}{y}\,\ln\frac{Q^2_{\mathrm{max}}}{Q^2_{\mathrm{min}}} - 2\,m_{\mathrm{e}}^2\,y\left(\frac{1}{Q^2_{\mathrm{min}}} - \frac{1}{Q^2_{\mathrm{max}}}\right)\right\}. \tag{1.9}$$

Q^2_{min} is the lower kinematic limit given by

$$Q^2_{\mathrm{min}} = \frac{m_{\mathrm{e}}^2\, y^2}{1-y}\,. \tag{1.10}$$

[2]The kernel $\frac{1}{y}\left(1+(1-y)^2\right)$ is called the *splitting function* $P_{\mathrm{e}\gamma}$, and it describes the energy splitting of the outgoing electron and photon.

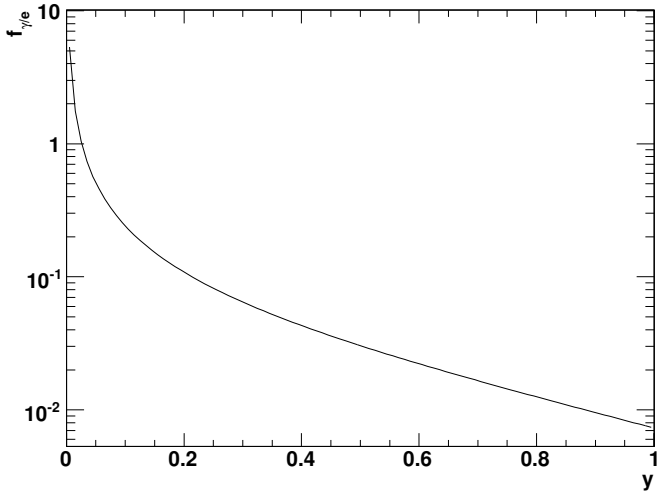

Figure 1.4: The energy spectrum of quasi–real photons, emitted by electrons, is shown as a function of the scaled photon energy $y = E_\gamma/E_e$ for a maximum virtuality of $Q^2_{max} = 0.01\,\mathrm{GeV}^2$.

Typical values are of the order of $10^{-7}\,\mathrm{GeV}^2$. The energy spectrum of quasi–real photons is shown in Fig. 1.4. The number of photons rises steeply towards small photon energies.

The accuracy of the Weizsäcker–Williams approximation has been calculated for the case of photoproduction at HERA[BS89]. For events where the electron is detected at small scattering angles in the laboratory $1 < \theta < 10\,\mathrm{mrad}$ (*tagged* photoproduction), the WWA is better than 1 %. For jet production with transverse jet energies $E_t \gg \sqrt{Q^2}$ and *untagged* electrons with $Q^2 < 4\,\mathrm{GeV}^2$, corrections to the WWA are at the level of a few percent[KKS95].

The calculation of the γp scattering cross–section, $\sigma_{\gamma p}$, is subject of the next section.

1.3 Photoproduction

The first generation of fixed–target photon–nucleon scattering experiments revealed that, to a very good approximation, the photon behaves like a hadron that is quantitatively described by the vector dominance model (VDM). For a review see [B$^+$78, B$^+$79].[3] QCD gives interesting and significant modifications to the VDM by predicting processes where the photon couples directly with quarks, leading to hard parton scattering and jets in the final–state (*c. f.* Fig. 1.5 for the terminology).

Significant deviations from the VDM were found by several fixed–target experiments at CERN and FNAL with centre–of–mass energies up to $\sqrt{s_{\gamma p}} = 27\,\mathrm{GeV}$. They observed an excess of final–state hadrons with large transverse momenta

[3] A more general review on photoproduction is given in [Erd97].

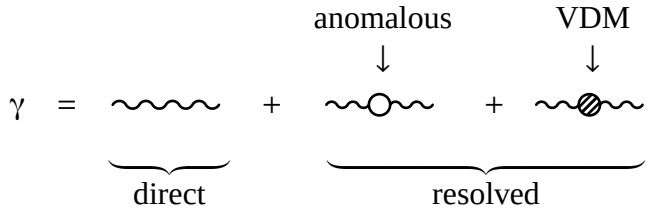

Figure 1.5: Apart from the bare photon state (direct), the photon can fluctuate into quark–anti–quark pairs without forming a hadronic bound state (anomalous), or form a vector meson (VDM). The photon can therefore interact *directly*, or through its *resolved* states.

(*high* p_t), which can be quantitatively explained by direct photon–nucleon interactions [Pau92]. The existence of the anomalous coupling was first shown in measurements of two–photon reactions at the e^+e^- colliders PETRA and PEP [BW87, Kol84, KZ88].

At HERA the ep cross–section for the $Q^2 \approx 0$ region is dominated by processes where the photon fluctuates in a vector meson. Thus photoproduction is very similar to hadron–hadron collisions. The cross–sections there show a universal behaviour, rising as [DL92]

$$\sigma_{hh} \propto s_{hh}^{0.08} . \tag{1.11}$$

Therefore the s_{ep}–dependence of the photoproduction cross–section in ep collisions is analogous that of hadron–hadron collisions. The γp cross–section is obtained by unfolding the photon–flux. Its $s_{\gamma p}$–dependence is shown in Fig. 1.6. A fraction of the events shows hard γp scattering processes, which manifest themselves in jets with high transverse energies. It should also be mentioned that roughly 10 % of all γp events at HERA show a large rapidity gap in the forward distribution of the measured energy flow. This is explained by the exchange of a colourless object. The events are referred to as *diffractive* events.

Figure 1.7 shows FEYNMAN diagrams of prominent examples of QCD processes at HERA both for direct and resolved photoproduction.

1.3.1 Lifetime of $e \to e\gamma$ and $\gamma \to q\bar{q}$ Fluctuations

The time of an electron fluctuating to an electron–photon state eγ and then into a $q\bar{q}$ pair given in the target rest frame can be estimated with the help of the HEISENBERG energy–time uncertainty relation [Hoy95].

The lifetime $t(e \to e\gamma)$ of the electron-photon state is required to be larger than that of the $\gamma \to q\bar{q}$ fluctuation. At HERA collisions between protons and quasi–real photons are studied at γ energies equivalent to 20 TeV in the proton

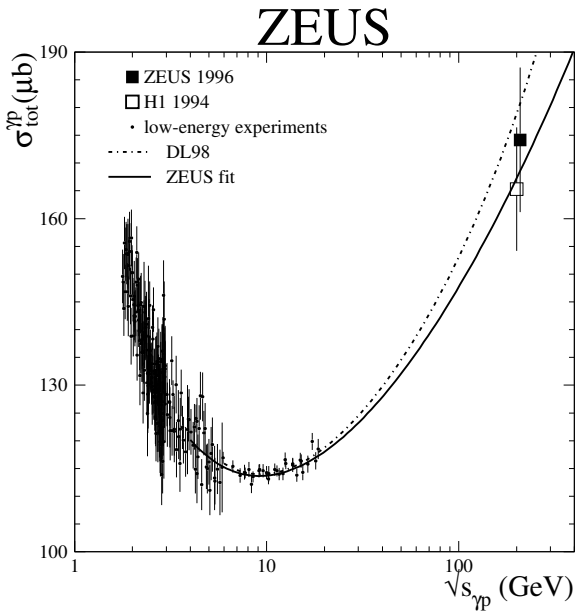

Figure 1.6: Measurement of the total γp cross–section at different centre–of–mass energies [C+01]. The energy dependence is compatible with that found in hadron–hadron measurements (the dot–dashed curve is a parametrisation based on [DL92]).

rest frame. For highly virtual photons with momentum transfers around $Q^2 \approx 100\,\mathrm{GeV}^2$, $t(\mathrm{e} \to \mathrm{e}\gamma) \approx 1\,\mathrm{fm}/c$, whereas for quasi–real photons at the kinematic limit $Q^2_{\mathrm{min}} \approx 10^{-7}\,\mathrm{GeV}^2$ the lifetime is larger than 1 μm. Fluctuations of the photon into a $\mathrm{q\bar{q}}$ pair depend on the energy fraction x_γ, which is carried by the quark relative to the photon energy E_γ. For quasi–real photons a symmetric configuration between the quark and the anti–quark, *i. e.* $x_\gamma = \frac{1}{2}$, gives the longest lifetime for such a $\mathrm{q\bar{q}}$ state. For HERA this results in a time $t(\gamma \to \mathrm{q\bar{q}}) = 10^4\,\mathrm{fm}/c$. As mentioned above, the formation of a $\mathrm{q\bar{q}}$ pair from an electron via a photon is only allowed if the time of the $\mathrm{q\bar{q}}$ fluctuation lies within the eγ state. At large $Q^2 \gg 1\,\mathrm{GeV}^2$ the time $t(\gamma \to \mathrm{q\bar{q}})$ is therefore limited by the time $t(\mathrm{e} \to \mathrm{e}\gamma)$.

The time of fluctuations involving radiation of gluons is typically 1—2 orders of magnitude shorter than that of quark fluctuations. Also, because the time of the photon fluctuation is finite, both direct and resolved photon interactions are expected.

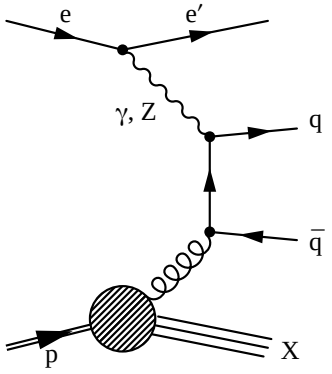

(a) Boson–gluon–fusion in direct photoproduction

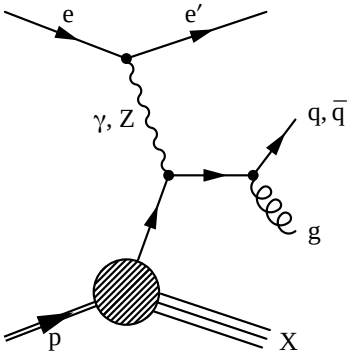

(b) QCD Compton scattering in direct photoproduction

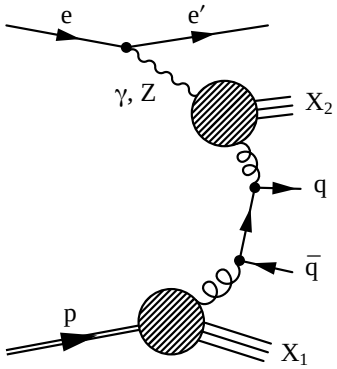

(c) Boson–gluon–fusion in resolved photoproduction

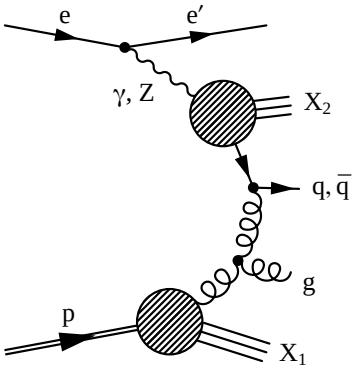

(d) Excitation in the photon

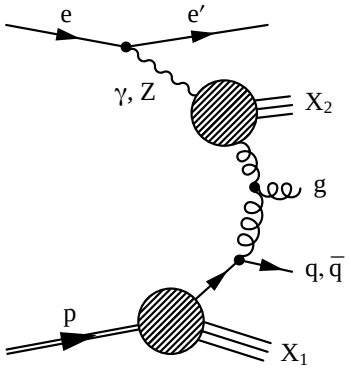

(e) Excitation in the proton

Figure 1.7: Examples of leading order QCD diagrams for (a,b) direct and (c–e) resolved photoproduction at HERA. The resolved photon and proton structure are depicted by the hatched areas. Excitation processes (d,e) are resolved processes in which the (heavy flavoured) outgoing quark originates from either the photon or the proton. The outgoing partons usually fragment into jets in addition to the photon and proton remnants (labelled X_1 and X_2).

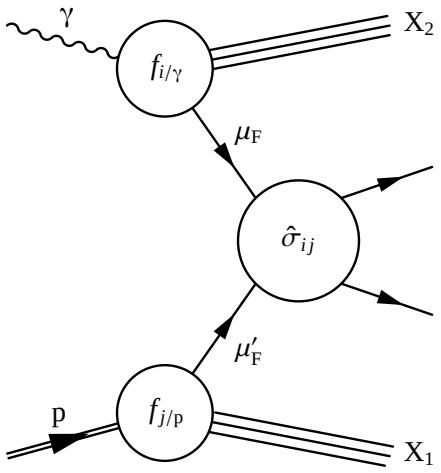

Figure 1.8: General scheme for the factorisation of the photoproduction process into a hard sub-process, denoted by $\hat{\sigma}_{ij}$, calculable with perturbative QCD, and soft processes hidden in the parton distributions of the photon and the proton. The factorisation scales μ_F, μ'_F separate the short–distance hard scatter from the parton distributions. Only leading order is shown.

1.3.2 Generalised Photoproduction Model

The differential γp cross–section can be written as the sum of the direct and resolved contributions

$$\mathrm{d}\sigma_{\gamma p}(p_\gamma, p_p) \;=\; \mathrm{d}\sigma_{\gamma p}^{\mathrm{direct}}(p_\gamma, p_p) \;+\; \mathrm{d}\sigma_{\gamma p}^{\mathrm{resolved}}(p_\gamma, p_p)\,. \tag{1.12}$$

With the help of the factorisation theorems in QCD [EGM+79, CSS89] the process can be split up as depicted in Fig. 1.8

$$\begin{aligned}\mathrm{d}\sigma_{\gamma p}^{\mathrm{direct}}(p_\gamma, p_p) \;&=\; \sum_i \int \mathrm{d}x\; f_{i/p}(x,\mu_F) \\ &\quad\cdot\; \mathrm{d}\hat{\sigma}_{\gamma i}\left(p_\gamma, x p_p, \alpha_s(\mu_R), \mu_R, \mu_F, \mu_\gamma\right), \end{aligned}\tag{1.13}$$

$$\begin{aligned}\mathrm{d}\sigma_{\gamma p}^{\mathrm{resolved}}(p_\gamma, p_p) \;&=\; \sum_{ij} \int \mathrm{d}x\,\mathrm{d}x_\gamma\; f_{j/\gamma}(x_\gamma,\mu_\gamma)\; f_{i/p}(x,\mu'_F) \\ &\quad\cdot\; \mathrm{d}\hat{\sigma}_{ij}\left(x_\gamma p_\gamma, x p_p, \alpha_s(\mu'_R), \mu'_R, \mu'_F, \mu_\gamma\right), \end{aligned}\tag{1.14}$$

where $\mathrm{d}\hat{\sigma}$ denotes the short–distance cross–section of the hard sub-process. The soft processes not calculable by pQCD are hidden in the parton distributions of the photon and the proton, $f_{i/p}$ and $f_{j/\gamma}$, giving the probability of scattering a parton i and j in the proton and the photon respectively. The renormalisation scales μ_R, μ'_R of the strong coupling constant, α_s, are set proportional to the transverse momentum, $\hat{p}_t$, of the final–state partons (or their masses). Since α_s has to be small for reliable predictions, the parton transverse momentum (or its mass) has to be above some minimum value, usually taken to be about $\hat{p}_t \approx 2\,\mathrm{GeV}$.[4] The

[4] In the case of heavy quarks an often used scale is the combination of the transverse momenta and the mass of the outgoing partons, m_{HQ}, given as $\mu_R = \sqrt{\frac{1}{2}\left(\hat{p}_{t,1}^2 + \hat{p}_{t,2}^2\right) + m_{HQ}^2}$.

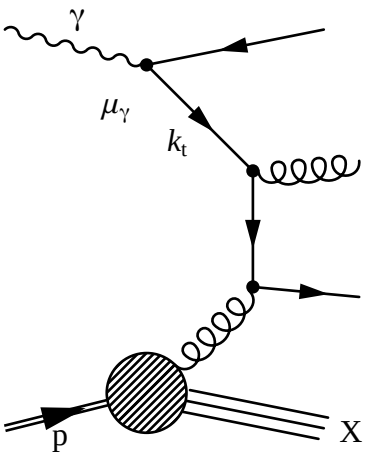

Figure 1.9: Ambiguity of direct and resolved classification in γp interactions. If the virtuality k_t of the parton propagator is lower than the factorisation scale μ_γ, the splitting process is included in the photon structure of the resolved calculation at *leading* order; otherwise it is regarded as direct process at *next–to–leading* order.

small $\hat{p}_t$ region corresponds to the regime where the majority of the parton cross–sections diverge (*c. f.* Sec. 1.3.3), that is at small and very large scattering angles. A lower cut–off in $\hat{p}_t$ therefore simultaneously solves the divergency problem and guarantees small α_s. The factorisation scales μ_F, μ'_F and μ_γ separate the hard scatter from the soft long–range interactions in the photon and the proton. They usually are set equal to the renormalisation scale.

The separation of direct and resolved processes becomes ambiguous beyond leading order and depends on the factorisation scale of the photon, μ_γ, as shown in Fig. 1.9. There is a strict interplay between the direct and resolved component. The divergences arising from collinear emission of quarks from the incoming direct photon are re-absorbed into the parton densities in the photon appearing in the resolved component. Thus only the sum of the direct and resolved components has a physical meaning.

The short–distance cross–sections are the only components that are "pure" QCD predictions. The observable inclusive cross–sections rely on all the input distributions mentioned above, and on the factorisation of the different input distributions. Turning the argument around: Since QCD has been confirmed by many different experiments, comparisons of data with such calculations potentially give new information on the input distributions.

1.3.3 Basic Aspects of the Parton Scattering Process

In a simple approach, the hard scatter can be described by elastic parton scattering in leading–order. The differential cross–section can be written in the form

$$\frac{d\hat{\sigma}}{d\hat{t}} = \frac{|M|^2}{16\pi\,\hat{s}^2}\,, \tag{1.15}$$

with the matrix element M for massless partons listed in Tab. 1.1. The MANDELSTAM variables used there for a LORENTZ–invariant representation of the matrix ele-

Resolved process	$\lvert M\rvert^2/\pi^2$
$qq' \to qq'$[5]	$\frac{64}{9}\,\alpha_s^2\,\left(\frac{\hat{s}^2+\hat{u}^2}{\hat{t}^2}\right)$
$qq \to qq$	$\frac{64}{9}\,\alpha_s^2\,\left(\frac{\hat{s}^2+\hat{u}^2}{\hat{t}^2}+\frac{\hat{s}^2+\hat{t}^2}{\hat{u}^2}-\frac{2}{3}\,\frac{\hat{s}^2}{\hat{u}\hat{t}}\right)$
$q\bar{q} \to q'\bar{q}'$	$\frac{64}{9}\,\alpha_s^2\,\left(\frac{\hat{t}^2+\hat{u}^2}{\hat{s}^2}\right)$
$q\bar{q} \to q\bar{q}$	$\frac{64}{9}\,\alpha_s^2\,\left(\frac{\hat{s}^2+\hat{u}^2}{\hat{t}^2}+\frac{\hat{t}^2+\hat{u}^2}{\hat{s}^2}-\frac{2}{3}\,\frac{\hat{u}^2}{\hat{s}\hat{t}}\right)$
$q\bar{q} \to gg$	$\frac{128}{3}\,\alpha_s^2\,\left(\frac{4}{9}\,\frac{\hat{t}^2+\hat{u}^2}{\hat{t}\hat{u}}-\frac{\hat{u}^2+\hat{t}^2}{\hat{s}^2}\right)$
$qg \to qg$	$16\,\alpha_s^2\,\left(\frac{\hat{s}^2+\hat{u}^2}{\hat{t}^2}-\frac{4}{9}\,\frac{\hat{s}^2+\hat{u}^2}{\hat{s}\hat{u}}\right)$
$gg \to q\bar{q}$	$\frac{8}{3}\,\alpha_s^2\,\left(\frac{1}{3}\,\frac{\hat{t}^2+\hat{u}^2}{\hat{t}\hat{u}}-\frac{3}{4}\,\frac{\hat{t}^2+\hat{u}^2}{\hat{s}^2}\right)$
$gg \to gg$	$72\,\alpha_s^2\,\left(3+\frac{\hat{t}^2+\hat{u}^2}{\hat{s}^2}-\frac{\hat{s}^2+\hat{u}^2}{\hat{t}^2}+\frac{\hat{s}^2+\hat{t}^2}{\hat{u}^2}\right)$
Direct process	$\lvert M\rvert^2/\pi^2$
$\gamma g \to q\bar{q}$	$16\,\alpha_s\,\alpha_{em}\,e_q^2\,\left(\frac{\hat{t}^2+\hat{u}^2}{\hat{t}\hat{u}}\right)$
$\gamma q \to qg$	$\frac{128}{3}\,\alpha_s\,\alpha_{em}\,e_q^2\,\left(-\frac{\hat{s}^2+\hat{u}^2}{\hat{s}\hat{u}}\right)$
$\gamma\gamma \to q\bar{q}$	$32\,\alpha_{em}\,e_q^4\,\left(\frac{\hat{t}^2+\hat{u}^2}{\hat{t}\hat{u}}\right)$

Table 1.1: Leading–order QCD matrix elements for resolved and direct scattering processes. The three direct processes are referred to as boson–gluon fusion, QCD Compton and two–photon process, respectively. Taken from [Kol84, Lev92].

ments are connected to the parton energies and scattering angle of the sub-process (see Fig. 1.10) by the following relations:

$$\hat{s} = 4\,E_1E_2\,, \tag{1.16}$$

$$\hat{t} = -\frac{1}{2}\,\hat{s}\,\left(1-\cos\hat{\theta}\right)\,, \tag{1.17}$$

$$\hat{u} = -\frac{1}{2}\,\hat{s}\,\left(1+\cos\hat{\theta}\right)\,. \tag{1.18}$$

Since forward and backward scattering cannot be distinguished by the experiment, only the absolute value of $\hat{\theta}$ is relevant. In Fig. 1.11 the shapes of the event rates for the direct and resolved processes are shown as a function of $|\cos\hat{\theta}|$. As predicted the resolved processes rise more steeply than the direct ones. In terms of the transverse parton momentum $\hat{p}_t = \frac{1}{2}\sqrt{\hat{s}}\,\sin\hat{\theta}$ the relative contribution of the direct processes to the total cross–section increases with $\hat{p}_t$. This is

[5] Equivalent to $q\bar{q}' \to q\bar{q}'$.

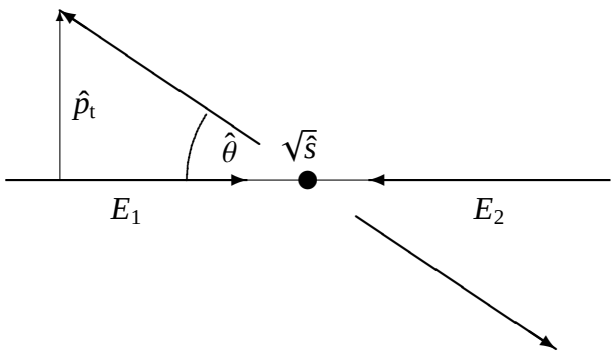

Figure 1.10: An elastic parton scattering process shown in the parton–parton centre–of–mass system. The centre–of–mass energy is denoted by $\sqrt{\hat{s}}$, the scattering angle is $\hat{\theta}$, and $\hat{p}_t$ is the transverse momentum of the scattered parton.

reflected in Fig. 1.12 in which the relative contributions of the individual parton sub–processes to the inclusive jet cross–section are shown as a function of the jet transverse energy, E_t .

Most of the matrix elements diverge at $|\cos\hat{\theta}| = 1$ which corresponds to small–angle forward and backward scattering. These divergencies are avoided by introducing a renormalisation scale in the strong coupling constant α_s, as already mentioned above.

A total of four variables are needed to describe the partonic state. The parton centre–of–mass energy, $\sqrt{\hat{s}}$, can be calculated from the photon and parton fractional energies and the beam centre–of–mass energy, s

$$\hat{s} = y\, x_\gamma\, x_p\, s\,. \tag{1.19}$$

Neglecting intrinsic transverse momenta of the partons from the photon and the proton, the transformation from the parton centre–of–mass system (PCMS) to the laboratory frame is given by [6]

$$p_t = \hat{p}_t\,, \tag{1.20}$$

$$\eta = \hat{\eta} + \eta_{\mathrm{PCMS}}\,. \tag{1.21}$$

Since the parton configuration in the PCMS is back–to–back, their rapidity sum is $\hat{\eta}_1 + \hat{\eta}_2 = 0$. The boost of the PCMS with respect to the laboratory system can be

[6]The *rapidity* denotes the argument in the hyperbolic functions of the mixed space–time rotations characterising a LORENTZ boost and thus is an additive number. In the *infinite momentum frame* neglecting all transverse momenta in the proton, the massless approximation of the rapidity, the *pseudo–rapidity* η is given by $\frac{1}{2}\ln[(E+p_z)/(E-p_z)]$, where p_z is the component of the proton momentum along the beam axis. In the laboratory frame η is connected with the scattering angle, θ, by the relation $\eta = -\ln[\theta/2]$.

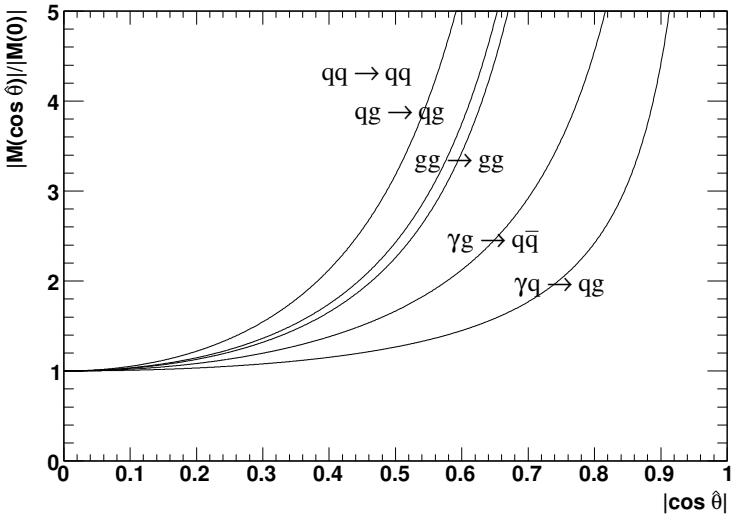

Figure 1.11: Shapes of the parton angular $\hat{\theta}$ distributions are compared for different parton scattering processes. Event rates of resolved interactions rise more steeply than those of direct processes.

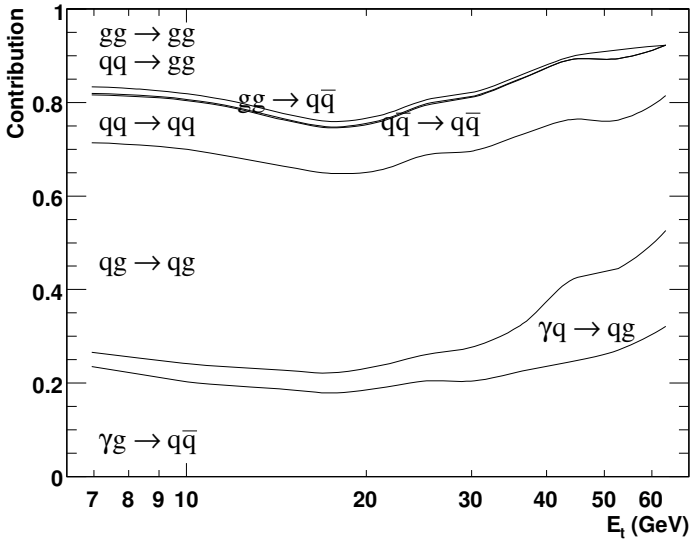

Figure 1.12: The relative contributions to jet production in γp scattering are shown as a function of the transverse jet energy, E_t. The jets were found with a k_t–clustering algorithm with $E_t > 7\,\text{GeV}$ and pseudo–rapidities $-2.5 < \eta < 2.5$ which were determined in the HERA laboratory frame. The calculated was done using the PYTHIA event generator (*c. f.* Sec. 1.7.1) for $\sqrt{s_{ep}} = 318\,\text{GeV}$. The contributions are drawn stacked, *i. e.* the area below each line includes the sum of all contributions below.

calculated from the parton rapidities in the laboratory frame

$$\eta_{\text{PCMS}} = \frac{1}{2}(\eta_1 + \eta_2)\,. \tag{1.22}$$

The rapidity difference is LORENTZ–invariant under boosts along the beam–axis

$$\Delta\eta \equiv \eta_1 - \eta_2 = \hat{\eta}_1 - \hat{\eta}_2 = -2\,\ln\tan\frac{1}{2}\hat{\theta}\,. \tag{1.23}$$

From this the scattering angle in the PCMS can be computed from the rapidity difference

$$\cos\hat{\theta} = \tanh\frac{1}{2}\Delta\eta\,. \tag{1.24}$$

The scaled photon energy y was defined in Eqn. 1.4. For quasi–real photons ($Q^2 \approx 0$), y then results from the energies of the beam lepton E_e and the scattered lepton E'_e

$$y = 1 - \frac{E'_\text{e}}{E_\text{e}} \tag{1.25}$$

Alternatively y can be determined from the proton four–vector and all final–state partons, including the photon and proton remnants. Then the scaled photon energy is given by the transverse momenta and rapidities of all partons

$$y = \sum_i \frac{p_{\text{t},i}\,e^{-\eta_i}}{2\,E_\text{e}}\,. \tag{1.26}$$

In the same manner the parton fractional energies x_γ and x_p can be recovered from the final–state partons

$$x_\gamma = \frac{p_\text{t}}{2\,yE_\text{e}}\left(e^{-\eta_1} + e^{-\eta_2}\right)\,, \tag{1.27}$$

$$x_\text{p} = \frac{p_\text{t}}{2\,yE_\text{p}}\left(e^{+\eta_1} + e^{+\eta_2}\right)\,. \tag{1.28}$$

In the case of untagged (refer to Sec. 2.2) photoproduction Eqns. 1.26–1.28 are the only way to reconstruct the initial partonic state, since the scattered lepton remains undetected.

For direct photoproduction x_γ is expected to be one, while for resolved events it should be less than one. This has been observed in dijet γp events at ZEUS, see Fig. 1.13 [B$^+$98a]. The distributions exhibits two peaks, the large peak at $x_\gamma = 0.2$ corresponds to resolved photon–proton scattering processes, the smaller peak at $x_\gamma = 0.8$ is associated with the direct photon–proton interactions. For the latter the values are not exactly at one due to higher order effects, the hadronisation process and detector effects. The agreement in shape between the data and

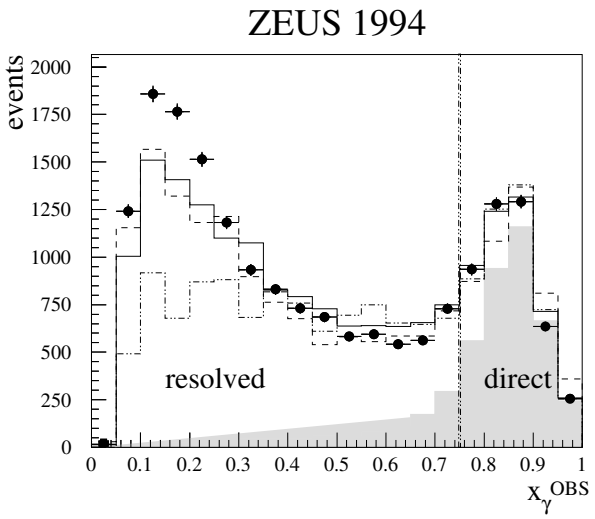

Figure 1.13: The x_γ distribution observed in dijet γp events for ZEUS data (black dots) compared with HERWIG (solid line and dotted line) with and without multiple parton interactions (*c. f.* Sec. 1.6), and PYTHIA Monte Carlo generator with multiple parton interactions (dashed line) [B$^+$98a]. The shaded area represents direct only events as generated by HERWIG and the vertical dotted line is the experimental cut to separate direct and resolved processes. The Monte Carlo generators are explained in detail in Sec. 1.7.

the Monte Carlo prediction is good except below 0.3. Here the soft underlying event is not correctly described by the generators, even if multiple parton interactions are allowed. A cut on $x_\gamma = 0.75$ is used to enrich direct and resolved γp events respectively and measure their angular dependence. Figure 1.14 confirms the QCD prediction. The resolved sample show a steeper rise due to the spin–1 gluon propagator as already predicted in Fig. 1.11.

1.3.4 Heavy Quark Photoproduction

In heavy quark production[7] up to NLO, two main schemes have been proposed. In the *fixed flavour–number scheme*, often referred to in the charm and beauty case as the *massive scheme*, the incoming photon and proton are given hadronic structures (*c. f.* Sec. 1.4) which contain only three quark flavours (u, d, s), the heavy quarks do not contribute to the evolution of the running coupling constant and the structure functions. QCD interactions are then generated in a hard scattering subprocess which produces heavy quark pairs, whose dynamics are calculated using a realistic quark mass assignment, m_{HQ}. Since the heavy quark excitation processes

[7] For a good review see *e. g.* [Beh05].

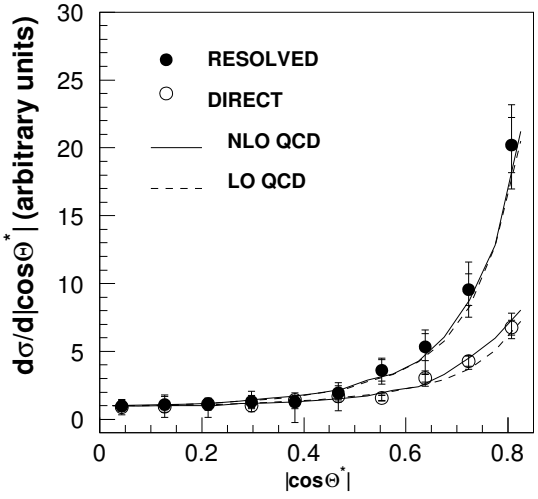

Figure 1.14: Dijet angular cross–sections for resolved (black dots) and direct (open circles) photoproduction at ZEUS compared to leading–order and next–to–leading order predictions [D$^+$96].

(see next paragraph) are not treated, and may be important at high energies, this scheme is expected to work best at $p_t = O(m_{HQ})$, because at high p_t neglected terms of the form $\ln(p_t^2/m^2)$ become large, and the series diverges. In the massive scheme, soft and collinear divergences are treated by generating sequences of correlated events such that cancellation of the sequences occur. This method developed in [MNR91] removes the need for artificial regularisation required when a light parton accompanies the heavy quark pair. The massive calculation for photoproduction [FMNR94] is heavily based on the hadroproduction calculations [MNR92, MNR93]. The calculation is implemented as an "effective parton Monte Carlo generator", known as the FMNR program.[8]

To enable heavy quark excitation to take place (see Fig. 1.15), charm and beauty are treated as active flavours in the proton or photon. In the more common *massless* versions, the mass m_{HQ} is set to zero allowing the resummation of the logarithms in p_t/m^2. QCD processes taking place at $p_t \approx m_{HQ}$ may therefore not be accurately described, but this approach should work well at high p_t [CG96]. Unfortunately up to now no computer codes for massless calculations in higher orders are available for ep scattering neither for photoproduction nor for deep inelastic scattering.

[8]For deep inelastic scattering the program HVQDIS is available [HS95].

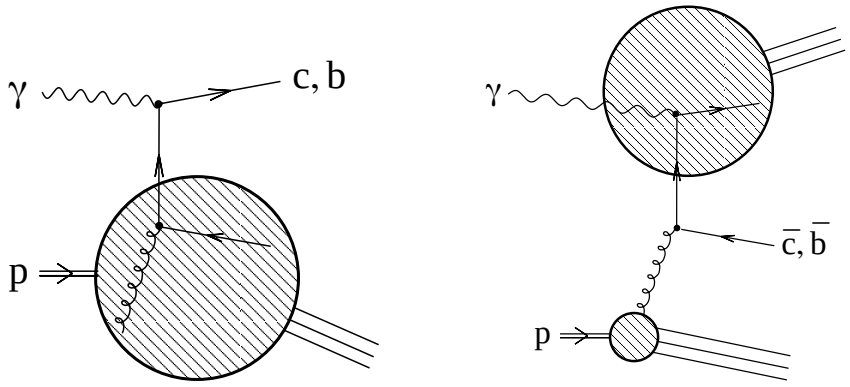

(a) p excitation (b) γ excitation

Figure 1.15: Examples of quark excitation processes. In (a) the heavy quark comes from gluon splitting in the proton. Its counterpart remains undetectable in the proton remnant. In (b) the heavy quark comes from a fluctuation of the photon.

1.4 Parton Distributions

1.4.1 Photon Structure

The splitting of a photon into a quark–antiquark pair can be calculated in the quark parton model (QPM). When a photon splits into a $q\bar{q}$ pair, the quark carries an energy fraction x_γ, measured relative to the photon energy. The functional form of $f_{q/\gamma}$ is the same as that of $f_{\gamma/e}$ given in Eqn. (1.9), scaled by the square of the quark charge, e_q, ignoring the correction term $2m_e^2 y\,(1/Q^2_{\min} - 1/Q^2_{\max})$:

$$f_{q/\gamma}(x_\gamma)[\mathrm{QPM}] = \frac{\alpha_{em}\, e_q^2}{\pi}\left(x_\gamma^2 + (1-x_\gamma)^2\right)\ln\frac{Q^2}{m_q^2}\,. \tag{1.29}$$

Here m_q is a measure of the mass of "free" quarks.[9] To compare with experiments, the probabilities $f_{q/\gamma}$ are summed over all colours and flavours resulting in a prediction for the photon structure function F_2^γ

$$F_2^\gamma(x_\gamma, Q^2) \;=\; 3x_\gamma \sum_{n_f} e_q^2\, f_{q/\gamma}(x_\gamma, Q^2)\,, \tag{1.30}$$

$$F_2^\gamma(x_\gamma, Q^2)[\mathrm{QPM}] \;=\; 3\sum_{n_f} \frac{\alpha_{em}\, e_q^4}{\pi}\, x_\gamma \left(x_\gamma^2 + (1-x_\gamma)^2\right)\ln\frac{Q^2}{m_q^2}\,. \tag{1.31}$$

[9] Interestingly enough a measurement of the analogous QED process resulted in a precise determination of the μ mass [C$^+$84].

This structure function has three features that are different from the hadronic structure functions:

1. The quark charges e_q contribute with the fourth power, compared with quadratic contributions in the hadronic case.
2. F_2^γ increases with increasing energy fraction x_γ.
3. The quasi–real photon depends directly on the scale Q^2 at which it is probed by a highly virtual photon. In hadronic structure functions, Q^2 only enters via the parton evolution (see below).

QCD corrections to the simple QPM photon structure function can be calculated, *e. g.* from DGLAP evolution equations[10][GL72, AP77, Alt82, Lip75, Doc77]

$$\frac{\mathrm{d}\, f_{q/\gamma}(x_\gamma, Q^2)}{\mathrm{d}\ln Q^2} = \frac{\alpha_{em}}{2\pi} e_q^2 P_{q\gamma}(x_\gamma) + \frac{\alpha_s}{2\pi}\left\{P_{qq}(x_\gamma) \otimes f_{q/\gamma}(x_\gamma, Q^2) + P_{qg}(x_\gamma) \otimes f_{g/\gamma}(x_\gamma, Q^2)\right\} \tag{1.32}$$

$$\frac{\mathrm{d}\, f_{g/\gamma}(x_\gamma, Q^2)}{\mathrm{d}\ln Q^2} = \frac{\alpha_s}{2\pi}\left\{2P_{gq}(x_\gamma) \otimes \sum_{n_f} f_{q/\gamma}(x_\gamma, Q^2) + P_{gg}(x_\gamma, n_f) \otimes f_{g/\gamma}(x_\gamma, Q^2)\right\} \tag{1.33}$$

Here $P_{ij}(z)$ denotes the splitting functions. The first term on the RHS of 1.32 describes the pointlike coupling of the photon. The sum in 1.33 runs over all quark flavours n_f. Explicit calculations of the leading order QCD diagrams show that[11]

$$P^0_{qq}(z) = \frac{4}{3}\left[\frac{1+z^2}{1-z}\right]_+, \tag{1.34}$$

$$P^0_{qg}(z) = \frac{1}{2}\left[z^2 + (1-z)^2\right], \tag{1.35}$$

$$P^0_{gq}(z) = \frac{4}{3}\left[\frac{1+(1-z)^2}{z}\right], \tag{1.36}$$

$$P^0_{gg}(z) = 6\left[\frac{z}{(1-z)_+} + \frac{1-z}{z} + z(1-z)\right] + \left(11 - \frac{2n_f}{3}\right)\delta(1-z). \tag{1.37}$$

[10]The convolution integral is defined as $a(x_\gamma) \otimes b(x_\gamma) = \int_{x_\gamma}^1 \frac{\mathrm{d}y}{y}\, a(x_\gamma/y)\, b(y)$.

[11]The "plus prescription" regularises the divergences of the splitting functions at $z = 1$. It is defined as $\int_x^1 \mathrm{d}x\, \phi(x)\, [F(x)]_+ = \int_x^1 \mathrm{d}x\, [\phi(x) - \phi(1)]\, F(x) - \phi(1) \int_0^x \mathrm{d}x\, F(x)$.

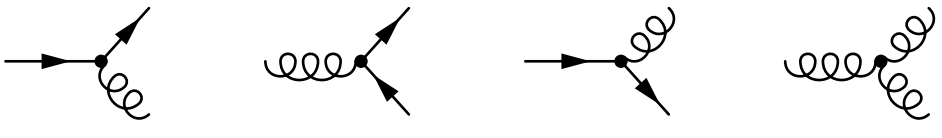

P_{qq} P_{qg} P_{gq} P_{gg}

Figure 1.16: The lowest order splitting functions. The splitting function $P_{qq}(x/z)$ is the probability that a parton q with momentum fraction z emits a gluon and goes down to momentum x. The same for splitting functions P_{gq}, P_{gg} and P_{qg}.

The physical interpretation of the splitting function P_{ij} is given by the variation of the parton densities. For a variation in $\ln Q^2$ it is the probability of finding a parton i inside parton j with a fraction z of the parent momentum. The DGLAP equations express the fact that a quark or gluon with momentum fraction x could have originated from a parent quark with momentum z, where $x < z < 1$ in the splitting function $P_{qq}(x/z)$, see Fig. 1.16. Hence in the DGLAP evolution one integrates over the momentum fraction z from x to 1. One can interprete the equations as description how the momentum distribution of the quark changes as Q^2 is increased, due to an increase of the resolution of the photon with which the partons are probed.

It can be shown that these QCD corrections preserve the $\ln Q^2$ dependence of the QPM photon structure function (*c. f.* Eqn. 1.29)[Wit77]. The leading order QCD prediction for the quark density in the photon is given by

$$f_{q/\gamma}(x_\gamma) = e_q^2 \frac{\alpha_{em}}{\pi} \left(x_\gamma^2 + (1 - x_\gamma)^2 \right) \ln \frac{Q^2}{\Lambda_{QCD}^2} . \tag{1.38}$$

The corresponding expression for the photon structure function is

$$F_2^\gamma(x_\gamma, Q^2) = 3 \sum_{n_f} e_q^4 \frac{\alpha_{em}}{\pi} x_\gamma \left(x_\gamma^2 + (1 - x_\gamma)^2 \right) \ln \frac{Q^2}{\Lambda_{QCD}} . \tag{1.39}$$

This equation accounts for the pointlike and anomalous photon contribution. Note that possible bound states of quark pairs are not included since they are not calculable by perturbative theory.

The photon structure function F_2^γ can be directly measured by deep inelastic electron–photon scattering experiments (see Fig. 1.17). This was done at the e^+e^- colliders PETRA and LEP. These experiments have established the anomalous photon component and the Q^2 scale dependence given in Eqn. 1.31. A compilation of the experimental results is given in Fig. 1.18. Since the anomalous photon

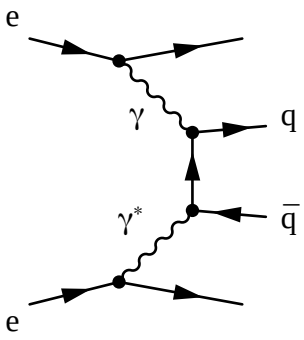

Figure 1.17: Deep inelastic eγ scattering: a highly virtual photon γ^* ($Q^2 \gg 1\,\mathrm{GeV}$) probes the quark content of a quasi–real photon γ ($Q^2 \approx 0\,\mathrm{GeV}^2$).

component cannot be separated in a unique way from the hadronic part of the photon structure function experimentally, a precise determination of Λ_{QCD} from the measured scale dependence is not possible.

Parametrisation of the Parton Distributions in the Photon

The parton distributions of the photon can be extracted from the measurements of the photon structure function using Eqn. 1.31 and the evolution equations 1.32 and 1.33. For use in simulations, parametrisations of the parton distributions were introduced, which contain the parton momenta at some scale, Q_0^2, and their Q^2 evolutions. More than a dozen parametrisation sets exist with most of them available in the PDFLIB [PB93]. They form the basis for the predictions of particle and jet production in hard photon–proton scattering at HERA.

Throughout this thesis a complete parametrisation of the real photon provided by Glück, Reya and Vogt (GRV) is used [GRV92]. This is available at leading and next–to–leading order (NLO) constructed at very low $Q_0^2(\mathrm{LO}) = 0.25\,\mathrm{GeV}^2$. Here it is assumed that the quark distributions in the photon have the same shape as in the pion structure function. The gluon content is set proportional to the quark content. The difference between the π and the γ distributions results from the first term in the evolution equation (1.32). They fit only one parameter to the DIS eγ data. Results are shown in Fig. 1.18.

It has to be noted that the DIS eγ data does not contain the gluon distribution in the resolved photon meaning that for low $x_\gamma \lesssim 0.2$ the two–jet rate at HERA cannot be explained by the quark contribution of the photon alone. However, there are indications that its shape and normalisation are correctly described by the GRV–LO parametrisation[A+95a].

1.4.2 Proton Structure

In contrast to the photon, the structure of the proton does not depend directly on the scale Q^2, but enters only via the parton evolution equations 1.32 and 1.33. In lowest order QCD the parton distributions in the proton do not depend on Q^2 at all. This experimentally observed “scaling” of the structure functions in DIS

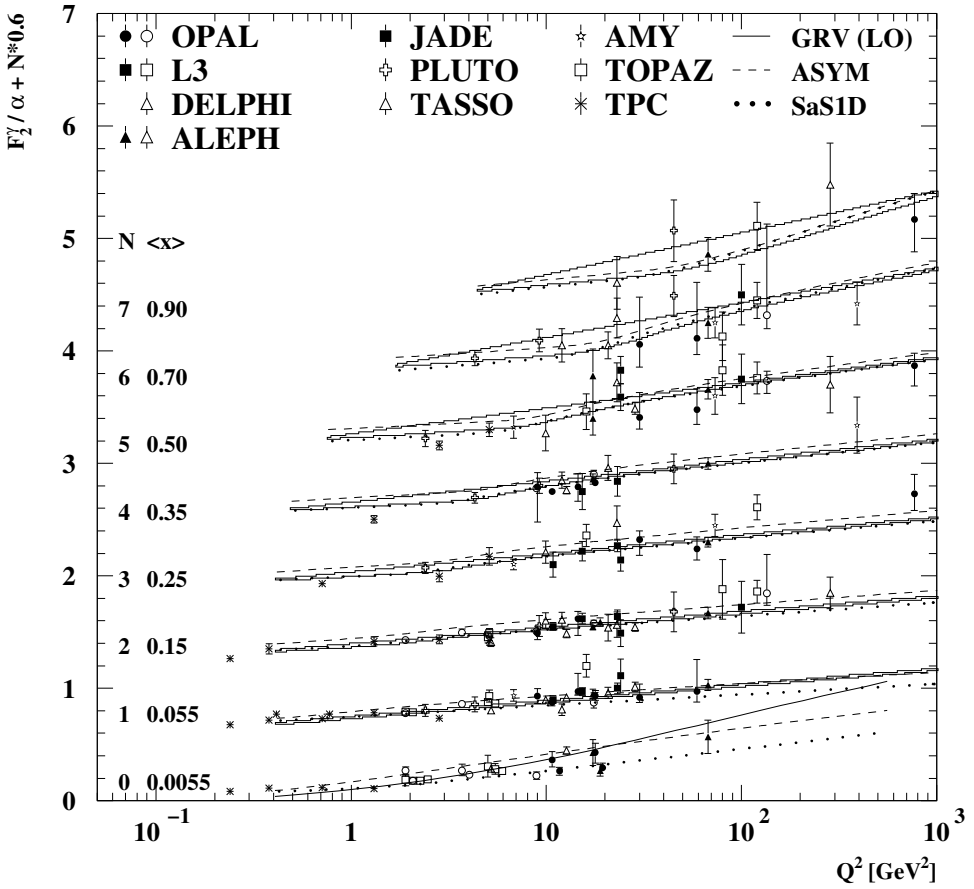

Figure 1.18: Measurements of the structure function F_2^γ. The data are drawn as a function of the photon virtuality Q^2 and at different parton energy fractions x_γ. The data are compared with LO parametrisations by GRV[GRV92] and others. This plot is an updated version (state of 2003) of that in [Nis00] taken from the author's website. Note the artificial vertical off-set of each set of measurements ($0.6 \cdot N$).

experiments was the first indication that hadrons consist of pointlike objects, the partons [Bjö69, Fey69, BP69].

Small violations of this scaling behaviour of the structure functions are generated by radiative QCD corrections. Calculations of these processes show that they are logarithmically UV divergent. These logarithmic divergences, parametrised by a scale $\mu_R^2 = Q_0^2$, are absorbed in the definition of the parton distribution functions. Moving to a different scale Q^2, the parton distribution functions are redefined to absorb the logarithmic terms in Q^2. Hence the parton distributions at different

values of Q^2 are related. As stated above the quark structure function can be computed for any values of Q^2 with the help of the DGLAP evolution, given some reference value $f_{q/\mathrm{p}}(x_\mathrm{p}, Q_0^2)$.

At high Q^2 a quark may have radiated a gluon and consequently have a fractional momentum, x_p, less than its original value. Alternatively it may have arisen from gluon splitting. At large values of x_p, where the valence quarks dominate, the quark density falls slightly with increasing Q^2, whereas at low x_p, the number of "sea" quarks and gluons is larger, so F_2^p increases with Q^2. This dependence of F_2^p on Q^2 has been demonstrated at HERA[A$^+$93, D$^+$93] as seen in Fig. 1.19.

At small values of x_p both the gluon and quark distributions grow rapidly due to the splitting of partons in the DGLAP equations. In this region most quarks are "sea quarks" originating from small–x_p gluons. The gluon splitting function is singular for $x_\mathrm{p} \to 0$, see Eqn. 1.37. This indicates that in higher order perturbation theory the terms which contain singular parts $1/x_\mathrm{p}$ become important at low x. In fact, for moderate Q^2, they contribute more than the leading logarithmic terms in Q^2. As an alternative to the DGLAP evolution equations, which resum the leading logarithmic terms in Q^2, the Balitsky, Fadin, Kuraev, Lipatov (BFKL) equations [BL78, KLF76, KLF77] resum the singular $\frac{1}{x_\mathrm{p}}$ terms. A unification of the two methods leading to a complete description of the parton distribution function's x_p and Q^2 dependence is an obvious goal, but its experimental verification as well as the theoretical treatment are challenging.

Parametrisations of the Proton Structure Functions

Similar to the photon parton distribution functions, all parametrisations of the proton structure functions are based on the QCD evolution of the universal quark distributions. These PDFs are evolved using the DGLAP equations and thus yield a parametrisation of the PDFs at all x_p and Q^2 given a boundary condition at a particular value $Q^2 = Q_0^2$. The aim is to chose the parton distributions at Q_0^2 such that the predicted cross–sections match all measured lepton–hadron and hadron–hadron data. In practice this means that at Q_0^2 a functional form for the quark distributions is chosen, which contains a number of free, tunable parameters. In a fit procedure the parameters are adjusted to obtain a parametrisation of the parton densities that match the existing data from deep inelastic scattering experiments.

There are a number of groups performing the global fit procedures for the hadronic structure functions. They all use next–to–leading order or even next–to–next–to-leading order QCD predictions for the evolution and, for DIS, use the NLO convolutions with the hard scattering to obtain the structure functions.

In this thesis the parametrisation of the CTEQ group [B$^+$93] is used, which is based on a NLO QCD evolution around $Q_0^2 = 4\,\mathrm{GeV}^2$. The flavours $\mathrm{u}, \bar{\mathrm{u}}, \mathrm{d}, \bar{\mathrm{d}}$ and $\mathrm{s}, \bar{\mathrm{s}}$ are evolved separately. In total approximately 30 free parameters are included.

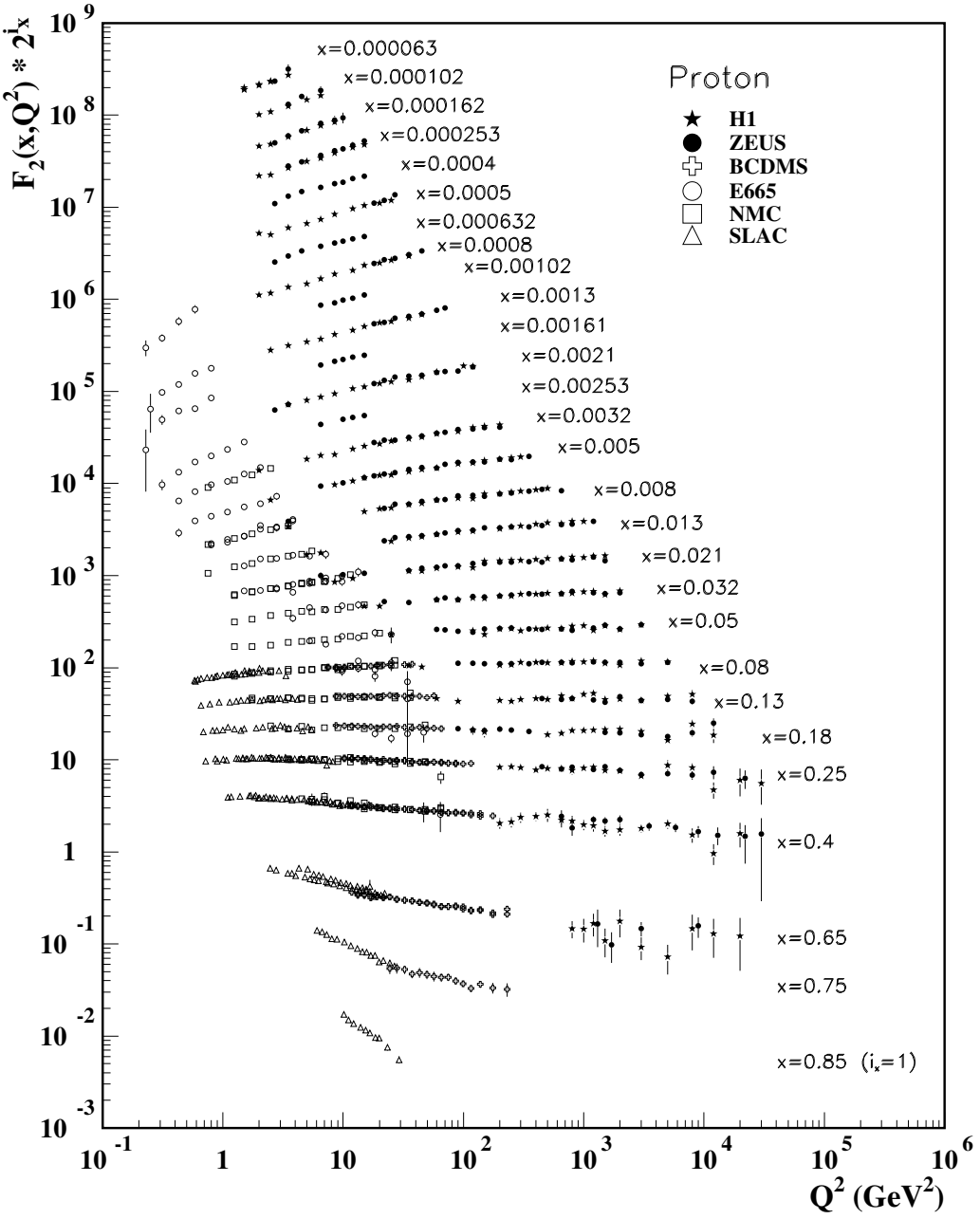

Figure 1.19: Dependence of the proton structure function $F_2^{\mathrm{p}}(x, Q^2)$ on the scale, Q^2, at fixed values of x_{p}. For large x_{p} the structure function is almost independent of Q^2 and depends only on x_{p}. For low x_{p} the structure function increases with Q^2 indicating that at high Q^2 the proton momentum is shared by many partons mainly due to the contributions of gluon splitting to $\mathrm{q\bar{q}}$ pairs (from [Y+06])

1.5 Fragmentation and Hadronisation

In the end the final–state parton cross-sections have to be transformed into measurable ones via a fragmentation process. Here, infrared safety must be preserved. A common method is to convolute the parton cross-sections with a fragmentation function $D_{h/k}(z, \mu_{frag})$ describing the fragmentation of a final–state parton, k, into a hadron, h, where $z = E_h/E_k$ denotes the energy fraction of the hadron relative to the parton energy, and μ_{frag} is the fragmentation scale usually set equal to the (mean) hadron transverse momentum $\mu_{frag} = p_t^h$. The fragmentation functions have been parametrised from results of e^+e^- and $p\bar{p}$ experiments. A standard representation of the fragmentation function of heavy quarks, based on phenomenological considerations, is the PETERSON fragmentation function:[P+83]

$$D_{h/k}(z) = \mathcal{P}_{h/k} \cdot \frac{\mathcal{A}}{z \cdot \left(1 - \frac{1}{z} - \frac{\epsilon}{1-z}\right)^2}, \tag{1.40}$$

where $\mathcal{A}$ is a normalisation constant and $\mathcal{P}_{h/k}$ the total probability for the quark k to fragment to h. The PETERSON–parameter ϵ is determined from experiment ([A+91a, A+92a], [B+88] and [A+96a, A+98, B+00, A+00b]). For a review see [NO99] or [NO00]. In Fig. 1.20 the fragmentation function $D_{h/k}(z)$ is shown using typical values for charm and beauty. As expected B hadrons are generated with a harder spectrum than charm hadrons. The accuracy of the quark and gluon fragmentation functions is of the order of a few percent [BKK95]. A list of the properties of the most frequently produced beauty and charm hadrons is given in Tab. 1.2. The practical side of modelling the fragmentation process will be discussed in more detail in Sec. 1.7.

For the light quarks the "LUND symmetric fragmentation function" [BA83] is often used:

$$D_{h/k}(z) = \mathcal{P}_{h/k} \cdot \frac{\mathcal{A}}{z}(1-z)^a \, e^{-bm_{t,h}^2/z}, \tag{1.41}$$

with $m_{t,h}$ denoting the transverse mass of the hadron in question. The parameters a and b are usually chosen to 0.3 and $0.58\,\mathrm{GeV}^{-2}$, respectively.

Beside the prediction of inclusive cross–sections of hadrons, which is used in Monte Carlo event generators and the subsequent detector simulation, cross–sections for jet production are also possible. Here, jet algorithms (*c. f.* Sec. 3.2) are used to integrate the energy of the fragmenting parton, as the energy is distributed to several hadrons during the fragmentation process.

Hadron	Content	Mass / MeV	$c\tau$ / μm	$I(J^P)$
$B^{\pm}$	bu	5279.0 ± 0.5	501	$\frac{1}{2}(0^-)$
B^0	bd	5279.4 ± 0.5	460	$\frac{1}{2}(0^-)$
B_s^0	bs	5369.6 ± 2.4	438	$0(0^-)$
Λ_b	udb	5624 ± 9	368	$0(\frac{1}{2}^+)$
$D^{\pm}$	cd	1869.4 ± 0.5	311.8	$\frac{1}{2}(0^-)$
D^0	cu	1864.6 ± 0.5	123.0	$\frac{1}{2}(0^-)$
$D_s^{\pm}$	cs	1968.3	147.0	$0(0^-)$
Λ_c^+	cud	2284.9 ± 0.6	59.9	$0(\frac{1}{2}^+)$

Table 1.2: Properties of the most frequently produced beauty and charm hadrons. The former have both a higher mass and a longer life–time. The higher mass is given by the b quark mass whereas the longer life–time results from mainly from the smaller CKM matrix element $||V_{cb}|| = 0.04$ compared with $||V_{cs}|| = 0.97$ [Y+06].

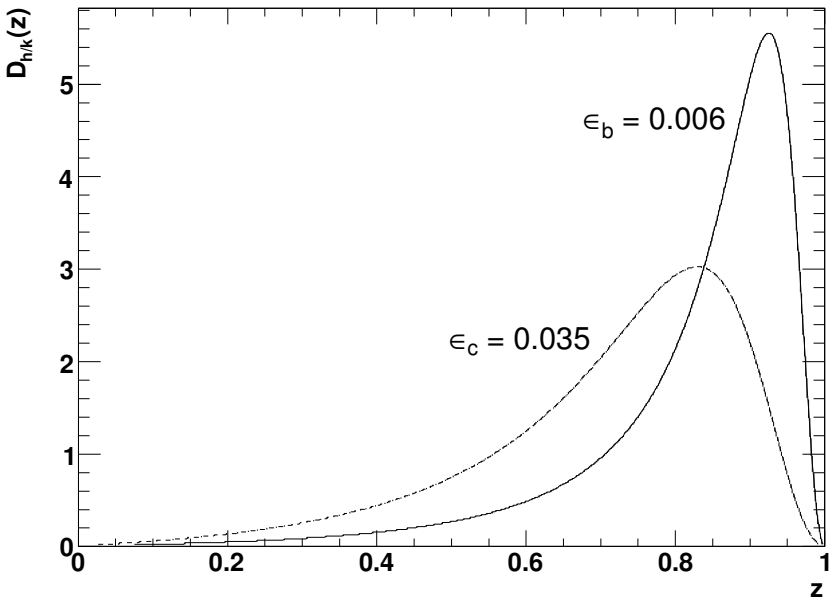

Figure 1.20: The PETERSON fragmentation $D_{h/k}(z)$ for typical values of ϵ for beauty and charm. Both functions shown are normalised to one. For heavy quarks a hard spectrum with a peak close to one is expected, since the hadron absorbs most of the parton's energy.

1.6 Multiple Parton Interaction

The QCD parton cross–section given above has two inherent problems: It diverges at small transverse momenta $\hat{p}_t$ of the scattered partons (see Eqn. 1.15), which is usually solved by introducing a lower cut–off. In addition it was shown that the integrated parton cross–section exceeds the measured total cross–section at high centre–of–mass energies [A$^+$95b, D$^+$94a]. A possible solution is to consider the proton and the resolved photons as beams of partons and to allow for more than one parton interaction in one observable γp event [SS93, SvZ87]. This also helps to describe the large measured underlying event energy which is seen for low x_γ [D$^+$94b].

1.7 Event Generators

For a quantitative analysis of scattering processes and unfolding of cross–sections event generators based on Monte Carlo methods are used. In combination with a detailed detector simulation they produce final–states comparable with real data.

A schematic view of a QCD event generator for ep scattering is shown in Fig. 1.21. The core of the program are the parton scattering processes Eqn. 1.15 together with the matrix elements given in Tab. 1.1. The partons from the photon and the proton coming into the hard sub–process are chosen via the parton distribution functions $f_{i/\gamma}$ and $f_{j/p}$. Parton showers originating from initial–state or final–state partons simulate higher order QCD processes. All partons, including those of the beam remnants, fragment into hadrons. Some generators allow for interactions between the beam remnants in addition to the hard parton scattering process.

In this work the PYTHIA event generator described below had been used. For completeness the HERWIG program, which is also used very often, will be discussed too.

1.7.1 PYTHIA

The PYTHIA program [S$^+$02] together with a generator for quasi–real photons generates γp interactions. It is based on leading order QCD matrix elements and includes initial–state and final–state parton showers. Usually the strong coupling constant, α_s, is computed to first order in QCD using $\Lambda_{QCD} = 200\,\text{MeV}$ with four flavours. Renormalisation and factorisation scales are both set to the transverse mass of the two outgoing partons, given by

$$\mu_F^2 = \frac{1}{2}\sqrt{m_1^2 + \hat{p}_{t,1}^2 + m_2^2 + \hat{p}_{t,2}^2}\,. \tag{1.42}$$

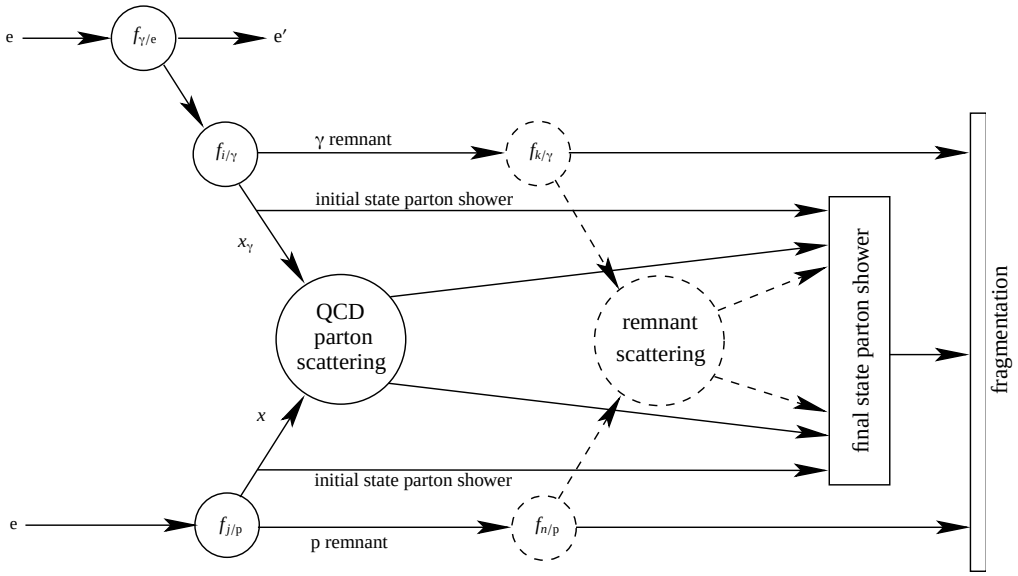

Figure 1.21: Schema of an event generator for hard scattering processes in ep collisions. The central part is the hard scatter given by the QCD parton cross–section ((1.15). The input parton distribution functions are $f_{i/\gamma}$ for the photon and $f_{j/p}$ for the proton. The γ luminosity $f_{\gamma/e}$ is described by the Weizsäcker–Williams approximation. Incoming and outgoing partons can radiate other partons (initial–state and final–state parton shower). Together with the spectator partons of the beam remnants they fragment into hadrons. Optionally, interactions between the two beam remnants can be generated in addition to the primary hard parton scattering process (multiple parton interactions).

For comparisons with data a lower cut–off around $\hat{p}_t^{cut} \approx 2\,\text{GeV}$ is used to avoid divergences for small transverse momenta.

The parton showers are computed with the help of the DGLAP evolution equations. Since the hard sub–process sets the overall event kinematics, the initial–state parton shower is evolved backwards in a sequence of decreasing space–like virtualities Q^2 starting at a scale Q^2_{max} down to a cut–off $Q_0^2 \approx 1\,\text{GeV}^2$. In a similar way the final–state radiation is evolved backwards in time–like showers. Branchings on both sides are interweaved in a common sequence of decreasing Q^2 values.

The LUND string fragmentation scheme[SB87] is used (Fig. 1.22). Partons are connected by "strings", the strength of which is about $1\,\text{GeV/fm}$. As the partons move away from each other, the strings become more energetic, finally breaking to produce $q\bar{q}$ pairs. When the energy of a string is too small to enable further separation the partons, hadrons are formed. The transverse momenta of the generated $q\bar{q}$ pairs are Gaussian distributed, while the longitudinal component is obtained by using the PETERSON function for heavy quarks and the LUND symmetric fragmentation function for light flavours (Sec. 1.5).

In addition to the primary parton–parton scattering multiple parton interactions may be generated. These are calculated as leading order QCD processes between partons from the photon and proton remnants. The number of additional interactions is typically between 1 and 4. The process with the highest momentum in the final–state can be any quark or gluon process (Tab. 1.1). This process includes initial–state and final–state parton radiation effects and its partons are connected to the beam remnants by strings. The remaining low momentum interactions are calculated as gluon–gluon scattering processes.

1.7.2 HERWIG

The HERWIG[12] generator is based on leading order QCD calculations [MWA+92] too. The number of free parameters is much reduced. Particular attention is paid to being as independent as possible from non–perturbative parameters. The factorisation scale for the hard sub–process, μ_F, is given by

$$\mu_F^2 = \frac{2\,\hat{s}\cdot\hat{t}\cdot\hat{u}}{\hat{s}^2+\hat{t}^2+\hat{u}^2} \tag{1.43}$$

where $\hat{s}$, $\hat{t}$ and $\hat{u}$ are the Mandelstam variables of the parton scattering process. The lower cut–off for the transverse momentum of the scattered partons is set to $\hat{p}_t^{cut} \approx 2.5\,\text{GeV}$. In contrast to PYTHIA the Weizsäcker–Williams approximation is only used for resolved processes. For direct events, leading order matrix elements for $2 \rightarrow 3$ scattering are applied. The program includes a parton shower model, which allows for interference between initial–state and final–state showers, so-called *colour coherence* [MW84, MW88]. A cluster model is used for describing the hadronisation effects (see Fig. 1.22). In this model gluons at the end of the parton shower are split into $q\bar{q}$ pairs which are then grouped into colour neutral clusters adjacent in phase–space. Each of these clusters is then fragmented into two hadrons or the lightest hadron of its flavour if the cluster is not massive enough. The advantage of the cluster fragmentation over the string model is its small number of free parameters. Also, no assumption about transverse and longitudinal momentum distributions are needed. HERWIG also has options of allowing for interactions between the beam remnants in order to describe the soft underlying event.

In this analysis PYTHIA was used for the simulation. The main reason was, that large Monte Carlo samples produced with PYTHIA for other analyses were already existing. This saved a lot of computing time.

[12] Hadron Emission Reactions with Interfering Gluons

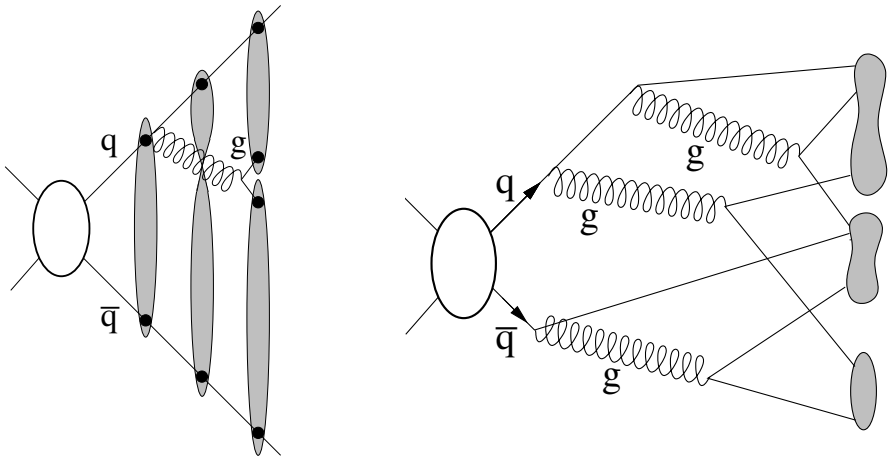

(a) String fragmentation (b) Cluster fragmentation

Figure 1.22: In (a) the colour dipole field of the outgoing $q\bar{q}$ pair is represented by a uniform colour flux tube (string) whose energy increases linearly with its length when the quarks are moving apart. At some point the energy density becomes high enough, forcing the string to break up forming a new $q\bar{q}$ pair. The cluster fragmentation (b) is directly connected with the parton shower. Radiated gluons are split into $q\bar{q}$ pairs forming colourless cluster close by in phase–space. The clusters usually fragment into two hadrons.

1.8 Semi–Leptonic Decays

Beauty quarks in hadrons decay weakly into a c or a u quark, where the former is much more dominant due to the CKM matrix elements. The following decay channels do exist:

1. External W radiation. Here, the b quark decays into a c quark radiating a W–boson. The W creates either $\ell\bar{\nu}_\ell$ or $d\bar{u}$, $s\bar{d}$ pairs. The decay products are independent of the newly created charmed hadron. The process is described in the *spectator model*: Due to its large mass the decay of the b quark is not affected by the other constituents in the hadron — they merely act as spectators. This process is by far the dominant one.

2. Internal W radiation. The W creates a $q\bar{q}$–pair whose parts connect both with the decay product of the b quark and the spectator quarks. The process is suppressed due to colour conservation.

3. W exchange and W annihilation. Both decay channels are suppressed by helicity arguments. W exchange is further suppressed by colour conservation, while the small value of the CKM matrix element V_{ub} diminishes the annihilation process.

Hadron	Content	Mass [MeV]	τ[ps]	Fraction [%]
B^+	$\bar{b}u$	5279.0 ± 0.5	1.638 ± 0.011	39.8 ± 1.2
B^0	$\bar{b}d$	5279.4 ± 0.5	1.530 ± 0.009	39.8 ± 1.2
B_s^0	$\bar{b}s$	5367.5 ± 1.8	1.466 ± 0.059	10.3 ± 1.4
Λ_b	bdu	5624 ± 9	1.230 ± 0.074	10.0 ± 2.0

Table 1.3: B hadron properties[Y$^+$06]. The fraction denotes the amount of a particular hadron type in B hadron admixtures at high energies.

4. Penguin decays. These are higher order flavour changing neutral current processes which are forbidden in leading order and thus very rare.

Table 1.3 lists a few properties of common B hadrons. On average B hadrons decay with a probability of 10.57 ± 0.22 % semi–leptonically into an electron or muon and the respective neutrino [Y$^+$06]. Modern predictions given by the heavy quark effective theory (HQET) are in good agreement with the latest measurements from the B factories BABAR and BELLE [A$^+$03, A$^+$02].

Figure 1.23 shows semi–leptonic decay spectra of B mesons into electrons measured by BABAR and BELLE. Good agreement with the PYTHIA prediction is found. The PYTHIA prediction is also valid in different production environments as shown in Fig. 1.24. Therefore the validity of the PYTHIA calculations for semi-leptonic B decays at HERA is well supported.

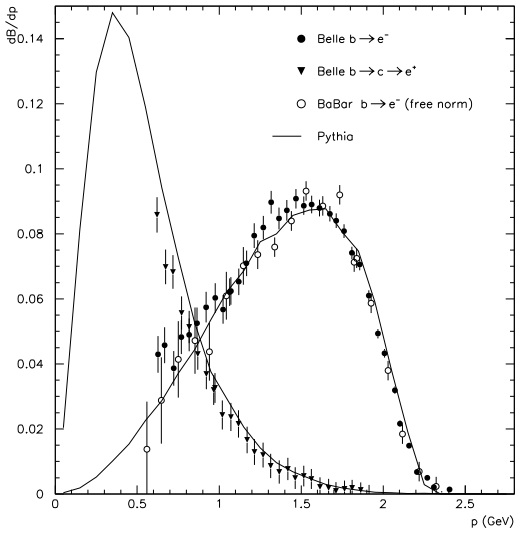

Figure 1.23: Branching ratios of semi–leptonic B meson decays into electrons dependent on the electron momentum in the centre–of–mass system of the B meson as measured by the BABAR and BELLE collaborations. The circles show the spectrum for direct decays whereas the triangles show cascade decays. The measurements are compared to the PYTHIA prediction. Courtesy of [A$^+$03, A$^+$02].

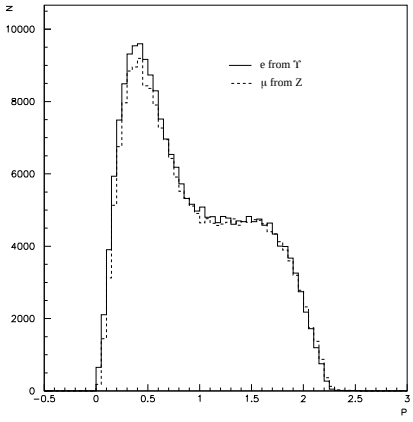

Figure 1.24: Comparison of predictions for semi–leptonic decays of B hadrons into electrons and muons made with PYTHIA. Shown are event rates dependent on the electron momentum in the B hadron rest frame for B hadron admixtures at the ϒ(4s) resonance at BABAR/BELLE (solid line) and at the Z pole at LEP (dotted line). Figure taken from [CT04].

1.9 Experimental Results

1.9.1 Heavy Quark Production in Fixed–Target Experiments

Pair production of beauty and charm has been studied at a number of fixed–target experiments. Since in most of these experiments the centre–of–mass energy typically is between 10 and 40 GeV, the beauty cross-sections are quite small there. In Fig. 1.25 a compilation of results for total cross–sections is shown. Overall, good agreement with QCD next–to–leading order predictions can be seen. The default choices for the factorisation scale, μ_F, and the renormalisation scale, μ_R, are $\mu_F = 2m_c$, $\mu_R = m_c$ for charm, and $\mu_F = \mu_R = m_b$ for beauty.[13] The bands around the predictions are obtained by varying μ_R between half the central value and twice this value and, in case of beauty by varying also μ_F in the same way.

1.9.2 Heavy Quark Production at HERA

The study of heavy quark production at HERA is a subject of great interest since the HERA collider operates at centre–of–mass energies of the γp system roughly one order of magnitude larger than those of fixed–target experiments. At these energies the $c\bar{c}$ production cross–section is of the order of 1 μb while the beauty cross–section is about 10 nb. In the following results for charm and beauty production obtained by the H1 and ZEUS experiments are discussed.[14]

[13] This is because the adopted parametrisations of parton densities are given for Q^2 larger than 5 GeV^2.

[14] A recent summary is found in [Beh05].

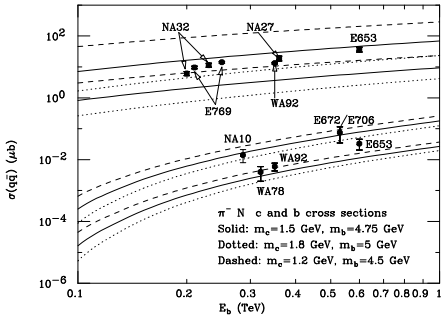

(a) Beauty and charm production in π^-N collisions.

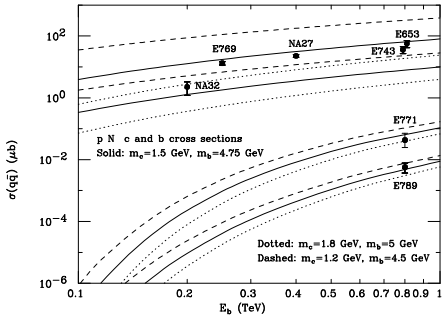

(b) Beauty and charm production in pN collisions

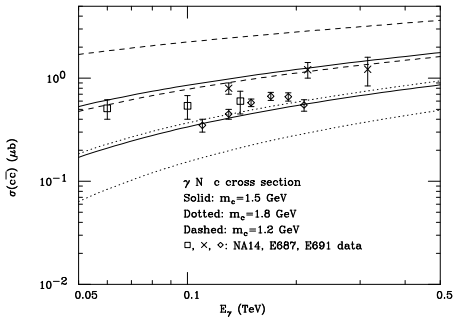

(c) Charm production in γN collisions

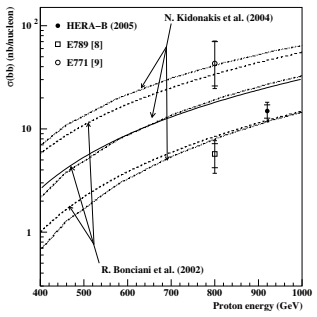

(d) Beauty production in pN collisions

Figure 1.25: Different total cross–sections for beauty and charm production in hadro– and photoproduction observed in fixed–target experiments. The data is in good agreement with NLO QCD predictions also shown. Figures taken from [FMNR98] and [A$^+$05a].

Charm Photoproduction

For charm production the uncertainties of the next–to–leading order predictions are large [FMNR95]. The cross–sections for the direct photon component changes by a factor of four when varying the charm mass in the range $1.2 < m_c < 1.8\,\text{GeV}$, and by a factor of two when varying the renormalisation scale. The choice of the proton parton distribution functions gives a 50 % uncertainty at $\sqrt{s_{\gamma p}} = 300\,\text{GeV}$. The situation is even worse for the resolved part since the gluon distribution in the photon is poorly known (*c. f.* Sec. 1.4.1). Figure 1.26 shows a comparison between the experimental results and the next–to–leading order QCD predictions. The calculations were made for different sets of parametrisations of the parton distributions for the photon and the proton. Only the uncertainty due to a vari-

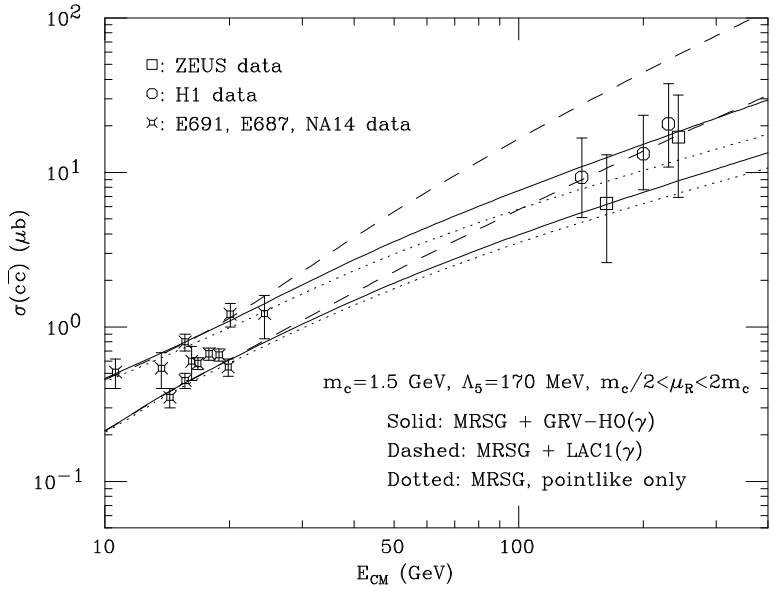

Figure 1.26: Total cross–section for charm photoproduction as a function of the γp centre–of–mass energy. Measurements of fixed–target and the HERA experiments are shown. The NLO prediction is shown for three different set of photon and proton parton distribution functions. Only the uncertainties due to the choice of the renormalisation scale is displayed. The fixed–target data is the same as in Fig. 1.25(c), the HERA data was taken from [A^+96b, D^+95a]. Figure courtesy of [FMNR98].

ation of the renormalisation scale, as described above, is displayed. Although the theoretical uncertainties are huge, it is noteworthy that a single choice of input parameters is sufficient to describe the data in the whole energy range. Also, the importance of the resolved photon component becomes clear from the figure. It has to be noted that the measured cross–sections are extrapolated to the full pseudo–rapidity and transverse momentum range. This usually involves extrapolation to the small–x region for which the parton distributions are not very well determined, as mentioned above.

Charm is often tagged by searching for "golden decays" of $D^{*\pm}$ into $K\pi\pi$ via a D^0 intermediate state. In Fig. 1.27 the transverse momentum distribution of D^* as measured at HERA is shown together with next–to–leading order predictions computed in a massless and a massive scheme (*c. f.* Sec. 1.3.4). Neither of the schemes is able to describe the data well. The massless prediction is better at low p_t, while the massive one looks better at high transverse momenta.

Measurements of the angular dependence in the parton sub-system (for details see Sec. 1.3.3) of charm dijet events show evidence for a large charm component in the resolved photon.

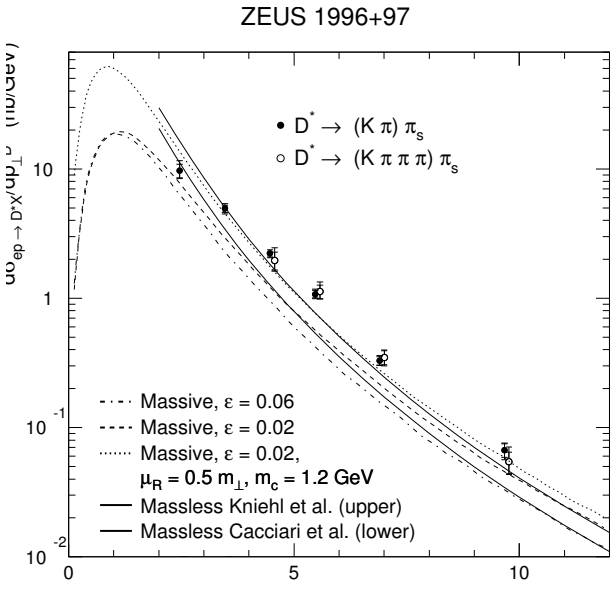

Figure 1.27: Transverse momentum spectrum of D^* in γp interactions at HERA compared with massive [FMNR95, F^+95] and massless [K^+97, B^+97, C^+97] next–to–leading order predictions. The NLO calculations are generally below the measured cross–sections. Figure taken from [B^+99].

Charm in Deep Inelastic Scattering

Measurements of the Q^2 dependence of charm production cross–sections in deep inelastic scattering events provide information about the proton structure. A direct determination of the gluon density in the proton is possible via the boson–gluon–fusion which dominates the charm production. These observations are in agreement with indirect measurements of the gluon density.

In addition, the charm contribution to the proton structure function, $F_2^{c\bar{c}}$, can be measured. The ZEUS collaboration has performed such measurements which are shown in Fig. 1.28 together with a next–to–leading order QCD prediction [C^+04d]. The charm contribution increases with decreasing x_p and increasing Q^2 due to the increasing gluon density in this region. Charm fractions up to 30 % to the proton structure function F_2^p are seen at small x_p.

In general, the charm DIS data is well described by massive next–to–leading order QCD models.

Beauty Photoproduction

Because of the higher quark mass, perturbative QCD predictions for $b\bar{b}$ production should be more reliable than those for charm. All the uncertainties discussed above for charm are strongly reduced. In direct photoproduction the uncertainty is a factor two if all parameters are varied together [FMNR98]. The resolved component still has larger uncertainties, but is much smaller than in charm production, because the small–x_p region is probed to a lesser extent.

The production rates for beauty are much reduced due to the smaller phase–

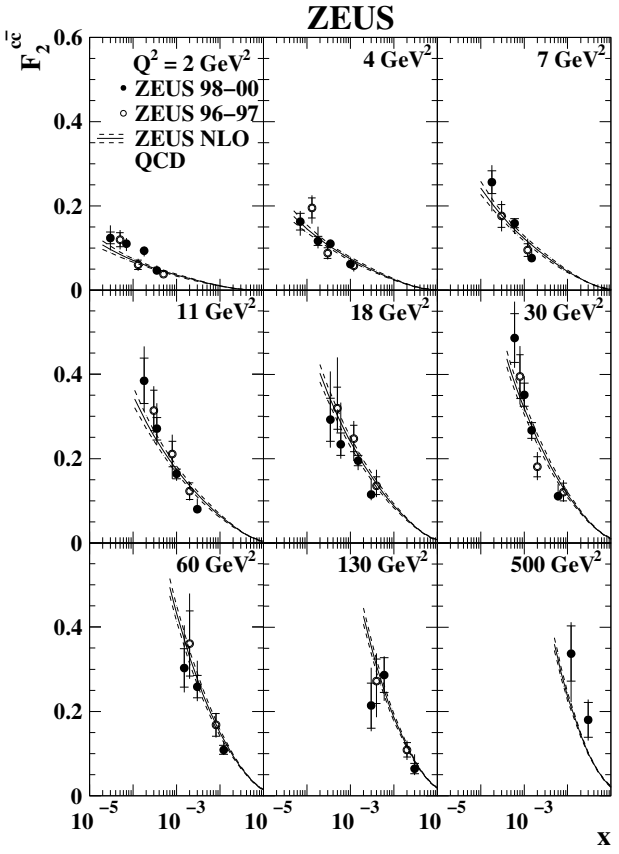

Figure 1.28: Measurements of the charm contribution to the proton structure function, $F_2^{c\bar{c}}$, at ZEUS in terms of the Björken scaling variable, x_p, for different four–momentum transfers, Q^2. A fit with QCD next–to–leading order predictions is also shown.

space. The total production cross–section ratios are roughly $\sigma_{uds} : \sigma_{c\bar{c}} : \sigma_{b\bar{b}} \approx 2000 : 200 : 1$ at HERA. The kinematical threshold for heavy quark production via the boson–gluon–fusion process at HERA is estimated by

$$x_g > \frac{m_{HQ}^2}{E_\gamma \cdot E_p} \approx \begin{cases} 10^{-4} & \text{charm production,} \\ 10^{-3} & \text{beauty production.} \end{cases} \quad (1.44)$$

From this it becomes clear that beauty production suffers less from the ignorance of the small–x_p region of the proton structure than in the charm case.

First measurements of open beauty production at ZEUS had been done in dijet photoproduction events of the data taken in 1996/97, corresponding to an integrated luminosity of 38.5 pb^{-1}, by looking for electrons coming from semi–leptonic B decays [B$^+$01, Win99]. The transverse momentum of the electron relative to the closest jet, p_t^{rel}, was used for determination of the beauty fraction by fitting template distributions of beauty, charm and light–flavour Monte Carlo samples to the data (see Fig. 1.29). Here, the p_t^{rel} distribution of electrons coming from beauty decays is supposed to be harder due to the large B hadron mass. The

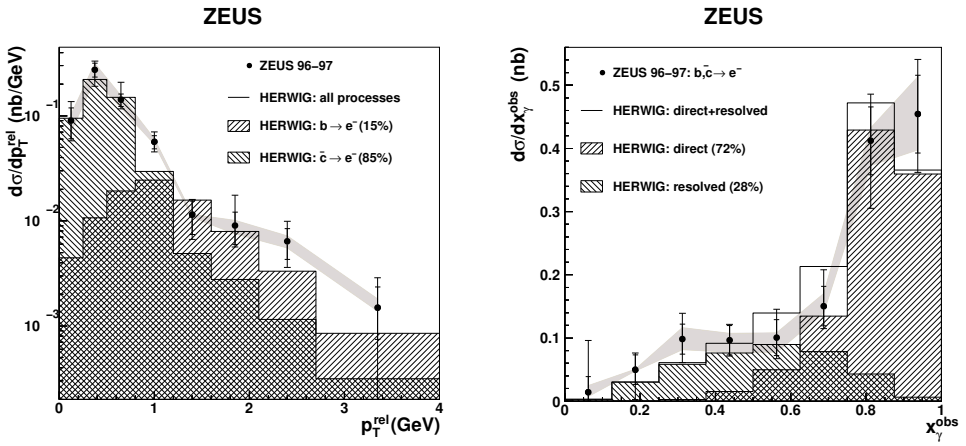

(a) p_t^{rel} distribution (b) x_γ distribution

Figure 1.29: First measurements of open beauty production at ZEUS by means of semi–leptonic B decays into electrons. From the p_t^{rel} distribution (a) a beauty fraction of 15 % was determined [B$^+$01]. In addition the amount of resolved events was observed to be ≈ 28 % with the help of the x_γ distribution. The light bands denote the uncertainty due to the jet energy scale.

electron identification was done in a simple way by using energy loss measurements in the central drift chamber of the ZEUS detector. This analysis was very limited in statistics due to the small amount of data available at that time. Also, it suffered a lot from systematic uncertainties, in particular in the estimation of the hadronic background and the energy loss measurements. For that reason positrons coming from the semi–leptonic beauty decays could not be used at all, cutting the statistics by half. The measured cross–section is substantially above a massive next–to–leading order prediction (open circle in Fig. 1.30).

Because of their much easier identification, muons from semi–leptonic B decays are often used instead of electrons. However, for a good background suppression the muon has to have a relatively high minimal transverse momentum, usually above $p_t^{min} \gtrsim 2$ GeV. Such measurements have been performed first by the H1 collaboration [A$^+$99, A$^+$05c] and later also by ZEUS [Tur02, C$^+$04a, Gut05]. Some results can be seen in Fig. 1.30 (filled circles). All of the measurements lie systematically above the NLO prediction.

Such measurements can be improved by using life–time information about the B hadrons in addition to the p_t^{rel} variable. For this the beauty decay vertices are measured by micro–vertex detectors such as the Central Silicon Tracker in the H1 detector, which has been operational since 1997, or the Micro–Vertex Detector in ZEUS, which is part of the detector since the beginning of the HERA-II period. Figure 1.31 shows the latest results published by the H1collaboration using only

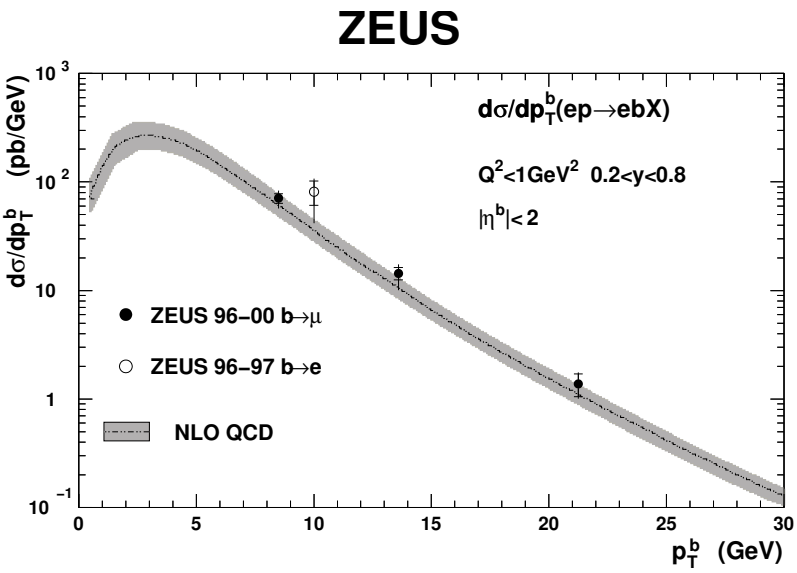

Figure 1.30: Measurements of beauty photoproduction in events containing two jets at ZEUS for the HERA-I running period. Shown are the results of two measurements, one observing semi–leptonic B decays to electrons (empty circle) and the other decays into muons (filled circles). Also shown is a massive next–to–leading order QCD prediction calculated with the FMNR program. Figure taken from [C$^+$04a].

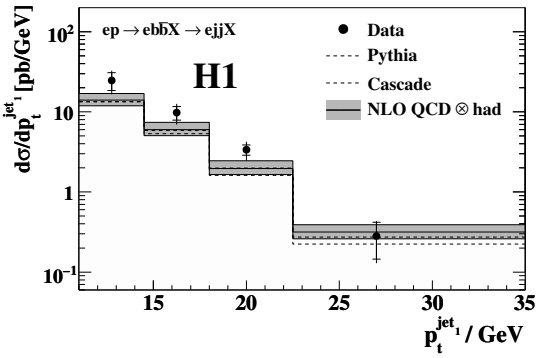

Figure 1.31: H1 latest measurement of beauty photoproduction based on impact parameter distributions compared to leading order and next–to–leading order QCD predictions [A$^+$06a].

impact parameter[15] information [A$^+$06a].

Other methods for measuring beauty production cross-sections at HERA are life–time tagging of J/ψ mesons originating from B decays [Lüd01] or measure-

[15]The *signed* impact parameter is the shortest lateral distance between the beam–spot and a track helix multiplied by the sign of the helix charge. For tracks originating from long–living B hadrons the impact parameter is supposed to concentrate at large positive values. The impact parameter is much easier to reconstruct than the actual decay length of a B hadron.

ments of correlated $D^*\mu$ systems in B cascades decays or di-muons in $b\bar{b}$ events [Blo05]. Here also an excess of the measured cross-sections compared to the QCD predictions is seen.

Beauty in Deep Inelastic Scattering

Similar measurements as above have been done for deep inelastic scattering [C+04c, A+06b]. From this the beauty contribution to the proton structure function can be determined. First results given by the H1 collaboration are shown in Fig. 1.32.

Summary on Open Beauty Production at HERA

Figure 1.33 summarises the present situation of open beauty production at HERA both for photoproduction and deep inelastic scattering. Since the measurements are defined using different experimental acceptances, they are plotted as a ratio of the measured cross–sections to the massive QCD predictions at next–to–leading order. The integrated beauty cross–sections at HERA lie constantly above the theory whenever the experimental errors permit such a statement. The measurements get much more precise by using impact parameter information. Still, improved measurements are desirable in order to falsify particular approaches at next–to–leading order.

For the sake of simplicity theoretical uncertainties are not shown. Only changes in the prediction caused by using different parametrisations of the proton structure are indicated. Uncertainties due to variations of the renormalisation and factorisation scales depending on the b quark mass in the end, and also due to the ignorance of the gluon contribution to the photon structure are expected to be large. Massless calculations are not available for the full Q^2 range at HERA. Recent approaches like the FONLL scheme (see below) do not exist at all for ep collisions.

1.9.3 Heavy Quark Production at LEP

Measurements of open heavy quark production in two–photon processes have been made at the LEP experiments OPAL, DELPHI and L3. The process used for the production of heavy quarks is that of deep inelastic $e\gamma$ scattering (*c. f.* Fig. 1.17) which is very sensitive to the parton distributions in the photon. Beauty and charm contributions were determined by fitting p_t^{rel} distributions of electrons and muons. The L3 results [A+05b] are shown in Fig. 1.34. While the charm cross–sections are described fairly well by a next–to–leading order prediction, the beauty measurement is 3σ above the expectation.

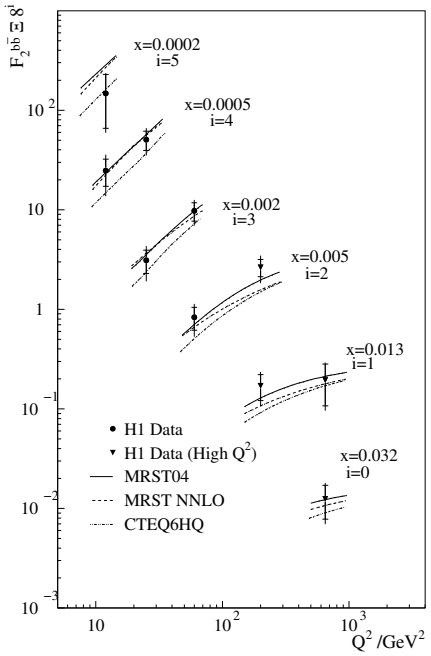

Figure 1.32: Measurements of $F_2^{b\bar{b}}$ based on the impact parameter method [A$^+$06b]. Shown are sets of measurements for different values of the Björken scaling variable x_p as a function of the four–momentum transfer, Q^2. Also shown are different parametrisations of the proton structure.

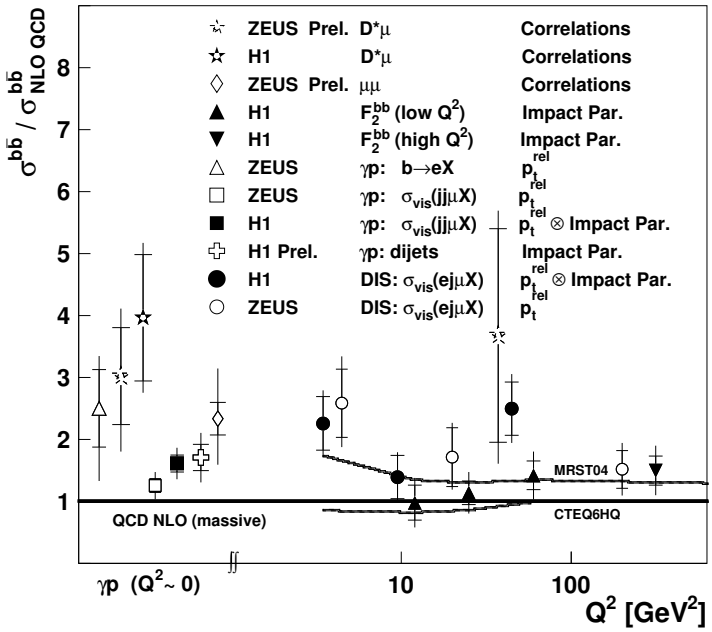

Figure 1.33: Open beauty production at HERA as a function of Q^2. Plotted is the ratio of the measured total cross–sections to massive NLO predictions. On the left are the γp measurements at $Q^2 \approx 0$. Only theoretical uncertainties due to different parametrisations of the proton structure are indicated.

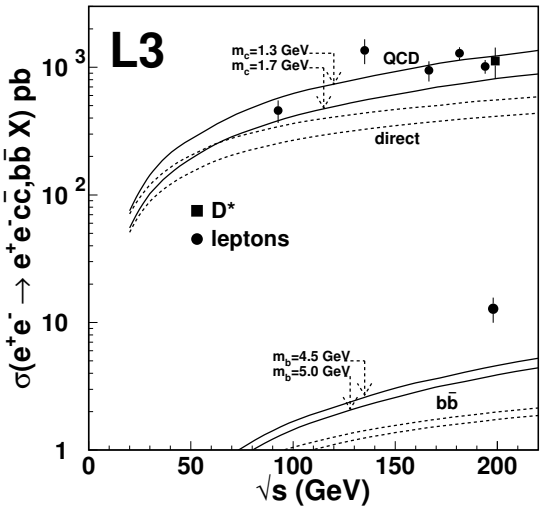

Figure 1.34: Production cross–sections for open charm and beauty dependent on the LEP centre–of–mass energy, measured by the L3 collaboration [A+05b]. In contrast to the beauty measurement, which is above the NLO prediction, the measured charm cross–sections agree well with the predictions.

1.9.4 Heavy Quark Production at the Tevatron

Beauty production has also been studied in $p\bar{p}$ collisions at the Tevatron at the highest possible centre–of–mass energies above 1.8 TeV. The Tevatron run I measurements confirmed the observations made by LEP and HERA. The beauty production cross–sections are systematically above the QCD predictions as seen in Fig. 1.35(a). Over the last years this long standing difference has been reduced by refining the experimental and most particularly the theoretical methods (for a review see [Man04]). The latter was achieved by introduction of the *fixed order and next–to–leading log scheme* (FONLL) resumming higher terms in $\ln(p_t/m)$ of the heavy quarks [FM97], and the use of improved fragmentation and parton distribution functions. An example of these promising results is given in Fig. 1.35(b). Unfortunately those new predictions are not yet available for ep collisions.

1.10 Summary

1. QCD is the present theory of the strong interaction describing an large number of phenomena. Theoretical predictions in high energy physics are based on perturbation theory by means of power series in terms of the strong coupling constant, α_s.

2. Heavy quark production in γp scattering processes at HERA is described with the help of the QCD factorisation theorems by dividing the process in a short–range hard scatter and external soft processes summarised in parton distribution functions of the photon and the proton. Here, the photon reveals a large hadronic component, since in the target rest frame the time of $\gamma \to q\bar{q}$

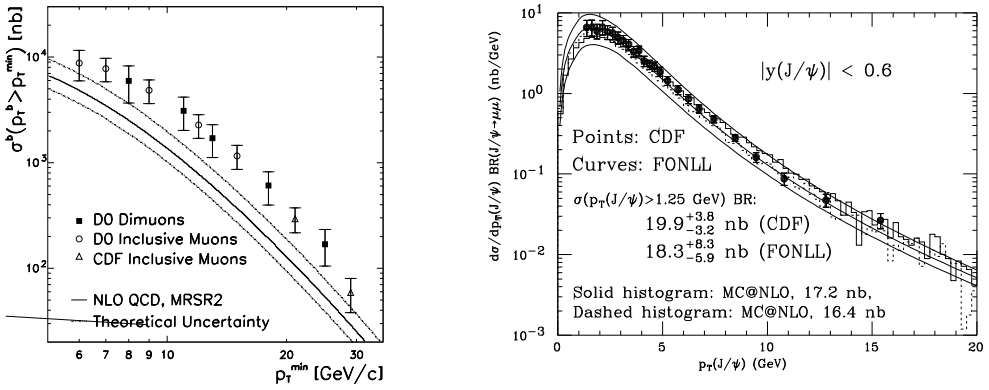

(a) Run I (b) Run II

Figure 1.35: Open beauty production in $p\bar{p}$ collisions at the Tevatron. In (a) older measurements from the CDF and D0 collaborations are shown [A$^+$00a]. The beauty contribution was determined with the help of muons coming from semi–leptonic B decays. The beauty production cross-sections, shown as function of the transverse b quark momenta, p_t^b, differ a lot from a QCD next–to–leading order prediction also shown. The situation is much improved in (b). Here, results of an analysis of J/ψ mesons originating from B decays in Tevatron run II data are shown with improved NLO calculations, FONLL (see text) and MC@NLO. The latter is a first try of a next–to–leading order QCD Monte Carlo event generator developed recently. Figure taken from [Man04].

fluctuations is very large compared to the size of a nucleon.

3. For the hard sub-process, predictions at leading order and next–to–leading order exist. The latter are of great interest, for the dependence on the factorisation and renormalisation scales is much reduced compared to leading order. Still, uncertainties due to those dependencies are large, for charm production more than for beauty. Different schemes such as the massive or the massless schemes have been developed for controlling divergences in the calculations. From the experimental point of view a decision between the different approaches is not yet possible.

4. Due to soft interactions and bound states the parton distributions in the photon are not fully calculable by perturbative QCD. Measurements from $\gamma\gamma$ scattering do exist, although they are not very precise. In particular our ignorance about the gluon and sea–quark contributions to the photon lead to a substantial uncertainty. The proton structure has been determined very precisely by analysing deep inelastic scattering events at HERA over a wide kinematic range. However, the small–x region is not measured very well, which in particular affects the predictions for charm production.

5. Hard gluon radiation and splitting is described by evolution of the parton distributions mainly by using the DGLAP equations. The fragmentation process of outgoing partons into final–state hadrons is modelled by phenomenological approaches.

6. Heavy quark production has been observed in fixed–target experiments as well as in recent collider experiments at LEP, HERA and the Tevatron. Many measurements and analyses of the still increasing data are ongoing leading to more precise results. Beside measurements of integrated and single–differential cross–sections, first measurements of doubly differential cross–sections have been published, providing more stringent tests of QCD. By using different experimental methods, cross–checks and reduction of systematic mis-measurements are possible. The ZEUS collaboration will publish first measurements utilising its micro–vertex detector in due time.

7. The overall situation of heavy quark production at HERA is unsatisfactory. Our knowledge, both experimentally and theoretically, is somewhat mixed and limited. While the experimental side is improving steadily, developments on the theoretical side are gradual. Many massless calculations are missing and most important, a generally applicable NLO Monte Carlo event generator is overdue. The next decade of high energy particle physics will be dominated by the large hadron collider, LHC. A detailed understanding of QCD is mandatory before it is possible to claim new physics beyond the standard model.

Chapter 2

The ZEUS Detector at HERA

In this chapter first the HERA machine is introduced and next an overview of the ZEUS detector is presented. In addition the ZEUS data acquisition system and the on-line reconstruction is discussed.

2.1 HERA Collider

The lepton–proton collider HERA located at DESY Hamburg, Germany started operation in 1992. The centre–of–mass energies are one order of magnitude above previous similar experiments and reach up to $\sqrt{s_{\mathrm{ep}}} \approx 300,\ 318\,\mathrm{GeV}$ for the HERA-I running period and 318 GeV for HERA-II, respectively.[1] The separate storage rings for the protons and electrons have a circumference of 6.3 km and provide four interaction regions. Two of them are used for the collision experiments H1 and ZEUS. Figure 2.1 shows the HERA ring system.

The energy of the proton beam had been $E_{\mathrm{p}} = 820\,\mathrm{GeV}$ at the beginning and was increased in 1998 to 920 GeV. The electron energy was $E_{\mathrm{e}} = 26.7\,\mathrm{GeV}$ and was slightly raised to 27.5 GeV in 1994 corresponding to a centre–of–mass energy $\sqrt{s_{\mathrm{ep}}} = 300\,\mathrm{GeV}$. This was increased to 318 GeV by setting the proton beam energy to 920 GeV in 1998. Instead of electrons more often positrons were filled to get more stable running conditions. A full list of the HERA running conditions is given in Tab. 2.1. The asymmetric beam energies satisfy the need for high centre–of–mass beam energies at minimal synchrotron radiation losses. In principle, a maximum of 210 electron and proton bunches, separated in time by 96 ns, can be filled. About 10 electron (proton) bunches are filled without a proton (electron) bunch partner, so-called pilot bunches, in order to monitor the background in the experiments. Spread of the interaction points along the beam direction is

[1] It is planned to run the machine at different lower energies towards the end of the HERA-II running period in order to measure the longitudinal proton structure $F_{\mathrm{L}}^{\mathrm{p}}$.

determined by the proton bunch lengths, and shows an approximatily Gaussian distribution with a width of 11 cm. A proton fill usually lasts one day, a positron fill around 7 h. The proton storage ring uses superconducting magnets operating at approximately 4 K, producing a magnetic field of about 4.7 T. The beam currents are roughly 50 mA for the $e^{\pm}$ beam and more than 120 mA for the proton beam at the beginning of a fill. The machine luminosity has increased steadily and has reached $\mathcal{L} = 7.7 \cdot 10^{30}\,\mathrm{cm}^{-2}\mathrm{s}^{-1}$ at the end of the HERA-I running period. A key feature of the HERA-II upgrade was the increase of the machine luminosity by a factor of four to five.

2.2 The ZEUS Detector

The ZEUS detector is a multi-purpose detector covering almost the full solid angle. The detector design had to consider the boost in the proton direction of the final–state particles due to the asymmetric beam energies: *e. g.* a particle, which was scattered at 90° in the γp centre–of–mass system is at $\theta \approx 15°$ in the laboratory system (Fig. 3.4). The energy of the particle in the laboratory system is approximately a factor of four above its centre–of–mass energy. This was accounted for by adapting the interaction lengths in the calorimeter to these conditions and also by elongating the tracking system in the proton direction. An elaborate description of the detector is given in [ZEU93]. Here, only a short description of those parts that are relevant to this thesis is given.

The right–handed ZEUS coordinate system [Hil86, GS88] is depicted in Fig. 2.2. It is referenced to zero at the nominal interaction point having the proton beam direction defining the *z*–axis. The *x*–axis is perpendicular to the beam direction pointing towards the centre of the HERA ring and the *y*–axis upwards.

Figure 2.3 shows cross–sections through the ZEUS detector. As can be seen, the detector is almost hermetic, with just the beam–pipes preventing it from having 4π coverage. Starting from the interaction point and moving radially outwards, the ZEUS detector consists of charged particle tracking detectors surrounding the beam–pipe . Since 2001 the innermost section is the micro–vertex detector (MVD) made of silicon strips for measuring secondary vertices at the mm level. However, only collision events recorded in the years 1996—2000 are the subject of this thesis, so the MVD will not be discussed further. The next outermost component is the Central Tracking Device (CTD) which is surrounded by a superconducting magnet providing a magnetic field of 1.43 T.[2] The CTD is a central component for this analysis, used both for tracking and particle identification, and

[2] A high–field solenoid ($B = 5$ T) situated behind the RCAL compensates the effect of the main solenoid on the electron beam.

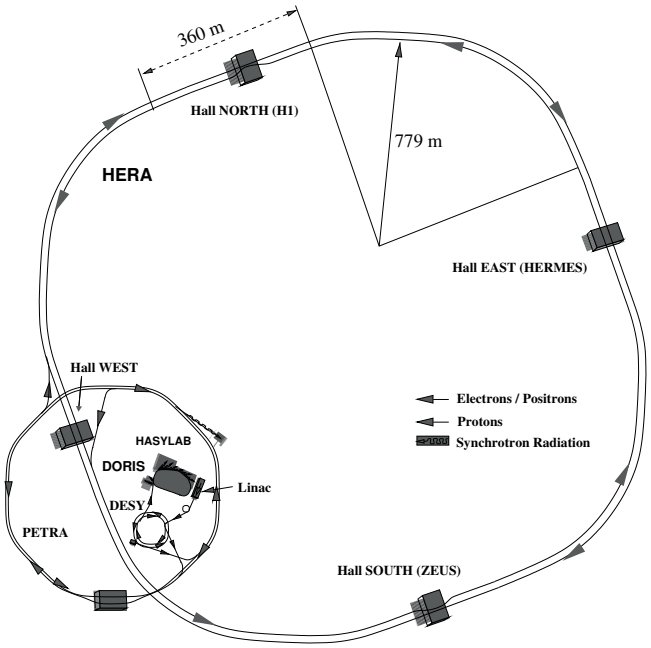

Figure 2.1: Schematic view of the HERA collider [Deu], four experimental halls and the pre-accelerator ring with the injection system [Wii91, Wal95]. The ZEUS detector is located in the south hall.

Year		E_e/GeV	E_p/GeV	Lepton	delivered $\mathcal{L}$/pb^{-1}
HERA-I	1992 — 1993	26.7	820	electrons	0.03
	1993 — 1994	27.5	820	electrons	2.2
	1994 — 1997	27.5	820	positrons	70.9
	1998 — 1999	27.5	920	electrons	25.2
	1999 — 2000	27.5	920	positrons	95.0
HERA-II	2003 — 2004	27.5	920	positrons	84.5
	2004 — 2005	27.5	920	electrons	204.8

Table 2.1: HERA running conditions. In 1998 the energy of the proton beam was raised from 820 GeV to 920 GeV increasing the centre–of–mass energy, $\sqrt{s_{ep}}$, from 300 GeV to 318 GeV. Since 2003 HERA provides much higher specific luminosities.

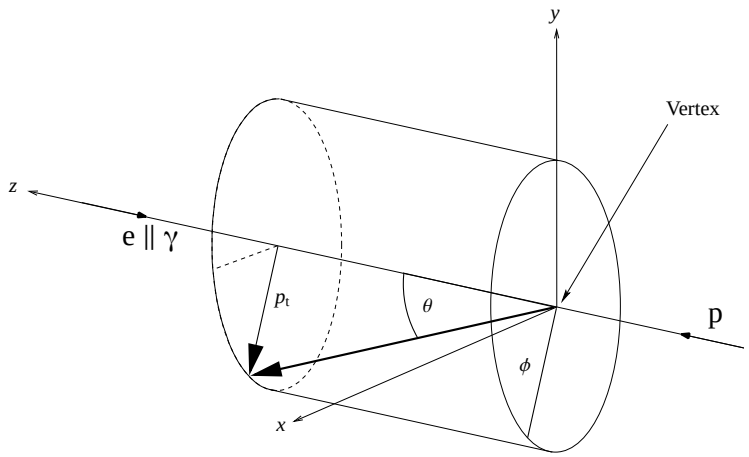

Figure 2.2: Definition of the ZEUS coordinate system. The z–axis points in the direction of the proton beam, while the x–axis points towards the centre of the HERA ring, and the y–axis upwards. The transverse momentum of a final–state particle, p_t, is measured with respect to the beam axis. The azimuthal angle around the beam axis is denoted by ϕ. The polar angle, θ, is measured relative to the proton direction. Instead of θ the pseudo–rapidity $\eta = -\ln[\tan(\theta/2)]$ is frequently used.

so will be discussed in more detail in Sec. 2.2.1. At both ends of the CTD there are planar drift chambers, the Forward and Rear Tracking Devices (FTD and RTD). During the HERA-I running period the FTDs had been interlaced by transition radiation detectors (TRD) being used for particle identification in the forward direction.[3] The four TRD modules were replaced in 2001 by two straw–tube trackers (STT) to improve the forward tracking. The last tracking detector is the Small angle Rear Tracking detector (SRTD) which improves the position resolution for particles, particularly used for the scattered lepton, in the rear direction. All the tracking components combined provide an angular acceptance of $7.5^\circ < \theta < 170^\circ$ for charged particles.

Outside the superconducting magnet lies the ZEUS calorimeter. The ZEUS calorimeter is a high resolution depleted–uranium scintillator calorimeter (UCAL) and is divided into three sections: the forward (FCAL), barrel (BCAL) and rear (RCAL) calorimeter. As the calorimetry is important for the measurement of jets and cell clusters, which are used to aid electron detection, and the reconstruction of the hadronic final–state, it will also be discussed in more detail (see Sec. 2.2.2). In front of the calorimeter scintillating tiles, called the presampler, are used for the detection of pre-showering particles improving the energy measurement in the calorimeter. Allied to the UCAL, the yoke of the solenoid serves as addi-

[3]The combination of the three FTD chambers and the four TRD modules is called the Forward Detector FDET.

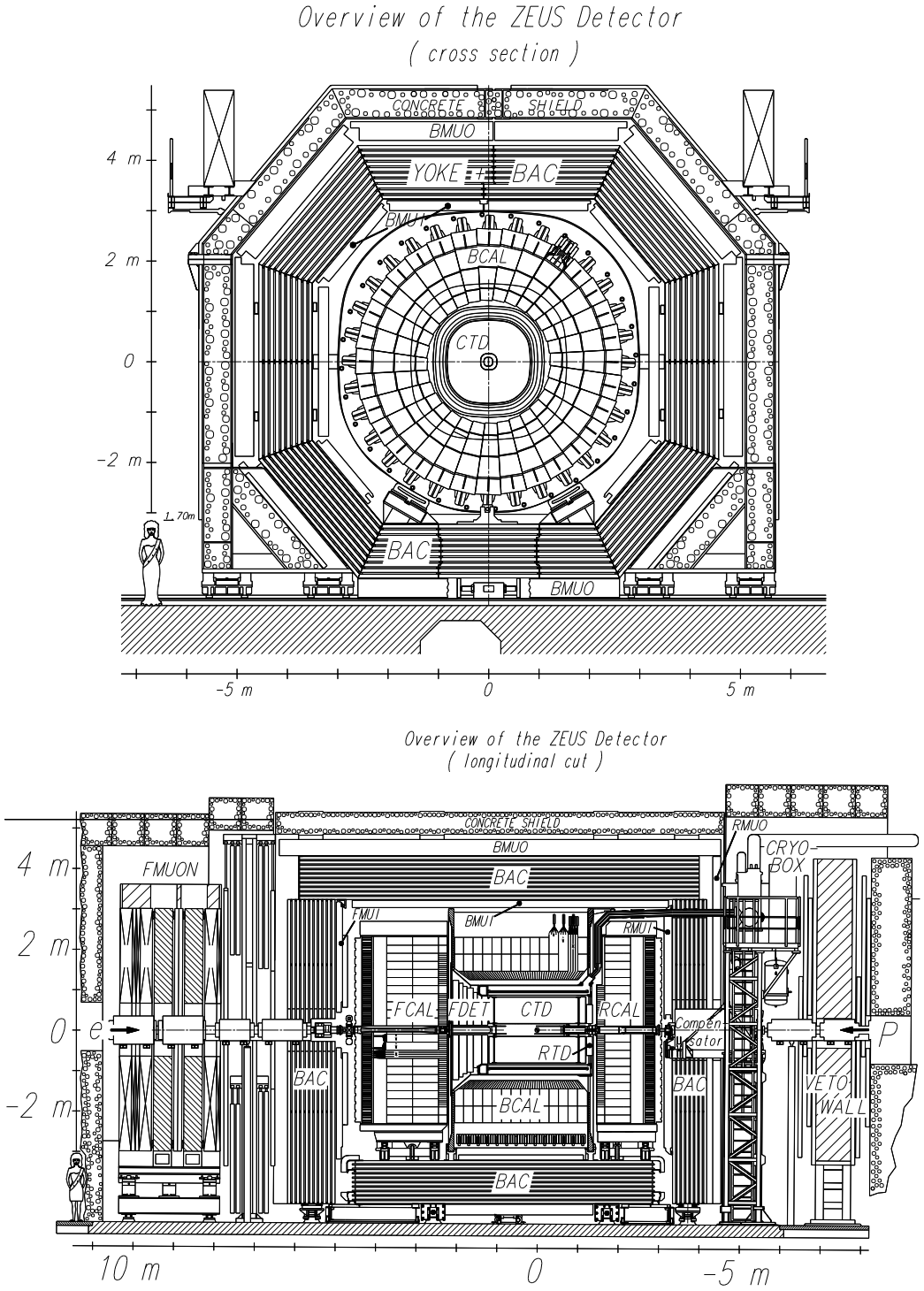

Figure 2.3: Cross–sections of the ZEUS detector, shown perpendicular to (top) and along (bottom) the beam direction.

tional calorimeter (Backing Calorimeter, BAC) by instrumenting the iron with aluminium proportional tubes, providing measurements of late showering particles and energy leakage of the uranium calorimeter.

Before and behind the BAC are muon chambers surrounding the iron yoke. These are used together with information of the inner tracking devices for measuring tracks of muons that traverse the calorimeter, *e. g.* for identifying muons from semi–leptonic beauty decays, as well as the suppression of cosmic muon events.

The VETO wall and the C5 counter signal particles that enter the detector from the rear direction. The VETO wall is a large iron wall (7.6×0.9 m) covered on both sides with scintillation counters, positioned 7 m from the interaction point in the upstream proton direction. It shields the detector against particles from the proton beam halo and provides a veto against beam–gas interactions that induce a trigger in the main detector. The C5 counter is positioned around the beam–pipe at 312 cm from the interaction point in the upstream proton direction, near the C5 collimator. It consists of two planes of scintillator separated by 5 cm of lead. The time information of the C5 counter is crucial to measure the arrival times of the beams, monitor synchrotron radiation and to reject proton beam–gas events. Further in the direction of the electron beam, two lead scintillators are located at $z=-34$ m and $z=-44$ m which can be used for tagging of photoproduction events.

2.2.1 Central Tracking Device

The CTD [B$^+$98b, FMS$^+$94] is a large cylindrical wire drift chamber with an overall length of 240 cm and an outer radius of 85 cm. The active volume has a length of 203 cm with inner and outer radii of 19 cm and 78.5 cm, respectively, providing a large angular coverage of $15^\circ < \theta < 164^\circ$. It contains 72 concentric sense wire layers, arranged in 9 superlayers (see Fig. 2.4). Each superlayer is divided azimuthally into cells of 8 sense wires. The number of cells increases from 32 in the innermost superlayer (N$^\alpha$ 1) to 96 in the outermost superlayer (N$^\alpha$ 9). The total number of sense wires is 4608. The sense wires are read out and digitised every 9.6 ns by flash analogue to digital converters (FADCs) with a resolution of 8 bits. The position resolution achieved in (r,ϕ) is 190 μm. The wires of the odd–numbered superlayers are stretched parallel to the beam axis, whereas the ones contained in the even–numbered superlayers are tilted by stereo angle of $\approx \pm5^\circ$. With this configuration the z–position of a track can be reconstructed with an accuracy of about 2 mm. All wires of superlayer 1 and half the wires of superlayers 3 and 5 are additionally instrumented with a z–by–timing system in which both ends of the wires are read out and the z–position is calculated from the difference in the arrival times of the pulses at the two ends. This system achieves a resolution in z of 4.4 cm [BFH$^+$97] and is used primarily for trigger purposes.

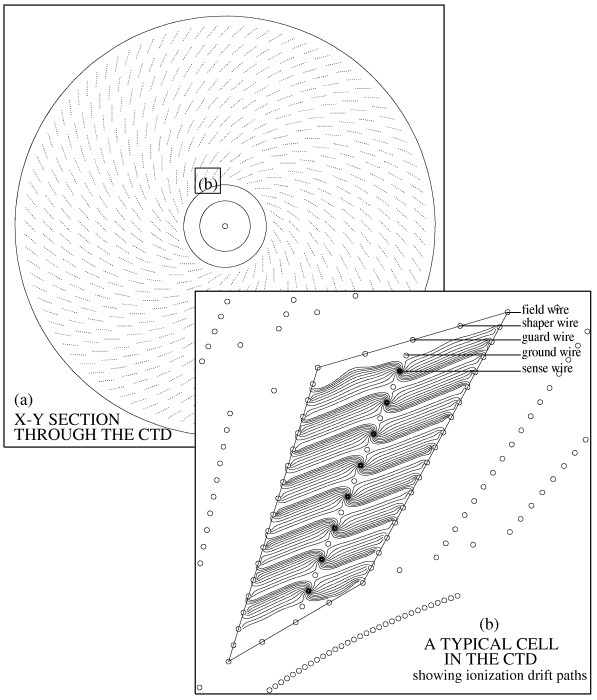

Figure 2.4: Cut through the CTD in the *xy*–plane. In (a) the nine concentric superlayers surrounding the beam–pipe are shown. In (b) a single cell consisting of sense and field forming wires (see text) and the ionisation drift paths are depicted. The arrangement of the wires and their potential ensures a LORENTZ angle of 45° requiring the drift electrons to follow straight paths.

A CTD cell is formed by 8 sense wires, made of gold–plated tungsten, alternated with 9 wires at ground potential in order to make gain and drift field adjustment independent of each other. The boundaries between neighbouring cells are defined by the field planes of 19 wires, two of which at either end are at maximum negative potential. Four shaper wires along the radial boundary, together with the guard wires at the end of the sense wire chain, ensure the uniformity of the drift field, making the drift velocity of approximately 50 μm/ns constant throughout the cell volume. The magnetic field is perpendicular to the electric field. The cells are inclined by an angle of 45° with respect to the radial direction, so that a straight track emitted at at the interaction point will cross the sense wire planes and always produce hits that are close to one or more sense wires.[4] These hits have a drift time short enough ($t < 96$ ns) for the CTD first level trigger (*c. f.* Sec. 2.2.4) to assign the track to the correct beam crossing. The field strengths and the gas mixture are tuned such that the LORENTZ angle also equals 45°. As a result, paths of the drift electrons are almost azimuthal (see Fig. 2.4(b)), *i. e.* perpendicular to high momentum tracks coming from the interaction point, which ensures optimal resolution.

[4]The orientation of the inclination angle and the magnetic field direction have been chosen to improve the reconstruction of negatively charged particles rather than positive ones. Originally HERA was intended to run most of the time with electrons instead of positrons.

Hits from the outer axial superlayers are combined to form a "seed", which is extrapolated back to the vertex. As the procedure of extrapolation occurs, more hits are gathered thereby increasing the precision. Bad parts of the CTD are excluded. The pattern recognition is further refined to choose quality tracks which are fitted to a helix model. The primary and secondary vertices are found by performing χ^2–fits on subsets of these tracks, achieving more precise helix parameters for the vertex–associated tracks in turn.[5] The resolution in transverse momentum for vertex–refitted tracks is [HWMN+99]

$$\frac{\sigma_{p_t}}{p_t} = 0.0058 p_t[\text{GeV}] \oplus 0.0065 \oplus \frac{0.0014}{p_t[\text{GeV}]}, \tag{2.1}$$

where the first term corresponds to the resolution of the hit positions, the second term to smearing from multiple scattering within the CTD and the last term to multiple scattering before the CTD. A detailed description of the track reconstruction can be found in [HIL+97, Har98].

The CTD is filled with a gas mixture of argon, carbon dioxide and ethane in the ratio 83 : 5 : 12, which is bubbled through ethanol. This mixture has been chosen on the grounds of safety and detector life–time [BHP+86].

The CTD is also equipped for measurements of the ionisation energy loss of particles. The measurement process and ways of using the energy loss information for particle identification will be described in Chap. 5.

2.2.2 Uranium–Scintillator Calorimeter

The ZEUS calorimeter [A+91b, Ber93, CGM+92, DGH+91] is a high resolution compensating calorimeter essential for the reconstruction of the hadronic final state. It has been designed as a sampling calorimeter, where absorber layers alternate with scintillator layers, which are read out optically. Uranium is an advantageous absorber for hadron calorimetry, since it provides a high yield of spallation neutrons. These impart their energy to the hydrogen nuclei of the scintillator. In combination with an additional contribution of photons from neutron capture in the uranium, this helps to compensate the signal loss that hadrons suffer from the loss of binding energy, nuclear fission fragments and from undetected decay products. Also, the EM component of the shower due to π^0 production is detected with

[5] At ZEUS the following five parameters are used for the representation of the track helices: The distance in the xy–plane of the point of closest approach w. r. t. some reference point (usually the beam–line), D_h, its z–position, Z_h, the track curvature times the particle's charge, Q/R, the azimuth of the track tangent w. r. t. the x–axis at the point of closest approach and the cotangent of the polar angle, $\cot\theta$. For vertex tracks the distance of closest approach collapses to zero, *i. e.* the reference point matches with the vertex.

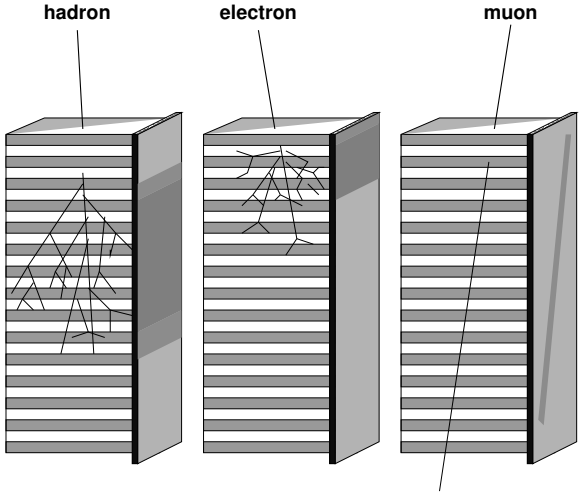

Figure 2.5: Different types of shower shapes in the calorimeter. The uranium–scintillator sandwich structure is drawn for three towers (see text) with the wave–length shifters on the right side. The penetrating hadrons produce a large shower. The electron shower is small. The light signal of minimum ionising muons is equally spread over the depth of the tower.

the same efficiency as the hadronic component. Hadron showers are spread laterally and penetrate deeper into the calorimeter. A parametrisation of the shower development [Krü92] shows that for an 10 GeV hadron 95 % of the transverse energy is contained in a cylinder with radius of approximately 20 cm, and penetrates up to an equivalent of 150 radiation lengths, X_0[6].

In contrast electrons and photons do not suffer such losses as they interact predominantly with the atomic electrons (QED processes like COMPTON scattering, bremsstrahlung or pair–production) and not with the nuclei. Electro–magnetic showers are small. About 95 % of the energy is contained laterally within two times the Molière radius, which is typically $R_M = 2$ cm. The shower penetrates the calorimeter to a maximum depth of about 25 radiation lengths, X_0.

Highly energetic muons behave as minimum ionising particles. They lose only a small amount of energy, which is proportional to the number of uranium layers they traverse. The differences in the shower development for electro–magnetic showers, hadron showers and muon penetration are used for particle identification. The difference of the various types of showers is depicted schematically in Fig. 2.5.

[6]For the ZEUS calorimeter the mean free path of hadronic interactions, λ, corresponds roughly to $25\,X_0$.

Section	Polar angle	Pseudo–rapidity
FCAL	$2.2^\circ < \theta < 39.9^\circ$	$1.0 < \eta < 4.0$
BCAL	$36.7^\circ < \theta < 129.1^\circ$	$-0.7 < \eta < 1.1$
RCAL	$128.1^\circ < \theta < 176.5^\circ$	$-3.5 < \eta < -0.7$

Table 2.2: Angular acceptance of the CAL

Performance of the Calorimeter

In the ZEUS calorimeter, depleted uranium[7] plates of 3.3 mm thickness, encased in a thin stainless steel sheet, serve as the absorber, while polystyrene scintillator layers of 2.6 mm thickness are used for particle detection. This configuration provides equal signals for hadrons and electro–magnetic particles of the same initial energy ("compensating calorimeter"). The signal integration time is 100 ns. Test beam measurements have verified that the signal heights for hadrons and electrons agree within 3 % for momenta greater than 2 GeV. The permanent irradiation by particles from nuclear decays of the uranium plates is detected and used for stabilising the detector calibration within 1 %. The energy resolution for electrons and hadrons was measured in the test beam to be

$$\frac{\sigma_\mathrm{e}}{E[\mathrm{GeV}]} \approx \frac{18\,\%}{\sqrt{E[\mathrm{GeV}]}}\,, \tag{2.2}$$

$$\frac{\sigma_\mathrm{h}}{E[\mathrm{GeV}]} \approx \frac{35\,\%}{\sqrt{E[\mathrm{GeV}]}}\,. \tag{2.3}$$

For energies between 15 and 110 GeV the calorimeter response to electrons is linear within 1–2 %.

Mechanical Layout

The CAL is divided into three independent sections (see Tab. 2.2), which altogether cover more than 99 % of the 4π solid angle around the nominal interaction point. For photon–proton collisions as analysed in this thesis, this calorimeter is especially well suited to measure the hadronic energy depositions over a wide range in the photon fragmentation region (*c. f.* Fig. 3.4) of the γp centre–of–mass system with a single calorimeter type. The three calorimeter sections are divided into 80 modules, the largest of which is shown in Fig. 2.6.

The FCAL modules consist of 185 layers of absorbers and scintillators, which are transversely segmented to form calorimeter *towers*. The total depth of an FCAL tower is 7 nuclear absorption lengths, λ. The towers are longitudinally divided into three sections, the electro-magnetic and hadronic calorimeters (EMC,

[7] DU, alloy of 98.4 % ^{238}U, 1.4 % Nb and less than 0.2 % ^{235}U.

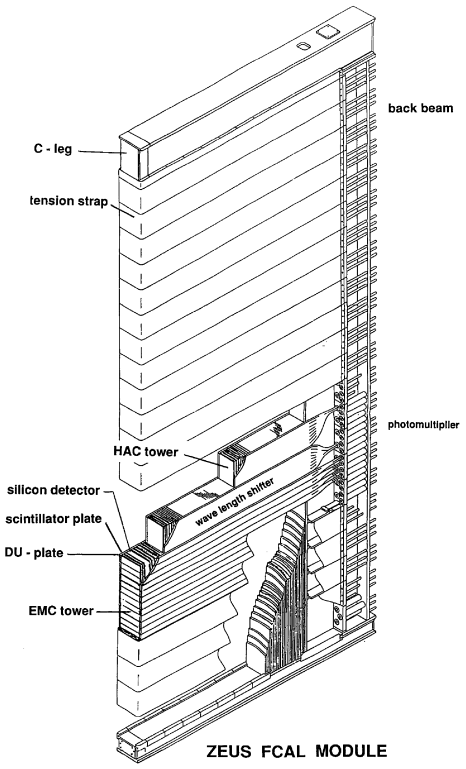

Figure 2.6: Cut–away view of a FCAL module. The particles enter the module from the left traversing the sandwich structure of the towers made of uranium and plastic scintillators. The wave–length shifters mounted on the right collect (mainly blue) light emitted by the scintillators and guide it to the photo–tubes converting it to green light on the way.

HAC1 and HAC2), which are read out independently. Electro–magnetic particles deposit most or all of their energy in the EMC, which has a thickness of 26 radiation lengths, X_0, and is transversally segmented into cells of $5\,\text{cm} \times 20\,\text{cm}$. For energetic hadrons the particle shower extends beyond the EMC into the HAC sections, which are $85\,X_0$ deep each. The HAC cells are $20\,\text{cm} \times 20\,\text{cm}$ wide. Wave-length shifters guide the light generated in the scintillator plates to photo–multiplier tubes on either side of the tower for measuring the pulse–height and arrival time. For energy deposits more than 4 GeV the resolution of the arrival time measurement is better than 1 ns.

The RCAL modules do not have HAC2 towers, because the hadronic energies in the backward direction are kinematically limited to the value of the electron beam energy. The rear EMC is less finely segmented than in the FCAL and has a cell size of $10\,\text{cm} \times 20\,\text{cm}$.

The BCAL consists of 32 wedge–shaped modules, which are tilted by 2.5° in ϕ to prevent particles from running undetected along the cracks between the modules. Its EMC and HAC 1+2 sections are only $23\,X_0$ and $52\,X_0$ deep, respectively, amounting a total of 5λ. The front face dimensions of the EMC towers are $4.9\,\text{cm} \times 23.3\,\text{cm}$. One HAC tower covers four EMC towers, except for the front (rear) ring, where only two (three) EMC towers are covered by one HAC tower.

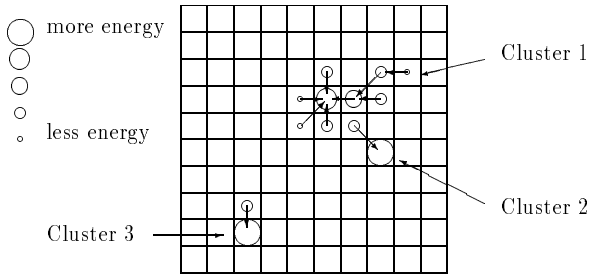

Figure 2.7: Schematic view of the island clustering algorithm in the ZEUS calorimeter.

Island Finding

The clustering algorithm used in this thesis to aid in the electron identification is depicted in Fig. 2.7. Energy deposits in the calorimeter are clustered to *islands* which are helpful for the reconstruction of the total energy of a single or a bunch of incident particles. The island finding is performed on calorimeter cells (*i. e.* sections within a tower). For each cell the neighbouring cell, which has the highest energy, is determined and an arrow from each cell to its highest energy neighbour is drawn. When the cell has no neighbour of higher energy than itself, this is then considered a "peak", which will be a centre for an island. Then considering all cells again and following the arrows until the peak is reached, it is found that all cells are uniquely associated with some peak and all those associated with a peak are classified as islands. The island finding is done for each calorimeter section individually, and they are then joined across boundaries. The centre of the island is defined by the mean position of all associated cells weighted with the logarithm of the energy of each cell content.

Energy Flow Objects

The islands described above are two–dimensional objects existing in a particular layer of calorimeter cells (EMC, HAC1, HAC2). However, in real life a particle might spread its energy over more than one cell layer. Thus it is wise to combine cell islands to 3–dimensional, so-called *cone islands* representing the energy flow of a single particle or a very narrow shower. For charged particles the energy measurement can be further improved by using the momentum of the matched particle track[8], if the relative uncertainty of the momentum measurement is smaller than that of the energy measurement in the calorimeter. In this case the sometimes ambiguous correction of the energy flow for dead material in front of the calorimeter

[8]For the conversion from momentum to energy, the particle is supposed to be a pion.

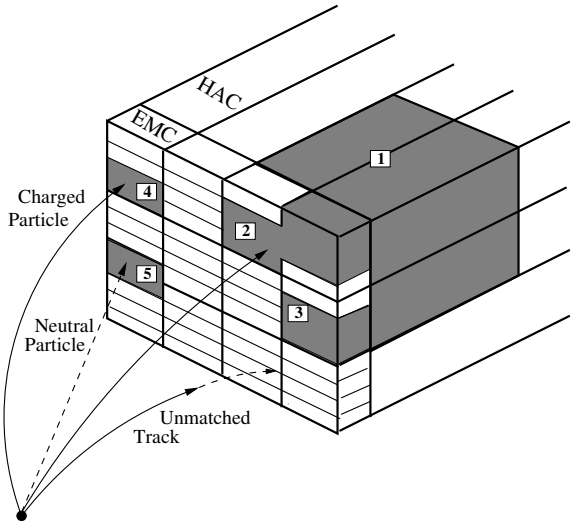

Figure 2.8: Reconstruction of energy flow objects: EMC cell islands 2 and 3 are joined with HAC cell island 1 to form a cone island. In the next step the cone islands are matched to tracks (4). Good tracks which are not associated with any calorimeter object are counted as charged energy. Calorimeter objects not associated with any track are counted as neutral energy (5). Courtesy of [Tun01].

is not needed resulting in a more precise energy determination.[9] The resulting energy flow objects (EFOs) consist in the case of charged particles of a cone island or a particle track, or both. For neutral particles only a cone island is seen. The situation is depicted in Fig. 2.8. A detailed description of the EFO reconstruction is given in [Tun01]. The reconstructed energy flow objects are used for jet finding and the reconstruction of the hadronic final–state (*c. f.* Chap. 3).

2.2.3 Luminosity Monitor

At ZEUS the luminosity measurement is based on the very precisely known Bethe–Heitler process, $ep \rightarrow e'\gamma p$, where an electron scatters off a proton under emission of a bremsstrahlung photon [BH34]. The total cross–section of this QED process is about 326 mb for photon energies $0.1 < E_\gamma < 26.7$ GeV [PZ94].

The bremsstrahlung photons emitted in ep collisions at the interaction point leave the beam–pipe through a copper–beryllium window 82 m downstream in the electron beam direction and are detected in a $22\,X_0$ deep lead–scintillator calorimeter [A$^+$92b] at a distance of 107 m from the interaction point (*c. f.* Fig. 2.9). A carbon filter shields the photon calorimeter from synchrotron radiation. The photon impact point is reconstructed with a precision of 2 mm. The energy resolution under experimental conditions is $\sigma(E)/E = 26\,\%/\sqrt{E}$, with E measured in GeV. Since the differential cross–section is a function of the photon energy, the luminosity is calculable from the Bethe–Heitler formula [BH34]. The largest background arises from electron bremsstrahlung on the residual gas. Measuring the currents in the paired and unpaired electron bunches and the bremsstrahlung rate

[9] In some regions these corrections are larger than 20 %.

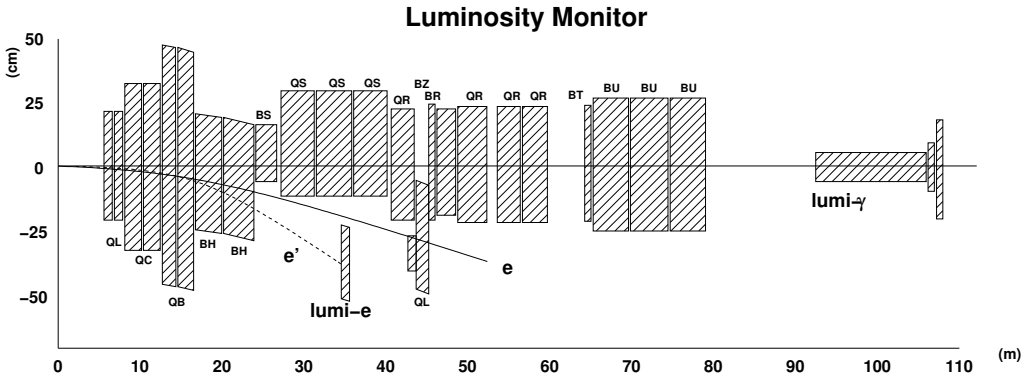

Figure 2.9: The ZEUS luminosity monitoring system. The hatched blocks indicate bending (B) and quadrupole (Q) magnets. The detectors at 35 m and 44 m measure electrons that are scattered under very small angles and are used for tagging γp events with a corresponding centre–of–mass energy within the range $70 < \sqrt{s_{\gamma p}} < 120$ GeV.

for the unpaired electron bunches, the beam–gas background can be subtracted statistically. A detailed description of the procedure can be found in [PZ94, PZ95].

2.2.4 Trigger and Data Acquisition

Only a few of the huge number of interactions actually correspond to genuine ep collision events. The bulk of triggers, however, are due to background events of various types which have to be recognised and removed. In particular, the cross–section for collision between protons and rest gas molecules in the beam–pipe is huge. The rate of this type of interactions is estimated to be approximately 0.5 kHz/m. The spray of particles that is produced during these proton–gas interactions, or products from secondary interactions with accelerator elements such as magnets and collimators, can enter the calorimeter and deposit energy, thereby producing a trigger signal. In general, the proton gas interactions occur all along the proton beam–line, but the signature in the detector depends on their vertices. First, the particles emanating from proton–gas interactions that have the vertex downstream of the main detector do not enter the calorimeter and apart from the fact that they reduce the proton life–time, are completely harmless. Second, the interactions can occur inside the detector. These background events can deposit a large amount of energy in the forward calorimeter FCAL, in the direction of the incident proton, whereas the RCAL remains empty. This type of events is recognised with the help of energy–momentum conservation. The third class of

proton–gas interactions occurs upstream of the detector and the spray of particles can hit both the RCAL and the FCAL. Beam–gas interactions with vertices up to $z \approx 100\,\mathrm{m}$ are visible in the calorimeter. The total rate seen in the detector is of the order of 50 kHz, approximately five times lower than bunch–crossing rate. This large class of proton–gas interactions is rejected with the beam monitor time counter C5 and the calorimeter timing information. The VETO wall is also used to reject this type of background.

A source of the electron beam induced background is the collinear synchrotron radiation from the electrons. However, most of this radiation occurs at large curvature of the HERA ring, far away from the experiments. Shielding with a set of masks and collimators in the electron beam reduces the remaining fraction of this type of background considerably. The electrons can also collide with nuclei of the remaining rest–gas in the beam–pipe. The collisions of such background events are analogous to fixed–target events with $\sqrt{s} \approx 7\,\mathrm{GeV}$. This type of background events is especially dangerous when it occurs inside the main detector close to the nominal vertex. The rate of these electron–gas events can be estimated with the electron pilot bunches, and proved to be small.

Separate classes of non-colliding beam background are the cosmic muon and beam halo muon events which are rejected by the help of the muon reconstruction.

On-line Trigger

The ZEUS on-line trigger system aims at a rejection factor of 10^5 while maintaining full efficiency for interesting physics events. The system operates on three levels (see Fig. 2.10), that reduce the beam crossing rates of 10 MHz to accepted trigger rates of 1 kHz, 100 Hz and 5 Hz respectively [S$^+$89, Wig87, vdL93].

First Level Trigger (FLT) Each detector component has its own custom built front–end and read–out electronics and a logical first level trigger, which provides a first decision based on a sub-set of the data by means of very fast hardware *e. g.*, programmable gate arrays, look-up tables. The global first level trigger (GFLT) synchronises the component triggers with the HERA clock. The GFLT expects the FLT decisions from the subdetectors 31 clock cycles[10] after the bunch crossing, and needs additional 15 clock cycles until an accepted signal is generated from the logical OR of 64 local trigger slots. Since it takes additional cycles until the accepted signal has been propagated, components like the calorimeter keep their signals in data pipelines. The CAL is one of the most important components contributing to the GLFT decision. For the FLT the calorimeter is divided into 448 non-overlapping trigger towers for both the EMC and the HAC sections. Each trigger tower

[10] One HERA clock cycle takes 9.6 ns.

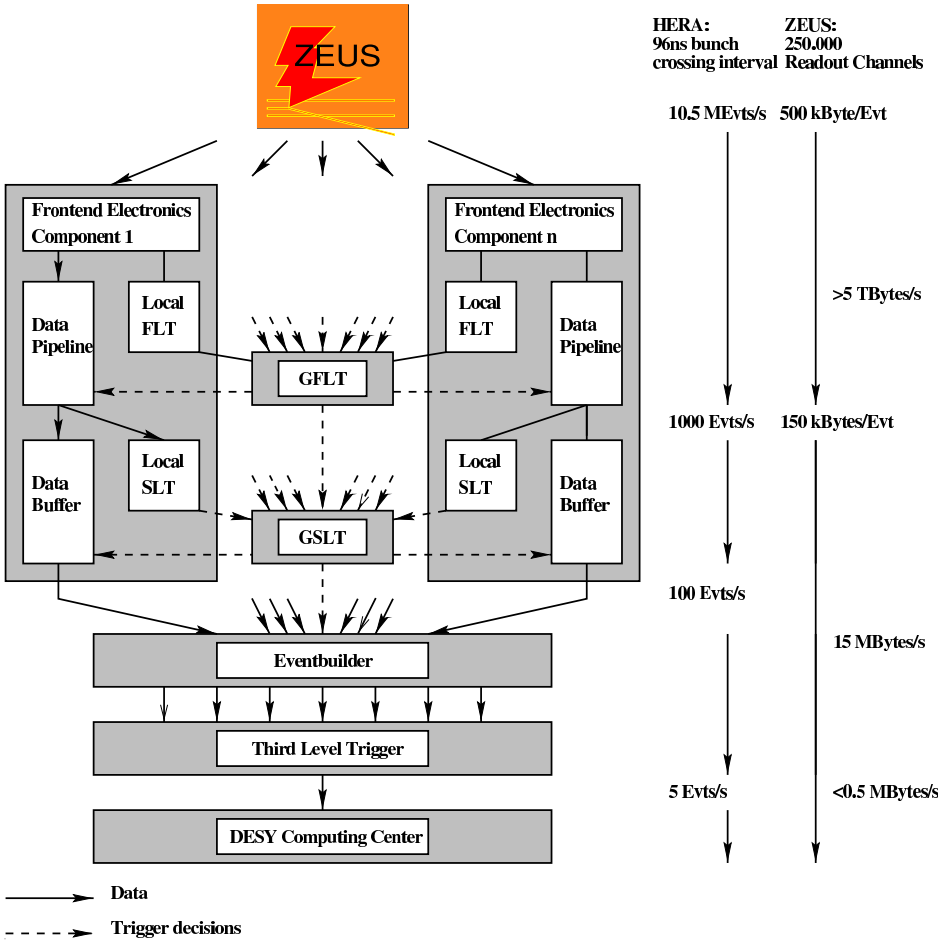

Figure 2.10: The ZEUS trigger and data acquisition system. The event rates shown are the design values.

is typically formed by a pair of adjacent cells. Whenever the energy deposit in one of those towers exceed a programmable threshold, a FLT–accept is issued. The C5 counter is used to veto triggers that are inconsistent with the beam arrival times. The GFLT is supposed to reduce the rate below 1 kHz. The experimental dead–time due to trigger and read–out is less than 0.1 %.

Second Level Trigger (SLT) Accepted events are fully digitised and copied to the second level trigger, which again is local to most of the components. This step typically takes 30 µs and thus creates approximately 3 % dead–time at 1 kHz. On the SLT level, objects like track momenta, the event vertex and calorimeter clusters are reconstructed, permitting a more restrictive trigger decision. The result is sent to the global SLT (GSLT) together with the reconstructed variables for an overall evaluation. Like many of the SLTs,

the GSLT is based on a transputer network. Each transputer is devoted to a particular task such as general vetoing or the recognition of certain event signatures, leading to further reduction down to a level of 50—100 Hz.

Third Level Trigger (TLT) For each event that passes the GSLT, the data from the various components are handed over to the event builder, which is a network of custom made transputer models. It combines all the data of an event into a single record of ADAMO [F$^+$93] database tables and distributes the assembled events over the processor nodes of the third level trigger. The ADAMO format is the data structure used at all subsequent levels up to physics analysis programs. The TLT is a computer farm. Each computer individually analyses and classifies a single event with a custom version of the off-line reconstruction software, which uses the full event information. The accepted events pass the TLT at a rate of ≈ 5 Hz with a size of ≈ 150 kB each and are written to the event repository consisting of tape robots in the DESY computer centre.

Event Reconstruction

The ZEUS physics reconstruction program (ZEPHYR) operates on the ADAMO data structures made by the event builder. In a first phase, ZEPHYR reconstructs the calibrated energies and track segments for each detector component separately. After a full reconstruction of the recorded events, a data summary tape (DST), again in ADAMO format, is created for physics analysis. The physics groups supply appropriate routines that flag the interesting events to reject a large fraction of definitely non-interesting triggers.

Monte Carlo Simulation

The complete chain between the ep collisions and reconstruction of the events is duplicated in Monte Carlo simulation programs. These are indispensable for a correct understanding of the detector response and background events. The simulated events are used to understand the background events and to correct the data for acceptance and detector smearing. Event generators such as PYTHIA produce four–vectors according to the desired type of ep scattering. The four–vectors are fed into the GEANT3.1 based ZEUS Monte Carlo simulation program [B$^+$87]. It provides an accurate description of the complete ZEUS detector including a detailed configuration of all sub-detectors with both active and dead material, as well as it simulates the response and read–out electronics. For the calorimeter, the shower routines were adapted and modified such that the results of the ZEUS test–beam data were reproduced by the simulation. An overview of the data and simulation chain is presented in Fig. 2.11.

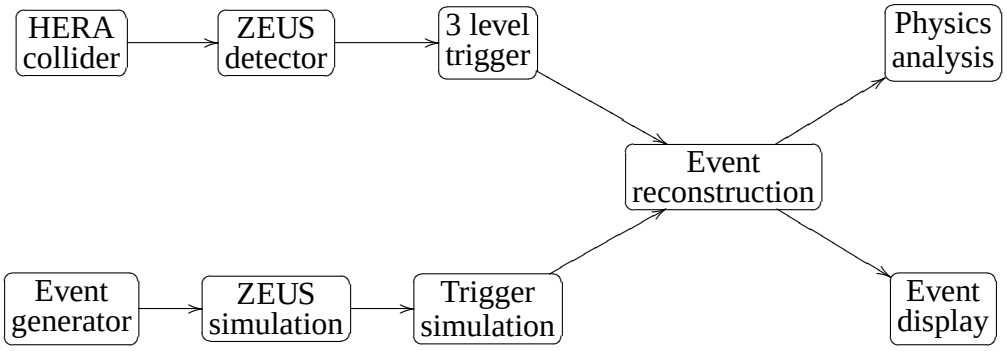

Figure 2.11: Overview of the data and simulation chain.

In principle, the output of the simulation program is indistinguishable from the data and is processed by the next module, the simulation of the ZEUS trigger system. Here, the Monte Carlo events that would have been rejected by the trigger system are identified and marked.

Chapter 3

Event Selection

In this chapter the selection of γp events containing beauty in ep collisions at HERA is described. They are represented by the reaction

$$e^{\pm}p \;\rightarrow\; b\bar{b} + e'^{\pm}X \;\rightarrow\; e_{sl}{}^{\pm} + \text{dijet} + e'^{\pm}X\,. \tag{3.1}$$

Here, X indicates the proton and photon remnants, while electrons originating from the semi–leptonic B decays are denoted by e_{sl} .

3.1 Data Sets

For this analysis all physics triggers recorded with the ZEUS detector in the years 1996—2000 are used. Events for which the detector was not in an appropriate state, because some important component was being switched off or the HERA machine had not been working properly, are excluded.[1] The data sets are summarised in Tab. 3.1. In total an integrated luminosity $\mathcal{L} = 120.4\,\text{pb}^{-1}$ is available, corresponding to 130 million events.

From 1996—2000 the HERA collider was operated with an energy of the electron beam $E_e = 27.5\,\text{GeV}$, while the proton energy was raised from 820 GeV to 920 GeV in 1998 leading to an increase of the centre–of–mass energy from $\sqrt{s_{ep}} = 300\,\text{GeV}$ to 318 GeV. The machine was running most of the time with positrons, only in 1998 and some of 1999 electrons had been injected.

Event simulation, mainly needed for unfolding the cross–sections in the end, had been done with the PYTHIA6.2 generator [S+02], whose basic features are described in Sec. 1.7.1. All QCD processes given in Tab. 1.1 are simulated in leading order perturbation theory. The simulation was done separately for the

[1] This is done with the help of the EvTake database [ZEU06].

Year	E_e[GeV]	E_p[GeV]	Lepton	$\mathcal{L}$ [pb^{-1}]	#Events/10^6
1996 — 1997	27.5	820	positrons	38.6	45.008
1998 — 1999	27.5	920	electrons	16.7	21.420
1999 — 2000	27.5	920	positrons	65.1	63.016
				$\sum$ = 120.4	$\sum$ = 129.444

Table 3.1: Data sets used for the analysis. In 1998 the proton energy was raised from 820 GeV to 920 GeV and the lepton beam switched from positrons to electrons for some months. $\mathcal{L}$ denotes the integrated luminosity gathered with the ZEUS detector.

beauty signal, charm and the light flavours (u, d, s).[2] The beauty sample is further split into the different process classes: resolved and direct processes (Sec. 1.3) as well as excitation in the proton and the photon (Fig. 1.15). In the case of the charm and light flavours only the direct and resolved processes had were generated separately — the excitation processes are part of the resolved samples. The different samples are listed in Tab. 3.2.

For all samples the parametrisations of the proton structure CTEQ–4L (see Sec. 1.4.2) and GRV–LO (Sec. 1.4.1) for the photon structure were used.[3] The beauty signal samples were generated with the masses $m_b = 4.75\,\text{GeV}$ and $m_c = 1.35\,\text{GeV}$ for the heavy quarks, and massless light–flavours. In the charm and light flavour samples *all* quarks including the heavy ones are massless. The PETERSON fragmentation parameter ϵ was chosen to 0.041 for both beauty and charm (OPAL fit [A$^+$98]).

Both in real data and in the Monte Carlo, high–E_t dijet events are pre-selected with the help of the third level trigger HPP 14 at an intermediate step. The trigger decision is mainly based on the results of a fast and simple cone–jet finder (see the next section about jet finders). The energy threshold is rather low ($E_t > 4.5\,\text{GeV}$), to prevent the off-line event selection described in the following from bias. In addition the trigger requires a high total E_t in the calorimeter and uses some simple decisions to reject beam–gas collisions and other non-physics background. The complete definition of the HPP 14 trigger is listed in the appendix A. It should be noted that the selection of dijet γp events discussed in the following is well established in ZEUS analyses (see [Tur02, Gut05, Blo05] for instance), and will therefore only be briefly addressed.

[2] Actually the samples for charm and the light flavours originate from the same source, a big inclusive dijet sample containing all quark flavours. In the charm case this was achieved by vetoing those events containing b or u, d, s quarks not produced in the fragmentation process; while for light–flavour selection all events containing b or c quarks not coming from the fragmentation are rejected.

[3] Here "L" or "LO" denotes versions of the parametrisations computed in *leading order*.

Configuration	Flavour	Process	σ/nb	#Events/10^6	$\mathcal{L}$/pb^{-1}
E_p = 820 GeV	b	direct γp	4.08	1.02	249.911
	b	resolved γp	0.82	0.21	256.475
	b	excitation in γ	1.50	0.36	240.171
	b	excitation in p	0.31	0.09	286.481
	u,d,s,c,b	direct γp	630.36	28.36	44.988
	u,d,s,c,b	resolved γp	6900.20	309.38	44.745
E_p = 920 GeV	b	direct γp	4.39	1.98	450.573
	b	resolved γp	0.91	0.42	459.945
	b	excitation in γ	1.66	0.72	434.538
	b	excitation in p	0.36	0.18	506.273
	u,d,s,c,b	direct γp	664.594	57.562	86.613
	u,d,s,c,b	resolved γp	7493.29	566.458	75.288

Table 3.2: Monte Carlo Samples. The samples for charm and light–flavours were taken from a large inclusive sample containing all flavours. The two configurations contain events simulated in the correct fractions for different trigger and detector configurations and vertex distributions according to the situation in real data taking.

3.2 Jet Reconstruction

Jets are important objects for the characterisation of high–p_t events. They are built from particle energies by *jet finding algorithms*. At ZEUS the "k_t–clustering" algorithm [CDW92, CDSW93] is most common. The older "cone" algorithm is used for trigger purposes only.

The Snowmass Convention [H$^+$92] sets the standard for cone jet algorithms. Here a two–dimensional grid is used in the plane of the pseudo–rapidity, η, and the azimuthal angle, ϕ, requiring a minimum energy deposit in one of the cells of the grid. The size of the cone is typically chosen to be $R = \sqrt{\Delta\eta^2 + \Delta\phi^2} = 1$. The transverse jet energy is calculated from the sum of the transverse energies found inside the cone $E_t^{\text{jet}} = \sum_i E_t(\eta_i, \phi_i)$. The rapidity and azimuthal positions of the jet axis are computed from the weighted energy sums of the contributing cells.

The Snowmass Convention does not address the question of overlapping jets and seed finding for the cone algorithm. This leads to theoretical ambiguity with respect to jet merging in the final–state and the process is not infrared safe at next–to–next–leading order (NNLO) without modifications [Sey97]. These problems are avoided by the use of the k_t–algorithm, which decomposes the event topology into large combined clusters of energy depositions. Based on the opening angle between two energy depositions, E_n, E_m, and their energy, the quantity $k_t = \min(E_n^2, E_m^2) \cdot (1 - \cos\theta_{m,n})$ is calculated for all pairs of cluster combinations. The pair with the minimum k_t value is combined into a common cluster. The

process is repeated until no two clusters can be found with k_t below ξE_t^2, where E_t is the total transverse energy found in the event, and ξ is a cut–off parameter. In photoproduction analyses the algorithm is usually run in the laboratory frame using the inclusive recombination scheme [ES93] in a mode which is invariant under longitudinal boosts. For this, massless clusters are assumed. However, in this analysis the k_t–clustering algorithm was run in the *massive* mode, since heavy quark jets are involved.[4] Furthermore, the "inclusive" mode of the jet finder was used, in which all clusters including the beam remnant are probed — in contrast to the "exclusive" mode, where the algorithm tries to separate the hard final state from the soft beam remnants explicitly.

In this work three different sets of jets are used, all being reconstructed with the k_t–clustering algorithm.

Detector level jets: These jets are reconstructed both in real data and Monte Carlo. Here, the energy flow objects, defined in Sec. 2.2.2, are used as input for the jet finder.

Hadron level jets: The hadron level is defined as the true hadronic final–state in front of the calorimeter and thus valid only in Monte Carlo events. All stable final-state particles except neutrinos are used for the jet finding.[5]

Parton level jets: The jet finder runs over all partons just before the fragmentation process produced by the event generator. All partons originating from the QCD sub-process and the parton showers are included.

3.3 Kinematics of Photoproduction Events

At ZEUS γp events can be selected in two ways: either by detection of the scattered lepton in the electron detector or luminosity system (*c. f.* Sec. 2.2.3) in the kinematical region below $Q^2 < 0.01\,\mathrm{GeV}^2$ and between $150 < \sqrt{s_{\gamma p}} < 250\,\mathrm{GeV}$ ("tagged photoproduction"), or by selecting events without scattered lepton seen in the detector, since at small scattering angles w. r. t. the beam direction the electron disappears undetected ("untagged photoproduction"). This method is often used in order to increase statistics, since in the case of tagged photoproduction the geometric acceptance is small. Untagged γp events have an average virtuality $Q^2 = 10^{-3}\,\mathrm{GeV}^2$ and a maximum virtuality of $Q^2 = 4\,\mathrm{GeV}^2$ [D$^+$95b]. In the

[4] In the massive mode the four–vectors of the clusters are simply added. Pion masses are used here to obtain the four–vector of each cluster.

[5] Note however, that in some analyses different definitions of the hadron level are used like the set of all sufficiently stable hadrons. In particular the B hadrons are not yet decayed in this definition.

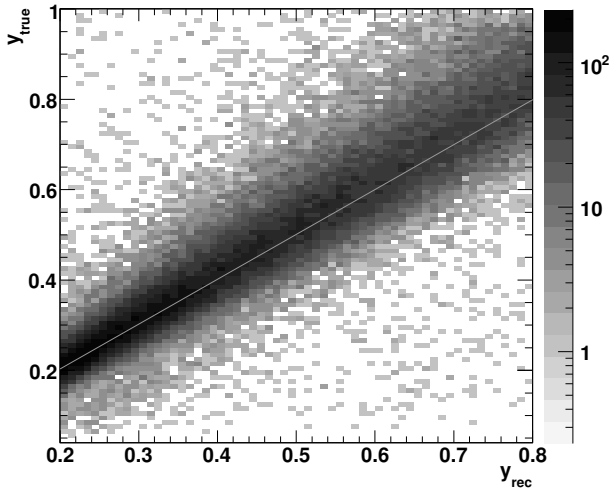

Figure 3.1: Reconstruction of the fractional γ energy, y, in simulated $b\bar{b}$ events of direct photoproduction. Shown are the true values of y versus the values reconstructed with Eqn. 3.2. The light–grey line represents the bisecting line.

case of tagged photoproduction the photon energy is derived from the scattered electron energy (Eqn. 1.25) and in the untagged case from the final–state hadrons with the help of Eqn. 1.26. Here, the sum over the partons has to be replaced by a sum running over all reconstructed hadronic final–state objects — the energy flow objects (EFOs, *c. f.* Sec. 2.2.2). This method is sometimes referred to as the "JAQUET–BLONDEL method" [JB79].

$$y = \frac{1}{2E_\mathrm{e}} \sum_{i \in \text{ all EFOs}} (E_i - p_{\mathrm{z},i}) \,. \tag{3.2}$$

Since the EFO energies are already corrected, no systematic correction of y is needed, as exemplarily shown in Fig. 3.1 for simulated $b\bar{b}$ events in direct photoproduction.

In this analysis the method of untagged photoproduction is used to gather as much statistics as possible to compensate for the small beauty production cross–section. All events containing a scattered electron candidate found by the SINISTRA electron finder (see the selection of DIS events in Sec. 4.4.1) with an electron probability $\mathcal{P}_{e'} > 0.9$, and an electron momentum $p_{e'} > 5\,\mathrm{GeV}$ are rejected. However, sometimes the electron finder mis-identifies photons originating from π^0 decays as electrons. In order not to throw away too many good γp events, the above rejection cuts are tightened by the requirement of $y_\mathrm{e} < 0.9$. Here, y_e denotes the y determined by the "electron method". This method utilises — in contrast to the JAQUET–BLONDEL method — the information of the scattered electron and gives a better reconstruction of y in the case of neutral current DIS events.

$$y_\mathrm{e} = 1 - \frac{E'_\mathrm{e}}{2E_\mathrm{e}}(1 - \cos\theta_\mathrm{e}) \,. \tag{3.3}$$

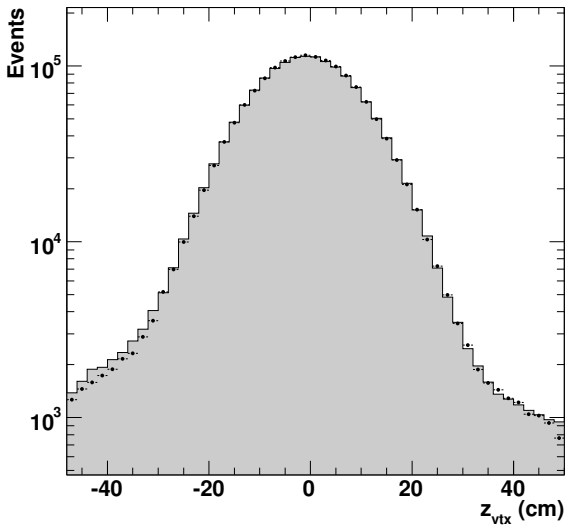

Figure 3.2: Distribution of the z–position of the primary vertex for real data (solid circles) and Monte Carlo (shaded histogram). The width of the resolution is about 11 cm.

Further suppression of residual DIS events is achieved by exploiting the conservation of the longitudinal momentum, $\sum_i (E_i - p_{z,i})$, which is expected to be around two times the energy of the incoming electron for DIS events. A cut on $y < 0.8$ is used, corresponding roughly to an $\sum_i (E_i - p_{z,i})$ of 45 GeV.

Background suppression of beam–gas collisions is achieved by the requirement $y > 0.2$. These events can be thought of as proton collisions on a fixed target, the produced particles have a small polar angle so that $\sum_i (E_i - p_{z,i}) \to 0$. Further cleaning is done with a cut on the z–position of the primary vertex $|z_{\mathrm{Vtx}}| < 50$ cm, which is almost five times the width of the z–vertex distribution, as shown in Fig. 3.2.

The parton kinematics defined by the fractional energies, x_γ and x_p, can be reconstructed in dijet events using Eqns. 1.27 and 1.28 with the outgoing partons replaced by the two jets

$$x_\gamma = \frac{1}{2yE_\mathrm{e}} \sum_{i \in \mathrm{jet1,2}} E_{\mathrm{t},i}\, e^{-\eta_i}\,, \tag{3.4}$$

$$x_\mathrm{p} = \frac{1}{2E_\mathrm{p}} \sum_{i \in \mathrm{jet1,2}} E_{\mathrm{t},i}\, e^{\eta_i}\,. \tag{3.5}$$

For the study of hard scattering processes, events with sufficiently high transverse jet energies, E_t, are required. In this analysis only events containing at least two jets with $E_\mathrm{t} > 7$ GeV for the higher energetic jet and $E_\mathrm{t} > 6$ GeV for the second jet, respectively, are selected. The geometric acceptance is limited by the calorimeter

to $|\eta| < 2.5$.[6] As mentioned in the last section, for the jet finding the k_t–clustering algorithm was used with a massive inclusive recombination scheme running in the laboratory frame.[7] In Fig. 3.3 different jet configurations corresponding to different regions of the parton kinematics are shown. The boost of the γp centre–of–mass system with respect to the laboratory system is on average $\Delta\eta = 2$ (compare the configurations with the event display shown in Fig. 3.11). Figure 3.4 gives a schematic view of the total tranverse energy of the final–state as a function of the photon–proton centre–of–mass rapidity, $\eta_{\gamma p}$. The laboratory variables η and θ are indicated by additional axes. The region within ±1 units around $\eta_{\gamma p} = 0$ is called the "mid-rapidity" region dominated by the dijet system. The proton remnant particles appear as enhancement at positive rapidities, while the photon remnant is located at negative rapidities. The scattered electron is indicated at large negative values of $\eta_{\gamma p}$. The geometric acceptance of the ZEUS detector is shown also. The main detector covers a large fraction of the γ fragmentation region, the central γp collision region, and a small part of the proton fragmentation region.

In Fig. 3.5 distributions of the number of jets per event and the jet variables E_t and η for the most energetic jet in dijet γp collisions are shown, both for real data and Monte Carlo. The distributions of E_t and η exhibit a good agreement between real data and the simulation, whereas the number of jets is not very well described in particular for the higher jet multiplicities. This is a known weakness of the PYTHIA program. There are indications that the reason is a wrong azimuthal distribution in the case of higher order jets which might be caused by a breakdown of the collinear ansatz made in the DGLAP evolution [LZ06].

3.4 Pre-Selection of Electron Candidates

The identification of electrons from semi–leptonic beauty decays is described in the next two chapters. Before doing so, a pre-selection of possible candidates is necessary. Since for the particle identification tracking and calorimeter information will be used, the energy flow objects (EFOs, see Sec. 2.2.2) are a good starting point. Of those several classes exist, depending on the track–island–relationship and the method of energy determination. The situation is depicted in Fig. 3.6 for the simulated beauty events described in Sec. 3.1. Roughly 90 % of the electrons and positrons have an unequivocal track–island relationship, are isolated and their

[6] The actual geometric acceptance of the CAL is wider ($-3.5 < \eta < 4$), however due to the finite spatial resolution the full range cannot be used. The calculation of η is done w. r. t. the reconstructed vertex position.

[7] In a first step the jet finder is run with a minimum cut of $E_t > 4\,\text{GeV}$. Afterwards the cuts of 7(6) GeV are applied to the two most energetic jets found (thus affecting the number of jets per event).

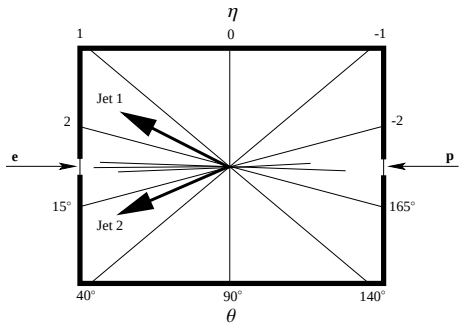

(a) Low x_γ and high x_p

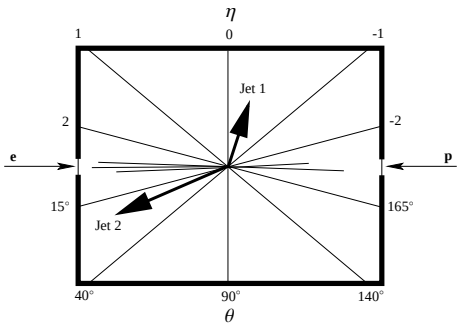

(b) High x_γ and high x_p

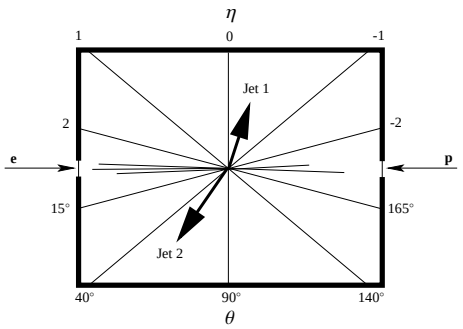

(c) High x_γ and low x_p

Figure 3.3: The configuration of the jets and the remnants in two-jet γp events depends on the parton kinematics: In events with low x_γ and high x_p, both jets are typically found at large rapidities, η (a). At high x_γ and high x_p, one jet is at positive and the other at negative rapidities (b). At high x_γ and low x_p, both jets are at rapidity $\eta \approx 0$. The proton remnant always points in the proton direction and remains mainly undetected. The photon remnant goes in the direction of the incoming lepton in the case of direct γ interactions. For resolved photoproduction the direction is changed and might be partially or fully observed.

momenta are precisely determined by the central drift chamber (labelled by "CTD 1:1" in the figure). Only these are selected for further analysis.

Special care needs to be taken in the region of the super–cracks, the gaps between the forward and barrel calorimeter, and between the rear and barrel calorimeter, respectively. If the energy of a particle is distributed across a calorimeter boundary, the clustering does not work properly, leading to wrongly reconstructed energies and barycentres. Although the EFO reconstruction tries to correct this, the results are still poor. Therefore these cases are filtered out, which is accomplished by a cut on the EFO depth

$$d < \left(\frac{(\theta - 90^\circ)^2}{500} + 18 \right) \text{cm} \,. \tag{3.6}$$

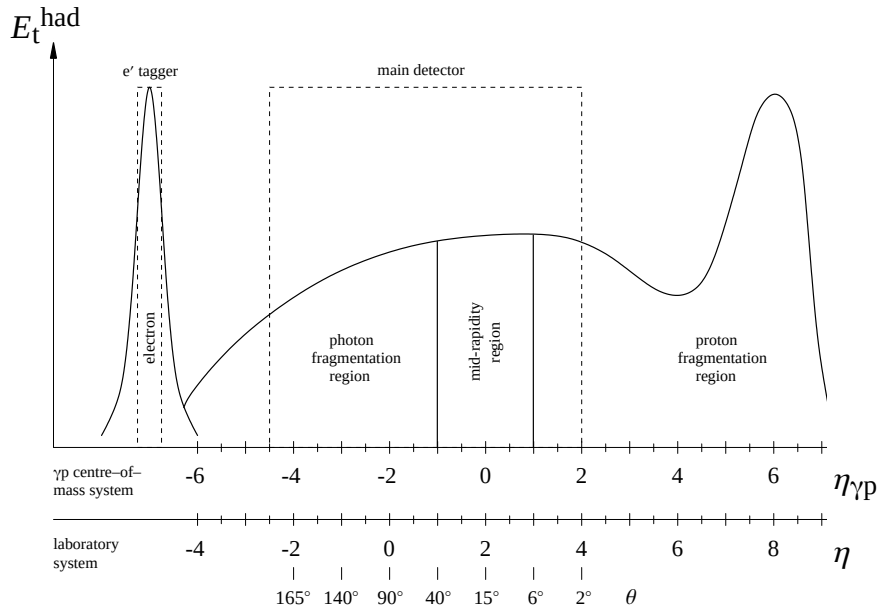

Figure 3.4: Schematic view of the total transverse energy of the final–state, E_t^{had}, as a function of the γp centre–of–mass rapidity, $\eta_{\gamma p}$. Also shown are the corresponding observables in the laboratory frame, η and θ (a mean boost of $\Delta\eta = 2$ between the two systems is assumed here). The position of the main detector and the electron tagger are indicated by the dashed lines. The electron peak on the left is not to scale.

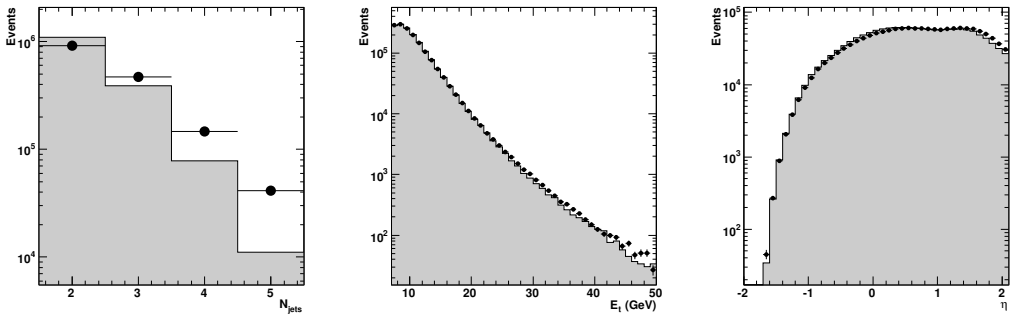

Figure 3.5: The number of jets per event and E_t and η of the most energetic jet in dijet photoproduction events. The filled circles indicate real data while the shaded histograms represents the simulation. The latter have been normalised to the area of the data distributions. All plots have been made for the 98—00 running period.

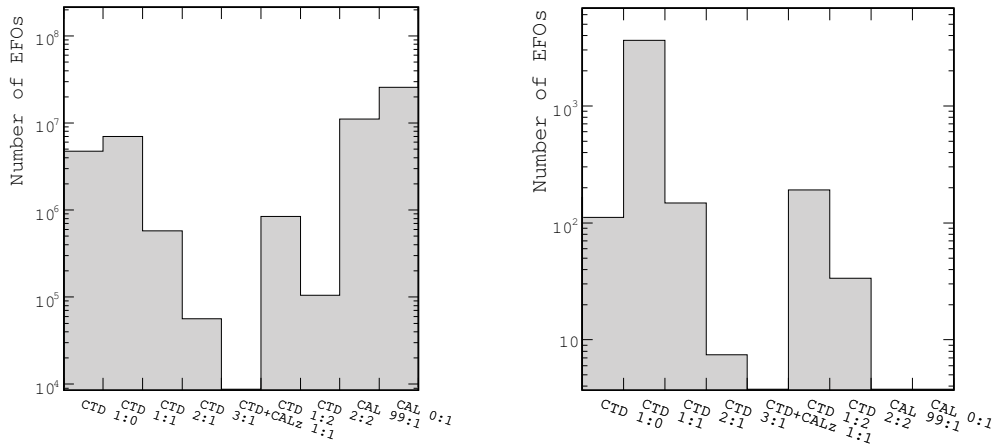

(a) All particles (b) $e^{\pm}$ only

Figure 3.6: Distribution of EFO classes in simulated $b\bar{b}$ events for all particle types (a), and electrons only (b). The classes describe the $n:m$ relationships of tracks and islands. Energies are either determined by the CTD or the CAL (*c. f.* Sec. 2.2.2). Most of the electrons possess a 1:1 track–island relationship.

In this context the EFO depth is defined as the distance of the EFO barycentre from the entry point of the particle in the calorimeter. Equation 3.6 is motivated by Fig. 3.7. The super–crack regions are clearly visible. In addition, this cut helps reducing the pion background.

The electron candidates are further constrained by requiring tracks of good quality which are not possible γ conversion candidates (see Sec. 4.4.1). For further background suppression, in particular those from photon conversions and DALITZ decays, a minimum transverse momentum of $p_t^e > 0.9\,\mathrm{GeV}$ is required, being a compromise between background suppression and signal acceptance as defined by the beauty decay spectrum. With this cut a large fraction of the signal is kept. Note that this particular cut is much lower than the corresponding one in the $B \to \mu$ analyses, which is usually $p_t^\mu \gtrsim 2.5\,\mathrm{GeV}$ cutting most of the signal away and thus restricting the visible cross–section very much.

Another requirement is a good reconstruction of the ionisation loss measurement, dE/dx, of the electron candidate, which is most important for the electron identification. Here, a minimum number of truncated hits per track, which is the number of CTD hits used for the dE/dx reconstruction process (for details see Sec. 4.2.2), is required. As discussed in Sec. 4.4.3, a cut of $n_{\mathrm{trunc}} > 12$ is appropriate.

For the identification of semi–leptonic decay electrons it is also necessary to match the electron candidate with its parent jet. This is best achieved by

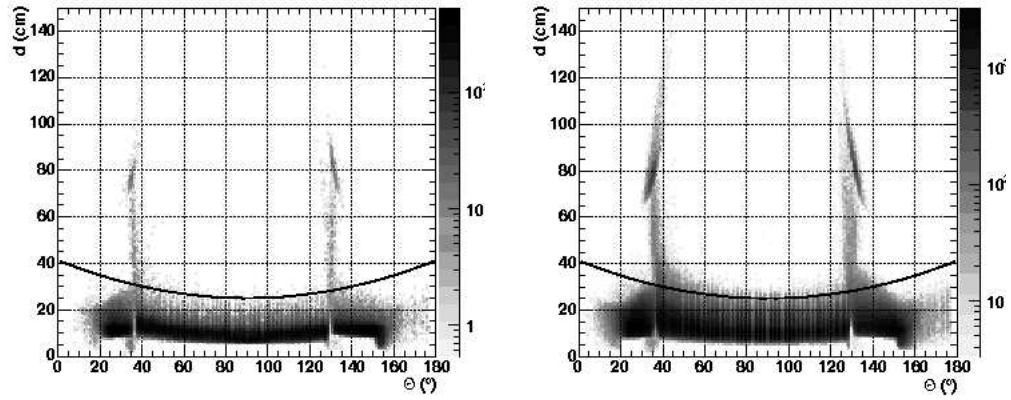

(a) Electrons (b) Pions

Figure 3.7: EFO distribution as a function of the depth, d, and the polar angle, θ, for electrons (a) and pions (b). The regions of the super–cracks at $\theta \approx 35°$ and $\theta \approx 130°$ are clearly visible. The cut defined in Eqn. 3.6 is represented by the black line. Figure taken from [Jün05].

cutting on the distance between the candidate and the jet in the (η, ϕ)–plane, $d_{\text{jet}} = \sqrt{(\Delta\eta)^2 + (\Delta\phi)^2} < 1.5$, as seen in Fig. 3.8.

3.5 Summary

In the previous sections the selection of dijet photoproduction events containing possible $e^{\pm}$ candidates from semi–leptonic decays of heavy hadrons has been described. The impact of the selection cuts on the total number of events is shown in Fig. 3.9. An example of such an event is displayed in Fig. 3.11. Control distributions of the event kinematics of those are presented in Fig. 3.10. Here, for the sake of completeness, the electron candidates have been further refined by a cut on the electron test hypothesis function as will be explained in Sec. 6.3. The distributions for real data and Monte Carlo agree well except for the high x_{p} and the low x_{γ} region. The discrepancy for low x_{γ} values results from the incomplete description of the soft underlying event. Although the PYTHIA program has the ability for simulating multiple parton interactions, it is known that the model is not sufficient to fully describe all the soft interactions at taking place at low x_{γ}. The same holds for other Monte Carlo generators too, and the topic is the subject of recent measurements and discussions (see for instance [Aco]).

In the next two chapters the identification of the electrons from semi–leptonic decays will be discussed, which is needed for the extraction of the beauty and charm signals.

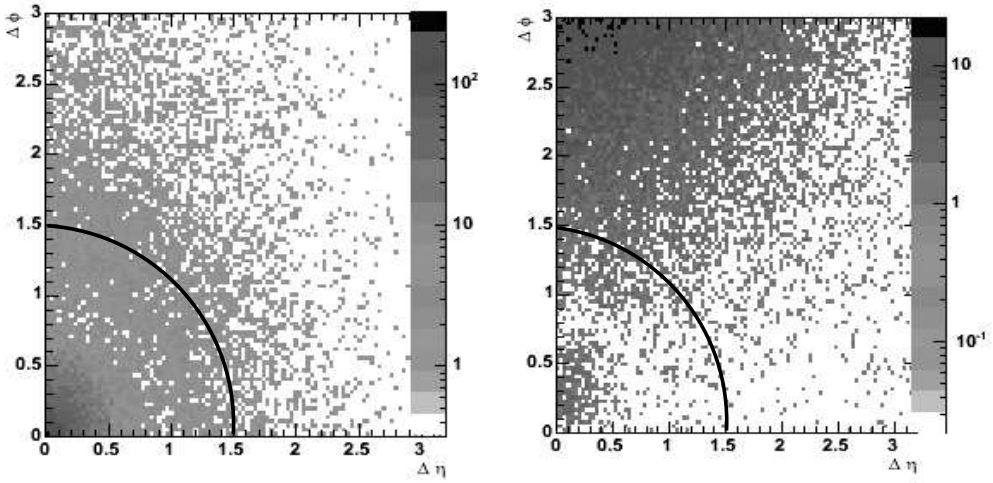

(a) Close–by jet (b) Distant jet

Figure 3.8: Distance of electron candidates to leading jets in the ($\eta\phi$)–plane. In (a) the distances to the nearest jet are shown, while the distribution (b) includes the distances to the more distant jet. The radius cut at 1.5 is needed for avoiding ambiguous matchings at large distances. Courtesy of [Jün05]

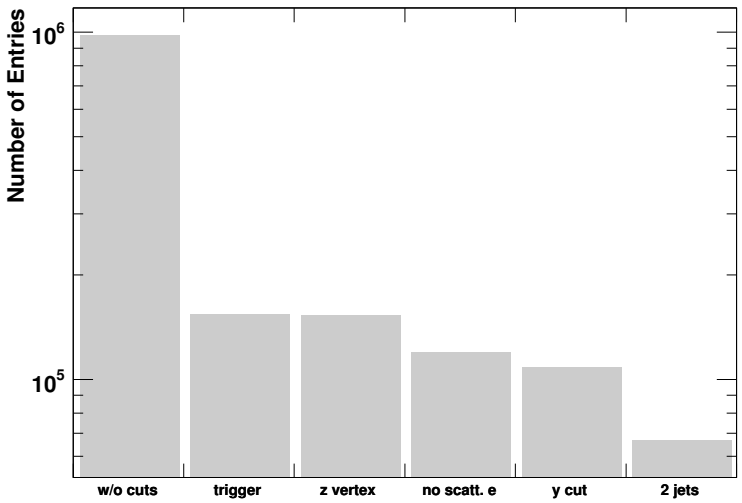

Figure 3.9: Effect of the cuts used for the event selection on the total number of events. A detailed description of the selection criteria is given in the text. Shown are the numbers for the 98—00 running period.

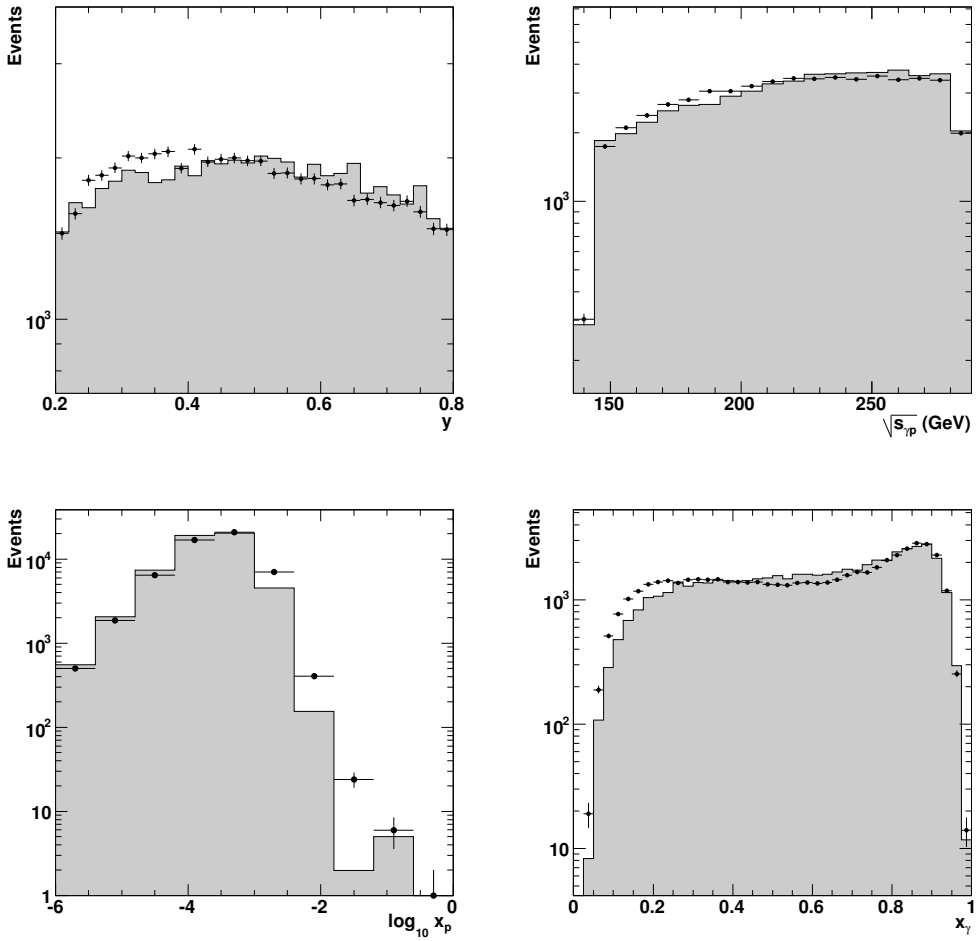

Figure 3.10: Control distributions of the event kinematics in γp events containing at least two jets and an $e^{\pm}$ candidate coming from a semi–leptonic decay of a beauty or charm hadron. Shown are the fractional photon energy, y, and the corresponding centre–of–mass energy in the γp system, $\sqrt{s_{\gamma p}}$, as well as the fractional momenta, x_p and x_γ, of the proton and the photon participating in the hard scatter. The Monte Carlo distributions (shaded histograms) are normalised to the area of the distributions for real data (black dots). The distributions shown are that for the 98—00 running period ($\sqrt{s_{ep}} = 318\,\text{GeV}$).

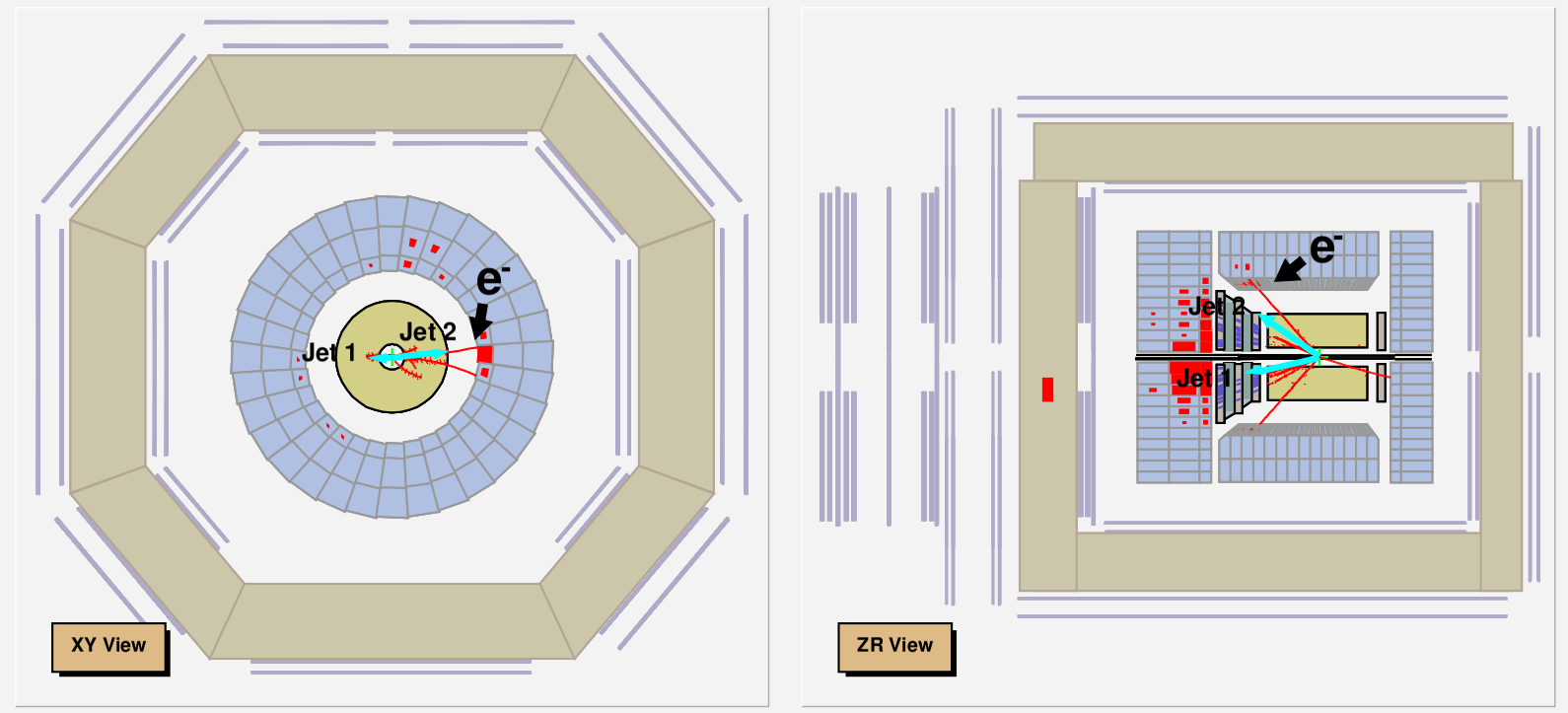

Figure 3.11: Event display of a simulated $b\bar{b}$ photoproduction event. On the left side the *xy*–projection of the ZEUS detector in the direction of the electron beam is shown and the right side shows the *zr*–projection of the event. Here, the electron enters the detector from the left, while the proton comes from the right. The dijet system going in the forward direction is indicated by the two arrows. The B hadron in the lower energetic jet has decayed semi–leptonically into an e^-, which is indicated too. The electron track in the central drift chamber is clearly visible as well as its energy deposit in the EMC section of the calorimeter. For details about the event display program ZEVIS see Appendix E.

Chapter 4

Ionisation Loss Measurements

In this chapter the identification of charged particles by means of energy loss due to ionisation, $\mathrm{d}E/\mathrm{d}x$, in the central tracking chamber is discussed. The particle identification is needed later for the identification of electrons from semi–leptonic decays in order to enrich a beauty signal.

In the past, particle identification with $\mathrm{d}E/\mathrm{d}x$ has been used only in a few ZEUS analyses and then only in crude ways. A favoured method is that of *statistical subtraction* which has been used at ZEUS for identifying electrons produced in semi–leptonic decays [Win99, Vac05]. Here, an electron–enriched sample (EMC fraction $f_{\mathrm{EMC}} = 1$) and a hadron–enriched one ($f_{\mathrm{EMC}} < 0.4$) are selected and their $\mathrm{d}E/\mathrm{d}x$ distributions are subtracted from each other. The tiny difference then is simply fitted with a GAUSSian which is used for defining a cut on the $\mathrm{d}E/\mathrm{d}x$ variable (see figure 4.1). All tracks with a higher $\mathrm{d}E/\mathrm{d}x$ value are defined as electron signal and then used for further analysis. This method has several drawbacks. The biggest one is the assumption that the hadronic background in the electron–enriched sample is described correctly by the hadron sample. This assumption is not necessarily fulfilled, because hadrons with $f_{\mathrm{EMC}} = 1$ might differ significantly from the ones with a lower EMC fraction. In particular the latter ones contain much more soft pions and anti-protons. This can lead to non-controllable systematic errors. Indeed it has been shown that this method has not worked for beauty or charm decaying semi–leptonically into positrons, only electrons.[1] Also, the hard cut on $\mathrm{d}E/\mathrm{d}x$ reduces the statistics even further which results in large statistical uncertainties for the whole analysis.

Another method used sometimes is just *cutting the* $\mathrm{d}E/\mathrm{d}x$ *bands* [C$^+$04b]. Given that the resolution of the energy loss measurement in the CTD usually is in the order of 10 % this results in a certain amount of contamination in the selected sample which is unwanted. Even more, in regions of crossing bands this

[1] The beam particle had been always a positron in this analysis.

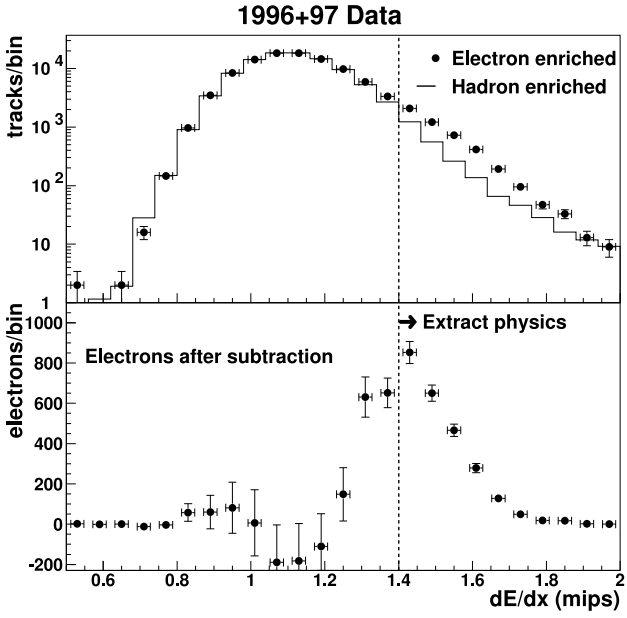

Figure 4.1: Statistical subtraction method. The hadron–enriched sample which estimates the background is subtracted from the electron–enriched sample [Win99].

method is not applicable at all which means that large ranges in momentum have to be cut out. Table 9.1 of [BR93] shows the allowed momentum ranges for a 2σ identification of particles in argon.[2]

A better way to identify particles is combining all available information in some hypothesis test. From the view of statistics the best possible test is the *likelihood ratio test*, which in easy words is the ratio of the likelihood for the hypothesis to test (the particle being of the type in question) and sum of the likelihood for the hypothesis and the anti-hypothesis (the particle being of any other type). This is the method used here which has been applied for identifying B hadrons decaying semi–leptonically into $e^{\pm}$. It will described in more detail in Sec. 6.2.

After a brief introduction to the passages of charged particles through matter, the measurement process of energy losses in the CTD is discussed. Next, the calibration of the reconstructed dE/dx for the HERA-I running period is performed together with a description of the calibration samples needed for this. The last section deals with ways of using dE/dx in Monte Carlo events. The combined particle identification using ionisation loss measurements and calorimeter information will be discussed in Chapter 5.

[2]Note that here a much better resolution is assumed.

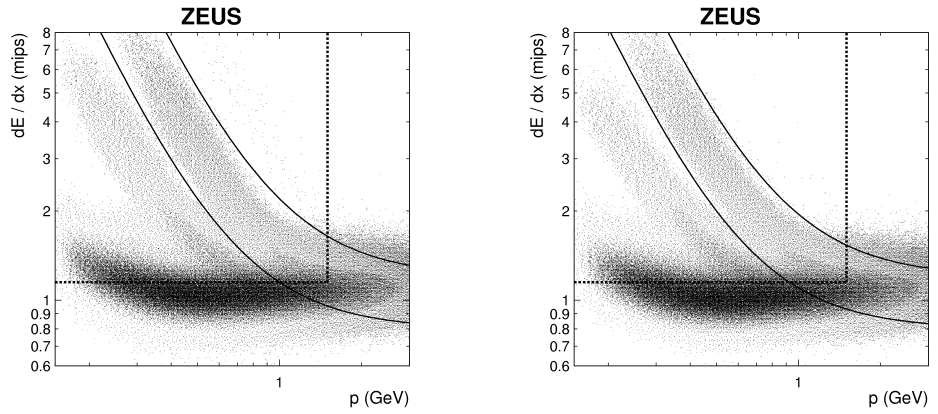

(a) Positive charge (b) Negative charge

Figure 4.2: This picture illustrates cutting the dE/dx bands of positive (a) and negative (b) charged tracks. Used for pion–proton separation within the θ^{++} analysis [C$^+$04b].

4.1 Ionisation Losses of Particles in Matter

Charged particles traversing the CTD mainly interact by ionisation and excitation of the gas molecules in the chamber. Other processes like bremsstrahlung etc. are negligible in the momentum range considered. The energy required for the gas ionisation is taken from the particle's kinetic energy and is very small, typically a few keV per centimetre of gas in normal conditions. The released ionisation electrons of every track segment drift through the gas and are amplified at the signal wires in avalanches.[3] Electrical signals that contain information about the original location and ionisation density of the segment are recorded.[4]

First predictions of energy losses caused by the passage of charged particles through matter, first observed by Bragg [BK05], were made by Bethe and Bloch [BB33] and their famous formula. Here, the energy loss per unit of pathlength is given by

$$\frac{\mathrm{d}E}{\mathrm{d}x} = \frac{4\pi N e^4}{m_\mathrm{e} c^2 \beta^2} z^2 \left(\ln \frac{2 m_\mathrm{e} c^2 \beta^2 \gamma^2}{I} - \beta^2 \right), \tag{4.1}$$

where z denotes the charge of the travelling particle, N the number density of electrons in the matter traversed and I the mean excitation energy of the atom. The latter is calculable for simple atoms, but has often been considered a parameter to be fitted from the measurements of the ionisation energy loss near the minimum. A collection of such determinations of I is contained in [SB82]. The Bethe–Bloch formula includes the integral over all the energies lost to the individual

[3] For the CTD the gas gain is of the order of 10^4.

[4] Ample reviews on this subject can be found at [Sau77] and [BR93].

atoms of the medium extending up to the maximum transferable energy, and is for this reason only valid for travelling particles heavier than electrons. These are indistinguishable from their collision partners resulting in a half as large maximum energy [Bha38].[5] However, when averaging only over transfer energies up to a certain limit ~10—100 keV [Ueh54], which is much larger than the binding energies, yet sufficiently small, the energy loss is the same for electrons and hadrons [Bet30].

At low velocities, the energy loss falls rapidly with increasing $\beta\gamma$ due to the fact that the collision time, during which an atomic electron experiences the electric field of the charged particle passing by, becomes shorter. After the fast decrease dominated by the $1/\beta^2$ term, the energy loss reaches its minimum around $\beta = 0.97$ and slowly increases for $\beta \to 1$ (relativistic rise). This rise is mainly caused by the LORENTZ boost flattening the electric field of the particle, enabling more distant atoms to take part in the process.

First corrections to this model were made by FERMI [Fer40] correctly stating that the relativistic rise would not continue to indefinitely large values of γ. The restriction is caused by the 'density effect' which describes the coherent effect of surrounding polarisable atoms shielding the field of the travelling particle. More precise calculations of the correction term and the inclusion of higher order effects were later performed by STERNHEIMER et al. [SBS84] and also BARKAS and BERGER [BB64].

Equation 4.1 cannot be used directly for the determination of the track ionisation in a drift chamber. Above a certain energy, an electron knocked out of a gas atom will form a second track, a δ electron, and will not contribute to the primary track any more. Depending on the range of the δ–ray, its ionisation is no longer attributed to the first track, causing large fluctuations in the energy loss measurement and thus bringing a statistical aspect into that issue.[6] A first analytical formulation of the problem (*c. f.* Eqn. 4.2 and Fig. 4.3) was given by LANDAU for thin materials [Lan44]. The fact that in thin materials the total energy loss is given by a small number of interactions, each one with a very wide range of possible energy transfers, determines a characteristic shape of the energy loss distribution, which in a simplified form had been written by LANDAU as

$$f(\lambda) = \frac{1}{\sqrt{2\pi}} e^{-\frac{1}{2}\left(\lambda + e^{-\lambda}\right)}, \tag{4.2}$$

[5] In addition, spin and mass effects had been neglected.

[6] For example, in 1 cm argon under normal conditions one out of the twenty electrons produced on average has an energy of 3 keV and a practical range of 100 μm. The energy dependence of the practical range is almost quadratic up to several hundred keV. Electrons with energies above 30 keV have a range larger than 1 cm of argon, and will escape detection from that layer. By the way, for such high energies the δ–electrons are emitted *perpendicular* to the incident track. However, multiple scattering quickly randomises the direction of motion of the electrons.

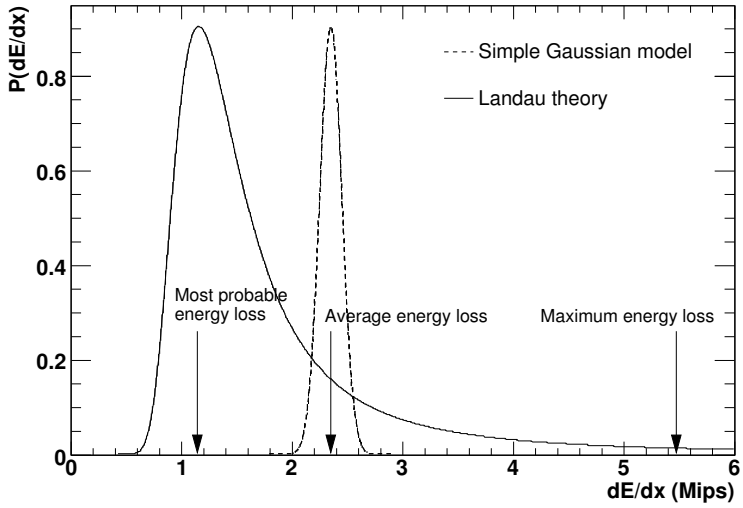

Figure 4.3: Probability density function of the energy loss. The LANDAU theory takes the statistical fluctuations of single ionisations into account (solid line) while the classical BETHE–BLOCH prediction (dashed line) is valid only for the average of a large number of ionisation processes by means of the Central Limit Theorem. In case of the LANDAU function the most probable $\mathrm{d}E/\mathrm{d}x$ value is different from the mean. The energy loss is limited by the maximum transferred energy in the ionisation process (maximum energy loss). Without this cut–off the weighted mean $\mathrm{d}E/\mathrm{d}x$ value of the LANDAU curve would not be finite.

where the reduced energy variable, λ, represents the normalised deviation from the most probable energy loss, $\mathrm{d}E/\mathrm{d}x_{\mathrm{MP}}$:

$$\lambda = \frac{\mathrm{d}E/\mathrm{d}x - \mathrm{d}E/\mathrm{d}x_{\mathrm{MP}}}{\xi}\,, \tag{4.3}$$

with the scaling factor, ξ, being related to the sampling length, $\mathrm{d}x$, and the particle's velocity, β, by $\xi \propto \mathrm{d}x/\beta$.[7]

The situation is depicted (in absolute units) in Fig. 4.3. The LANDAU function exhibits a long tail at large energy losses, corresponding to events where one or more energetic δ–electrons have been produced. The energy resolution of a thin detector for fast particles is therefore very poor.

The LANDAU distribution is based upon several assumptions and therefore restricted in application. A statistical formulation, treated with Monte Carlo methods, is better suited. The *photo–absorption ionisation model* (PAI) by ALLISON and COBB [AC80] does exactly this. Here, the properties of the medium enter through

[7] This is valid only for large sampling length of several cm [CE76].

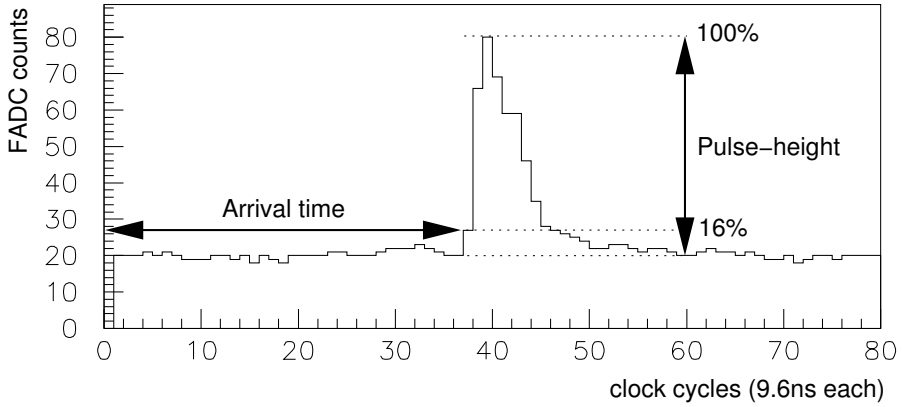

Figure 4.4: Pulse train on a CTD signal wire. The signal pedestal is determined by averaging the first bins. The pulse–height is the peak level minus the pedestal. The arrival time of the pulse is defined by a 16 % increase of the signal above the pedestal.

the frequency dependence of the di-electric constant, which in turn is derivable from experimental photo–absorption coefficients. BLUM and ROLANDI give a generalised parametrisation for a description of measured ionisation curves based on the PAI model [BR93]:

$$\frac{\mathrm{d}E}{\mathrm{d}x} = \frac{p_1}{\beta^{p_4}} \left\{ p_2 - \beta^{p_4} - \ln\left(p_3 + \frac{1}{(\beta\gamma)^{p_5}} \right) \right\} , \tag{4.4}$$

where the p_i are five free parameters, to be determined by a fit to the measurements. The exact knowledge of the form given in Eqn. 4.4 can then be used for testing particle hypotheses of a given track, which will be the subject of Chapter 5.

The large fluctuation in energy loss for individual events has several consequences. First, the amplification electronics of the chamber has to be capable of handling the large dynamic range of the signals. Secondly, a single measurement of a track contains very little information about the average energy loss. Thus when trying to identify particles, one is obliged to sample each track as many times as possible.

4.2 Energy Loss Measurements

4.2.1 Single Wire Measurements

The avalanche of ion pairs caused by the incident particle passing the drift cell induce a signal on the sense wire. The electrons drifting with a drift velocity of

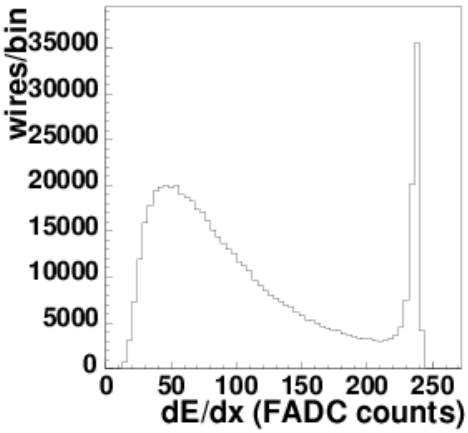

Figure 4.5: Typical pulse–height spectrum for low momentum pions exhibiting the expected LANDAU shape. The large spike on the right is caused by saturation effects due to the 8–bit limitation of the FADCs.

47 μm/ns towards the anode are absorbed quickly producing a fast signal there. The ions moving much more slowly to the cathodes — their drift velocity is several 100 μm/ns — cause a much slower but nevertheless larger signal because they experience the almost full potential between the electrodes. The front–end (r, ϕ) read–out electronics is de-coupled via a capacitor from the wire and designed in a way such that the read–out signal height is proportional to the electric charge in the avalanche which in turn is a linear function of the energy loss due to the primary ionisation.[8] After being shaped and amplified, the signals are digitised every 9.6 ns by an 8–bit FADC awaiting the FLT decision. For accepted events, the signals are pushed to a digital signal processor (DSP), which analyses sequences of digitisations, *pulse trains*, one sample of which is shown in Fig. 4.4. The DSP determines the pedestal of the signal and its peak level above the pedestal (the *pulse–height*), as well as the arrival time of the pulse, which is defined as the moment when the pulse reaches 16 % of its pulse–height. Both, the arrival time and the pulse-height are used for track reconstruction, the latter characterising also the energy loss of the particle in the vicinity of the wire.

The limitation of the read–out to 8 bits causes an artificial saturation of pulse–heights exceeding the maximum allowed value. This leads to a large spike in the pulse–height spectrum as seen in Fig. 4.5.

Hit Rejection

Pulse–heights below a certain threshold are rejected for noise suppression, as well as hits too close to cell boundaries, since the electric field is very distorted there.

[8] Unfortunately this is not entirely true. As the main purpose of the CTD is the reconstruction of particle tracks, it had been optimised for a high spatial resolution. The chamber had been run during the HERA running period with high voltage of 1800 V implying that the CTD operates at the upper edge of the ‘proportional mode’.

Similarly, hits with drift distances less than 100 μm are rejected, because of the rapidly increasing electric field close to the wire, the space–time correlation becomes invalid leading to a drift distance measurement not usable for the track reconstruction. Multiple hits on a single wire separated less than 100 ns in time are discarded as are hits on noisy or hot wires.

Phase 1 Corrections

The main objective of the CTD has never been particle identification and also the truncated mean (Sec. 4.2.2) of pulse–height measurement is only a rough estimator of the true energy loss. Hence, the observed $\mathrm{d}E/\mathrm{d}x$ has to undergo many kinds of corrections to become independent of systematic effects and comparable with the true energy loss. Those corrections are described briefly here and in the following section.

During the on-line phase 1 reconstruction several empirical corrections for detector and geometry effects are applied to the pulse–height measurements. This is done when the track reconstruction is finished so that the 3–dimensional information of the hits and the exact particle trajectory is already known. The notation used for describing the geometry is explained in Fig. 4.6.

1. Path length corrections depending on $1/\sin\theta$.
2. The relative gain on the signal wires.
3. Corrections depending on the angle ψ'. This provides a crude — though not satisfactory — correction of the differences between positively and negatively charged particles. A more detailed discussion on this effect and a solution to the problem is given in Sec. 4.3.
4. Corrections for the local LORENTZ angle, λ depending on the (z, r) position of the hit. As it turned out this correction is simply wrong, as the $\mathrm{d}E/\mathrm{d}x$ is not influenced by the LORENTZ angle at all. However, for technical reasons this correction cannot be removed from the phase 1 reconstruction anymore, so that the correction has to be eliminated later on (see also Sec. 4.3).
5. Due to dispersion of the signal when propagating along the wire, corrections in terms of the z position of the hit are applied.
6. Drift distance corrections. The drift length relative to the cell size is divided into ten bins for which correction factors exist. This also turns out to be insufficient and needs further refinement (*c. f.* Sec.4.3).

The so corrected pulse–heights, still in FADC units, are comparable now and called energy loss, $\mathrm{d}E/\mathrm{d}x$.

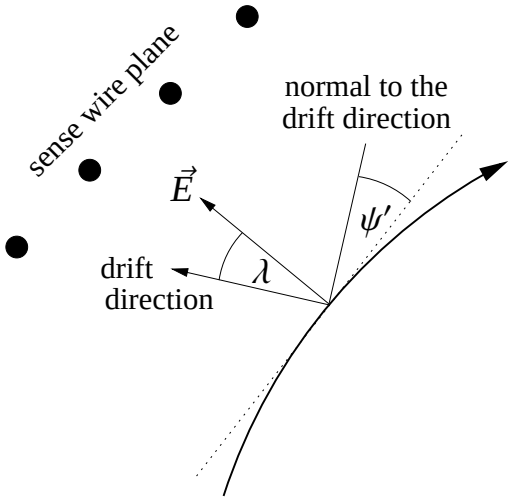

Figure 4.6: Definition of the LORENTZ angle, λ, by which the drift electrons are deflected due to the magnetic field, and the azimuthal angle ψ', which is enclosed by the normal to the drift direction and the track tangent.

4.2.2 The Truncated Mean Method

The best way of combining the single–wire measurements of the energy loss for particle identification would be using likelihood methods. However, at ZEUS those measurements are not stored at the MDST level, which is commonly used for physics analyses, due to considerations of disk space.[9] Instead, during the phase 1 reconstruction the single hit measurements are averaged along each track and the resulting mean energy loss per track is stored. Certain fractions of the lowest and highest pulses of a track are removed from the sample, so that the resulting mean value becomes close to the most probable value. The is called the *truncated mean*, which for large samples yields almost the same accuracy as that of likelihood methods [JLL+73].

The percentage of hits to be discarded is optimised for best resolution. If the fraction of selected hits is too low, the truncated mean fluctuates owing to low statistics; if it is too high, the hits from the tails of the (LANDAU–shaped) distribution cause substantial fluctuations by their large weight (*c. f.* the difficulties described Sec. 4.4.3). For the CTD a rejection of the 10 % lowest and 30 % highest values was chosen.

If too many saturated hits[10] are used for the computation, the result underestimates the truncated mean. In that case the procedure of the *variable truncated mean* is applied [Ver98]: If for more than 30 % of the hits the pulse–heights are beyond the saturation limit, all saturated hits are removed before averaging. In a second step the loss of their contribution is compensated by shifting the truncated

[9] The full information is still available from the raw–DSTs. However, those are very hard to access and any analysis using the raw–DSTs would require a full reconstruction of the data consuming a significant fraction of the computing power at DESY for several months.

[10] Pulses which have driven the FADC into saturation are marked by the DSP.

mean value artificially towards a higher value. If n_{kept} is the number of hits kept, and n_{totsat} the total number of saturated hits after the rejection procedure described above, then the number of hits used for the truncated mean calculation is given by

$$\begin{aligned} n_{\mathrm{low}} &= \mathrm{int}(0.1 n_{\mathrm{kept}} + 0.5)\,, \\ n_{\mathrm{up}} &= \mathrm{int}(0.3 n_{\mathrm{kept}} + 0.5)\,, \\ n_{\mathrm{used}} &= n_{\mathrm{kept}} - n_{\mathrm{low}} - n_{\mathrm{up}}\,, \end{aligned} \tag{4.5}$$

with int(. . .) denoting the truncation of a floating point number to its integer value. The number of remaining saturated hits then is simply

$$n_{\mathrm{sat}} = \max(0,\, n_{\mathrm{totsat}} - \mathrm{n})\,. \tag{4.6}$$

Thus the number of hits finally used for the variable truncation is

$$n_{\mathrm{trunc}} = n_{\mathrm{used}} - n_{\mathrm{sat}}\,. \tag{4.7}$$

The (variable) truncated mean of the pulse–heights, ph_i, is computed by

$$\left\langle \frac{\mathrm{d}E}{\mathrm{d}x} \right\rangle = \frac{a(n_{\mathrm{kept}}, n_{\mathrm{totsat}})}{n_{\mathrm{trunc}}} \sum_{i=n_{\mathrm{low}}+1}^{n_{\mathrm{low}}+n_{\mathrm{trunc}}} ph_i\,. \tag{4.8}$$

The correction factor a used for shifting the mean value upwards in case of saturation is defined as

$$a(n_{\mathrm{kept}}, n_{\mathrm{totsat}}) = \begin{cases} 1; & n_{\mathrm{totsat}} \le n_{\mathrm{up}} \quad (\text{saturation} < 30\,\%)\,, \\ f(0.7)/f(x); & \text{otherwise}\,. \end{cases} \tag{4.9}$$

The correction function $f(x)$ is a fourth–order polynomial fitted to the data:

$$f(x) = 71.508x^4 - 100.4x^3 + 55.685x^2 + 30.92x + 26.95\,, \tag{4.10}$$

with

$$x \equiv (n_{\mathrm{kept}} - n_{\mathrm{totsat}})/n_{\mathrm{kept}}\,.$$

A minimum number of $n_{\mathrm{trunc}} = 4$ is required, the maximum possible number is $n_{\mathrm{trunc}} = 43$.

4.2.3 Run–by–Run Calibration

The measured pulse–heights are affected by additional factors not yet considered. Variations of the high voltage, the atmospheric pressure and the gas mixture affect the gas gain and the drift velocity in the chamber. These effects are corrected on

a run–by–run basis at the MDST level, *i. e.* the truncated mean values undergo corrections in the off-line physics analysis.[11] To obtain the dE/dx scale of each run, minimum ionising pions are used. These are selected by requiring tracks with momenta in the range 300—400 MeV. Since most of the pions are minimum ionising in this range, the dE/dx spectrum exhibits a large peak. By fitting a GAUSSian function[12] to the peak, the number of FADC counts corresponding to the energy loss of minimum ionising particles (mips) is found,which under normal operation conditions corresponds to $3\,\mathrm{keV/cm}$.[13]

The measured dE/dx values surprisingly show a decrease with rising atmospheric pressure. Naïvely one would expect an increase due to the also increasing electron density. However, there are two contrary effects dominating over the rise in the electron density [Sid95]: The drift velocity is reduced with higher density of the medium, altering the height–to–area relation of the pulses[14], and in addition argon possesses an absorption edge at 12 eV, which increasingly prohibits ionisation with growing pressure, leading to a reduction of the gas gain. The air pressure effects are eliminated by adjusting the measured dE/dx to a nominal pressure of 1013 hPa.

It was shown, that variations of the energy loss *within* a run, even long ones, are small (typically below 2 %), and thus are negligible [Dep99].

4.3 Systematic Corrections of the Energy Loss

When first used for physics analyses [Dep99, Win99], distributions of the mean dE/dx values per track indicated that the corrections mentioned above are not sufficient and more corrections of detector systematics would be necessary. An example is shown in Fig. 4.7, in which the energy loss of electrons produced in $\gamma \to e^+e^-$ reactions is depicted as a function of the track polar angle. A large dip at the centre of the distribution of nearly 10 % is seen. This was the first indication for the *space–charge effect* which is explained below. A simple correction of the angular dependence, as done in [Win99], did not really solve the problem. This became clear when the analysis which is subject of this thesis was started. More peculiarities showed up. Energy loss measurements of positive and negative charged tracks were inconsistent, which was seen partially in [Win99], since this

[11] The correction factors are provided for each run by the CTD group.

[12] Which is expected, since the spectrum is a distribution of pulse–height *mean* values.

[13] It has to be noted however, that the fitted peak position is below the true minimum at 550 MeV for pions. This is due to systematic uncertainties explained in Sec. 4.3. Since the fitted value is only used for normalising the dE/dx measurements, making the results from different runs comparable, it does not cause any harm here.

[14] Remember: A linear dependency between the height of the pulses and their time integral, *i. e.* the collected electric charges, is assumed.

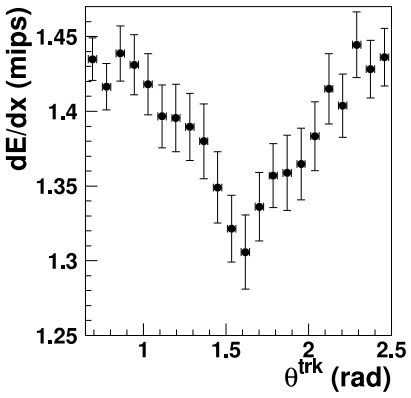

Figure 4.7: Measured energy loss, $\mathrm{d}E/\mathrm{d}x$, of electrons produced in γ conversions as a function of the polar angle, θ^{trk}, of the electron track. The distribution exhibits a dramatic effect of almost 10 % for very central tracks. Figure taken from [Win99].

analysis was not able to deal with $\mathrm{d}E/\mathrm{d}x$ of positrons, only with that of electrons.[15]

Therefore extensive studies of systematics effects on energy loss measurements with the CTD were started, together with developments of appropriate corrections. The rich results of this work, ongoing for several years, are collected in [Bar06b, Bar06a], and can only be briefly discussed here.

Space–charge effect Due to the slow ion drift, tracks with shallow polar angles generate clouds of ions around the wire shielding the wire for subsequent drift electrons, thus reducing the measured ionisation. The effect is dependent on $1/\cos\theta$ and vanishes for $\theta \to 90°$.

Drift–time differences The pulses of positively charged tracks are more pronounced than that of negatively ones. Because of the 45° tilt of the drift cells, positive tracks are running for a long time close to an isochrone leading to almost simultaneous ionisation clusters piling-up to a huge signal on the wire (see Fig. 4.8). In contrast, negative tracks cut across the isochrones in the positive direction most of the time, which results in many small pulses on the wire well separated in time. This effect depends on the local angle between particle and drift direction, ψ'.

Threshold effect Signals with pulse–heights below a certain threshold are not accepted by the CTD read-out electronics in order to suppress noise. This

[15] One reason for the incomplete understanding of energy loss measurement systematics in drift chambers might be that the issue is not covered widely in literature. The effects have been studied — if at all — in test–beam set–ups, rather than under under realistic experimental conditions, especially in a collider experiment (*e. g.* [VRFC82]). Also the subject tends to be neglected, since the main goal of a drift chamber is the reconstruction of particle tracks, consuming most of the available manpower.

of course can affect the truncated mean value, for small contributions of energy loss are not considered, leading to a deceptive higher mean value.

Saturation In a similar way the truncated mean value needs to be corrected for saturated hits. The variable truncated mean described above covers most but not all of the effect.

Integer effect The truncated mean method cuts fractions of hits. Since hit numbers have to be integer values, the fractional values needs truncation, which results in artificial shifts of the truncated mean, in particular for low total hit numbers.

Neighbourhood effect Particles running close to each other can induce interfering signals on the same wire. This also would result in an overestimation of the truncated mean value.

Lorentz angle As mentioned above, the ionisation measurement is not affected by the LORENTZ angle. Although the magnetic field extends the drift paths of the ionisation electrons, this affects all tracks in the same way. Therefore the corresponding phase 1 correction must be undone.

Run–by–run corrections The run–by–run corrections already done are not sufficient. Remaining variations of a few percent exist, therefore additional corrections are needed here. Furthermore, since the run–by–run corrections are done before the other corrections, they affect the other corrections in the wrong way. This must be undone also.

Wire gain corrections Similarly, the wire gains show variations, which have to be corrected. For technical reasons this cannot be done for every single wire, but only for groups of eight wires (supercells).

Some of the corrections are functions of the true $\mathrm{d}E/\mathrm{d}x$ itself; therefore they are determined in an integrated iterative procedure, which converges after a few steps. The situation is further complicated by the fact that the hit information is not available, only the information per track. Hence, elaborate track extrapolations are necessary to gain information like ψ' or the z–position of the track etc. at each single wire. Sets of corrections have been made for different periods in time, in which the CTD had been in different operational states, *e. g.* due to variations in the gas mixture, changes of the high voltage etc. In 2000 the gas bubbled through water for several weeks to recover the CTD wires from aging effects. The corrected $\mathrm{d}E/\mathrm{d}x$ values are stable and comparable for all of these periods including the HERA-I to HERA-II transition. Also, all of the peculiar dependencies seen before have vanished. In particular differences between positive and negative charged particles

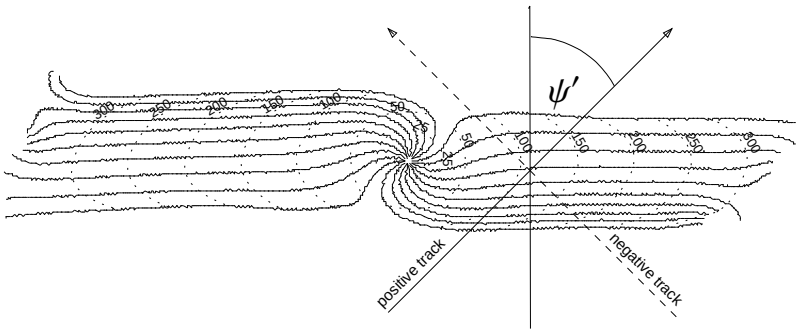

Figure 4.8: The drift time effect. Positive tracks are running close to the isochrones for a longer time than negative tracks causing larger pulses on the signal wire.

do not exist anymore. The correction procedure is a big success. Compared with ionisation energy loss measurements done with a drift chamber in other collider experiments those measurements at ZEUS are extremely well understood.

4.4 Energy Loss Calibration

In order to identify particles, measured values of the energy loss are compared to predicted ones. For the latter the energy scale of the CTD has to be known. This is done by fitting the data to theory for very well known particle samples of different type.

In theory energy losses for a particle are predicted dependent on its LORENTZ boost $\beta\gamma$ which is not known by default. However, if the particle's mass is known the boost can easily be computed by using

$$\beta\gamma = \frac{p}{m}\,. \tag{4.11}$$

In the case of Monte Carlo this is almost trivial. But here the problem occurs that the $\mathrm{d}E/\mathrm{d}x$ provided by the GEANT 3 program used at ZEUS is much too imprecise for a comparison.[16] Therefore real data has to be used. For this, final–state particles are chosen from very well defined particle reactions for which the type of the outgoing particles is known exactly. They are referred to in this context as "calibration samples". Note that samples from different reactions are used in order to avoid systematic errors from event topologies. This has the additional advantage that the particle identification is independent of the particular analysis which it is applied for. The samples differ in their range of momentum. In these regions a purity of at least 95 % has been achieved.

[16] This version of GEANT developed in the late eighties uses a simplified model for the energy loss calculations to save computing time, which had been a bigger issue at that time.

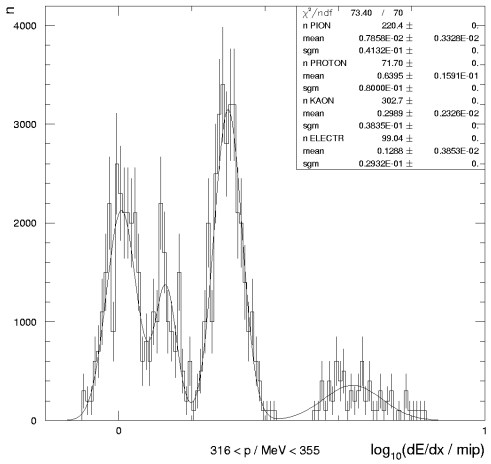

Figure 4.9: Fitting the BETHE–BLOCH curve with an inclusive sample — the multi–GAUSS method [Dep99].

Instead of using pure calibration samples for each particle type, one can also look at an inclusive sample of charged tracks [Dep99, Nac97]. Binning them in $\beta\gamma$ gives $\mathrm{d}E/\mathrm{d}x$ distributions containing more or less pronounced peaks for each particle type (e, π, K and p). Fitting a sum of four GAUSSians whose mean values are fixed to a single (still variable) BETHE–BLOCH function to all of the $\mathrm{d}E/\mathrm{d}x$ slices simultaneously and repeating this procedure iteratively in particular in regions of overlapping bands will give you a good idea of the "true" BETHE-BLOCH curve (see Fig. 4.9). This method — called the multi–GAUSS method — is fast and easy to implement, however it is limited in accuracy.

4.4.1 Calibration Samples

The following reactions are used to create pure samples of $\mathrm{e}, \pi, \mathrm{K}, \mathrm{p}$ and μ in real data:

$$\begin{array}{rcl@{\qquad}rcl} \mathrm{K}^0_\mathrm{s} & \to & \pi^+\pi^- & \Lambda^0 & \to & \mathrm{p}\,\pi \\ \rho & \to & \pi^+\pi^- & \phi & \to & \mathrm{K}^+\mathrm{K}^- \\ \gamma & \to & \mathrm{e}^+\mathrm{e}^- & \mathrm{J}/\psi & \to & \mathrm{e}^+\mathrm{e}^- \\ \mathrm{e}\,\mathrm{p} & \to & \mathrm{e}'\,\mathrm{X} & & & \end{array}$$

In addition *all* events containing high–quality muons (mostly from cosmic rays) are selected. Because of its low purity the following sample is used for cross-checking only:

$$\mathrm{D}^* \quad \to \quad \mathrm{K}\,\pi\,\pi_\mathrm{s}$$

The selections are now discussed in greater detail. All cuts used for the selections are very stringent to achieve high purity. For decays of the form $\mathrm{A} \to \mathrm{B} + \mathrm{C}$ the following notations for angles will be used:

1. The *opening angle*, α, between the outgoing tracks B and C in the laboratory system
$$\alpha = \sphericalangle\,(\vec{p}_{\mathrm{B}},\ \vec{p}_{\mathrm{C}})\ .$$

2. The *decay angle*, β, which is enclosed by the momentum vector of the decay particle A, measured in the laboratory frame, and the momentum of one of the outgoing particles (by convention the positive charged one) in the rest frame of A,
$$\beta = \sphericalangle\,(\vec{p}(\mathrm{B})|_{\text{rest frame of A}},\ \vec{p}(\mathrm{A})|_{\text{lab frame}})\ .$$

3. The angular difference, δ, between the reconstructed momentum vector of the decay particle A and the backward extrapolation from the decay vertex to the primary vertex
$$\delta = \sphericalangle\left(\vec{p}(\mathrm{A}),\ (\vec{v}_{\text{prim. vtx}} - \vec{v}_{\text{sec. vtx}})\right)\ .$$

4. *Good quality tracks* are tracks which have crossed at least 3 superlayers in the CTD, with a pseudo–rapidity $|\eta| < 1.9$ and minimum transverse momenta of $p_{\mathrm{t}} > 100\,\mathrm{MeV}$.

5. Tracks which are *possible photon conversions* are tested by the $\gamma \to \mathrm{e}^+\mathrm{e}^-$ conversion finder in a less rigorous way compared to *conversion candidates*. The search for the latter and details of the γ conversion finder are given below. The cuts used here are $D < 15$ (*c. f.* Eqn. 4.12) and $M_{\mathrm{ee}} < 250\,\mathrm{MeV}$ leading to an increase in the acceptance of the finder but reducing its purity at the same time. All possible pairs of tracks containing the track in question are checked.

The Decay of Neutral Short–Lived Kaons

The reaction $\mathrm{K}^0_{\mathrm{s}} \to \pi^+\pi^-$ is characterised by two oppositely charged tracks coming from a secondary vertex. Since the decay time, $c\tau$, of the $\mathrm{K}^0_{\mathrm{s}}$ is of the order of 2 cm, which is dilated by its boost, its decay vertex can be reconstructed quite well by the CTD. A cut on the invariant mass of the outgoing $\pi^+\pi^-$ pair is then used to select $\mathrm{K}^0_{\mathrm{s}}$ decays with high purity. Comparison with Monte Carlo shows a remaining background from Λ^0 decays which are discarded by a veto on the $\mathrm{p}\pi$ mass hypothesis.[17] Additional cuts are made for cleaning the sample.

- Invariant $\mathrm{K}^0_{\mathrm{s}}$ mass $0.492 < M_{\pi\pi} < 0.502\,\mathrm{GeV}$;
- $\mathrm{K}^0_{\mathrm{s}}$ proper decay time $0.05 < \tau < 0.40\,\mathrm{ns}$;

[17] The higher momentum track is supposed to be the proton.

- Veto on Λ^0 invariant mass $M_{p\pi} > 1.1\,\mathrm{GeV}$;
- Veto on γ conversions $M_{ee} > 0.25\,\mathrm{GeV}$;
- Momenta of the outgoing pion tracks $0.1 < p_\pi < 0.8\,\mathrm{GeV}$;
- Decay angle $\cos\beta < 0.8$;
- Extrapolation to primary vertex $|\delta| < 0.8\,\mathrm{rad}$;
- Quality of secondary vertex fit $\chi^2/\#(\mathrm{d.o.f.}) < 5$; [18]
- Primary vertex position $|z_{\mathrm{prim.\,vtx}}| < 50\,\mathrm{cm}$;
- The oppositely charged pion tracks are of good quality and not tagged as possible γ conversions (see above).

Lambda Decays

This decay $\Lambda^0 \to p\pi$ is similar to that of the K^0_s except for the different masses of the outgoing particles and the invariant mass to test. Here again, the higher momentum track is supposed to be the proton. The selection cuts are:

- Invariant Λ^0 mass $1.113 < M_{p\pi} < 1.119\,\mathrm{GeV}$;
- Decay length $d > 10\,\mathrm{cm}$;
- Veto on K^0_s decays $M_{\pi^+\pi^-} < 0.48\,\mathrm{GeV} \vee M_{\pi^+\pi^-} > 0.52\,\mathrm{GeV}$;
- Discard γ conversions $M_{ee} > 0.27\,\mathrm{GeV}$;
- Momenta of the outgoing tracks $0.2 < p_\pi < 0.9\,\mathrm{GeV} \wedge 0.4 < p_p < 3.0\,\mathrm{GeV}$;
- Minimal transverse track momenta $\min(p_t^p, p_t^\pi) > 0.2\,\mathrm{GeV}$;
- Opening angle $0.1 < \alpha < 1.2\,\mathrm{rad}$;
- Decay angle $\cos\beta < 0.9\,\mathrm{rad}$;
- Extrapolation to primary vertex $|\delta| < 0.1\,\mathrm{rad}$;
- Quality of secondary vertex fit $\chi^2/\#(\mathrm{d.o.f.}) < 5$;
- Again, the oppositely charged outgoing tracks have to be of good quality and not tagged as possible γ conversions.

[18] d.o.f. = degrees of freedom.

The Decay of Neutral Vector Mesons

Here, ρ, ϕ and J/ψ mesons are selected in elastic vector meson production events whose features are a low track multiplicity and a small four–momentum transfer squared on the proton side, t. Their decay times are too short for a proper reconstruction of secondary vertices. Instead two oppositely charged tracks coming from the primary vertex are searched for.

$\rho \to \pi^+\pi^-$:

- Only events containing 2 or 3 tracks coming from the primary vertex are taken;
- The track pair in question must be of opposite electrical charges. The tracks have to be of good quality and not marked as possible γ conversions;
- Invariant ρ mass $0.65 < M_{\pi\pi} < 0.88\,\mathrm{GeV}$
- At least one of the pion tracks must have a transverse momentum of $p_t^\pi > 0.5\,\mathrm{GeV}$;
- Transverse momentum of the ρ, $p_t^\rho > 1\,\mathrm{GeV}$;
- Veto on ϕ decays $M_{KK} < 1.01\,\mathrm{GeV} \vee M_{KK} > 1.03\,\mathrm{GeV}$.

$\phi \to K^+K^-$:

- Only events containing 2 or 3 tracks coming from the primary vertex are taken;
- The track pair in question must be of opposite electrical charges. The tracks have to be of good quality and not marked as possible γ conversions;
- Invariant ϕ mass $1.01 < M_{KK} < 1.03\,\mathrm{GeV}$
- At least one of the kaon tracks must have a transverse momentum of $p_t^K > 0.65\,\mathrm{GeV}$;
- Transverse momentum of the ϕ, $p_t^\rho > 1.1\,\mathrm{GeV}$;
- Veto on ρ decays $M_{\pi\pi} < 0.65\,\mathrm{GeV} \vee M_{\pi\pi} > 0.88\,\mathrm{GeV}$;
- The momentum transfer of the proton $t < 0.3$. In the case of exclusive vector meson production t can be computed by $t = -(p_\phi - p_{e'})_t^2$ with $p_{e'}$ being the four–momentum of the scattered electron.

$J/\psi \to e^+e^-$**:**

- Only 2 tracks per event coming from the primary vertex are allowed;
- Invariant J/ψ mass $3.02 < M_{ee} < 3.12\,\mathrm{GeV}$;
- Electron momenta $1.2 < p_e < 3.6\,\mathrm{GeV}$;
- Transverse electron momenta $p_t^e > 1\,\mathrm{GeV}$;
- Pseudo–rapidity of the electrons $|\eta_e| < 1.4$;
- Electro–magnetic energy fraction of the energy flow objects in the calorimeter (EFOs, *c. f.* Sec. 2.2.2) corresponding to the electron tracks $E_{EMC}/E_{tot} > 0.99$;
- The outgoing electron tracks have to be of good quality and not tagged as possible γ conversions.

Photon Conversions

Because of the zero–mass of the photon, the conversion e^+e^- pair is created with almost no opening angle between the tracks. Therefore γ conversions are found by looking at pairs of tracks in the CTD that are very close and become parallel at their point of closest approach. This is achieved by restricting the distance parameter

$$D = \sqrt{\left(\frac{\Delta xy}{\sigma_{\Delta xy}}\right)^2 + \left(\frac{\Delta\theta}{\sigma_{\Delta\theta}}\right)^2}, \tag{4.12}$$

which is composed of the separation Δxy of the two tracks in the (x, y) plane, and the polar angle difference, $\Delta\theta$ and their corresponding resolutions, $\sigma_{\Delta xy}$ and $\sigma_{\Delta\theta}$.[19] In addition, a hard cut on the invariant photon mass, is used. Further background reduction is done by selecting only those conversions happening in the inner CTD wall and the beam–pipe.[20] The full list of cuts is

- Distance parameter $D < 2.5$;
- Invariant γ mass $M_{ee} < 7\,\mathrm{MeV}$;
- Distance of the e^- and the e^+ track in z–direction at the conversion vertex $\Delta z < 0.7\,\mathrm{cm}$;

[19] The resolutions had been determined in [Ver98]. Their values are $\sigma_{\Delta xy} = (0.08 \pm 0.01)\,\mathrm{cm}$ and $\sigma_{\Delta\theta} = (0.017 \pm 0.001)\,\mathrm{rad}$ for real data, and $\sigma_{\Delta xy} = (0.11 \pm 0.02)\,\mathrm{cm}$ and $\sigma_{\Delta\theta} = (0.017 \pm 0.002)\,\mathrm{rad}$ for Monte Carlo.

[20] Due to the higher density conversions in the beam–pipe and the CTD vessel are much more likely than in the sensitive volume of the chamber. Note also, that the references point for the CTD and beam–pipe radii are different, since the beams are off-centre w. r. t. the beam–pipe.

- Radius of the conversion vertex with respect to the beam–pipe centre $5.5 < R_{\text{beam–pipe}} < 7.5\,\text{cm}$;
- Radius of the conversion vertex with respect to the centre of the CTD cylinder $5.5 < R_{\text{CTD}} < 7.5\,\text{cm}$;
- The outgoing tracks have to be of opposite charge and of good quality.

DIS Electrons

For the detection of scattered electrons and positrons in deep elastic scattering events, the SINISTRA electron finder [SV97, vS00] is mostly used. This finder is part of the ZEUS software and consists mainly of an artificial neural network based on energies of calorimeter cells and tracking information.[21] To obtain high purities only tracks with $p > 4\,\text{GeV}$ and an electron probability $\mathcal{P} > 99\,\%$ are selected.

Muons

Events containing at least one very good muon candidate are selected. The muon selection is done with the help of the ZEUS global muon finder GMUON. This package is built as a combination of the large collection of local muon finders using information of various sub-detectors like the muon chambers, the backing calorimeter, the CAL and the inner tracking. A description can be found, *e. g.* in [Blo05]. The GMUON finder assigns quality numbers in increasing order from 1—6 to the μ candidates. Here, only candidates with quality 6 are selected. Since all triggers have been used, the dominant part of this sample are muons from cosmic rays.

Kaons from D Meson Decays

Beside the decay of ϕ mesons, the "golden decay" of D^* mesons is a good source of detectable kaons. The decay happens via an intermediate D^0 meson, $D^* \to D^0\pi_s \to K\pi + \pi_s$ with π_s denoting a low momentum (slow) pion. The main characteristics of the decay is the small difference in the invariant masses of the D^* and the D^0. For reasons of charge conservation and double CABBIBO suppression only the combinations $D^{*+} \to K^-\pi^+\pi_s^+$ and $D^{*-} \to K^+\pi^-\pi_s^-$ dominate.

[21] These finders are tuned for the scattered electron which has on average momenta around 28 GeV and relies mostly on the calorimeter information. Thus they work best for the high momentum region above 10 GeV and are not applicable for the (low momentum) electrons which are the subject of this analysis. In the low momentum region the mis-identification rate of the calorimeter becomes too high. Energy loss measurements are not used.

- Invariant mass difference $0.1435 < \Delta(M_{\mathrm{D}^*} - M_{\mathrm{D}^0}) < 0.1475\,\mathrm{GeV}$;
- Invariant D^0 mass

$$\begin{aligned}
1.82 < M_{\mathrm{D}^0} < 1.91\,\mathrm{GeV} \quad &\text{for} \quad p_{\mathrm{t}}^{\mathrm{D}^*} < 3.25\,\mathrm{GeV} \\
1.81 < M_{\mathrm{D}^0} < 1.92\,\mathrm{GeV} \quad &\text{for} \quad 3.25 < p_{\mathrm{t}}^{\mathrm{D}^*} < 5.00\,\mathrm{GeV} \\
1.80 < M_{\mathrm{D}^0} < 1.93\,\mathrm{GeV} \quad &\text{for} \quad 5.00 < p_{\mathrm{t}}^{\mathrm{D}^*} < 8.00\,\mathrm{GeV} \\
1.79 < M_{\mathrm{D}^0} < 1.94\,\mathrm{GeV} \quad &\text{for} \quad p_{\mathrm{t}}^{\mathrm{D}^*} > 8.00\,\mathrm{GeV}\,;
\end{aligned}$$

- Transverse D^* momentum $p_{\mathrm{t}}^{\mathrm{D}^*} > 1.5\,\mathrm{GeV}$;
- Transverse momenta of the outgoing kaon and pion $p_{\mathrm{t}}^{\mathrm{K},\,\pi} > 0.4\,\mathrm{GeV}$;
- Transverse momentum of the slow pion $p_{\mathrm{t}}^{\pi_{\mathrm{s}}} > 0.12\,\mathrm{GeV}$;
- Good quality tracks originating from the primary vertex.

More details of the features of D^* decays can be found *e. g.* in [Irr04].

In Fig. 4.10 some properties of the calibration samples like invariant masses etc. are shown. All triggers of the 1996—2000 data were used, even those marked as background events in order to collect all the cosmic muons.

4.4.2 The Bethe–Bloch Fit

With the help of Eqn. 4.11 the Lorentz boost, $\beta\gamma$, of each particle in the calibration samples can be determined. Figure 4.11 shows scatter plots of the measured energy loss, $\mathrm{d}E/\mathrm{d}x$, per track versus $\beta\gamma$ for each particle type. The Bethe–Bloch bands are clearly visible. From these graphs profiles of $\mathrm{d}E/\mathrm{d}x$ in bins of $\beta\gamma$ are obtained by averaging the $\mathrm{d}E/\mathrm{d}x$ values of all entries inside each $\beta\gamma$ bin and assigning them to the bin centres (see Fig. 4.12). The bin widths are depicted by the horizontal line of the marker cross, while the vertical line corresponds to the statistical error on the $\mathrm{d}E/\mathrm{d}x$ mean. Outliers more than 3 standard deviations away from the expectation are removed during the filling process to suppress misidentified particles. Here, the $\mathrm{d}E/\mathrm{d}x$ expectation for a given $\beta\gamma$ value is obtained by interpolating the profile entries of the nearest bin centre and the adjacent bins with a third order polynomial. The procedure is illustrated in Fig. 4.12.

The profiles of all five particle types are then combined by computing the weighted mean of all profiles in each bin of $\beta\gamma$.[22] The so obtained profile is then

[22] The method described here has been improved very recently [Zim07]. Instead of the bin centre the barycentre in $\beta\gamma$ of a bin is used for positioning the $\mathrm{d}E/\mathrm{d}x$ mean in the $\beta\gamma$ direction. In addition, the outlier removal is changed. Here, the interpolation procedure is replaced by a direct

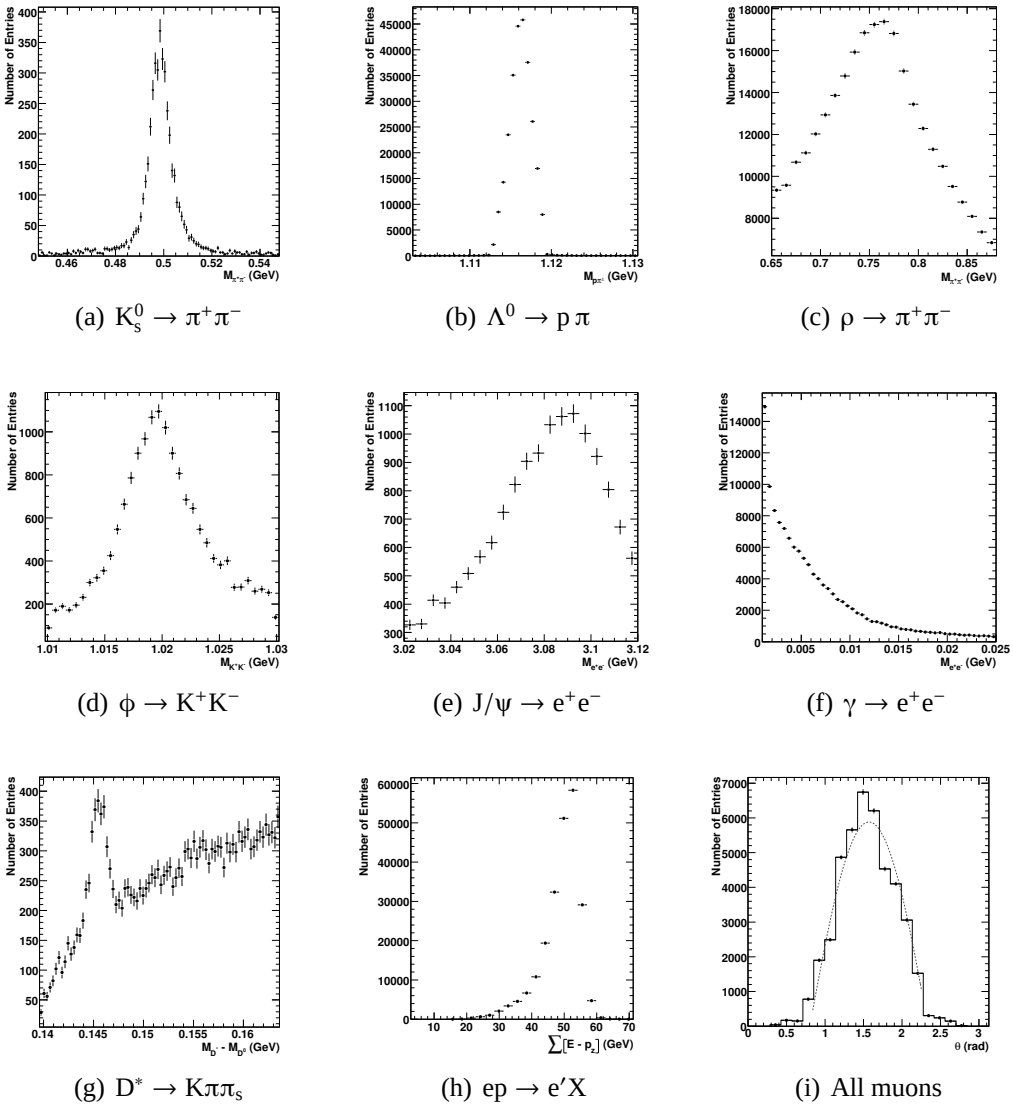

(a) $K^0_S \to \pi^+\pi^-$ (b) $\Lambda^0 \to p\,\pi$ (c) $\rho \to \pi^+\pi^-$

(d) $\phi \to K^+K^-$ (e) $J/\psi \to e^+e^-$ (f) $\gamma \to e^+e^-$

(g) $D^* \to K\pi\pi_S$ (h) $ep \to e'X$ (i) All muons

Figure 4.10: Characteristics of the calibration samples. In (a) — (f) invariant mass distributions of the various decays are presented. The distribution (g) shows the tiny mass difference between the D^* and the D^0 for the golden D^* decays. DIS electrons are characterised by their conserved longitudinal momentum, $\sum_i (E_i - p_{z,i})$, which is expected to be two times the electron beam energy (h). In (i) the distributions of the polar angle, θ, of all selected muons is shown. Most of them originate from cosmic rays, which is indicated by the dashed line showing the expectation for cosmic muons ($\propto \sin^2\theta$).

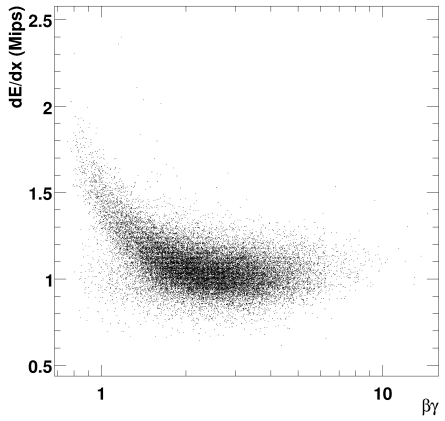

(a) Kaons

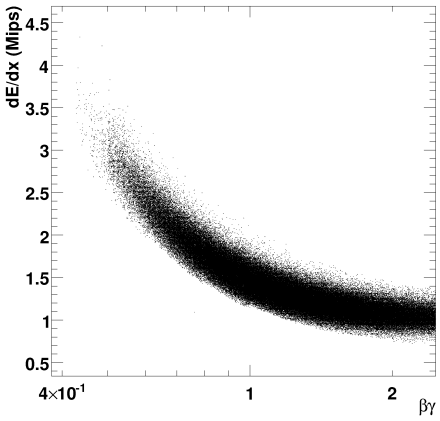

(b) Protons

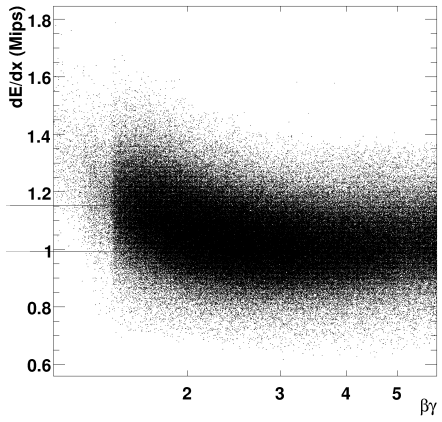

(c) Pions

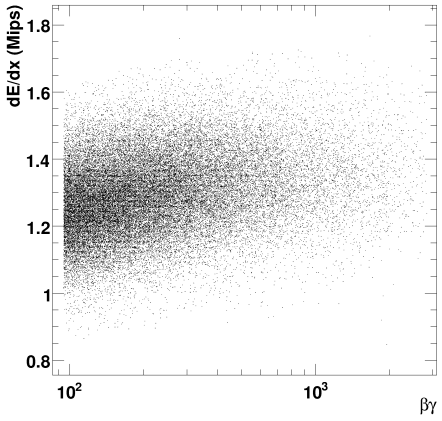

(d) Muons

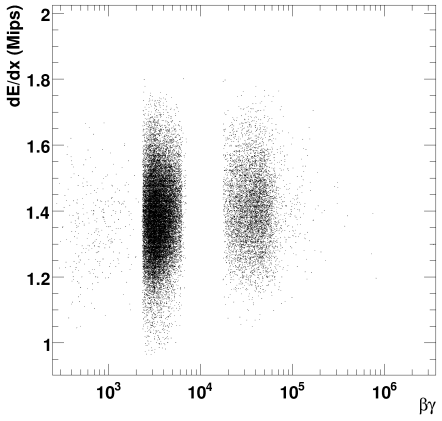

(e) Electrons

Figure 4.11: dE/dx versus $\beta\gamma$ for K, p, π, μ and e. The three electron samples are clearly separated; γ conversion electrons to the left, $e^{\pm}$ from J/ψ decays in the centre and DIS electrons on the right. Note the different $\beta\gamma$ ranges between the samples. The corresponding momentum ranges can be seen in 4.14.

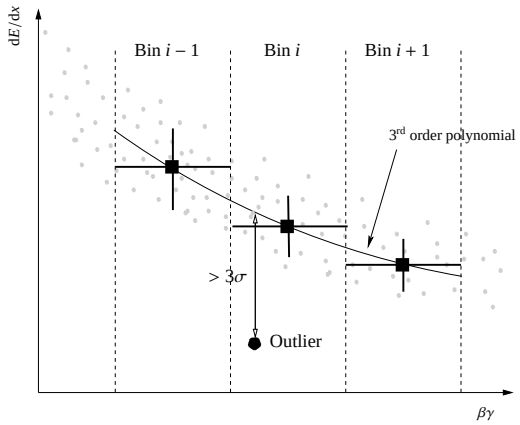

Figure 4.12: Testing for outliers. For each point the deviation from the dE/dx estimate is computed. If the deviation is greater than 3 standard deviations, the point will be discarded. The energy loss is estimated by interpolation the centres of 3 adjacent bins. The determination of the expansion coefficients of the interpolation polynomial is based on [PTVF92].

used for a χ^2–fit of Eqn. 4.4 (PAI model), which is shown in Fig. 4.13. The parameters of the function determined by the fit are

$$\begin{aligned} p_1 &= (0.2377 \pm 0.0079)\,\text{Mips}\,, \\ p_2 &= 4.363 \pm 0.110\,, \\ p_3 &= 0.08009 \pm 0.00672\,, \\ p_4 &= 1.499 \pm 0.004\,, \\ p_5 &= 0.5922 \pm 0.0093\,. \end{aligned} \tag{4.13}$$

The fit converges over the total $\beta\gamma$ range of 6 orders of magnitude. This is possible only because of the systematic corrections mentioned in Sec. 4.3.[23] In Fig. 4.14 the dE/dx scatter plots of all calibration samples are drawn together with the BETHE–BLOCH prediction as function of the track momentum, p, which demonstrates quite nicely that the method is working properly. The fit result can be used in order to obtain a dE/dx prediction for a given $\beta\gamma$, which is needed later in the hypothesis test used for the particle identification.

4.4.3 Resolution Functions

The second thing needed to compare observed values of the energy loss, dE/dx_{obs}, with predicted ones is the dE/dx resolution, or better the dE/dx distribution

computation of the significance of each point with the help of already existing dE/dx probability densities (*c. f.* Sec. 4.4.3). Since this method is not fully tested yet, it will not be part of this work but used in subsequent beauty analyses of HERA-II data.

[23] This is a clear contradiction to the statement at p. 100 in [Dep99], saying that the PAI is not applicable for some reasons. Without the systematic corrections described above, the data fits better to the old BETHE–BLOCH/STERNHEIMER model. With the included corrections, however, the PAI model gives the better description.

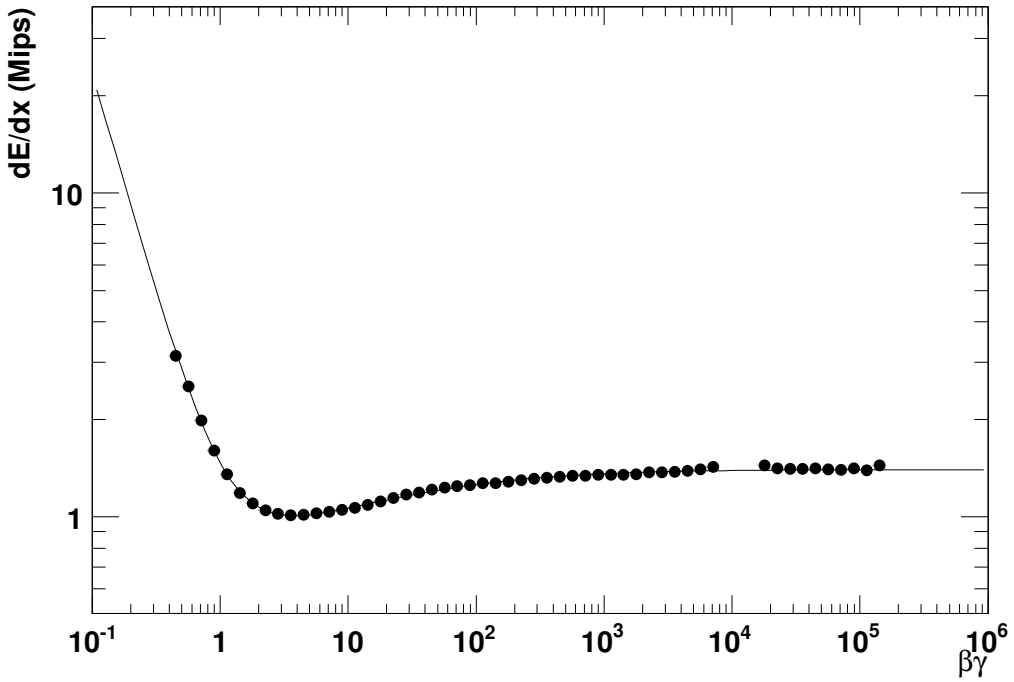

Figure 4.13: The Bethe–Bloch fit is done by fitting Eqn. 4.4 to the averaged dE/dx versus $\beta\gamma$ profiles of all calibration samples. The fit converges for the whole $\beta\gamma$ range.

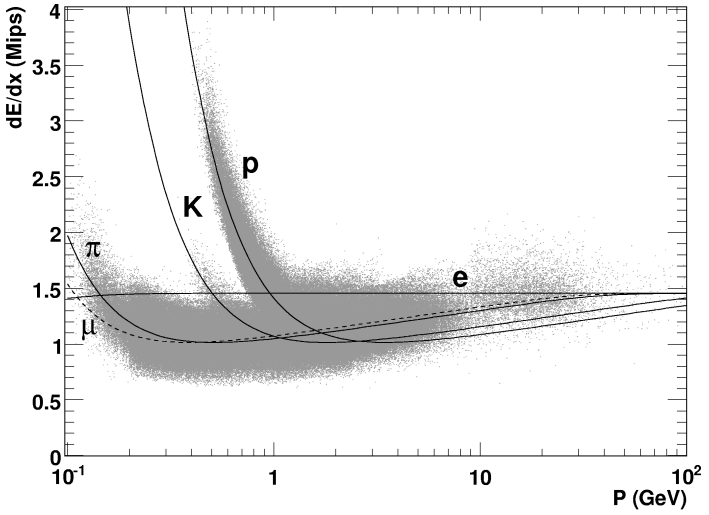

Figure 4.14: Scatter plot of dE/dx versus track momentum for all calibration samples. The results of the Bethe–Bloch fit for all particle types are drawn on top.

around its expectation value, $\mathrm{d}E/\mathrm{d}x_{\mathrm{pred}}$. To become independent from the actual $\mathrm{d}E/\mathrm{d}x$ value, *residuals* are used, which are distributions of the relative differences of the measured values to the predicted ones, $(\mathrm{d}E/\mathrm{d}x_{\mathrm{obs}} - \mathrm{d}E/\mathrm{d}x_{\mathrm{pred}})/\mathrm{d}E/\mathrm{d}x_{\mathrm{pred}}$. These distributions are obtained by looping over all calibration samples again and histogramming the residual $\mathrm{d}E/\mathrm{d}x$ value for each particle using Eqn. 4.11 and the Bethe–Bloch fit result for the predictions needed.

The width of the residual distribution is a function of the number of hits used in the truncated mean calculation, n_{trunc}, when reconstructing the $\mathrm{d}E/\mathrm{d}x$ values per track. From statistical grounds a dependence in the form of $\propto 1/\sqrt{n_{\mathrm{trunc}}}$ is expected, since the resolution should improve with an increasing number of hits, *i. e.* single measurements.

In Figs. 4.17 and 4.18 all residuals in bins of the number of truncated hits are shown. The data covers the region $8 < n_{\mathrm{trunc}} < 43$. Because of the rather limited number of measurements per track, the distributions show a remaining asymmetry due to the Landau–shaped distributions of the single–wire measurements not being fully removed by the truncation. The residuals, which later serve as probability density functions of the energy loss, need to be parametrised for easy access and to smooth out statistical fluctuations, in particular those in the tails of the distributions. The parametrisations are done by fitting the residuals with some analytical function. The form used here, is a piece–wise combination of several Gaussian functions to cover the asymmetry:

$$f(x) = \begin{cases} \dfrac{A_{\mathrm{tot}}}{\sqrt{2\pi}}\left(1 - \dfrac{A_2}{A_{\mathrm{tot}}}\right)\left\{\dfrac{1}{\sigma_{\mathrm{L1}}+\sigma_{\mathrm{R1}}}\, e^{-\frac{1}{2}(x-\mu)^2/\sigma_{\mathrm{L1}}^2} + \dfrac{1}{\sigma_{\mathrm{L2}}+\sigma_{\mathrm{R2}}}\, e^{-\frac{1}{2}(x-\mu)^2/\sigma_{\mathrm{L2}}^2}\right\} & \text{for} \quad x < \mu\,, \\ \dfrac{A_{\mathrm{tot}}}{\sqrt{2\pi}} \cdot \dfrac{A_2}{A_{\mathrm{tot}}}\left\{\dfrac{1}{\sigma_{\mathrm{L1}}+\sigma_{\mathrm{R1}}}\, e^{-\frac{1}{2}(x-\mu)^2/\sigma_{\mathrm{R1}}^2} + \dfrac{1}{\sigma_{\mathrm{L2}}+\sigma_{\mathrm{R2}}}\, e^{-\frac{1}{2}(x-\mu)^2/\sigma_{\mathrm{R2}}^2}\right\} & \text{for} \quad x \geq \mu\,, \end{cases} \tag{4.14}$$

with the argument, x, defined as

$$x = \frac{\mathrm{d}E/\mathrm{d}x_{\mathrm{obs}} - \mathrm{d}E/\mathrm{d}x_{\mathrm{pred}}}{\mathrm{d}E/\mathrm{d}x_{\mathrm{pred}}}\,. \tag{4.15}$$

The fit function contains 7 free parameters: the same expectation value, μ, for all four Gaussian functions, the four widths σ_{L1}, σ_{R1}, σ_{L2}, σ_{R2}, the total area, $A_{\mathrm{tot}} =$

$A_1 + A_2$ and the fraction of both, A_2/A_{tot}, where the areas A_1 and A_2 corresponds to each pair of GAUSSIAN functions defined over the whole range. The functions are further constrained by the requirement of a smooth transition for each pair of them. In addition, because of the low statistics or even zero entries in some bins, a maximum likelihood fit is used rather than a χ^2–fit. The results are drawn on top the residual distributions in Figs. 4.17 and 4.18 (solid line).

A different approach is to simulate the truncated mean method by a "toy model" and compare the result with the $\mathrm{d}E/\mathrm{d}x$ residuals. In this model the $\mathrm{d}E/\mathrm{d}x$ distribution of a single–wire measurement is approximated by the LANDAU function given in Eqn. 4.2. Random values of $\mathrm{d}E/\mathrm{d}x$ are generated according this distribution and used for the computation of truncated mean values as described in Sec. 4.2.2. The values for the most probable energy loss $\mathrm{d}E/\mathrm{d}x_{\text{MP}} = 2.0$ Mips and the scaling parameter $\xi = 0.5$ had been determined by the studying variations of the truncated mean values as a function of the number of truncated hits [Bar06b]. Frequency distributions of the average energy loss for each number of truncated hits are filled with 100,000 truncated mean values each. These distributions are then fitted to the residuals mentioned above to fix the normalisation. Results are given in Figs.4.17 and 4.18 (dashed line). This is mainly done for checking the analytical parametrisations of the residuals and also to estimate systematic uncertainties of the particle identification by means of the energy loss (see Sec. 7.3).

In Fig. 4.15 the mean values and widths of the fitted asymmetric GAUSSIAN functions are shown. As hoped for, the mean values are close to zero and the widths show a $\sim 1/\sqrt{n_{\text{trunc}}}$ behaviour. Only for low values of n_{trunc} significant deviations from this dependence are seen. These are caused by statistical fluctuations and systematic mis-measurements not yet taken into account.[24] A minimum number of truncated hits of $n_{\text{trunc}} > 12$ for good $\mathrm{d}E/\mathrm{d}x$ reconstruction is recommended.

The parametrised residuals are normalised and in the following interpreted as probability density functions for the energy loss. How these are used for the particle identification is described in Sec. 5.2.1.

4.5 Energy Loss in the Monte Carlo

In the case of Monte Carlo the question arises how to obtain $\mathrm{d}E/\mathrm{d}x$ values comparable to those of real data, since the ones generated by the GEANT program are

[24] In fact these deviations and also the wiggles have been studied and countermeasures are taken already by extending the systematic corrections [Bar06b] described in Sec. 4.3. These are mostly caused by uncertainties in the determination of n_{trunc}. As these are very recent developments, they cannot, unfortunately, be included in this thesis.

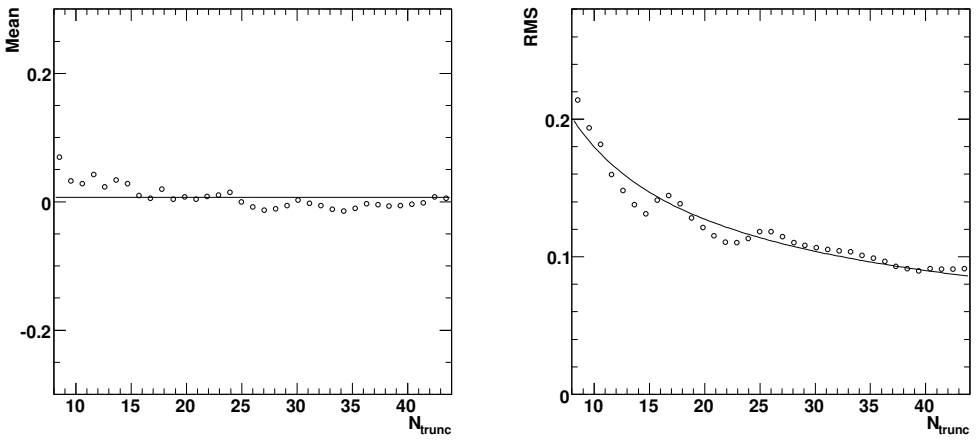

Figure 4.15: Mean values and r.m.s. as function of the number of truncated hits, n_{trunc}. Both show the expected behaviour: the men values are very close to zero, while the widths follow a $\sim 1/\sqrt{n_{\text{trunc}}}$ dependence. Only for low n_{trunc} significant deviations are seen.

not applicable as mentioned above.[25] This can be achieved easily by using the normalised $\mathrm{d}E/\mathrm{d}x$ residuals. After integrating over the full range and inverting, they are combined with a large–periodic random number generator, producing random $\mathrm{d}E/\mathrm{d}x$ values distributed according to the residuals for any given pair of n_{trunc} and $\beta\gamma$. The latter is needed for the back–transformation of the argument, x, of the residuals (*c. f.* Eqn. 4.15). In the Monte Carlo the particle type of every track is known, thus $\beta\gamma$ is computed easily with the help of Eqn. 4.11.[26] A random value for the energy loss is assigned to each track. Figure 4.16 shows the expected result. The $\mathrm{d}E/\mathrm{d}x$ spectra of all good quality tracks in deep elastic scattering events (a) are compared for real data (solid circles) and a Monte Carlo sample produced with the event generator ARIADNE (shaded histogram), as well in dijet γp events (b) described in Sec. 3.1. Both distributions show good agreement over the whole range supporting the fact, that this method is independent of the event topology.

[25] Of course, in the Monte Carlo the true type of every particle is known. However, in order to obtain detector acceptances for the determination of cross–sections, the same procedure of particle identification as used for real data has to be applied.

[26] Here, the connection between each reconstructed track and its corresponding true particle is needed. This is done by looking how many true hits produced by the GEANT program are shared by the track and any possible true particle [HIL+97].

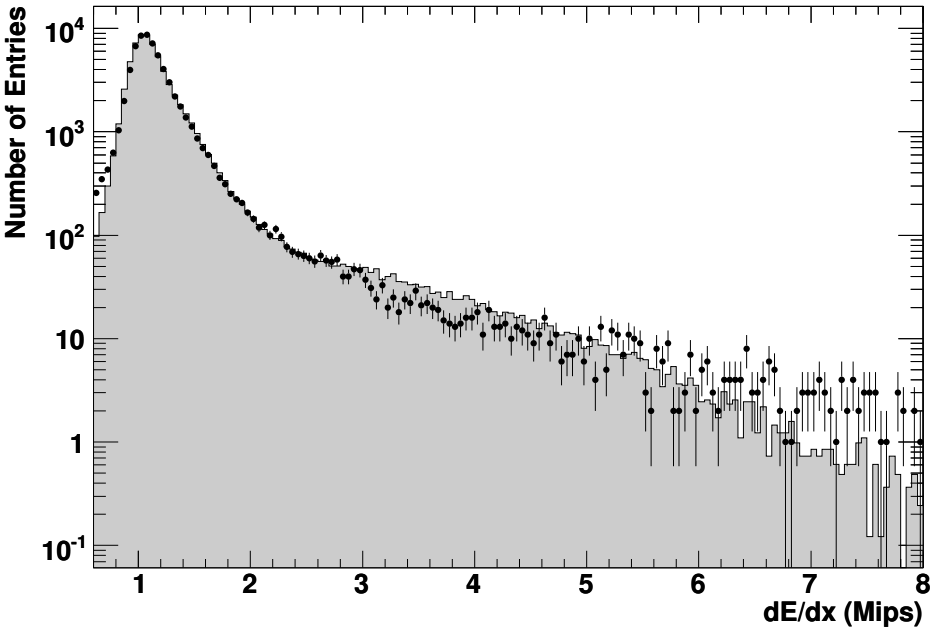

(a) Deep inelastic scattering

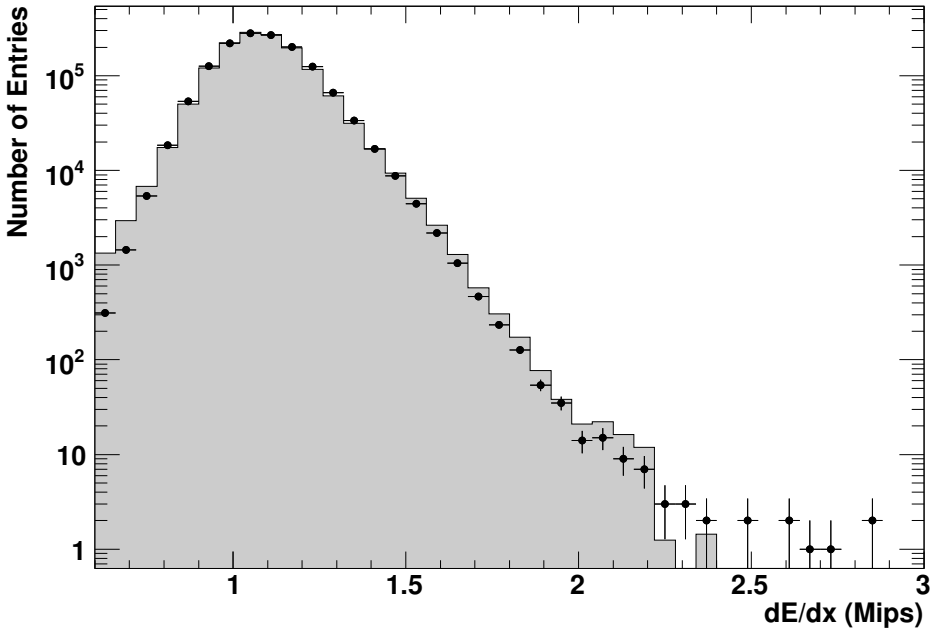

(b) Dijet photoproduction

Figure 4.16: Comparison between the measured energy loss in real data (solid circles) and the simulated values in case of Monte Carlo events (shaded histograms). The $\mathrm{d}E/\mathrm{d}x$ values in the Monte Carlo have been randomly produced according to the residuals determined with the help of the calibration samples. The distributions consist of all good quality tracks in deep inelastic scattering events (a) and dijet photoproduction (b). The Monte Carlo histograms are normalised to those of the real data.

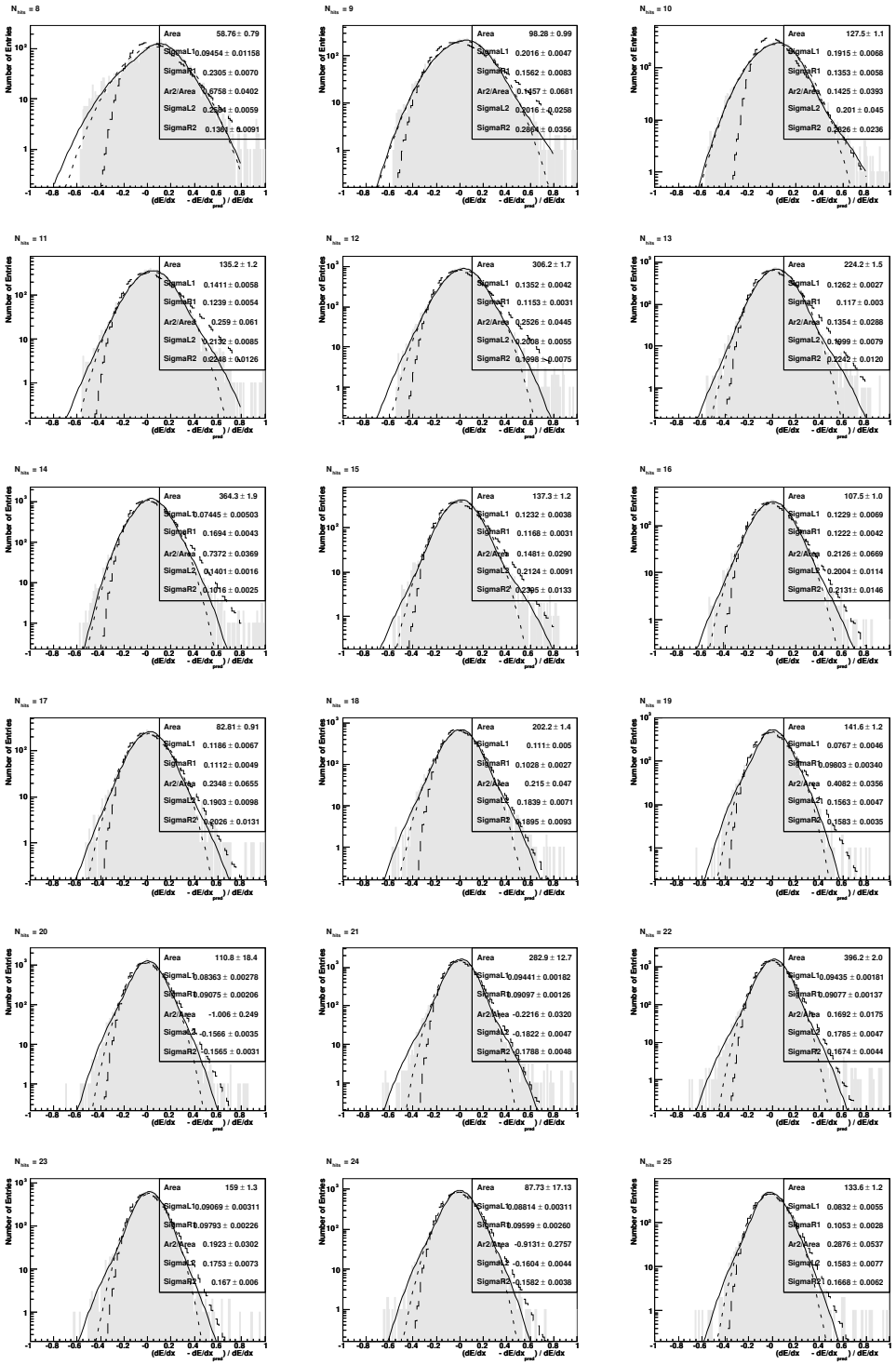

Figure 4.17: Fitting the dE/dx residuals. The shaded histograms are the residuals as a function of the number of truncated hits, n_{trunc}. The solid line is the asymmetric GAUSSIAN fit defined in Eqn. 4.14, while the dashed histograms represents the cross–check by fitting the results of the toy model (see Sec. 4.4.3 for details). For a better comparison the results of a *symmetric* GAUSSIAN fit are indicated also (dotted lines). The results of the asymmetric GAUSSIAN fit are shown in the text boxes. In this figure all distributions for the range $8 \leq n_{\text{trunc}} \leq 25$ are shown. All other distributions are plotted on the next page.

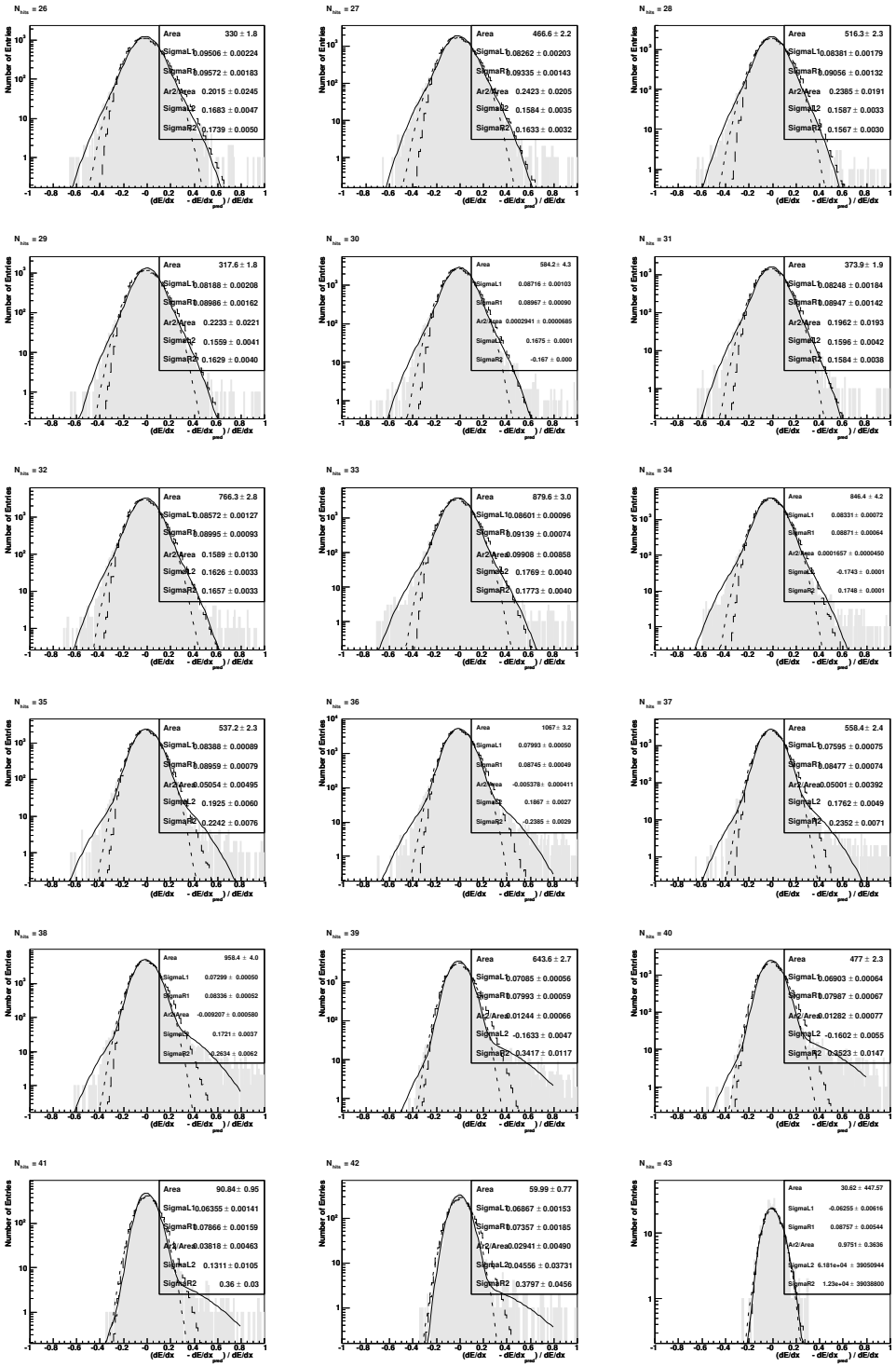

Figure 4.18: $\mathrm{d}E/\mathrm{d}x$ residuals for $26 \le n_{\mathrm{trunc}} \le 43$. For details see the caption of the figure on the previous page.

Chapter 5

Particle Identification

In the previous chapter energy loss measurements with the central tracking chamber of the ZEUS detector were presented. Details of the measurement, systematic corrections, the energy calibration and the determination of resolution functions were shown, laying the foundation for a particle identification algorithm, which in principle is generally applicable. This will be the topic of this chapter.

5.1 The Likelihood Ratio Test

The question of a particle being of a specific type is answered by a hypothesis test. Here, the likelihood for the particle being of the type in question (null–hypothesis) is compared with the likelihood for the particle being of all other types (anti-hypothesis). The likelihood, $\mathcal{L}_i$, for a particle type i is given by

$$\mathcal{L}_i = \prod_j \mathcal{P}(d_j \,|\, h_i)\,, \tag{5.1}$$

with $i \in \{\mathrm{e}, \pi, \mu, \mathrm{K}, \mathrm{p}\}$ and $\mathcal{P}(d_j \,|\, h_i)$ denoting the probability density of a particle track being observed with some discriminant variable, d_j, under the assumption of a particle hypothesis, h_i.

The best separation power is achieved with a *likelihood ratio test*. The test function, T, for a particle being of type i is the quotient of two likelihoods

$$T_i = \frac{\alpha_i \mathcal{L}_i}{\sum\limits_{j \in \{\mathrm{e},\pi,\mu,\mathrm{K},\mathrm{p}\}} \alpha_j \mathcal{L}_j}\,. \tag{5.2}$$

The α_i denote the *a priori* probabilities for the particle type i. These have to be determined by providing frequency distributions for each particle type in the event samples of the analysis (for details refer to Sec. 5.3).

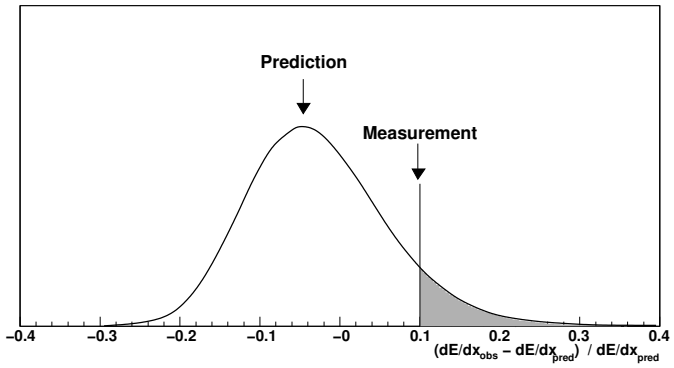

Figure 5.1: The $\mathrm{d}E/\mathrm{d}x$ residuals are used for a comparison of the observed energy loss, $\mathrm{d}E/\mathrm{d}x_{\mathrm{obs}}$, and the prediction, $\mathrm{d}E/\mathrm{d}x_{\mathrm{pred}}$, for a given mass hypothesis. The actual comparison is done by likelihood methods.

5.2 Discriminant Variables

The likelihood used for the particle identification provides a simple way to combine information of various sub-detectors. In our case information from the central drift chamber and the calorimeter is taken. These measurements are completely uncorrelated and also support each other, since the two detectors operate best in different momentum ranges. Three discriminating variables are used for the hypothesis test: the ionisation loss, $\mathrm{d}E/\mathrm{d}x$, as measured by the drift chamber, the fraction of electro–magnetic energy in the calorimeter, $f_{\mathrm{EMC}} = E_{\mathrm{EMC}}/E_{\mathrm{tot}}$ and the ratio of the calorimeter energy and the track momentum, $E_{\mathrm{CAL}}/p_{\mathrm{trk}}$.

5.2.1 Ionisation Loss

Here the relative deviation of the observed energy loss, $\mathrm{d}E/\mathrm{d}x_{\mathrm{obs}}$, in the CTD to the predicted one, $\mathrm{d}E/\mathrm{d}x_{\mathrm{pred}}$, for a given assumption $m = m_i$ made for the particle's mass, is being used. The latter is needed for computing a prediction for the energy loss with the help of the Eqns. 4.11 and 4.4. The probability densities are determined by the normalised residuals defined by Eqn. 4.14 and shown in Figs. 4.17, 4.18. The basic concept is depicted in Fig. 5.1. The ionisation loss per track contributes most in the separation of individual particle types.

5.2.2 Fraction of Electro–Magnetic Energy in the Calorimeter

The fraction of electro–magnetic energy in the EMC relative to the total energy, denoted as f_{EMC}, measured for an energy flow object in the CAL helps mostly in

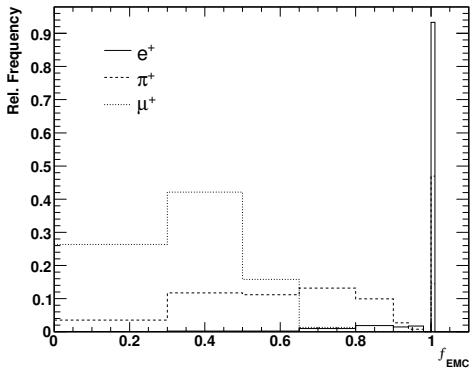

Figure 5.2: Amount of electro–magnetic energy for electrons, pions and muons in simulated $b\bar{b}$ events. Each entry corresponds to an energy flow object in the CAL. Almost all of the electrons leave their energy in the EMC section. The hadrons, represented by pions here, show a much wider distribution. Muons are shifted to lower values, since they are minimum ionising. All distributions are normalised to one individually.

separating electrons from hadrons.[1] Because of their short interaction length, the electrons lose all their energy within the electro–magnetic section of the calorimeter, while the hadrons and also the muons deposit a considerable amount in the hadronic part of the calorimeter, as shown in Fig. 5.2. Also seen in the figure is that a non-negligible amount of hadrons and even muons leave all of their energy in the EMC. Those are soft particles with momenta of only a few hundred MeV, which is not enough to reach the hadronic section of the calorimeter — they simply stuck in the EMC.

Hence the EMC fraction is momentum dependent and must be handled that way. In addition it might be influenced by the particle's charge. This is most obvious for protons and anti-protons. Thus for the computation of the likelihood normalised frequency distributions binned in f_{EMC} and track momentum, p, for each particle type are necessary. Some of them are shown in Fig. 5.3. An appropriate binning was chosen to prevent the distributions from fluctuating too much at the edges. Each slice in p was normalised to one individually in order to be used as a probability density function in the likelihood. The distributions were produced with the help all the Monte Carlo samples mentioned in Sec. 3.1. The distributions of the individual samples are luminosity–weighted before adding and normalising them.

5.2.3 Calorimeter Energy over Track Momentum

The original idea for this variable was to achieve a better separation of anti-protons. Due to the annihilation processes with the detector material, the ratio of the calorimeter energy of an energy flow object compared to its track momentum, $E_{\mathrm{CAL}}/p_{\mathrm{trk}}$, is larger than that of other particles, since for a compensating calorime-

[1] Obviously the energies used for the computation of f_{EMC} are those directly measured by the calorimeter rather than the energies corrected by the track momenta.

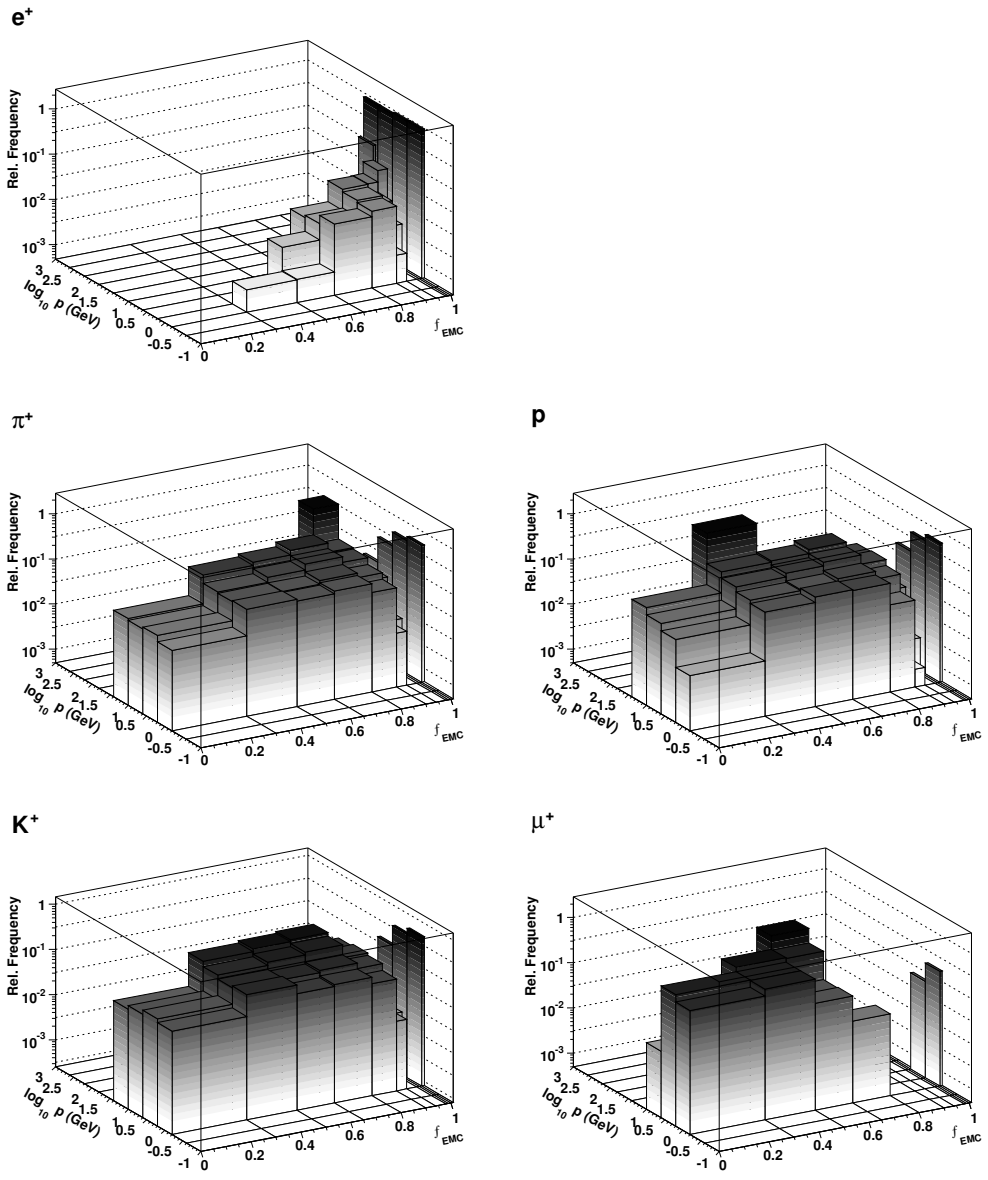

Figure 5.3: Frequency distributions of f_{EMC} versus track momentum, p, for all positive particle types. The distributions are made with the beauty, charm and light–flavour Monte Carlo samples appropriate for this analysis. Each momentum bin has been normalised individually.

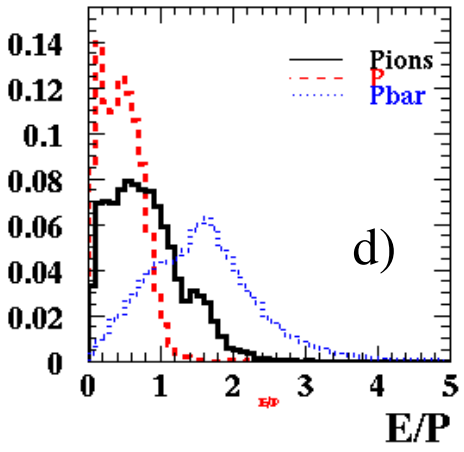

Figure 5.4: Distributions of $E_{\mathrm{CAL}}/p_{\mathrm{trk}}$ for pions, protons and anti-protons. Because of their annihilation in the calorimeter the anti-protons exhibit a peak around $E_{\mathrm{CAL}}/p_{\mathrm{trk}} = 2$ quite different from the other particle types (courtesy of [Bru04]). The distributions were made with 70,000 simulated events each containing only a single track for each particle type. For the track simulation an equidistant momentum distribution in the range $0.75 < p < 2.5$ GeV was used.

ter $E_{\mathrm{CAL}}/p_{\mathrm{trk}}$ usually is expected to be one. Such a behaviour is seen in Fig. 5.4. However, the distributions shown were generated under somewhat ideal conditions. Each of the simulated events contains only one track whose momentum and direction were generated randomly with the help of flat distributions. In physics events the situation looks different. The mean values of the $E_{\mathrm{CAL}}/p_{\mathrm{trk}}$ distributions are shifted dependent on the particle's mass, since the calorimeter compensation is a function of the particle's energy [Dep99]. The way of clustering the calorimeter energies may also play a role. As seen in Fig. 5.5 the distributions of the lighter particles are shifted to higher $E_{\mathrm{CAL}}/p_{\mathrm{trk}}$ values, while the heavy particles move to lower values. In this figure the normalised $E_{\mathrm{CAL}}/p_{\mathrm{trk}}$ distributions of all particles in the Monte Carlo samples used for this analysis are presented separately for positive and negative particles. The separation of anti-protons is much reduced, though it helps to identify muons.

Other methods of using additional calorimeter information for the particle identification have also been tried [Jün05], in particular longitudinal and lateral shower profiles. However, the granularity of the ZEUS calorimeter is too coarse for a clear distinction, at least in the momentum range considered, here below 10 GeV.

5.3 Particle Abundances

The relative abundances of the particle types e, π, μ, K, p and their anti-particles per event are also needed for the hypothesis test defined by Eqn. (5.2). These are determined with the help of the Monte Carlo samples introduced in Sec. 3.1. For a precise description the distributions are binned in the pseudo–rapidity, η, and the transverse momentum, p_{t}, of the particles. The binning has been optimised for

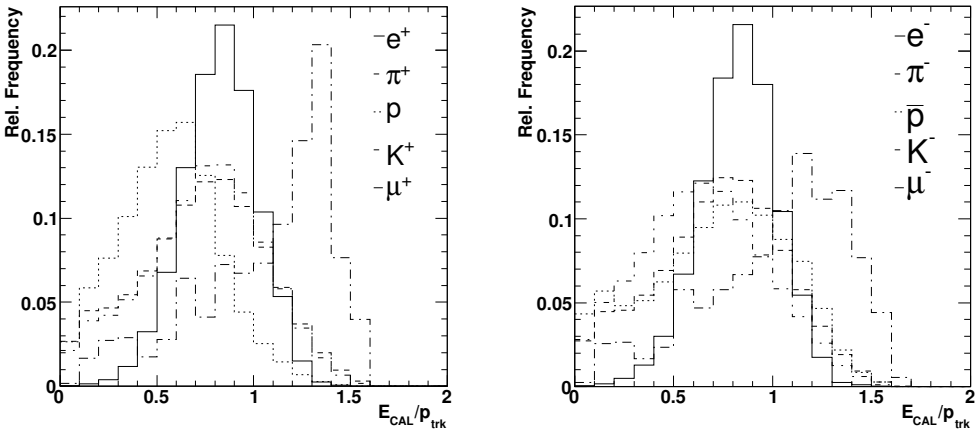

Figure 5.5: Relative frequency distributions of $E_{\mathrm{CAL}}/p_{\mathrm{trk}}$ for positively and negatively charged particles obtained from the energy flow objects in the Monte Carlo samples used for this analysis. The difference between protons and anti-protons is still visible. The $E_{\mathrm{CAL}}/p_{\mathrm{trk}}$ variable helps to separate muons from the other particle types.

electrons and positrons, since they are the particles in question. The distributions are normalised such that in each bin the sum of all equally charged particle types is equal to one. The distributions for electrons and positrons are given in Fig. 5.6, all others are depicted in Fig. 5.7.

5.4 Performance

With the information available it is now possible to compute the test function (5.2) for all electron candidates (see Sec. 3.4). The results are presented in Fig. 5.8. Here, the method described above was used to identify electrons and positrons in simulated beauty events of γp collisions containing two high–p_{t} jets. For details of the Monte Carlo simulation and the event selection, see Chap. 3. Figure 5.8 shows the test functions, T, for the $\mathrm{e}^{\pm}$ hypothesis and its anti-hypothesis. It is common to draw $-2\ln T$ rather than T.[2] In Fig. 5.8 a clear separation between the signal, located at low values, and the background at higher values is seen. The integral of the normalised test function, $-2\ln T$, up to a certain value can be directly interpreted as the efficiency to find an electron, ϵ_{e}, whereas the integral of the anti-hypothesis distributions gives the probability for mis-identifying a non-

[2]The reason is that $-2\ln T$ converges towards the χ^2–distribution for GAUSSian shaped probability densities or very large number of uncorrelated measurements.

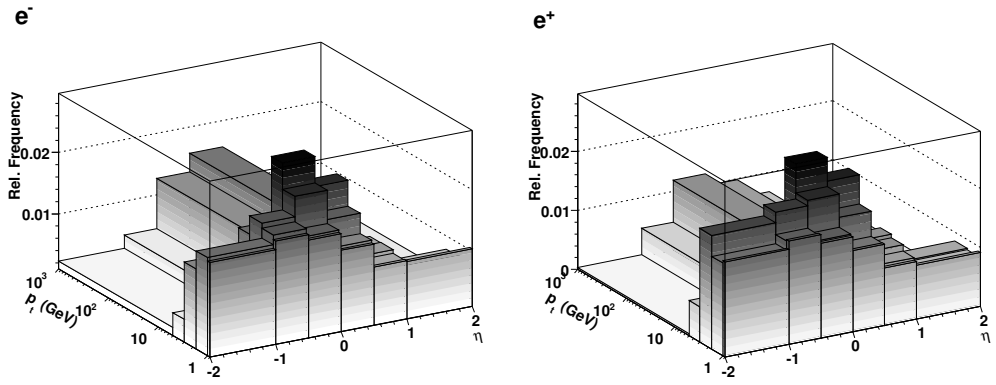

Figure 5.6: Relative abundances of electrons and positrons per event. The distributions were made from all Monte Carlo samples used for this analysis by luminosity weighting. The binning in η and p_t of the particles was chosen to minimise statistical fluctuations. Each bin is normalised in a way such that the sum of all particle types equals one.

electron as an electron, $\epsilon_{\text{non–e}}$. These are drawn in the upper right of Fig. 5.8. With the help of this diagram it is possible to determine the amount of mis-identification for a given electron finding efficiency.

5.5 Summary

In this and the previous chapter the foundations of a comprehensive particle identification for the ZEUS experiment have been laid. The method described here is in general applicable not only for electrons, but for all other particle types also, in any type of analysis. It is valid for a wide momentum range from several hundred MeV up to 10 or more GeV, which is the range of interest for most analyses at ZEUS. The geometrical acceptance is also large, reaching roughly from -1.9 to 1.9 in terms of the pseudo–rapidity, η. The method relies mostly on ionisation loss energy measurements in the CTD, which are quite stable and trustworthy because of the extensive systematic studies and corrections.

The likelihood method helps by combining the information best and reduces the mis-identification rate by a considerable amount. Still, for this analysis this is not enough. Suppose a beauty to light–flavour ratio of 1:2000 multiplied with a branching ratio of 20 % means that only every 10,000$^{\text{th}}$ event contains a beauty electron.[3] Even with a mis-identification efficiency of 0.1 ‰ the resulting sample

[3]This is a very conservative estimate, since the beauty to light–flavour ratio is much improved by selecting only events containing high–p_t jets and other kinematical cuts as applied in this anal-

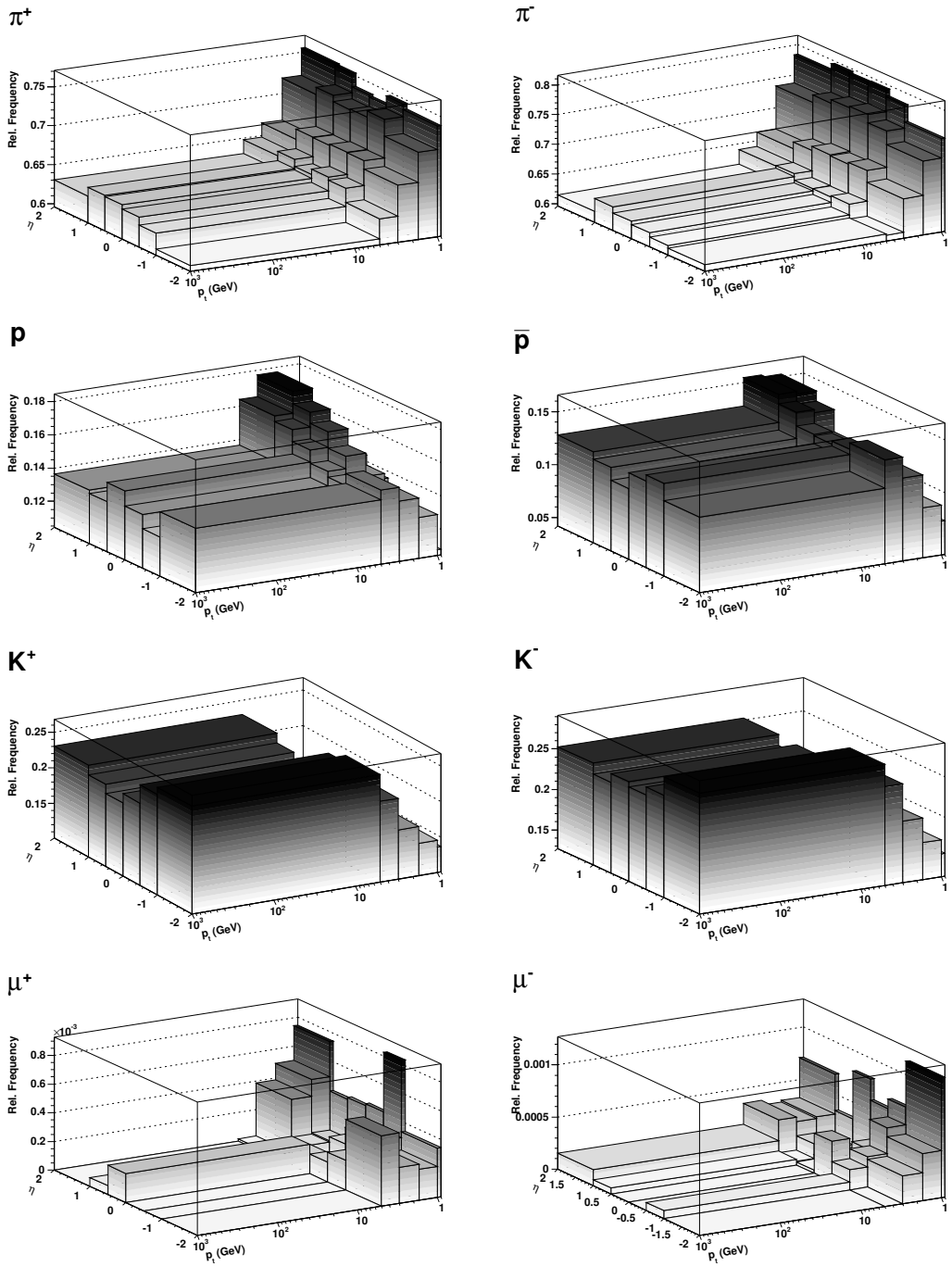

Figure 5.7: Abundances of $\pi, \mu, \mathrm{K}, \mathrm{p}$ and their anti-particles.

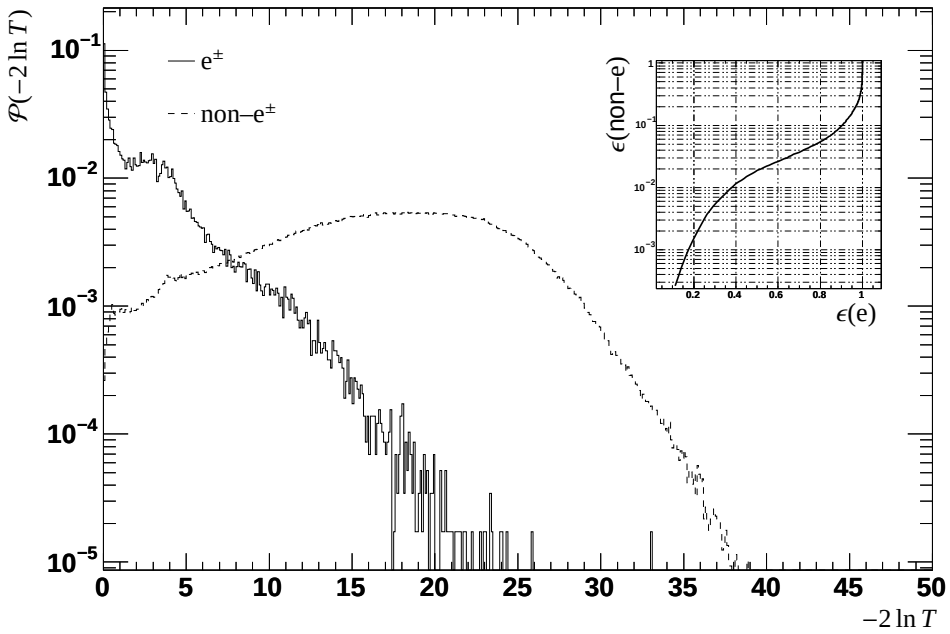

Figure 5.8: Performance of electron identification with the help of ionisation losses of particles in the CTD and calorimeter information for simulated beauty events. The test function is shown for the $e^{\pm}$ hypothesis of particle tracks (solid line) and the anti-hypothesis (dashed line). Both distributions are normalised to one for better comparison. From this distributions and the knowledge of the true particle type, the efficiency, ϵ_{e}, for finding electrons and positrons, and the efficiency, ϵ_{non-e}, for mis-identification of other particles as $e^{\pm}$ can be determined. Their dependence is shown in the upper right diagram.

would be hundred percent contaminated. A more stringent electron identification is therefore needed. Again, the likelihood method provides a way out, because it is simple to extend the likelihood with information. In our case, information about the semi–leptonic decay will be added. This is the subject of the next chapter.

ysis. See also the discussion in [Jün05].

Chapter 6

Signal Extraction

In this chapter the extraction of the beauty and charm signal is explained and the amount of those events is determined. This is done with the help of the particle identification described in the last two chapters. In addition some characteristic features of the semi–leptonic decay are used.

6.1 Semi–Leptonic Beauty and Charm Decays

Semi–leptonic decays provide a robust way to identify beauty and charm decays. The branching ratio for $B^{\pm}/B^{0}/B_{s}^{0}$/b–baryon admixture to $\ell\nu_{\ell}$+anything had been determined to 10.59 % [Y^{+}06], which makes a measurement of the beauty fraction feasible.

A modern way of improving the determination of the beauty and charm fraction is the use of life–time information as provided by micro–vertex detectors. However, at ZEUS such a detector is only available for the HERA-II running period, which is not part of this analysis. Thus other methods must be developed for the heavy quark tagging. In the next sections two more discriminant variables are introduced which will be plugged into the hypothesis test (5.2).

6.1.1 Decays of Heavy Hadrons

In the case of beauty hadrons the outgoing particles have a large phase–space to manoeuvre due to the high mass of the parent particles. Thus the electron emerging from the semi–leptonic decay has on average higher transverse momenta, p_{t}^{rel}, with respect to the jet axis than other particles (see the sketch in Fig. 6.1). The jet axis is chosen, because it is a reasonable estimate of the direction of the parent particle, which cannot be directly reconstructed. It is also necessary to match the electron candidate with the correct jet. This and the pre-selection of the electron

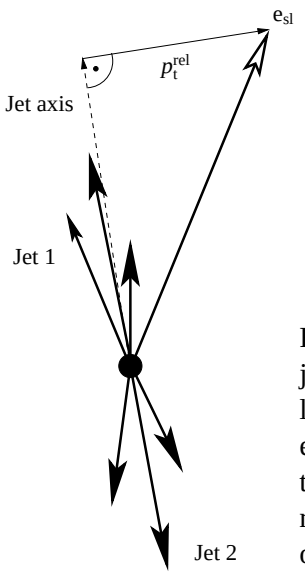

Figure 6.1: The heavy hadron being part of jet 1 decays after a short time. Due to the large mass of the beauty hadron the electron emerging from the semi–leptonic decay tends to have a higher tranverse momentum, p_t^{rel}, relative to the jet axis compared to the decays of the lighter flavoured hadrons.

candidates follows the procedure described in Sec. 3.4. Figure 6.2 shows p_t^{rel} distributions for true semi–leptonic beauty and charm decays as well as other decays, labelled as background. The distributions are made from the Monte Carlo samples for the different flavours described in Sec. 3.1. All the cuts used for the selection of dijet γp events are applied. The distributions presented here are the sum of the distributions of every sample weighted by its integrated luminosity. For later use and better representation each of the distributions are normalised to one. Because of its harder spectrum a good separation of the beauty decays from charm and other decays is possible. Charm cannot be separated from the background, though.[1]

6.1.2 Catching the Neutrino

Another source of information is the escaping neutrino from the semi–leptonic decay. Due to its very weak interaction with matter the neutrino will not be directly observed by the detector. However, since it carries momentum away it will cause an imbalance in the total four–momentum of the hadronic final–state. Because of the unknown LORENTZ boost of the hadronic final–state only the azimuthal component is reconstructable. In the absence of any neutrino the vectorial sum of

[1] In fact, the charm distribution is even below the background. This is a general feature, also seen in μ analyses. The reason is the higher track multiplicity of charm jets. They contain on average one particle more than the jets in the background samples, due to the charm decays. Thus the p_t^{rel} distribution of charm is shifted towards lower values. Beauty jets show a much different behaviour, because in this case the higher track multiplicity is compensated by the higher amount of available energy.

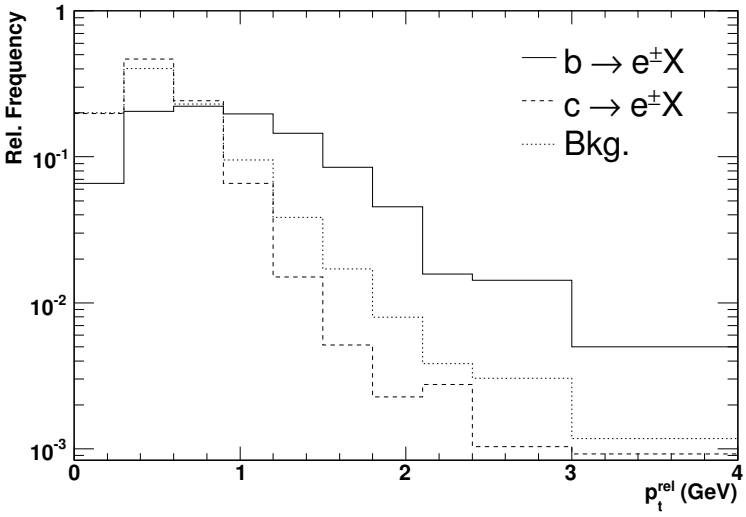

Figure 6.2: Relative frequency distributions of the p_t^{rel} variable for semi–leptonic beauty and charm decays and background. The beauty spectrum is harder than the other ones making a separation of beauty possible. Charm cannot be well–separated by the p_t^{rel} variable. The distributions are made from the beauty, charm and light–flavour Monte Carlo samples used of this analysis.

the projections of all reconstructed hadronic four–vectors (EFOs) onto the (x, y)–plane ought to be the zero vector due to four–momentum conservation. Any undetected neutrino will manifest itself in a non-zero vector sum, which is called the *missing transverse momentum*, $\not{p}_t$ and can be utilised for the neutrino reconstruction. Up to now this has only be done in charged current analyses at HERA (*c. f.* Fig. 1.2(b)) for tranverse ν momenta higher than $\sim 12\,\text{GeV}$ [Wes02]. Since the transverse momenta of the neutrinos from semi–leptonic beauty decays are of the order of several GeV only, a precise reconstruction of those is for sure not possible. However, their azimuth is determined fairly well as seen in Figs. 6.3, 6.4. The first one shows the residual $\not{p}_t$ azimuths comparing reconstructed and true values in simulated events. The quality of the azimuthal $\not{p}_t$ reconstruction is passable. In a next step the reconstructed $\not{p}_t$ azimuthal values are compared to the azimuths of true neutrinos from semi–leptonic decays in simulated events. Results are shown in Fig. 6.4. Both correlations and residual plots are presented. As seen it is possible to reconstruct the neutrino azimuthal direction with the help of the $\not{p}_t$ variable. The picture stays even if additional neutrinos appear in the event. These are mostly very soft thus not affecting the $\not{p}_t$ vector sum very much. This is indicated by Fig. 6.5.

For the identification of semi–leptonically decaying beauty and charm hadrons

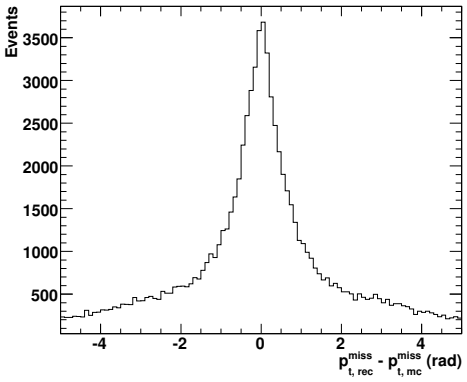

Figure 6.3: Goodness of the azimuthal $\not{p}_t$ reconstruction exemplary for $b\bar{b}$ simulated events in direct photoproduction. Shown is the difference of the azimuthal component between the reconstructed $\not{p}_t$ and the true one. Figure taken from [Jün05].

the azimuthal difference, $\Delta\phi$, between the outgoing neutrino and the lepton performs best. The neutrino direction is obtained with the help of the missing transverse momentum, which can be determined quite well as described above (see also Fig. 6.6 for the definition of $\Delta\phi$). The measurement of the lepton direction is very precise, much better than the determination of the direction of the hadronic decay products which is roughly described by the axis of the corresponding jet. Thus the $\Delta\phi$ variable is in some way complementary to the already mentioned p_t^{rel} variable. In Fig. 6.7 relative frequency distributions for electrons originating from semi-leptonic decays of beauty and charm decays are depicted as well as those for all other electrons (untagged γ conversions, DALITZ decays, DIS background etc.). The distributions are obtained from all selected dijet γp events in the beauty, charm and light–flavour Monte Carlo samples used in this analysis. A clear separation of the beauty and charm signals from the background is seen. In contrast to the p_t^{rel} variable, which identifies only the beauty, the $\Delta\phi$ variable discriminates likewise beauty and charm from the background making a simultaneous measurement of production cross–sections for beauty and charm possible.

6.1.3 Systematic Corrections

Both, the p_t^{rel} and the $\Delta\phi$ variable suffer from systematic mis-measurements. For the former this was already noticed in case of the $B \to \mu$ analyses at ZEUS (*c. f.* [Gut05]). Therefore it is necessary to correct the values of p_t^{rel} and $\Delta\phi$ in real data before using them for the identification of beauty or charm events. This is done by comparing the p_t^{rel} and $\Delta\phi$ distributions for real data to those of simulated events. The results are shown in Fig. 6.8. Deviations are seen for high p_t^{rel} and low $\Delta\phi$ values.

To avoid any systematic bias in the signal domain, the correction factors are determined in the non-signal region, as depicted in Fig. 6.9. This selection is done

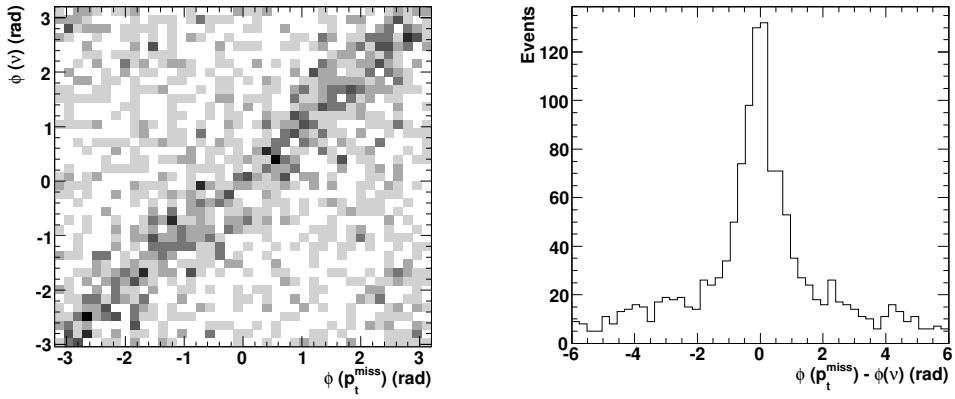

(a) One ν from semi–leptonic decays per event without any other neutrinos

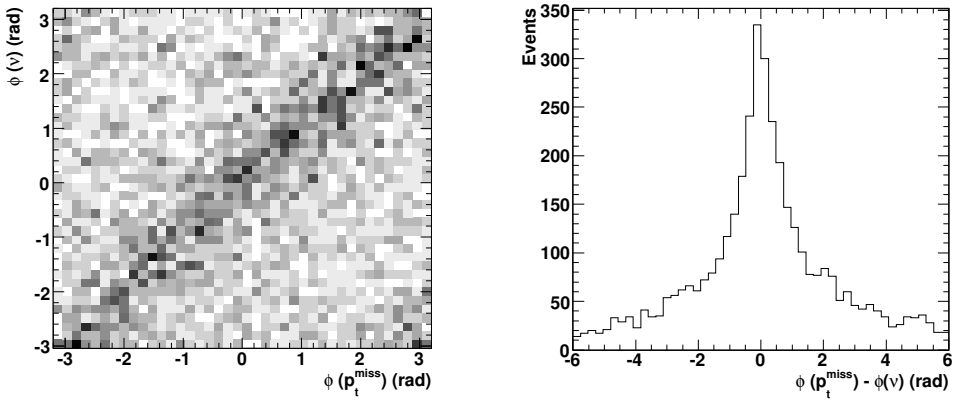

(b) One ν from semi–leptonic decays per event plus 3 more neutrinos

Figure 6.4: On the reconstruction of the azimuth of neutrinos from semi–leptonic decays in simulated $b\bar{b}$ events. On the left correlations of the true azimuth and the reconstructed one are shown, while on the right side the corresponding residual distributions for both values are presented. In (a) only one true ν per event is allowed, the one from the semi–leptonic decay, that is. A clear correlation of the true neutrino and the missing transverse momentum is seen. The correlation remains even if more neutrinos are part of the event (b) and the azimuthal resolution is similar. Figures taken from [Jün05].

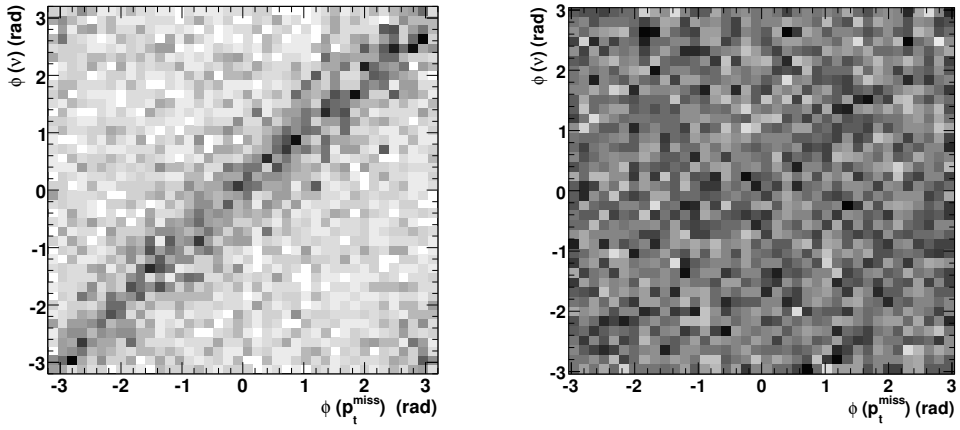

(a) Semi–leptonic decays (b) Other decays

Figure 6.5: Azimuth reconstruction of neutrinos from semi–leptonic (a) and all other decays (b). The correlation between the reconstructed and true azimuth seen for semi–leptonic decays disappears if one looks at the usually much softer neutrinos from other decays (from [Jün05]).

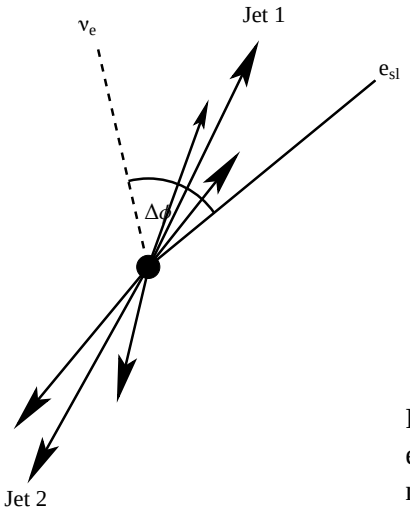

Figure 6.6: $\Delta\phi$ denotes the azimuthal angular difference between the neutrino and the electron both originating from the semi–leptonic decay.

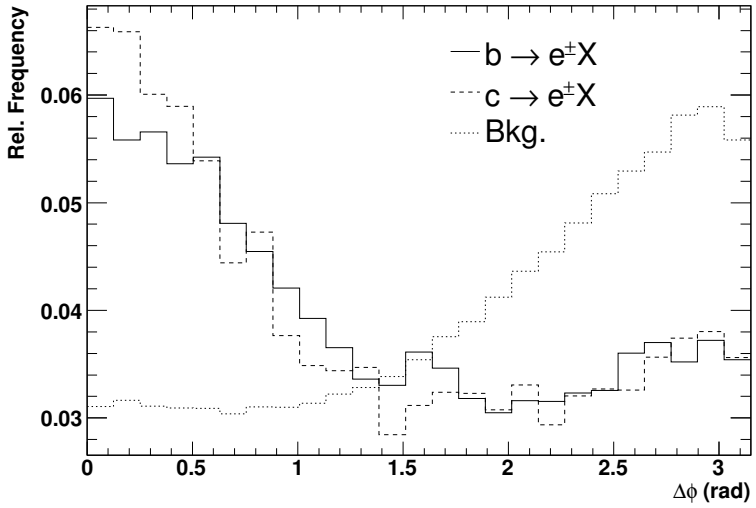

Figure 6.7: Relative frequency distributions of the $\Delta\phi$ variable for electrons from semi–leptonic decays of beauty and charm hadrons, and all other electrons (marked as background). The distributions are made with the help of all the beauty, charm and light–flavour Monte Carlo samples used in this analysis. The heavy hadron decays exhibit a large peak at low $\Delta\phi$ values, as expected, and are well separated from the background electrons which show a peak in the opposite direction. The double–peak structure of all distributions is explained by the dijet structure of these events.

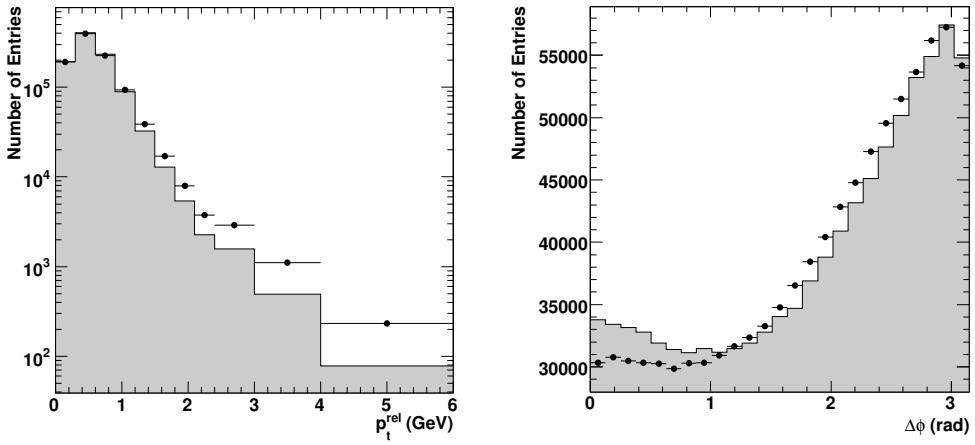

Figure 6.8: Distributions of $p_{\mathrm{t}}^{\mathrm{rel}}$ and $\Delta\phi$ of electron candidates for both real data (filled circles) and simulated events (shaded histograms). The latter are the luminosity–weighted sum of all Monte Carlo samples and normalised to the real data distributions.

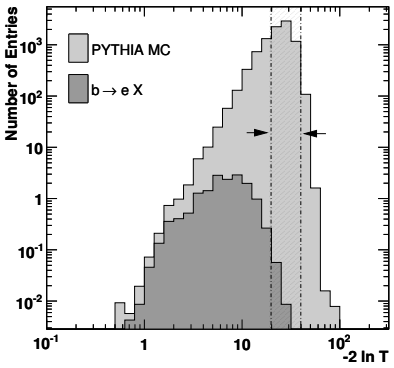

Figure 6.9: The corrections for p_t^{rel} and $\Delta\phi$ are determined in the non-signal region. Distributions of the test function (5.2) made of the energy loss in the CTD, the fraction of electro–magnetic energy in the calorimeter and the ratio of calorimeter energy to track momentum of electron candidates (as described in Sec. 5.2 are shown for all simulated events (light shaded histogram) and the beauty signal only (dark shaded histogram). The range used, $20 < -2\ln T < 40$, is indicated by the dashed–dotted lines. Figure taken from [Jün05].

by the help of the test function defined in Eqn. (6.3) which was made without any knowledge of p_t^{rel} and $\Delta\phi$, so as not to spoil the correction factors. These factors are determined by computing the ratio in every bin of p_t^{rel} and $\Delta\phi$ between real data and Monte Carlo. Figure 6.10 shows the achieved correction factors. The correction for the p_t^{rel} variable is large, in particular for the highest bin.[2] Reasons might be shortcomings in the parton shower and the hadronisation model, but also in the CAL shower simulation of the Monte Carlo. The situation is, of course, unpleasant. For future analyses, a better understanding of the origin of the systematics and a more thorough correction procedure is desirable. The correction of the $\Delta\phi$ variable are much smaller, of the order of a few percent only and therefore no real reason to worry. The corrections are applied to the respective probability density distributions whenever these are accessed.[3]

It should be emphasised that the correction factors do not change the values of p_t^{rel} and $\Delta\phi$ directly; they are rather applied to the probability density of a certain value of p_t^{rel} or $\Delta\phi$ when computing the likelihood function described in the next section.

6.2 The Combined Likelihood

With the help of the corrected values for the p_t^{rel} and $\Delta\phi$ variables it is now possible to extend the hypothesis test of electron candidates given in Eqn. 5.2 for testing the hypothesis whether the candidate originates from a semi–leptonic beauty or

[2] The corresponding p_t^{rel} correction factors of the B→ μ analyses at ZEUS (*e. g.* [Gut05]) show a similar behaviour in general, however, due to different kinematic ranges and isolation criteria of the muons, and also due to a different correction procedure they are not directly comparable to the electron corrections.

[3] In particular this means that the corrections are applied likewise for real and Monte Carlo data.

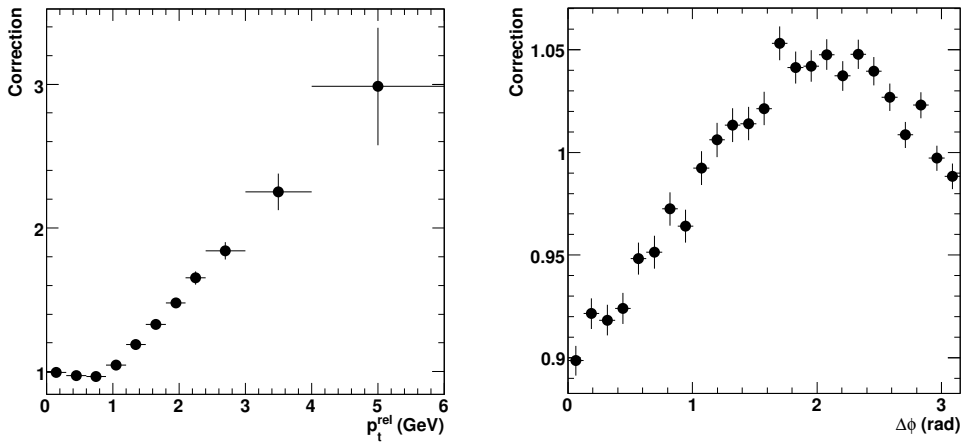

Figure 6.10: Correction factors for the p_t^{rel} and $\Delta\phi$ variables. These are obtained by dividing the data distributions in every bin by the corresponding Monte Carlo distributions in the non-signal region. The Monte Carlo distributions had been normalised to the data beforehand.

charm decay, or from something else. With the discriminants given in this and the last chapter the full likelihood (see Eqn. 5.1) then reads

$$\begin{aligned}\mathcal{L}_{i,j} \;=\; & \alpha_i(p_t,\eta)\cdot\mathcal{P}(\mathrm{d}E/\mathrm{d}x,\,p,\,n_{\mathrm{trunc}}\,|\,m_i)\cdot\mathcal{P}(f_{\mathrm{EMC}},\,p\,|\,i) \\ & \cdot\,\mathcal{P}(E_{\mathrm{CAL}}/p_{\mathrm{trk}}\,|\,i)\;\cdot \\ & \beta_j(p_t,\eta)\cdot\mathcal{P}(p_t^{\mathrm{rel}}\,|\,j)\cdot\mathcal{P}(\Delta\phi\,|\,j)\,, \end{aligned} \tag{6.1}$$

with α_i being the abundance of particle type i (*a priori* probabilities, *c. f.* Sec. 5.3) and β_j denoting the frequency of the different types of electron formation:

$$\begin{aligned} i \;&\in\; \{\,\pi^{\pm},\,\mathrm{K}^{\pm},\,p|\bar{p},\,\mathrm{e}^{\pm},\,\mu^{\pm}\,\}, \\ j \;&\in\; \{\,\mathrm{e}^{\pm}\text{ from semi–leptonic beauty decays, }\mathrm{e}^{\pm}\text{ from semi–leptonic} \\ &\qquad \text{charm decays, background}\,\}\,. \end{aligned} \tag{6.2}$$

The test function again is the ratio of the likelihood for the hypothesis, $i\wedge j$, to that for all hypotheses, $k\wedge l$

$$T_{i,j} \;=\; \frac{\mathcal{L}_{i,j}}{\sum\limits_{k,l}\mathcal{L}_{k,l}}\,. \tag{6.3}$$

This hypothesis test then is a combination of a test for a particle being an electron and a second test for the electron candidate originating from a semi–leptonic decay of a heavy–flavoured hadron. It helps to overcome the insufficient separation

power of the electron identification alone (*c. f.* Sec. 5.5). In the following the test function, T, denotes explicitly that for $e^{\pm}$ originating from semi–leptonic beauty or charm decays.

6.2.1 Decay Frequencies

Similar to the particle abundances, α_i, defined in Sec. 5.3, the relative frequencies of the different decays into electrons, β_j, have to be determined. Three types are of interest: Semi–leptonic charm and beauty decays defining the signals, and the background which covers all other sources of electrons like non-tagged γ conversions, DALITZ decays, DIS background etc. As with the particle abundances, the numbers are taken again from the Monte Carlo samples and binned in η and p_t for a more precise description. As an example, results for e^- are given in Fig. 6.11.

6.2.2 Control Distributions

Since the method of the beauty and charm extraction depends on the Monte Carlo simulation, its quality and agreement with real data has to be checked. The procedure for this is the same as used in Chap. 3. First all distributions of all eight Monte Carlo samples are added weighted with their integrated luminosities. The resulting distribution is then area–normalised to the distribution of real data, since the actual normalisation is unknown and only the shape is of interest.

The first variables to check are the five discriminants used in the likelihood ratio. In Fig. 6.12 the distributions for real data of all those variables are drawn on top of the corresponding simulated ones. Good agreement is seen for all of them, in particular for the dE/dx variable which is most important for the hypothesis test, indicating that the systematic corrections emphasised in Sec. 4.3 work. Also, the corrected data values of p_t^{rel} and $\Delta\phi$ (see Sec. 6.1.3) fit perfectly to the simulated ones.

Because the particle abundances and the decay frequencies used in the likelihood computation depend on the transverse momentum, p_t and the pseudo–rapidity, η, of the electron candidate, they are also checked as shown in Fig. 6.13. Here also, no significant deviations between real data and Monte Carlo simulation is seen.

6.3 Beauty and Charm Extraction

The fraction of beauty and charm in the selected dijet photoproduction events is determined by a fit of the Monte Carlo prediction to the real data. The fit is performed with distributions of the test function (6.3) for the hypothesis of a particle

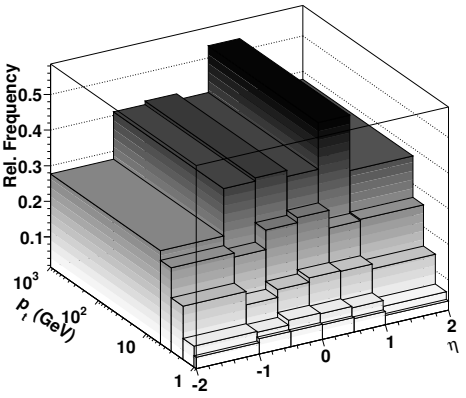

(a) e^- from semi–leptonic beauty decays

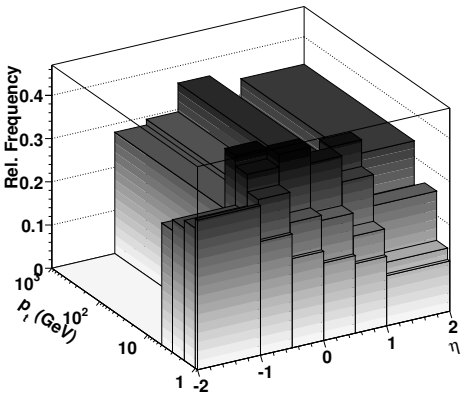

(b) e^- from semi–leptonic charm decays

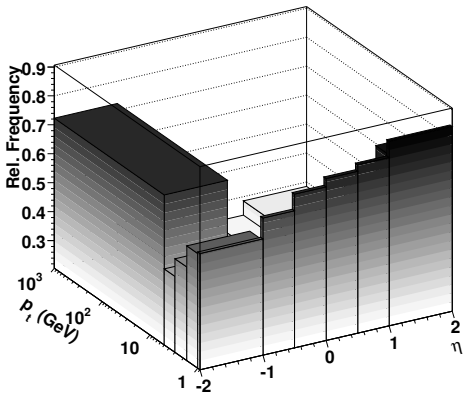

(c) all other e^-

Figure 6.11: Relative frequencies for different types of electron formation per event: Semi–leptonic beauty decays (a), semi–leptonic charm decays (b) and all other sources for electrons (c). The numbers are obtained with the help of the true information in all Monte Carlo events. The frequencies are given in bins of the transverse momentum, p_t and the pseudo–rapidity, η, of the electron. The distributions are normalised such that the sum of all entries in a certain bin of the three distributions equals one.

being an electron from a semi–leptonic beauty or charm decay. The test function, T, is computed for each electron candidate defined in Sec. 3.4. Distributions of $-2\ln T$ are filled separately for real data, for all simulated $b\bar{b}$ events, for all $c\bar{c}$ events and all the remaining events, which we denote as background.[4] In case

[4]The filling is done candidate–wise, which means more than one candidate per event is allowed (the probability for this is small).

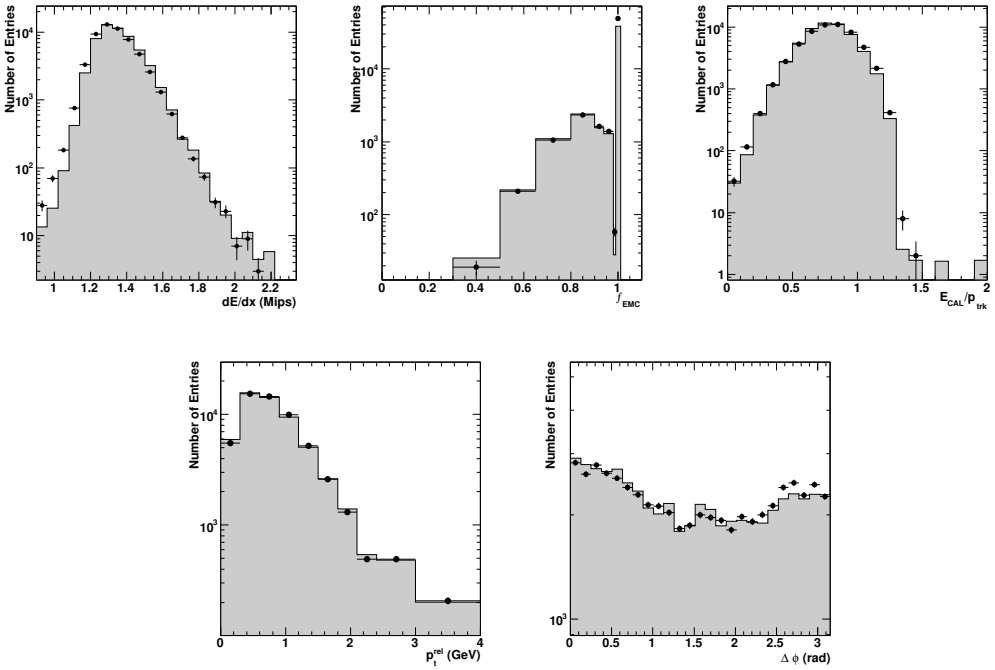

Figure 6.12: Control distributions for the five discriminant variables used in the hypothesis test. Real data is indicated by the solid circles while the shaded histograms represent the Monte Carlo distributions. The latter are the luminosity–weighted sum of all different Monte Carlo samples and have been area–normalised to the data. The histograms are made with the 98—00 data.

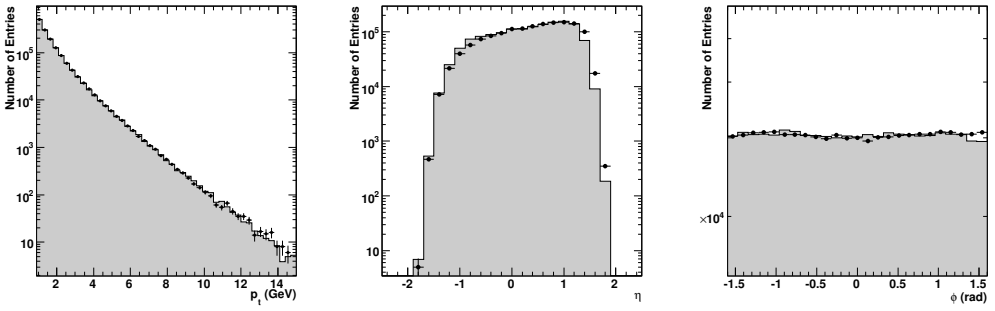

Figure 6.13: Control distributions for the transverse momentum, p_t, the pseudo–rapidity, η, and the azimuth, ϕ, of all electron candidates in 98—00 data. Symbols are the same as in the previous figure.

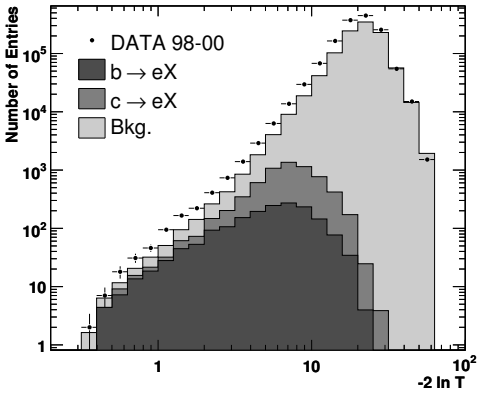

Figure 6.14: Distribution of the test function for all $e^{\pm}$ candidates in real data (solid circles) compared with different types of electron in the Monte Carlo samples (shaded histograms). The simulated distributions are drawn stacked. Their areas are luminosity–normalised to the data.

of the simulated events the decision of which class a particular event belongs to is made with the knowledge of the Monte Carlo generator data. Because we are interested in the total beauty and charm production cross–sections, electrons from semi–leptonic decays of charmed hadrons originating from beauty decays are assigned to the $b\bar{b}$ class. The procedure is done for each Monte Carlo sub-sample and the resulting distributions are added by means of their luminosity weights. In Fig. 6.14 all distributions are presented for both the 96—97 running period ($\sqrt{s_{ep}} = 300\,\text{GeV}$) and the 98—00 running period ($\sqrt{s_{ep}} = 318\,\text{GeV}$). The beauty signal is left-most, since the hypothesis test had been tuned for the identification of $B \to e$ events. The charm signal is located at the centre, while the background peaks at high values of $-2\ln T$. Here, the background exceeds the signal by several orders of magnitude. In order to prevent the fit from being dominated and spoiled by the background, the electron candidates are further constrained by the requirement of a minimum value of its test function. A cut at $-2\ln T_{\text{max}} = 10$ was chosen. This rejects most of the background, while the beauty and charm signals are only slightly diminished. Such a cut also removes the steep fall of the background distribution at the upper end, which might be difficult to describe. For a discussion on the stability of this cut see Sec. 7.3.

The fractions of beauty and charm signal in real data are determined by a fit of the simulated beauty, charm and background distributions of $-2\ln T$ to that of real data. The fractions f_b, f_c and f_{bkg} are varied by the fit, so that in each bin, i, the total number of simulated entries, $f_b N^{b,e}_{MC} + f_c N^{c,e}_{MC} + f_{bkg} N^{bkg}_{MC}$, is close to the number of entries for real data, $N^{e}_{Data} \cdot (N^{tot}_{MC}/N^{tot}_{Data})$.[5] Since the statistics is very low in some bins, a *binned maximum likelihood fit* is used here. Furthermore the

[5]The notation of N^{e}_{Data} is somewhat mis-leading, since the electron candidates in data include a considerable amount of background. However, the important thing to note is, that this number is meant candidate–wise rather than event–wise.

	$\sqrt{s_{ep}} = 300\,\text{GeV}$	$\sqrt{s_{ep}} = 318\,\text{GeV}$
f_b	0.038 ± 0.007	0.051 ± 0.006
f_c	0.091 ± 0.017	0.086 ± 0.011
f_{bkg}	0.871 ± 0.017	0.863 ± 0.010
$N_{Data}^{b,e}$	$1\,010 \pm 186$	$2\,853 \pm 336$
$N_{Data}^{c,e}$	$2\,420 \pm 452$	$4\,811 \pm 615$
N_{Data}^{bkg}	$23\,160 \pm 452$	$48\,282 \pm 559$

Table 6.1: Fit results for f_b, f_c and f_{bkg} and the corresponding absolute numbers $N_{Data}^{b,e}$, $N_{Data}^{c,e}$ and N_{Data}^{bkg}. The error of the latter is given by the statistical uncertainty of the fit.

(rather limited) statistics of the Monte Carlo samples is also taken into account.[6] The method used had been developed by BARLOW et al. [BB93]. The fit results are presented in Fig. 6.15. The obtained values for the fractions of beauty, charm and background, and the corresponding absolute numbers, $N_{Data}^{b,e} = f_b \cdot N_{Data}^{e}$, $N_{Data}^{c,e} = f_c \cdot N_{Data}^{e}$ and $N_{Data}^{bkg} = f_{bkg} \cdot N_{Data}^{e}$, are collected in Tab. 6.1. The goodness of a maximum likelihood fit can be estimated with the help of the likelihood ratio, λ, for the fit hypothesis [BC84]. In the case of GAUSSian distributed errors $-2\ln\lambda \equiv \tilde{\chi}^2$ converges towards χ^2. The values of $\tilde{\chi}^2$ divided by the number of degrees of freedom, $d.o.f.$, are[7]

$$\tilde{\chi}^2/d.o.f.\Big|_{\sqrt{s_{ep}}=300\,\text{GeV}} = 6.7\,/\,12\,,$$
$$\tilde{\chi}^2/d.o.f.\Big|_{\sqrt{s_{ep}}=318\,\text{GeV}} = 10.7\,/\,12\,.$$

The correlations of the fit parameters, f_b, f_c and f_{bkg} are given by the correlation matrix

$$C = \begin{pmatrix} f_{b,b} & f_{b,c} & f_{b,bkg} \\ f_{c,b} & f_{c,c} & f_{c,bkg} \\ f_{bkg,b} & f_{bkg,c} & f_{bkg,bkg} \end{pmatrix},$$

[6] Common fits consider only statistic uncertainties in the data to be fitted to, *i. e.* the real data distribution in our case. This is only valid if the uncertainties in the Monte Carlo samples are negligible. Therefore usually many more simulated events than real ones are produced (at least ten times more), which is in this analysis not possible due to the huge amount of light–flavour events.

[7] The number of degrees of freedom is 12, since the fit has two free parameters and one constraint, and the distributions consist of 15 bins.

with

$$C(\sqrt{s_{\mathrm{ep}}} = 300\,\mathrm{GeV}) = \begin{pmatrix} 1.00 & 0.60 & -0.24 \\ 0.60 & 1.00 & -0.77 \\ -0.24 & -0.77 & 1.00 \end{pmatrix},$$

$$C(\sqrt{s_{\mathrm{ep}}} = 318\,\mathrm{GeV}) = \begin{pmatrix} 1.00 & 0.68 & -0.21 \\ 0.68 & 1.00 & -0.67 \\ -0.21 & -0.67 & 1.00 \end{pmatrix}.$$

While the beauty signal is very well separated from the background, its correlation to charm is large. Also, charm is highly correlated with the background. The reason for the large charm correlation, resulting in a relatively large uncertainty, is two-fold: First, the test function is computed for the beauty hypothesis, not for a charm hypothesis. Second, one of the five discriminants, $p_{\mathrm{t}}^{\mathrm{rel}}$, separates only beauty from the background but not charm. However, the main objective of this analysis, the determination of the beauty fraction, has been reached. The measurement of the charm fraction, not even dreamed of in the beginning, is a welcome side–product of the analysis. Equipped with these results we can go on to the determination of cross–sections, which is subject of the next chapter.

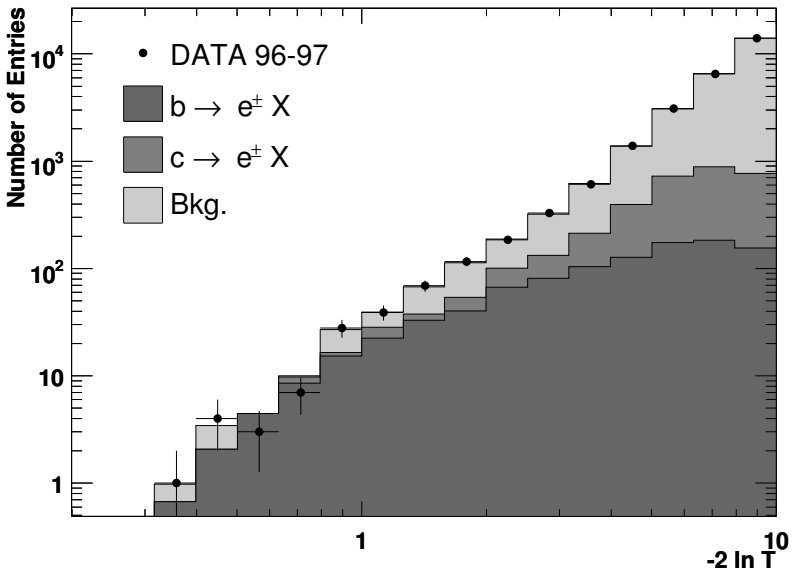

(a) Running period 96–97, $\sqrt{s_{\mathrm{ep}}} = 300\,\mathrm{GeV}$

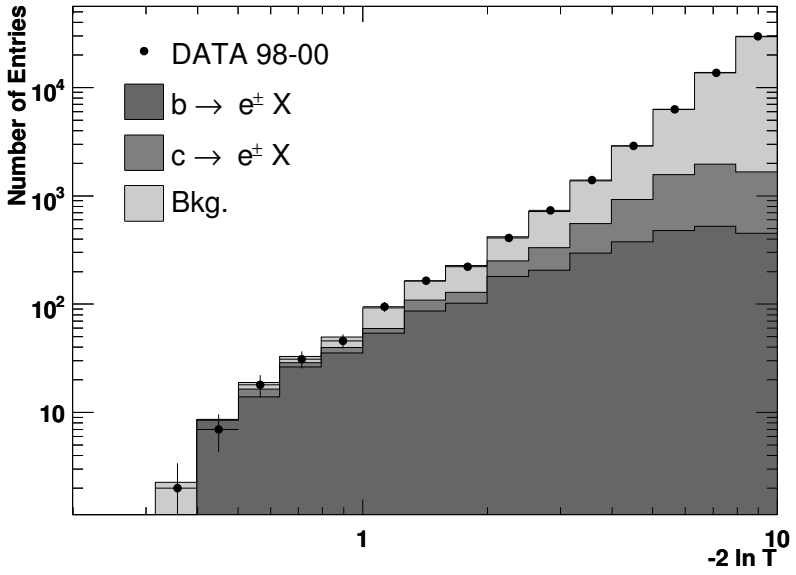

(b) Running period 98–00, $\sqrt{s_{\mathrm{ep}}} = 318\,\mathrm{GeV}$

Figure 6.15: Fit of the beauty and charm fractions for 96–97 running period (a) and 98–00 running period (b). The sum of the Monte Carlo distributions is fitted to real data. The fit range is restricted to $-2\ln T < 10$. The fit takes into account the statistical uncertainties of bins with low statistics as well as of the simulation.

Chapter 7

Cross–Section Measurements

7.1 Visible Cross–Sections

In the previous chapter the number of events for the dijet photoproduction reactions[1]

$$e^{\pm}p \;\rightarrow\; b\bar{b} + e'^{\pm}X \;\rightarrow\; e_{sl}{}^{\pm} + \text{dijet} + e'^{\pm}X\,, \tag{7.1}$$

$$e^{\pm}p \;\rightarrow\; c\bar{c} + e'^{\pm}X \;\rightarrow\; e_{sl}{}^{\pm} + \text{dijet} + e'^{\pm}X\,, \tag{7.2}$$

have been determined by fitting Monte Carlo templates to real data. With the numbers given in Tab. 6.1 the corresponding beauty and charm cross–sections can be computed with the help of the formula

$$\sigma^{i}_{e^{\pm}p\rightarrow e_{sl}{}^{\pm}+\text{dijet}+e'^{\pm}X} = \frac{f_i \cdot N^{e}_{\text{Data}}}{\mathcal{L}\cdot\alpha^{i}_{e}} \qquad \text{with } i \in \{\,b,\,c\,\}\,. \tag{7.3}$$

Here, $\mathcal{L}$ is the total gated luminosity for the considered running period, and α^{i}_{e} the $e^{\pm}$ candidate–wise acceptance corrections for beauty and charm given by

$$\alpha^{i}_{e} = \frac{N^{i,\,e}_{\text{MC, rec}}}{N^{i,\,e}_{\text{MC, gen}}}\,. \tag{7.4}$$

More details of the acceptance calculation are given in Appendix B. The numbers $N^{i,\,e}_{\text{MC, rec}}$ and $N^{i,\,e}_{\text{MC, gen}}$ represent the numbers of reconstructed and generated electron candidates with transverse momenta $p^{e}_{t} > 0.9\,\text{GeV}$ in the Monte Carlo. The results for the 1996/97 and 1998—2000 running periods are presented in Fig. 7.1.

[1] This includes also beauty and charm production in *excitation processes* mentioned in Sec. 1.3.4. In very rare cases beauty and charm are produced in the fragmentation process or in weak interaction. Cascade decays of beauty into charm are accounted as beauty production events.

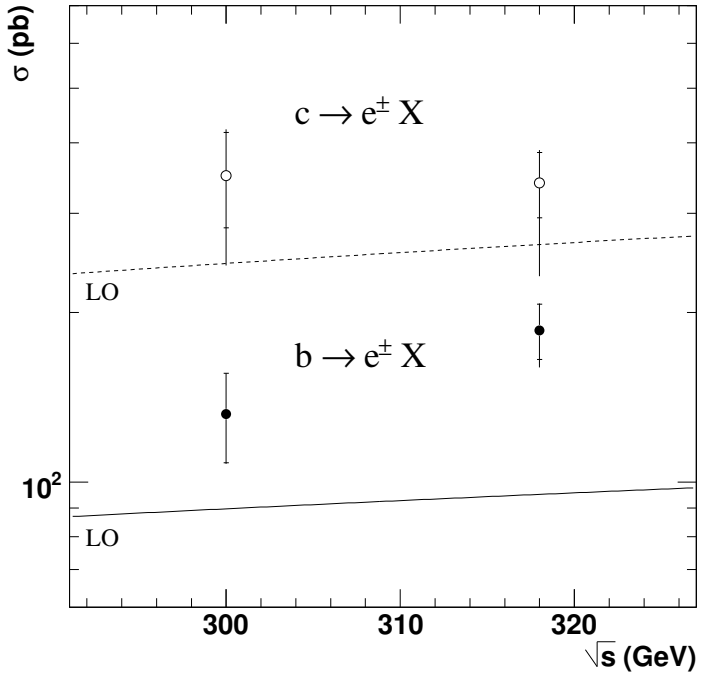

Figure 7.1: Total visible cross–sections for the reaction $e^{\pm}p \to e_{sl}{}^{\pm}$+dijet+$e'^{\pm}X$ for electrons and positrons with $p_t^e > 0.9$ GeV. The kinematic region is restricted to $0.2 < y < 0.8$. At least two jets are required with $E_t > 7(6)$ GeV and $|\eta| < 2.5$. The error bars denote the squared sum of the statistical and systematic uncertainties. The small horizontal bars mark the size of the statistical error. The lines represent the corresponding PYTHIA prediction in leading order QCD. Here, the $\sqrt{s_{ep}}$–dependence is drawn according to the parametrisation (1.11).

The exact numbers together with the luminosities and acceptances used are listed in Tab. 7.1. The statistical uncertainties of the cross–sections are the scaled uncertainties of the beauty and charm fractions given by the fitting procedure. Statistical uncertainties on the numbers of selected events are already included in these values. The systematic uncertainties of the cross–sections shown are discussed in Sec. 7.3. The PYTHIA predictions for $\sqrt{s_{ep}} = 300$ GeV and $\sqrt{s_{ep}} = 318$ GeV are interconnected with the help of the DONNACHIE–LANDSHOFF parametrisation $\sigma \propto s_{ep}^{0.08}$ mentioned in Sec. 1.3.

$\sqrt{s_{ep}}$ [GeV]	$\mathcal{L}$ [nb^{-1}]	α_e^b	σ_b [pb]	α_e^c	σ_c [pb]
300	38.6±0.7	0.20	$132 \pm 24^{+2}_{-5}$	0.18	$350 \pm 67^{+28}_{-84}$
318	81.6±0.9	0.19	$186 \pm 21^{+4}_{-16}$	0.18	$340 \pm 45^{+19}_{-98}$

Table 7.1: Total visible cross–sections for the reaction $e^{\pm}p \to e_{sl}{}^{\pm}$ + dijet+$e'^{\pm}X$.

$\sqrt{s_{ep}}$ [GeV]	σ_b [pb]	$\Delta_{\mathcal{L}}\sigma_b$ [pb]	$\Delta_{E_t}\sigma_b$ [pb]	σ_b^{LO} [pb]	σ_b/σ_b^{LO}]
300	$820 \pm 150^{+20}_{-30}$	± 15	± 0	556	1.5 ± 0.3
318	$1170 \pm 130^{+30}_{-100}$	± 18	$^{+20}_{-30}$	597	2.0 ± 0.2

Table 7.2: Total inclusive cross–sections for the reaction $e^{\pm}p \to b\bar{b} + e'^{\pm}X$. Systematic errors due to statistical uncertainties of the acceptances are omitted, since they are well below 1 pb.

7.2 Total Inclusive Cross–Sections for Open Beauty and Charm Production

For the determination of the inclusive cross–sections for beauty and charm production it is necessary to transform the $e^{\pm}$–wise values given above to event–wise ones. These are connected by the number of heavy quarks emerging from the hard sub-process[2] and the branching ratios for beauty and charm hadrons decaying semi–leptonically into electrons or positrons. Instead of using a fixed value for the branching ratio (*e. g.* from the Particle Data Group tables) the information incorporated in the PYTHIA Monte Carlo simulation is used, since the momentum spectra of the outgoing particles are considered here.[3] The validity of the PYTHIA model for semi–leptonic B decays has already been discussed in Sec. 1.8. In addition the restriction of the electron momenta, $p_t^e > 0.9\,\text{GeV}$, is released and the cross–section is extrapolated to the full range. All this is achieved by using acceptance corrections, α^i, for a flavour $i \in \{b,\, c\}$:

$$\alpha^i \equiv \frac{N^{i,\,e}_{\text{MC, rec}}}{N^{i,\,\text{evt}}_{\text{MC, gen}}}\,. \tag{7.5}$$

The denominator, $N^{i,\,\text{evt}}_{\text{MC, gen}}$, denotes the number of generated $b\bar{b}$ or $c\bar{c}$ production events in the Monte Carlo inside the considered kinematic region, $0.2 < y < 0.8$ and $E_t^{\text{jet}} > 7(6)\,\text{GeV}$, $|\eta^{\text{jet}}| < 2.5$ (see Sec. 3.3 for details). In principle these variables are reconstructed in the same manner as in real data; however, to become independent of the detector, they are reconstructed with respect to the hadron level (*c. f.* Sec. 3.2), except for y which is the true value given by the generator. This ensures the ability to compare with other experiments. The inclusive cross–sections then

[2] Usually this number equals 2, since the heavy quarks are produced in pairs. In excitation processes, however, one of the quarks might remain undetected in one of the remnants.

[3] In the PYTHIA program matrix elements of the form $|\mathcal{M}|^2 = (p_h p_\ell)(p_{\nu_\ell} p_h)$ are used to distribute the momenta of the decay products in semi–leptonic decays $H \to \ell\nu_\ell h$, where H is a beauty or charm hadron and h an ordinary hadron.

$\sqrt{s_{ep}}$ [GeV]	σ_c [pb]	$\Delta_{\mathcal{L}}\sigma_b$ [pb]	$\Delta_{E_t}\sigma_b$ [pb]	σ_c^{LO} [pb]	σ_c/σ_c^{LO}
300	$6470 \pm 1240^{+510}_{-1550}$	± 120	$^{+500}_{-270}$	4516	1.4 ± 0.3
318	$6150 \pm 820^{+350}_{-1770}$	± 150	$^{+310}_{-370}$	4780	1.3 ± 0.2

Table 7.3: Total inclusive cross–sections for the reaction $e^{\pm}p \to c\bar{c} + e'^{\pm}X$. Systematic errors due to statistical uncertainties of the acceptances are omitted, since they are well below 1 pb.

are defined by

$$\sigma_{e^{\pm}p \to b\bar{b} + e'^{\pm}X} = \frac{N^{b,e}_{Data}}{\mathcal{L} \cdot \alpha_b}, \tag{7.6}$$

$$\sigma_{e^{\pm}p \to c\bar{c} + e'^{\pm}X} = \frac{N^{c,e}_{Data}}{\mathcal{L} \cdot \alpha_c}. \tag{7.7}$$

In Fig. 7.2 the obtained cross–sections are shown, both for beauty and charm. The exact numbers are given in Tab. 7.2 and 7.3. These tables include also the cross–sections of the QCD leading order prediction, σ^{LO}, given by the PYTHIA program, and the ratios σ/σ^{LO}. The latter can be used to normalise the leading order prediction to the measured values for a better comparison of the shapes of the distributions. In the figure the result of a similar analysis [Tur02] is shown also.[4] In this analysis the beauty fraction for the ZEUS data 1996—2000 was determined by fitting p_t^{rel} distributions of muons from semi–leptonic B decays. The kinematical constraints on the total $b\bar{b}$ cross-section are the same as in this analysis. The muonic result is compatible with the results from the electron analysis.

7.3 Systematic Uncertainties and Consistency

In this section studies of possible systematic effects and consistency checks are described. These have been performed in order to detect unforeseen systematic mismeasurements and provide confidence in the measurements, as well as estimate the systematic uncertainties of the results gained from uncorrected systematic effects.[5] The following possible sources of systematic uncertainties were studied separately for beauty and charm measurements:

[4] The results for the two different ep centre–of–mass energies had been averaged.

[5] A rich and sometimes amusing source of information about systematic errors is found in [Bar02] and [Bar00].

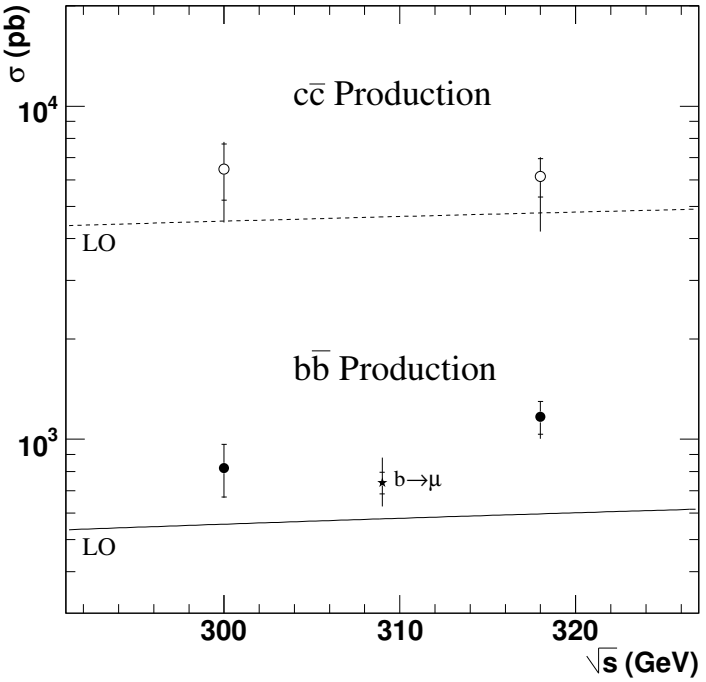

Figure 7.2: Total cross–sections of open beauty (solid circles) and charm (hollow circles) production for centre–of–mass energies $\sqrt{s_{\mathrm{ep}}} = 300\,\mathrm{GeV}$ and $\sqrt{s_{\mathrm{ep}}} = 318\,\mathrm{GeV}$. The kinematic region is restricted to $0.2 < y < 0.8$. At least two jets are required with $E_{\mathrm{t}} > 7(6)\,\mathrm{GeV}$ and $|\eta| < 2.5$. The lines indicate the corresponding leading order QCD prediction by the PYTHIA program. Their functional form is the same as in Fig. 7.1. The star denotes the result of a similar $b \to \mu$ analysis [Tur02].

1. Acceptance corrections. Due to statistical uncertainties of the acceptance correction factors determined by Eqn. B.5 the uncertainty of the cross–section measurement is increased. The relative uncertainty of the cross–section equals the relative statistical error of the acceptance.

2. The variation caused by the uncertainty of the luminosity measurement. According to [ZEU06] these are ±1.8 % for the $\sqrt{s_{\mathrm{ep}}} = 300\,\mathrm{GeV}$ running period and ±2.25 % for $\sqrt{s_{\mathrm{ep}}} = 318\,\mathrm{GeV}$ data. Here also, the relative uncertainties result in cross–section variations are of the same size.

3. The uncertainty of the jet energy scale was determined to be ±3 % in photoproduction events [C$^+$03].[6] In order to estimate the effect on the cross–

[6] In the case of deep inelastic scattering this can be improved by exploiting the fact, that the scattered electron has to balance the total hadronic system [Win02]. In such analyses the error on the jet energy can be decreased to ±1 % for jet energies above 10 GeV.

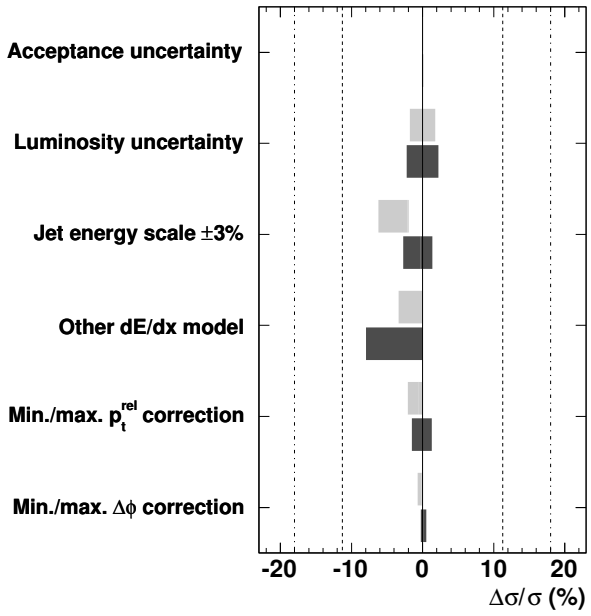

Figure 7.3: Results on the study of systematic uncertainties of the cross–section measurements for $b\bar{b}$ production. Shown are the relative deviations from the measured total cross–section for the cases studied (see text). The light shaded bar represents the variations for the $\sqrt{s_{ep}} = 300\,\mathrm{GeV}$ data and the dark shaded bars the ones for $\sqrt{s_{ep}} = 318\,\mathrm{GeV}$ data. The statistical error of the latter is indicated by the dashed lines, while the dashed–dotted line represent the statistical uncertainty of the former.

sections, the energy of jets in real data was varied up and down these values while leaving the energies unchanged in Monte Carlo data. Then the whole analysis chain is re-done and new cross–sections are obtained. Finally, the deviations from the original cross–sections are taken as systematic uncertainties.

4. The energy loss measurements are the key point for the electron identification. Although many systematic effects are corrected (see Sec. 4.3), one has to check for remaining effects, and also the stability of the fit model used to describe the $\mathrm{d}E/\mathrm{d}x$ residuals. The test is made by using the toy model introduced in Sec. 4.4.3 for the $\mathrm{d}E/\mathrm{d}x$ description, which is based on completely different arguments than the simple analytical model used otherwise. This is done for both real and Monte Carlo data. Afterwards one proceeds as in the previous item.

5. The p_t^{rel} discriminant used for the beauty and charm extraction is varied within the statistical uncertainties of the corresponding correction factors

determined in Sec. 6.1.3. For the variation in the upward direction the statistical error is added to correction factors larger than one, while being subtracted for the corrections lower than one. A reversed procedure is applied for the downward variation. The above procedure is applied when computing the test function for real data as well as for Monte Carlo data. However, since the p_t^{rel} distributions, which are changed by the corrections factors, are determined with the help of the Monte Carlo data only, the changes of the correction factors described here operate on the Monte Carlo actually. The analysis is rerun with the changed p_t^{rel} distributions and new cross–sections are obtained yielding an estimate for the magnitude of this systematic.

6. The systematic effect of the statistical uncertainty for the corrections of the $\Delta\phi$ variable is done in the same way as for p_t^{rel} described above.

The results of the studies are depicted in Fig. 7.3 for the case of beauty production and in Fig. 7.4 for charm. Beside the relative deviations of the cross–sections the statistical errors of the original measurements are shown also.

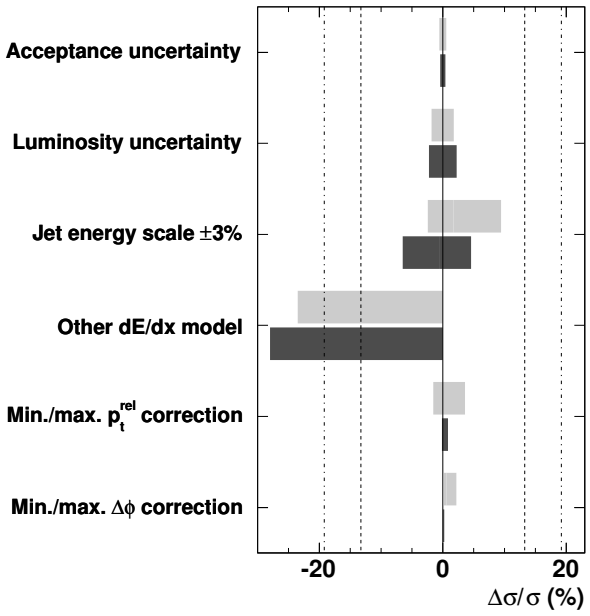

Figure 7.4: Study of systematic uncertainties of the cross–section measurements for charm production. The relative deviations from the measured total cross–section are presented for different effects (see text). The light shaded bars represent the variations for the $\sqrt{s_{ep}} = 300\,\text{GeV}$ data and the dark shaded bars the ones for $\sqrt{s_{ep}} = 318\,\text{GeV}$ data. The statistical error of the latter is indicated by the dashed lines, while the dashed–dotted line represent the statistical uncertainty of the former.

In beauty production no significant deviation from the original cross-sections is seen. Therefore only the acceptance uncertainty, the luminosity error and the jet energy scale uncertainty are taken into account, since we know for sure that these variable are tainted with systematic effects which we cannot correct for. A larger deviation is seen only for the changed $\mathrm{d}E/\mathrm{d}x$ model in the case of $\mathrm{c\overline{c}}$ production. The deviation points towards the same direction as the corresponding one in the case of beauty production (though it is much smaller there). Therefore the $\mathrm{d}E/\mathrm{d}x$ systematic is included in the total systematic uncertainty for beauty and charm production cross–sections. The total systematic uncertainties in upward and downward directions are computed separately by adding the respective parts in quadrature.

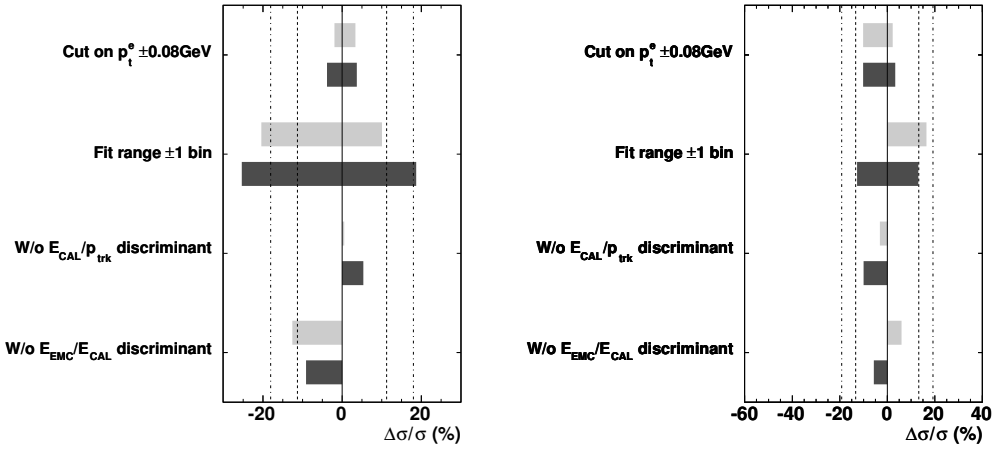

(a) Beauty production (b) Charm production

Figure 7.5: Various consistency checks (see text for details) of measurements for beauty production (a) and charm production (b). Shown are the relative deviations from the measured total cross–sections. The light shaded bars represent the variations for the $\sqrt{s_{\mathrm{ep}}} = 300\,\mathrm{GeV}$ data and the dark shaded bars the ones for $\sqrt{s_{\mathrm{ep}}} = 318\,\mathrm{GeV}$ data. The statistical error of the latter is indicated by the dashed lines, while the dashed–dotted line represent the statistical uncertainty of the former.

Beside the studies of systematic effects several consistency checks were performed to test the stability of the measurements and look for more possible systematic effects. The results of these studies are summarised in Fig. 7.5 and Tab. 7.4.

1. The stability of the cut on the transverse momentum of the electrons, $p_{\mathrm{t}}^{\mathrm{e}}$, is checked by varying this cut both in real and Monte Carlo data by the resolution of the tracking program, which is ±80 MeV according to Eqn. 2.1.

2. The fit stability was tested by varying the upper limit of fit range, which is

restricted by $-2\ln T < 10$, by one bin up and down, *i. e.* $^{+2.59}_{-2.06}$ in units of the test function, and re-do the fit for both cases. It should be mentioned that the variations of the fit limit has a big effect on the number of background candidates. In case of the increased limit the number of background candidates is almost doubled, while for the decreased limit it is only half as large.

3. The particle identification method is further checked by deliberately omitting discriminant variables from the likelihood ratio. This had been done separately for $E_{\mathrm{CAL}}/p_{\mathrm{trk}}$ and f_{EMC}. In order to fit the beauty and charm fractions successfully, the loss in separation power must be compensated by additional cuts. In the case of omitted $E_{\mathrm{CAL}}/p_{\mathrm{trk}}$ values $f_{\mathrm{EMC}} > 0.95$ were required, while for left out f_{EMC} values the energy over momentum fraction was restricted to $0.5 < E_{\mathrm{CAL}}/p_{\mathrm{trk}} < 1.2$. The procedure was applied for real data and Monte Carlo.

4. The independence of the beauty and charm extraction method from the particle charges is probed, for this is one of the most important claims of the extensive systematic corrections for the energy loss. In a first step, cross-sections for positively and negatively charged particles are determined separately. The method is further refined by further splitting the samples into e^+p and e^-p runs, which is also a check for a significant contamination of DIS events. Note however, that the statistical uncertainties of these cross–sections are significantly higher than those of the original measurements, because only sub-samples of the available tracks and events are used here.

Neither for the beauty nor for the charm production cross–sections significant discrepancies are seen, except for the case of decay electrons in e^-p collisions.

Another issue of some interest is the question of the isolation of the $e^\pm$ candidates. Measurements of the particle's energy or momentum could be spoiled by nearby particles. However this is already prevented by the requirement of 1:1 track–island relationships of the EFOs used (*c. f.* Sec. 3.4). This works quite well, as seen in Fig. 7.6. Here, the shortest distances from the $e^\pm$ candidate to the nearest track and energy flow object, respectively are histogrammed, both for real data and Monte Carlo data. In fact, the electron candidates are quite isolated, so no measures are taken.

7.4 Differential Cross–Sections

Single–differential cross–sections for the reactions $e^\pm p \to b\bar{b} + e'^\pm X$ and $e^\pm p \to c\bar{c} + e'^\pm X$ were determined for the electron variables p_t^e and η_e, the energy, E_t and the direction, η of the leading jet, the second most energetic jet as well as the

Check	σ_b [pb]	$\Delta\sigma_b^{stat.}$ [pb]	σ_c [pb]	$\Delta\sigma_c^{stat.}$ [pb]
All, $\sqrt{s_{ep}} = 300$ GeV	818	148	6465	1241
All, $\sqrt{s_{ep}} = 318$ GeV	1166	131	6147	815
Only e_{sl}^+, $\sqrt{s_{ep}} = 300$ GeV	784	208	6897	1655
Only e_{sl}^+, $\sqrt{s_{ep}} = 318$ GeV	1252	195	7410	1172
Only e_{sl}^-, $\sqrt{s_{ep}} = 300$ GeV	865	213	6051	1887
Only e_{sl}^-, $\sqrt{s_{ep}} = 318$ GeV	1143	189	4499	1300
Only e_{sl}^+ in e^+p events	1251	210	7742	1406
Only e_{sl}^+ in e^-p events	1354	549	5828	2522
Only e_{sl}^- in e^+p events	882	180	4948	1377
Only e_{sl}^- in e^-p events	2060	808	4997	7149

Table 7.4: Consistency checks for possible dependencies of the measured $b\bar{b}$ and $c\bar{c}$ cross–sections on the sign of the charge of the electrons (positrons) originating from the semi–leptonic decays and the incoming lepton. The first two rows indicate the original cross–sections for comparison. Note the, for some of the checks, largely increased statistical errors due to the reduced statistics.

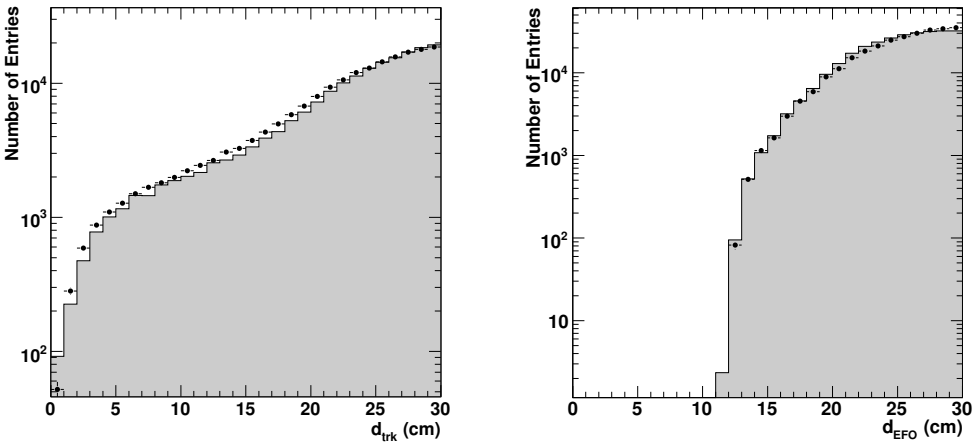

(a) Distance to nearest track (b) Distance to nearest EFO

Figure 7.6: Isolation of $e^{\pm}$ candidates, represented by the distance to the impact point of the nearest track (a) and the distance to the closest energy flow object (b). The black dots indicate the 1998—2000 data,while the shaded histograms show the corresponding Monte Carlo data. The different Monte Carlo samples are added with their luminosity weights and afterwards normalised to the area of the real data distributions. Note, that the left plot does not contain the 1:1 EFO requirement.

jet associated with the electron, the number of jets per event, N_{jet}, and the parton kinematics, y, x_γ and x_p.

The fitting procedure described in Sec. 6.3 is performed in bins of these variables, and the beauty and charm fractions are extracted. The binning of the different variables and the gained acceptances and purities are shown in Sec. B.1. The cross–sections in each bin are that of Equations (7.6) and (7.7) divided by the respective bin width. On top of each distribution the leading order PYTHIA prediction is drawn. For a better comparison the predictions are scaled by the ratios of the measured total cross–sections to the PYTHIA prediction, $\sigma/\sigma^{\mathrm{LO}}$, given in Tables 7.2 7.3, averaged for $\sqrt{s_{\mathrm{ep}}} = 300\,\mathrm{GeV}$ and $\sqrt{s_{\mathrm{ep}}} = 318\,\mathrm{GeV}$. The resulting scaling factors are 1.75 for beauty and 1.35 for charm production. Appendix C also contains all cross–section numbers together with their statistical and systematic uncertainties. The systematic uncertainties are those determined in the previous section for the total cross–sections appropriately scaled.

7.4.1 Beauty Production

In Fig. 7.7 the transverse momentum, $p_{\mathrm{t}}^{\mathrm{e}}$, and the pseudo–rapidity, η^{e}, of the electrons and positrons coming from the semi–leptonic decays are shown. The distributions show ample agreement with the scaled PYTHIA prediction drawn on top. The situation is similar for Fig. 7.8, where the energy and the pseudo–rapidity of the most energetic are presented. Also in Fig. D.2, which shows the cross–section as a function of the kinematic variables, x_γ, x_p and y, and the number of jets per event[7], N_{jet}, no significant deviation from the scaled PYTHIA prediction is seen. More figures on the second most energetic jets and the electron–associated jets are depicted in Sec. D.1. All cross-section numbers are given in Appendix C.

7.4.2 Charm Production

The same measurements were done for charm production. Figure 7.9 represents the electron variables, $p_{\mathrm{t}}^{\mathrm{e}}$ and η^{e}, while the properties of the leading jet are depicted in Fig. 7.10. The kinematic variables are shown in Fig. D.6. Differential cross–sections as a function of E_{t} and η of the second most energetic jet and the electron–associated jet are given in Sec. D.2. Again, all cross–section numbers are collected in Appendix C. Similar to $\mathrm{b\bar{b}}$ production, the scaled PYTHIA distributions agree reasonably well with the measured cross–sections.

[7] As mentioned earlier, the number of jets per events denotes the number of jets with at least 4 GeV of transverse energy in events containing two high energetic jets of $E_{\mathrm{t}} > 7(6)\,\mathrm{GeV}$. Thus one has to be careful when interpreting this variable.

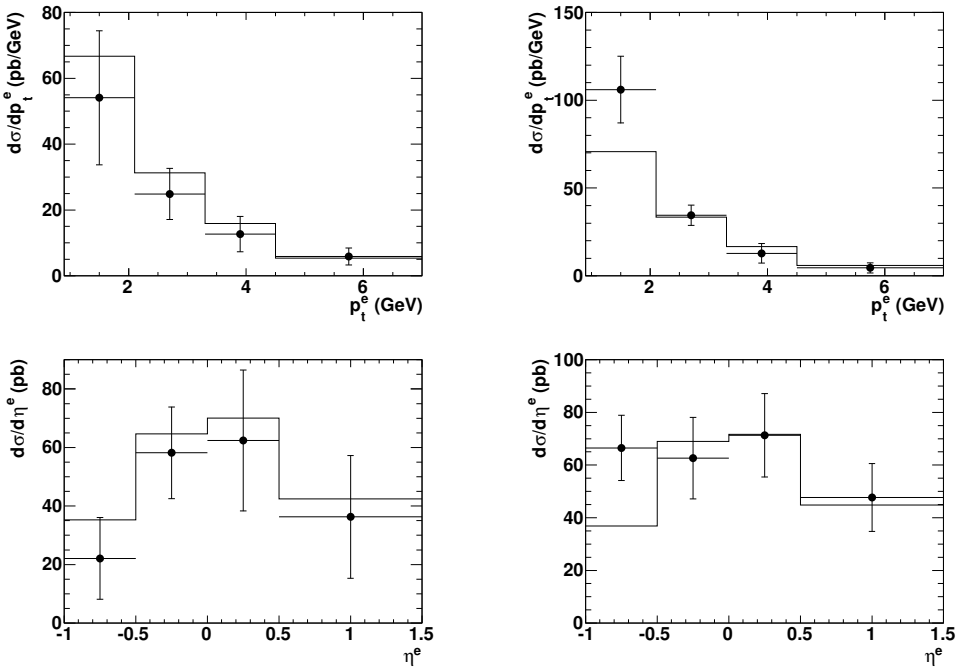

(a) $\sqrt{s_{ep}} = 300\,\text{GeV}$ (b) $\sqrt{s_{ep}} = 318\,\text{GeV}$

Figure 7.7: Cross–section dependence for beauty production as a function of the transverse momentum, p_t^e, and the pseudo–rapidity, η^e, of the semi–leptonic decay electron for centre–of–mass energies, $\sqrt{s_{ep}} = 300\,\text{GeV}$ (a) and $\sqrt{s_{ep}} = 318\,\text{GeV}$ (b). The measured cross–sections are depicted by the black dots, while the histograms represent the PYTHIA prediction, scaled by a factor of 1.75 .

7.5 Next–To–Leading Order Comparison

In this section the measurements are compared with massive fixed–flavour predictions in next–to–leading order QCD computed with the FMNR program, which is described in Sec. 1.3.4. This program produces series of $b\bar{b}$ or $c\bar{c}$ events with two or three partons in the final–state, which allows for computing production cross–sections on the heavy quark parton level. However, due to the non-zero parton masses a factorisation of the final–state fragmentation, as described in Sec. 1.5, is not possible. Instead, the b or c quark as generated by the FMNR program is hadronised into a beauty or charm hadron by re-scaling the three–momentum of the quark using the PETERSON fragmentation function (1.40) with a certain choice of parameters. The hadron then is decayed afterwards semi-leptonically into an electron (or muon) and further particles.[8] Jets are reconstructed by applying the

[8]For B hadrons cascade decays via charmed mesons are possible.

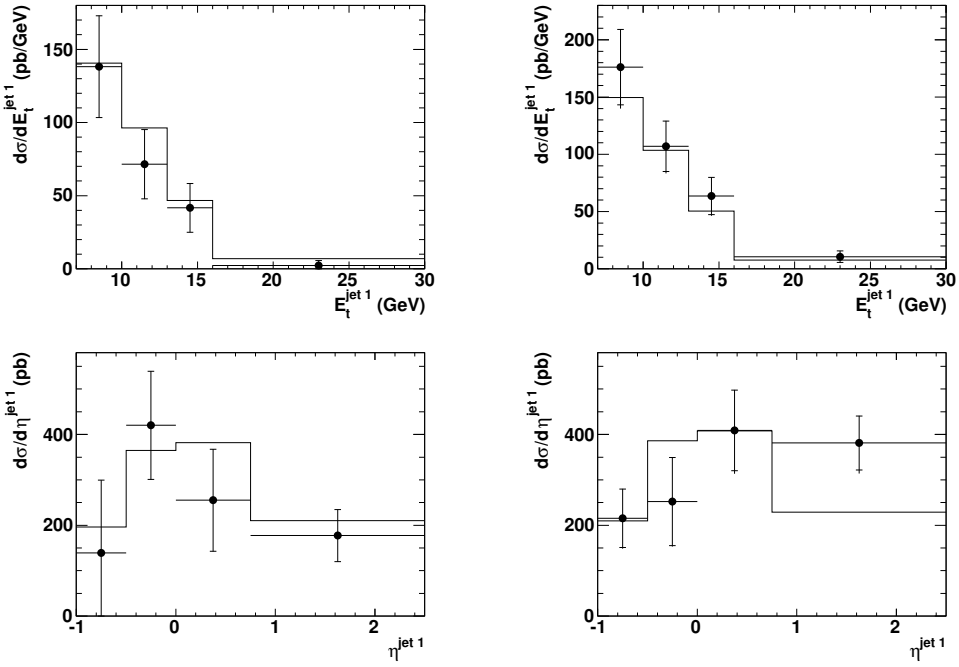

(a) $\sqrt{s_{\mathrm{ep}}} = 300\,\mathrm{GeV}$ (b) $\sqrt{s_{\mathrm{ep}}} = 318\,\mathrm{GeV}$

Figure 7.8: Cross–section dependence for beauty production as a function of the transverse energy, $E_{\mathrm{t}}^{\mathrm{jet}\,1}$, and the pseudo–rapidity, $\eta^{\mathrm{jet}\,1}$, of the leading jet in each event for centre–of–mass energies, $\sqrt{s_{\mathrm{ep}}} = 300\,\mathrm{GeV}$ (a) and $\sqrt{s_{\mathrm{ep}}} = 318\,\mathrm{GeV}$ (b). The measured cross–sections are depicted by the black dots, while the histograms represent the PYTHIA prediction, scaled by a factor of 1.75.

massive k_{t}–jet algorithm (*c. f.* Sec. 3.2) to the outgoing partons.[9] Because of this the measured hadron–level cross–sections presented in the previous sections have to be transformed into parton–level cross–sections before comparing them to the FMNR predictions.

The heavy quark masses used for the calculations are $m_{\mathrm{b}} = 4.75\,\mathrm{GeV}$ and $m_{\mathrm{c}} = 1.5\,\mathrm{GeV}$, respectively. The renormalisation and fragmentation scales are related by

$$\mu_{\mathrm{R}} = \mu_{\mathrm{F},\gamma} = \mu_{\mathrm{F,p}} \equiv \mu_0\,. \tag{7.8}$$

They are functions of the masses and the transverse momenta of the outgoing

[9] N. B.: The outgoing partons are the only "real" particles generated by the FMNR program. The hadronisation process and the semi–leptonic decays are accomplished by applying certain probabilities and branching ratios to the variables of interest before filling them into histograms.

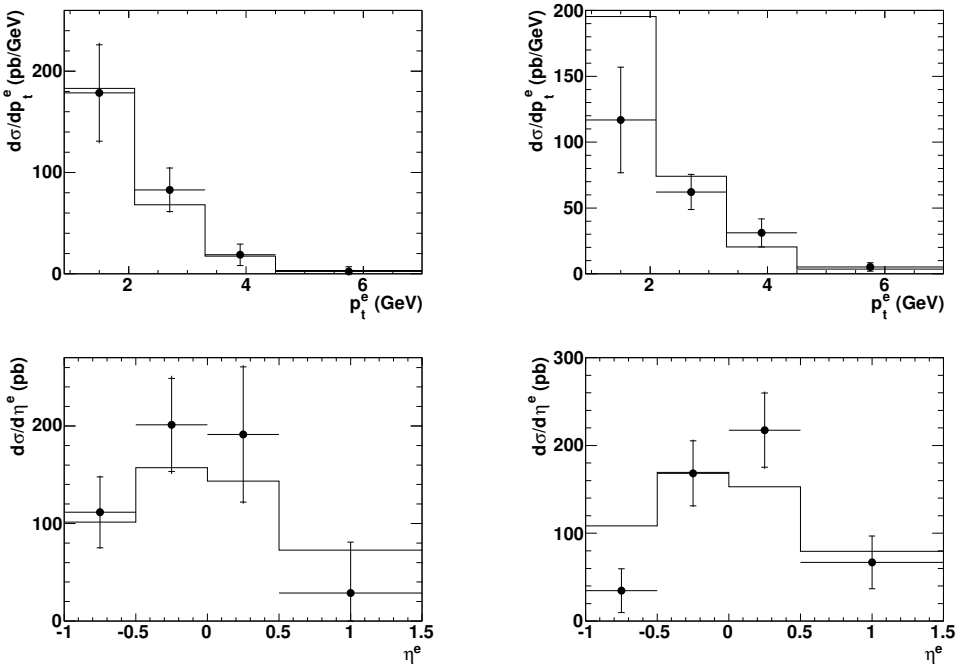

(a) $\sqrt{s_{ep}} = 300\,\text{GeV}$ (b) $\sqrt{s_{ep}} = 318\,\text{GeV}$

Figure 7.9: Cross–section dependence for charm production as a function of the transverse momentum, p_t^e, and the pseudo–rapidity, η^e, of the semi–leptonic decay electron for centre–of–mass energies, $\sqrt{s_{ep}} = 300\,\text{GeV}$ (a) and $\sqrt{s_{ep}} = 318\,\text{GeV}$ (b). The measured cross–sections are depicted by the black dots, while the histograms represent the PYTHIA prediction, scaled by a factor of 1.75.

heavy quarks. A common choice (*c. f.* Eqn. (1.42) is

$$\mu_0^2 = m_{\text{HQ}}^2 + \frac{1}{2}(\hat{p}_{\text{t},1}^2 + \hat{p}_{\text{t},2}^2)\,, \tag{7.9}$$

with $\hat{p}_{\text{t},1}$, $\hat{p}_{\text{t},2}$ denoting the transverse momenta of the heavy quark and its anti-particle in the parton rest–frame. The used parton distribution functions are CTEQ–5M in the case of the proton and GRV–HO for the photon.[10] The PETERSON fragmentation parameter, ϵ, was chosen to 0.035, also different to that used for the PYTHIA Monte Carlo generation.

The uncertainties of the FMNR prediction are large [FMNR98], in particular for charm production. At HERA energies the biggest uncertainty for charm is

[10] In contrast to the parametrisations of the parton distribution functions used for the PYTHIA prediction, the sets used here are computed in higher orders using the $\overline{\text{MS}}$ scheme for the proton and the DIS–γ scheme for the photon according to the used parametrisations of the structure functions (this includes a different running of the strong coupling, α_s).

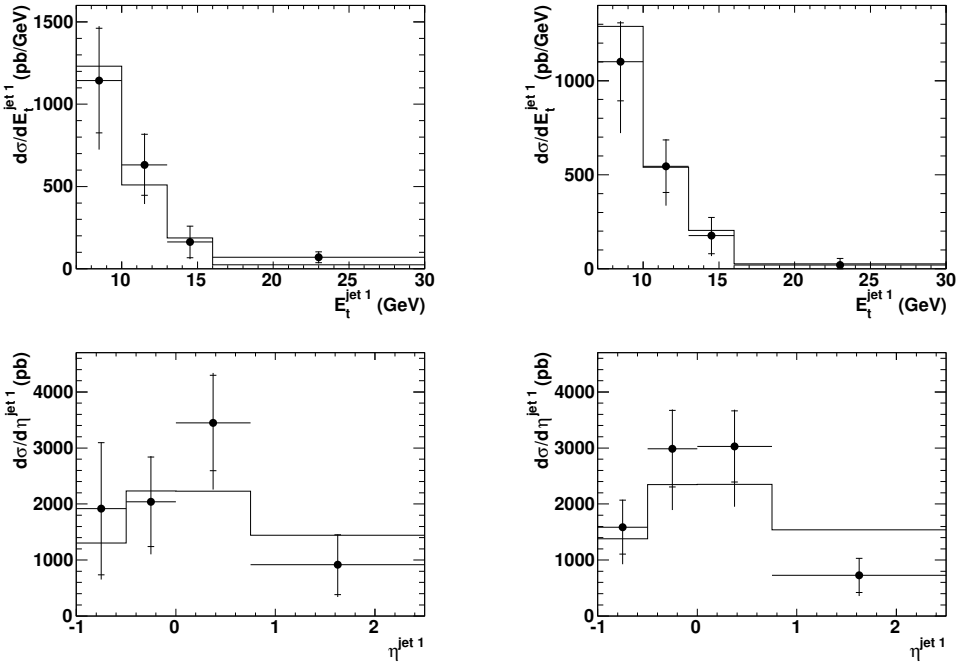

(a) $\sqrt{s_{\mathrm{ep}}} = 300\,\mathrm{GeV}$ (b) $\sqrt{s_{\mathrm{ep}}} = 318\,\mathrm{GeV}$

Figure 7.10: Cross–section dependence for charm production as a function of the transverse energy, $E_{\mathrm{t}}^{\mathrm{jet}\,1}$, and the pseudo–rapidity, $\eta^{\mathrm{jet}\,1}$, of the leading jet in each event for centre–of–mass energies, $\sqrt{s_{\mathrm{ep}}} = 300\,\mathrm{GeV}$ (a) and $\sqrt{s_{\mathrm{ep}}} = 318\,\mathrm{GeV}$ (b). The measured cross–sections are depicted by the black dots, while the histograms represent the PYTHIA prediction, scaled by a factor of 1.75.

mainly due to our ignorance of the gluon density in the photon PDF but also from that of the proton. Additional uncertainties come from the charm mass and the scales. Uncertainties by factors of 4—10 are to be expected. In the case of beauty production the uncertainties are much smaller due to the higher mass. Still the photon structure function is the dominant part. In total uncertainties of factors of 2—3 are common. Therefore one has to be very careful when comparing measurements to predictions of the FMNR program. Its main use is to study the effect of taking next–to–leading order processes into account. Here, a straight comparison with PYTHIA might be dangerous. Though PYTHIA utilises matrix elements in leading order QCD, it includes a mature parton shower model and some other phenomenological parts, such that in some sense it is valid to all orders.[11]

[11] For technical reasons in events generated by PYTHIA information about the partons is only accessible after the parton showering, just before fragmentation. This definition of the parton level differs from that of the FMNR program.

In order to get a rough estimate on the uncertainties of the FMNR predictions, the masses of the heavy quarks and the scale, μ, are varied according to Tab. 7.5. Variations of the structure functions are not part of this thesis. It should be emphasised that the estimation of the uncertainties given here and shown in the following plots in many cases underestimates the actual uncertainty by far.

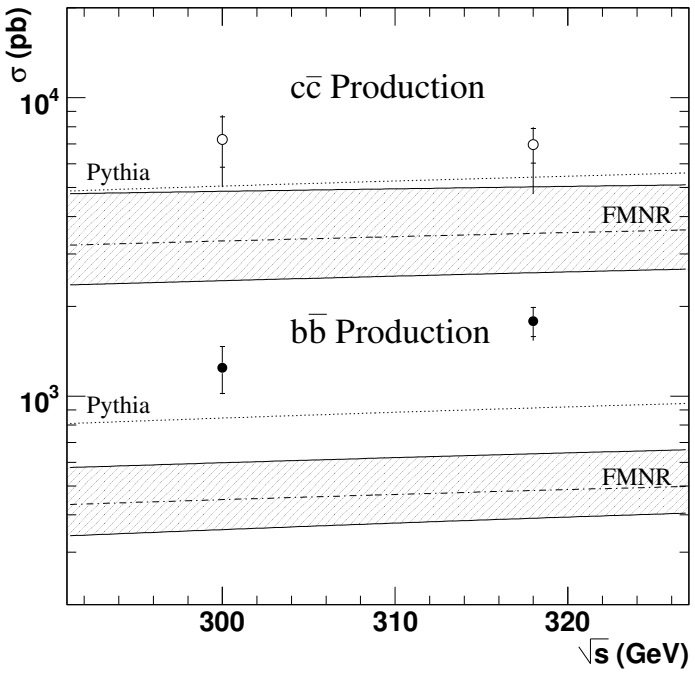

Figure 7.11: Predictions of the FMNR program for $c\bar{c}$ (upper dashed–dotted line) and $b\bar{b}$ production (lower dashed–dotted line). The predictions are made for centre–of–mass energies $\sqrt{s_{ep}} = 300\,\text{GeV}$ and $\sqrt{s_{ep}} = 318\,\text{GeV}$, and are connected with the help of the parametrisation (1.11). The hatched area around the predictions represents a rough estimate of the FMNR uncertainty (see Tab. 7.5). The circles indicate the measured production cross–sections for beauty (filled) and charm (hollow). The dotted lines are the corresponding PYTHIA predictions. All values are w. r. t. the parton level.

The FMNR predictions for the total inclusive production cross–sections of open beauty and charm production are presented in Fig. 7.11 together with the measurements and the PYTHIA prediction (unscaled). The $\sqrt{s_{ep}}$–dependence of the predictions is done in the same way as in Figures 7.1, 7.2. A comparison with other analyses can be seen in Fig. 7.12. Here, a collection of HERA results for $b\bar{b}$ production is shown as a function of Q^2. The plot is the same as shown already in Fig. 1.33, extended by the result of this thesis. Since the figure is a mixture

of total and visible cross–sections measurements, both of them are shown for this analysis (thick hollow circle and box). It is expected that the visible cross–sections are closer to the next–to–leading order predictions than the (extrapolated) total cross–sections, due to their tighter kinematical cuts. Thus it is hard to compare all the measurements actually. Even worse, the analyses differ in their kinematical ranges. However, all measurements lay systematically above the NLO predictions giving the hint, that recent next–to–leading order calculations are not yet mature enough for a thorough description of the problem.

Comparisons of the single–differential beauty and charm production cross–sections with the corresponding FMNR prediction are presented in Sec. D.3. The overall agreement is not very good.

	Upper limit	Lower limit
Beauty	$m_{\mathrm{b}} = 4.5\,\mathrm{GeV} \wedge \mu = \frac{1}{2}\mu_0$	$m_{\mathrm{b}} = 5.0\,\mathrm{GeV} \wedge \mu = 2\mu_0$
Charm	$m_{\mathrm{c}} = 1.2\,\mathrm{GeV} \wedge \mu = \frac{1}{2}\mu_0$	$m_{\mathrm{c}} = 1.8\,\mathrm{GeV} \wedge \mu = 2\mu_0$

Table 7.5: Variations of the heavy quark masses and the scales used in order to estimate the uncertainty of the FMNR predictions.

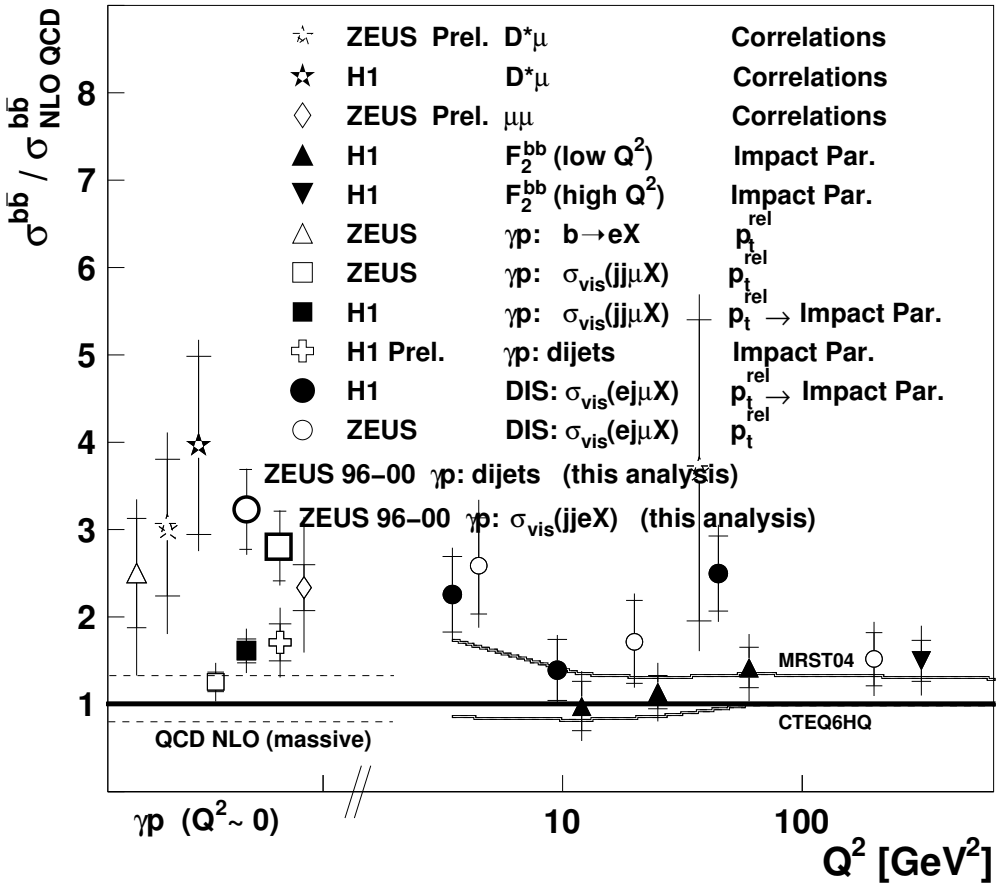

Figure 7.12: Open beauty production at HERA as a function of Q^2. Plotted is the ratio of the measured total cross–sections to massive NLO predictions. On the left are the γp measurements at $Q^2 \approx 0$ compared to predictions of the FMNR program. The deviation to the cross–section measured in this analysis (averaged for centre–of–mass energies $\sqrt{s_{ep}} =$ 300 GeV and $\sqrt{s_{ep}} = 318$ GeV), as determined in Fig. 7.11, is indicated by the thick hollow circle. The corresponding visible cross–section, scaled with the effective branching ratio, is shown also (thick empty box). The FMNR uncertainties given by Tab. 7.5 are displayed by the dashed lines in the photoproduction regime.

Chapter 8

Summary

The main objective of this thesis was to measure cross–sections for open $b\bar{b}$ production at HERA for centre–of–mass energies $\sqrt{s_{ep}} = 300\,\text{GeV}$ and $318\,\text{GeV}$. For this, ep collision data recorded with the ZEUS detector in the period 1996—2000 has been analysed. The beauty was tagged by looking for semi–leptonic decays of B hadrons into electrons or positrons. A dominant part of the analysis was the development of a proper electron and beauty identification. The kinematic range was restricted to photoproduction with four–momentum transfers $Q^2 \approx 0$. Here, the production rates for b quarks, which are more than three orders of magnitude lower than those for the light–flavoured quarks at HERA, are higher than in the case of deep inelastic scattering. Because the heavy quarks are produced mostly in boson–gluon–fusion–like processes, a common signature is high–p_t dijet events. Moreover, the jets were needed for the B identification.[1] Thus photoproduction dijet events form the basis of this analysis.

Setting up a proper electron identification procedure has been a demanding task. Since the identification of particles having momenta of several hundred MeV up to a few GeV depends much on measurements of the energy loss of charged particles in the central tracking chamber, a detailed understanding of the drift chamber and any possible systematic mis-measurements as well as ways of correcting them is necessary. Such corrections are now available pinning down the systematic uncertainty of the energy loss measurements to a level of a few percent only. In addition a general particle identification procedure for ZEUS data has been developed, which can be used for any type of particle.

In order to be able to find semi–leptonic B decays, the knowledge about the electron was combined with kinematic information of the electron, the neutrino and the jets. The full information was fed to a likelihood–ratio test enriching the

[1] Beauty identification without jets is possible with the help of life–time measurements. Unfortunately the ZEUS detector had not been equipped with a proper device for doing such measurements during the data taking period considered in this analysis.

signal. The amount of beauty in the signal region was obtained by fitting Monte Carlo templates to the real data distribution. A nice by-product of this method is its ability to determine the amount of $c\bar{c}$ production at the same time. The uncertainties of these measurements are larger than those for beauty, because the whole method was tuned for beauty identification and the intrinsic lesser separation power due to the fact, that the p_t^{rel}-distribution of charm is very similar to the background.

Measurements of the semi–leptonic decay channel into electrons are competitive to those with muons. The latter is widely used, because of the much simpler muon identification. However, the muons are required to have transverse momenta larger than ~2 GeV due to in-flight decays or mis-identified hadrons in the lower momentum region. Also, they have to be energetic enough to penetrate the calorimeter and reach the μ-chambers. Thus the acceptance is much reduced, since most of the muons and electrons originating from semi–leptonic decays of heavy quarks at HERA have lower momenta. The electron identification is more flexible. In the analysis presented here, electrons with transverse momenta down to 900 MeV are accepted, making the extrapolation to the full kinematical range more reliable.

The new method for the particle identification and the tagging of heavy hadrons has turned out to be very stable and robust, mainly due to its way of combining information from different sources. Moreover, it is superior to other methods used before at ZEUS, like the simple p_t^{rel} fits. These methods suffered a lot from known and unknown systematic effects. For example, in a previous analysis of $b \to e$ a proper use of positrons was not possible thus cutting the available statistics by half. With the new method this has changed. The particle identification now is independent of the sign of the charge of the particle in question. The relatively low contamination rates make this method — even in the $e^{\pm}$ case — competitive to μ analyses. It also provides a cross–check for the muon analyses done so far.[2]

Another important advantage of the new method is its simple extensibility. Information from the other sub-detectors, like life–time information, can easily be plugged into the likelihood function. Also, the method is not restricted to electrons — it can be applied to muons as well thus potentially gaining higher efficiencies. One could even think of analysing the electron and the muon channels in a single analysis, doubling the statistics.[3] This might be of some interest for double–differential cross–section measurements, for instance when extracting the proton structure functions $F_2^{b\bar{b}}$, $F_2^{c\bar{c}}$, or measurements of QCD correlations.

[2] At ZEUS, discrepancies in the efficiencies of the μ–chambers between real data and Monte Carlo data are seen. The systematic effects on the measured cross–sections caused by this are hard to estimate.

[3] The only thing needed is to change the definition of the hypothesis and the corresponding anti-hypothesis properly.

The measured $b\bar{b}$ and $c\bar{c}$ production cross–sections systematically exceed the prediction of the PYTHIA generator (matrix elements in leading order QCD plus parton shower). However, the shape of the distributions, in particular those for single–differential cross–sections, fit reasonably well to the prediction. Furthermore, the beauty measurement is compatible with measurements derived from the μ channel. The measured cross–sections were also compared to next–to–leading order QCD calculations, which have been performed in a fixed–flavour massive scheme. As in all other heavy quark analyses at HERA (and also elsewhere), large discrepancies are seen. The measurements are about three times higher than the prediction. However, the uncertainties of the predictions are large also. Here, improvements of the theoretical models, in particular massless NLO calculations or the promising mixture of massless and massive approaches, as well as appropriate Monte Carlo generators, are desirable for HERA.

Currently this analysis is being extended for the HERA-II running period. The ZEUS detector will collect data until summer 2007, and with the gated luminosity it will be possible to reduce the statistical errors of the measurements well below 10 % for the total cross–sections and 20 % for differential cross–sections. As mentioned earlier the likelihood approach forms a solid ground upon which many extensions of the recent analysis are easily possible. In addition to the electron channel, the muon channel will also be analysed with the method presented here using additional information from the μ–chambers and the micro–vertex detector. With the statistics available it should be possible to determine double–differential cross–sections, which allows for more stringent tests of QCD. In particular the gluon content in the photon could be more constrained, but also the amount of charm and beauty in the proton could be determined by extending the analysis to the DIS region, thus cross–checking the results determined from the scaling violations of F_2^p. The beauty and charm content of the proton are of particular interest for the LHC, since there the dominant process for heavy quark production will be the gluon gluon fusion. Therefore a precise knowledge of the proton structure is utterly needed.

Presently heavy flavour physics is a very active and rich field. The HERA collider at DESY, but also the Tevatron and in the near future the LHC, provide many measurements to test and to improve our present theory of the strongest force in the universe — Quantum Chromodynamics.

Appendix A

Trigger Definitions

In this appendix the trigger definitions used for the selection of dijet γp events (*c. f.* Chapter 3) are given.

A.1 First Level Trigger

FLT 40: exotic

- $E_{t,\,\mathrm{tot}}^{\mathrm{EMC}} > 15\,\mathrm{GeV}$ (the three innermost rings in the FCAL and the innermost ring in the RCAL excluded from the energy sum)

FLT 41: high E_{t}

- $E_{t,\,\mathrm{tot}}^{\mathrm{CAL}} > 30\,\mathrm{GeV}$ (two innermost FCAL rings excluded from the energy sum)

FLT 42: high E_{t}

- $E_{t,\,\mathrm{tot}}^{\mathrm{CAL}} > 15\,\mathrm{GeV}$ and
- at least one good track

FLT 43: high E_{t}

- $E_{t,\,\mathrm{tot}}^{\mathrm{CAL}} > 11.6\,\mathrm{GeV}$ (two innermost FCAL rings excluded from the energy sum)

A.2 Second Level Trigger

HPP 1: high E_t

- (FLT 40 or FLT 41 or FLT 42 or FLT 43) and
- (ep vertex or CTDoff) and
- at least one good track and
- $\sum_i (E_i - p_{z,i}) > 8\,\text{GeV}$ and
- $E_t^{box} > 8\,\text{GeV}$ and
- $(\sum_i (E_i - p_{z,i}) > 12\,\text{GeV})$ or $(\sum_i E_i / \sum_i p_{z,i} < 0.9)$

HPP 2: high E_t

- equivalent to HPP 1

HPP 3: high E_t

- HPP 1 and
- at least one EMC cluster with $E > 0.7\,\text{GeV}$ and
- $N_{trk}^{vtx}/N_{trk}^{all} > N$ with N being some function of N_{trk}^{all}

A.3 Third Level Trigger

HPP 14: high E_t dijet

- (HPP 1 or HPP 2 or HPP 3) and
- at least two cone–jets with $|\eta| < 2.5$ and $E_t \geq \begin{cases} 4\,\text{GeV}; & \text{96—98 running} \\ 4.5\,\text{GeV}; & \text{99—00 running} \end{cases}$

Appendix B

Acceptance Corrections

Acceptance corrections to the measured cross–sections are determined with the help of Monte Carlo simulations. Here, the acceptance of the detector and the reconstruction software is determined by comparing the number of reconstructed events in the simulation, N_{rec}, with the number of generated events, N_{gen}

$$\alpha = \frac{N_{\text{rec}}}{N_{\text{gen}}} \,. \tag{B.1}$$

This is done separately for the beauty and the charm signal Monte Carlo simulations. In the case of differential cross–sections acceptances are determined for each bin.

The error calculation of the acceptances is more subtle. Normally one would determine the statistical uncertainty of the acceptances by means of the binomial distribution for given N_{rec} and N_{gen}. However, since the signal Monte Carlos for beauty and charm consist of luminosity–weighted sub-samples (direct and resolved γp, excitation), binomial probabilities are no longer applicable. Instead, the common approach of GAUSSian error propagation is used. To do so, the number of generated events is split into the number of reconstructed (accepted) events and the number of rejected events

$$N' = N_{\text{gen}} - N_{\text{rec}} \,. \tag{B.2}$$

The acceptance is then the ratio of the weighted sum of the number of reconstructed events to the weighted sum of the number of generated events in all MC sub-samples. The weights w_i are defined by the luminosities, $\mathcal{L}_i$, of the sample i

$$w_i = \frac{\mathcal{L}_i}{\sum_i \mathcal{L}_i} \,. \tag{B.3}$$

Thus

$$\alpha = \frac{\sum_i w_i N_{\mathrm{rec},\,i}}{\sum_i w_i (N_{\mathrm{rec},\,i} + N'_i)} \,. \tag{B.4}$$

The statistical uncertainty of the acceptance is then given by

$$\Delta\alpha^2 = \sum_i \left(\frac{\partial \alpha}{\partial N_{\mathrm{rec},\,i}} \right)^2 \Delta N^2_{\mathrm{rec},\,i} + \sum_i \left(\frac{\partial \alpha}{\partial N'_i} \right)^2 \Delta N'^2_i \,, \tag{B.5}$$

with

$$\begin{aligned} \Delta N_{\mathrm{rec},\,i} &= \sqrt{N_{\mathrm{rec},\,i}} \,, \\ \Delta N'_i &= \sqrt{N'_i} \,. \end{aligned} \tag{B.6}$$

Special care needs to be taken in the case of acceptances very close to zero in combination with low N_{gen}, because α–$\Delta\alpha$ might become lower than zero here. In this case the lower error is truncated at zero and the corresponding length is added to the upper part of the error, such that the 1–σ integral of the statistical uncertainty is preserved. This is achieved with the help of the inverse error function.

Purities are calculated in a similar way. Here, the ratio of the number of events which have been both reconstructed and generated in the same bin[1], $N_{\mathrm{gen+rec}}$ to the number of reconstructed events, N_{rec} is taken as purity, π

$$\pi = \frac{N_{\mathrm{gen+rec}}}{N_{\mathrm{rec}}} \,. \tag{B.7}$$

The statistical uncertainties of the purity are computed by means of the Gaussian error propagation too. Since the purity is not only limited at zero, but also has an upper limit at one, asymmetric errors might occur at this limit also. The asymmetry is achieved in the same manner as at the lower limit.

B.1 Differential Cross–Sections and Binning

Differential cross–sections are measured in bins of the variable in question. The acceptance in each bin and also its statistical uncertainty are needed for the cross–section computation. In addition, the acceptances and purities give a good guidance for the choice of the binning. In the following graphs the acceptances and

[1] It might happen that events generated in another bin (see Sec. B.1) *migrate* into the bin in question and are reconstructed there.

purities in the bins of all variables, for which differential cross–sections are measured, are presented. Note, that the acceptances for the event–wise variables include beside the branching ratios for the semi–leptonic decay into electrons the extrapolation to the full momentum range of the electrons, which reduces the acceptances roughly by a factor of 5 in the case of beauty events and a factor of 20 in the case of charm events.

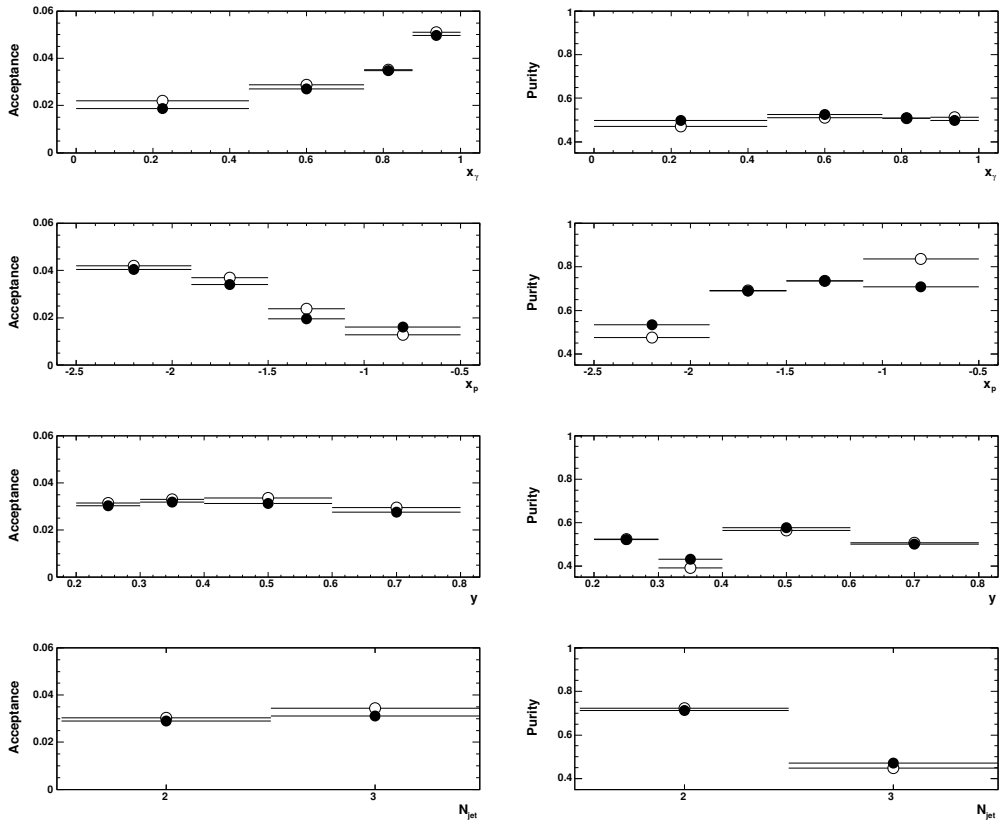

Figure B.1: Acceptances and purities in bins of the kinematic variables x_γ, x_p, y and N_{jet} in beauty events, both for $\sqrt{s_{ep}} = 300\,\text{GeV}$ (hollow circles) and $\sqrt{s_{ep}} = 318\,\text{GeV}$ (solid circles).

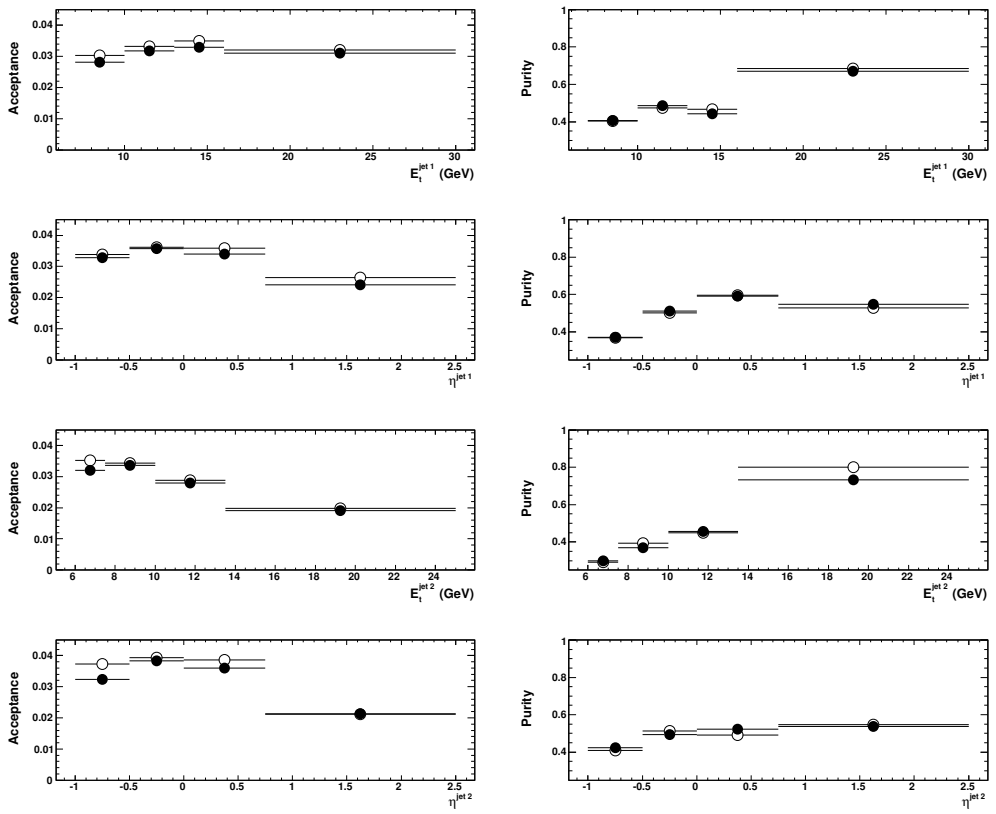

Figure B.2: Acceptances and purities in bins of the jet properties, η and E_t of the most energetic, the second most energetic and the electron jet in beauty events, both for $\sqrt{s_{ep}} = 300\,\text{GeV}$ (hollow circles) and $\sqrt{s_{ep}} = 318\,\text{GeV}$ (solid circles).

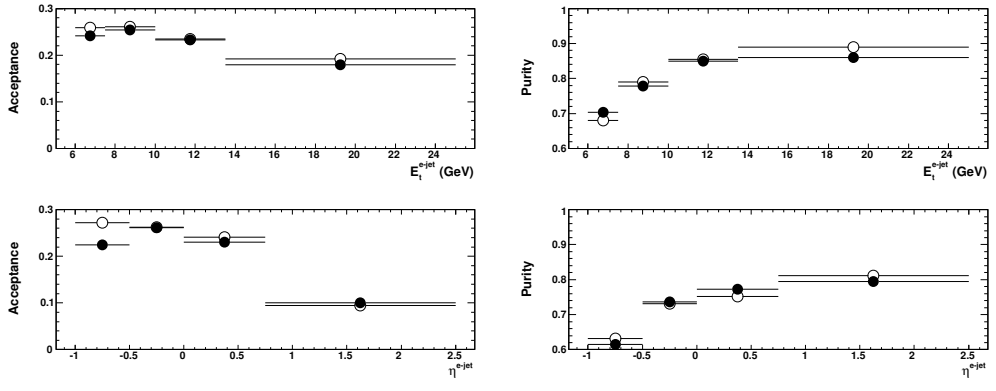

Figure B.3: Acceptances and purities in bins of the jet properties, η and E_t of the $e^{\pm}$–associated jets in beauty events, both for $\sqrt{s_{ep}} = 300\,\text{GeV}$ (hollow circles) and $\sqrt{s_{ep}} = 318\,\text{GeV}$ (solid circles).

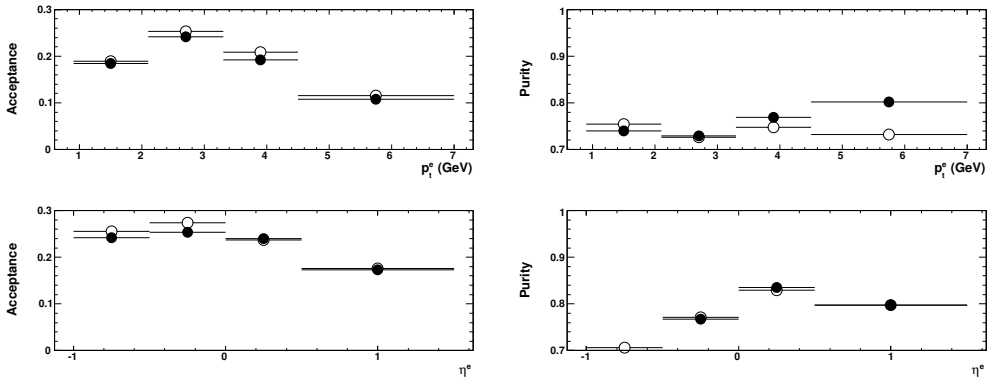

Figure B.4: Acceptances and purities in bins of the electron variables p_t^e and η^e in beauty events, both for $\sqrt{s_{ep}} = 300\,\text{GeV}$ (hollow circles) and $\sqrt{s_{ep}} = 318\,\text{GeV}$ (solid circles).

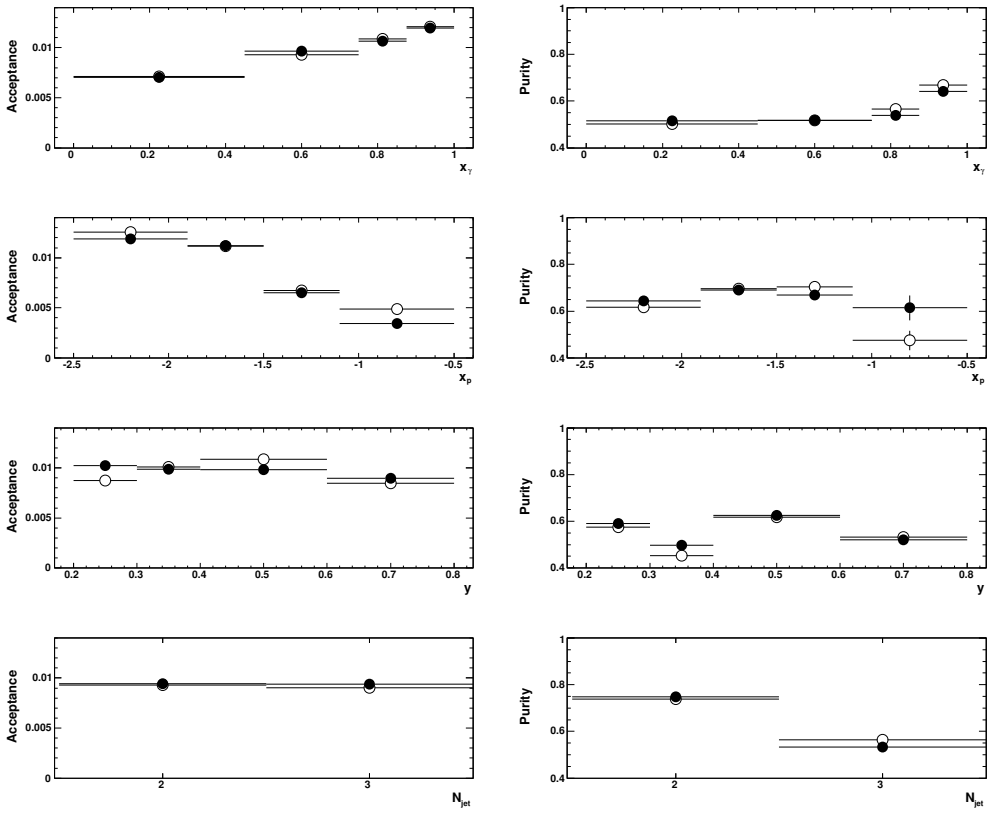

Figure B.5: Acceptances and purities in bins of the kinematic variables x_γ, x_p, y and N_{jet} in charm events, both for $\sqrt{s_{ep}} = 300\,\text{GeV}$ (hollow circles) and $\sqrt{s_{ep}} = 318\,\text{GeV}$ (solid circles).

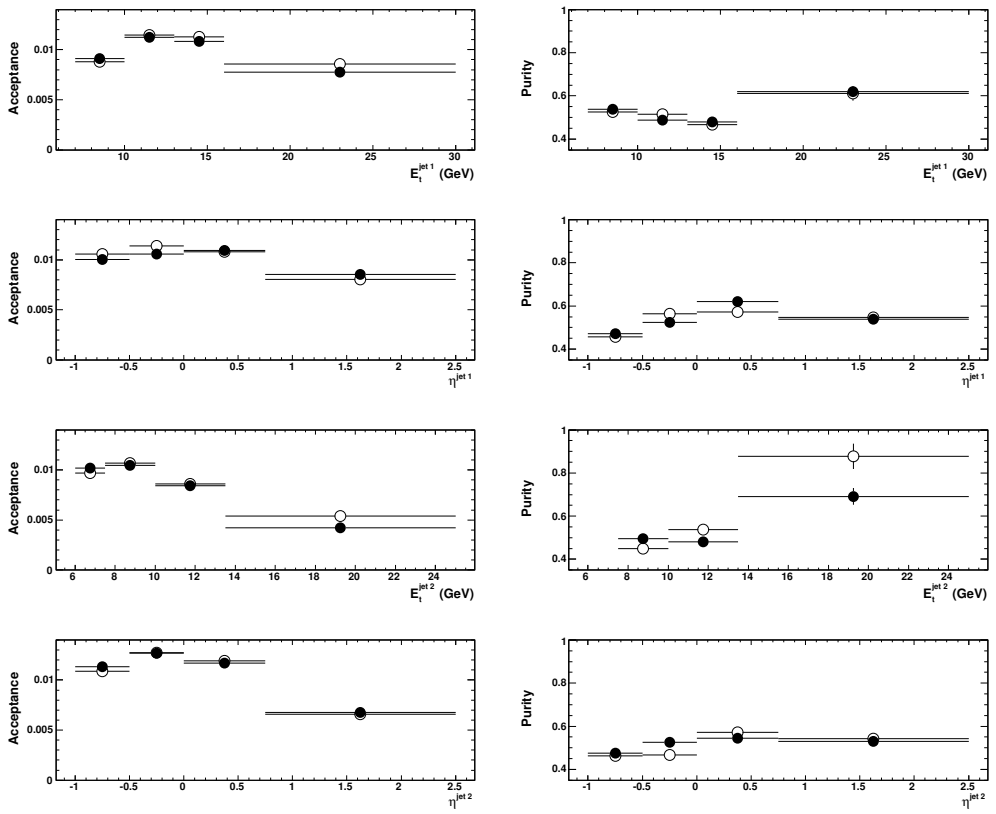

Figure B.6: Acceptances and purities in bins of the jet properties, η and E_t of the most energetic, the second most energetic and the electron jet in charm events, both for $\sqrt{s_{ep}} = 300\,\text{GeV}$ (hollow circles) and $\sqrt{s_{ep}} = 318\,\text{GeV}$ (solid circles).

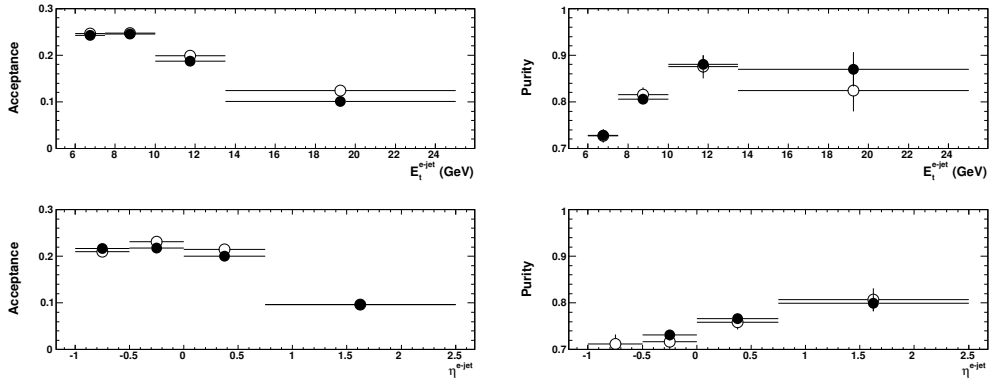

Figure B.7: Acceptances and purities in bins of the jet properties, η and E_t of the $e^{\pm}$–associated jets in charm events, both for $\sqrt{s_{ep}} = 300\,\text{GeV}$ (hollow circles) and $\sqrt{s_{ep}} = 318\,\text{GeV}$ (solid circles).

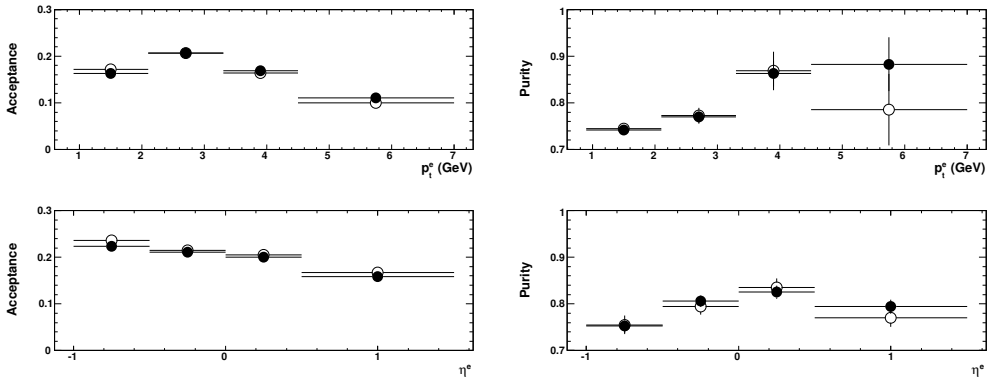

Figure B.8: Acceptances and purities in bins of the electron variables p_t^e and η^e in charm events, both for $\sqrt{s_{ep}} = 300\,\text{GeV}$ (hollow circles) and $\sqrt{s_{ep}} = 318\,\text{GeV}$ (solid circles).

Appendix C

Cross–Section Numbers

In the following tables the exact values of the cross–sections presented in Chapter 7 are collected. In addition to the numbers their statistical uncertainties are given as well as their upper and lower total systematic uncertainty. Details of the computation of the latter are explained in Sec. 7.3. In most cases the correlated parts of the systematic uncertainty, *i. e.* the uncertainty caused by the uncertainty of the luminosity measurement, $\Delta_{\mathcal{L}}\sigma$, and the jet energy scale, $\Delta_{E_t}\sigma$, are given as well. Acceptance uncertainties are negligible.

$\sqrt{s_{ep}} = 300$ GeV	$\frac{d\sigma_b}{dp_t^e}$ [pb/GeV]	$\Delta_{\mathcal{L}}(\frac{d\sigma_b}{dp_t^e})$ [pb/GeV]	$\Delta_{E_t}(\frac{d\sigma_b}{dp_t^e})$ [pb/GeV]
$0.9 \le p_t^e < 2.1$ GeV	$54 \pm 20^{+1}_{-2}$	± 1	$^{+0}_{--0}$
$2.1 \le p_t^e < 3.3$ GeV	$25 \pm 8^{+0}_{-1}$	± 0	$^{+0}_{--0}$
$3.3 \le p_t^e < 4.5$ GeV	$13 \pm 5^{+0}_{-0}$	± 0	$^{+0}_{--0}$
$4.5 \le p_t^e < 7.0$ GeV	$6 \pm 3^{+0}_{-0}$	± 0	$^{+0}_{--0}$
$\sqrt{s_{ep}} = 318$ GeV	$\frac{d\sigma_b}{dp_t^e}$ [pb/GeV]	$\Delta_{\mathcal{L}}(\frac{d\sigma_b}{dp_t^e})$ [pb/GeV]	$\Delta_{E_t}(\frac{d\sigma_b}{dp_t^e})$ [pb/GeV]
$0.9 \le p_t^e < 2.1$ GeV	$54 \pm 20^{+1}_{-5}$	± 1	$^{+1}_{-+1}$
$2.1 \le p_t^e < 3.3$ GeV	$25 \pm 8^{+1}_{-2}$	± 1	$^{+0}_{-+1}$
$3.3 \le p_t^e < 4.5$ GeV	$13 \pm 5^{+0}_{-1}$	± 0	$^{+0}_{-+0}$
$4.5 \le p_t^e < 7.0$ GeV	$6 \pm 3^{+0}_{-0}$	± 0	$^{+0}_{-+0}$
$\sqrt{s_{ep}} = 300$ GeV	$\frac{d\sigma_c}{dp_t^e}$ [pb/GeV]	$\Delta_{\mathcal{L}}(\frac{d\sigma_c}{dp_t^e})$ [pb/GeV]	$\Delta_{E_t}(\frac{d\sigma_c}{dp_t^e})$ [pb/GeV]
$0.9 \le p_t^e < 2.1$ GeV	$179 \pm 48^{+14}_{-43}$	± 3	$^{+14}_{-+7}$
$2.1 \le p_t^e < 3.3$ GeV	$83 \pm 22^{+7}_{-20}$	± 1	$^{+6}_{-+3}$
$3.3 \le p_t^e < 4.5$ GeV	$19 \pm 11^{+1}_{-4}$	± 0	$^{+1}_{-+1}$
$4.5 \le p_t^e < 7.0$ GeV	$2 \pm 5^{+0}_{-1}$	± 0	$^{+0}_{-+0}$
$\sqrt{s_{ep}} = 318$ GeV	$\frac{d\sigma_c}{dp_t^e}$ [pb/GeV]	$\Delta_{\mathcal{L}}(\frac{d\sigma_c}{dp_t^e})$ [pb/GeV]	$\Delta_{E_t}(\frac{d\sigma_c}{dp_t^e})$ [pb/GeV]
$0.9 \le p_t^e < 2.1$ GeV	$179 \pm 48^{+10}_{-51}$	± 4	$^{+9}_{-+11}$
$2.1 \le p_t^e < 3.3$ GeV	$83 \pm 22^{+5}_{-24}$	± 2	$^{+4}_{-+5}$
$3.3 \le p_t^e < 4.5$ GeV	$19 \pm 11^{+1}_{-5}$	± 0	$^{+1}_{-+1}$
$4.5 \le p_t^e < 7.0$ GeV	$2 \pm 5^{+0}_{-1}$	± 0	$^{+0}_{-+0}$

Table C.1: Single–differential cross–sections for the reactions $e^{\pm}p \to b\bar{b}+e'^{\pm}X$ and $e^{\pm}p \to c\bar{c}+e'^{\pm}X$ in terms of the transverse momentum, p_t^e, of the electron.

$\sqrt{s_{ep}} = 300$ GeV	$\frac{d\sigma_b}{d\eta^e}$ [pb]	$\Delta_{\mathcal{L}}(\frac{d\sigma_b}{d\eta^e})$ [pb]	$\Delta_{E_t}(\frac{d\sigma_b}{d\eta^e})$ [pb]
$-1.0 \le \eta^e < -0.5$	$22 \pm 14^{+0}_{-1}$	± 0	$^{+0}_{--0}$
$-0.5 \le \eta^e < 0.0$	$58 \pm 16^{+1}_{-2}$	± 1	$^{+0}_{--0}$
$0.0 \le \eta^e < 0.5$	$62 \pm 24^{+1}_{-2}$	± 1	$^{+0}_{--0}$
$0.5 \le \eta^e < 1.5$	$36 \pm 21^{+1}_{-1}$	± 1	$^{+0}_{--0}$
$\sqrt{s_{ep}} = 318$ GeV	$\frac{d\sigma_b}{d\eta^e}$ [pb]	$\Delta_{\mathcal{L}}(\frac{d\sigma_b}{d\eta^e})$ [pb]	$\Delta_{E_t}(\frac{d\sigma_b}{d\eta^e})$ [pb]
$-1.0 \le \eta^e < -0.5$	$22 \pm 14^{+1}_{-2}$	± 0	$^{+0}_{-1}$
$-0.5 \le \eta^e < 0.0$	$58 \pm 16^{+1}_{-5}$	± 1	$^{+1}_{-1}$
$0.0 \le \eta^e < 0.5$	$62 \pm 24^{+1}_{-5}$	± 1	$^{+1}_{-1}$
$0.5 \le \eta^e < 1.5$	$36 \pm 21^{+1}_{-3}$	± 1	$^{+1}_{-1}$
$\sqrt{s_{ep}} = 300$ GeV	$\frac{d\sigma_c}{d\eta^e}$ [pb]	$\Delta_{\mathcal{L}}(\frac{d\sigma_c}{d\eta^e})$ [pb]	$\Delta_{E_t}(\frac{d\sigma_c}{d\eta^e})$ [pb]
$-1.0 \le \eta^e < -0.5$	$112 \pm 36^{+9}_{-27}$	± 2	$^{+9}_{-5}$
$-0.5 \le \eta^e < 0.0$	$201 \pm 48^{+16}_{-48}$	± 4	$^{+15}_{-8}$
$0.0 \le \eta^e < 0.5$	$191 \pm 69^{+15}_{-46}$	± 3	$^{+15}_{-8}$
$0.5 \le \eta^e < 1.5$	$29 \pm 52^{+2}_{-7}$	± 1	$^{+2}_{-1}$
$\sqrt{s_{ep}} = 318$ GeV	$\frac{d\sigma_c}{d\eta^e}$ [pb]	$\Delta_{\mathcal{L}}(\frac{d\sigma_c}{d\eta^e})$ [pb]	$\Delta_{E_t}(\frac{d\sigma_c}{d\eta^e})$ [pb]
$-1.0 \le \eta^e < -0.5$	$112 \pm 36^{+6}_{-32}$	± 3	$^{+6}_{-7}$
$-0.5 \le \eta^e < 0.0$	$201 \pm 48^{+11}_{-58}$	± 5	$^{+10}_{-12}$
$0.0 \le \eta^e < 0.5$	$191 \pm 69^{+11}_{-55}$	± 4	$^{+10}_{-11}$
$0.5 \le \eta^e < 1.5$	$29 \pm 52^{+2}_{-8}$	± 1	$^{+1}_{-2}$

Table C.2: Single–differential cross–sections for the reactions $e^{\pm}p \to b\bar{b}+e'^{\pm}X$ and $e^{\pm}p \to c\bar{c}+e'^{\pm}X$ in terms of the pseudo–rapidity, η^e, of the electron.

$\sqrt{s_{ep}} = 300$ GeV	$\frac{d\sigma_b}{dE_t^{jet\,1}}$ [pb/GeV]	$\Delta_{\mathcal{L}}(\frac{d\sigma_b}{dE_t^{jet\,1}})$ [pb/GeV]	$\Delta_{E_t}(\frac{d\sigma_b}{dE_t^{jet\,1}})$ [pb/GeV]
$7.0 \le E_t^{jet\,1} < 10.0$ GeV	$138 \pm 35^{+2}_{-5}$	± 2	$^{+0}_{--0}$
$10.0 \le E_t^{jet\,1} < 13.0$ GeV	$72 \pm 24^{+1}_{-3}$	± 1	$^{+0}_{--0}$
$13.0 \le E_t^{jet\,1} < 16.0$ GeV	$42 \pm 17^{+1}_{-2}$	± 1	$^{+0}_{--0}$
$16.0 \le E_t^{jet\,1} < 30.0$ GeV	$2 \pm 3^{+0}_{-0}$	± 0	$^{+0}_{--0}$
$\sqrt{s_{ep}} = 318$ GeV	$\frac{d\sigma_b}{dE_t^{jet\,1}}$ [pb/GeV]	$\Delta_{\mathcal{L}}(\frac{d\sigma_b}{dE_t^{jet\,1}})$ [pb/GeV]	$\Delta_{E_t}(\frac{d\sigma_b}{dE_t^{jet\,1}})$ [pb/GeV]
$7.0 \le E_t^{jet\,1} < 10.0$ GeV	$138 \pm 35^{+3}_{-12}$	± 3	$^{+2}_{-3}$
$10.0 \le E_t^{jet\,1} < 13.0$ GeV	$72 \pm 24^{+2}_{-6}$	± 2	$^{+1}_{-2}$
$13.0 \le E_t^{jet\,1} < 16.0$ GeV	$42 \pm 17^{+1}_{-4}$	± 1	$^{+1}_{-1}$
$16.0 \le E_t^{jet\,1} < 30.0$ GeV	$2 \pm 3^{+0}_{-0}$	± 0	$^{+0}_{-0}$
$\sqrt{s_{ep}} = 300$ GeV	$\frac{d\sigma_c}{dE_t^{jet\,1}}$ [pb/GeV]	$\Delta_{\mathcal{L}}(\frac{d\sigma_c}{dE_t^{jet\,1}})$ [pb/GeV]	$\Delta_{E_t}(\frac{d\sigma_c}{dE_t^{jet\,1}})$ [pb/GeV]
$7.0 \le E_t^{jet\,1} < 10.0$ GeV	$1143 \pm 318^{+91}_{-274}$	± 21	$^{+88}_{-48}$
$10.0 \le E_t^{jet\,1} < 13.0$ GeV	$632 \pm 185^{+50}_{-151}$	± 11	$^{+49}_{-26}$
$13.0 \le E_t^{jet\,1} < 16.0$ GeV	$163 \pm 96^{+13}_{-39}$	± 3	$^{+13}_{-7}$
$16.0 \le E_t^{jet\,1} < 30.0$ GeV	$71 \pm 33^{+6}_{-17}$	± 1	$^{+5}_{-3}$
$\sqrt{s_{ep}} = 318$ GeV	$\frac{d\sigma_c}{dE_t^{jet\,1}}$ [pb/GeV]	$\Delta_{\mathcal{L}}(\frac{d\sigma_c}{dE_t^{jet\,1}})$ [pb/GeV]	$\Delta_{E_t}(\frac{d\sigma_c}{dE_t^{jet\,1}})$ [pb/GeV]
$7.0 \le E_t^{jet\,1} < 10.0$ GeV	$1143 \pm 318^{+64}_{-329}$	± 26	$^{+58}_{-69}$
$10.0 \le E_t^{jet\,1} < 13.0$ GeV	$632 \pm 185^{+35}_{-182}$	± 14	$^{+32}_{-38}$
$13.0 \le E_t^{jet\,1} < 16.0$ GeV	$163 \pm 96^{+9}_{-47}$	± 4	$^{+8}_{-10}$
$16.0 \le E_t^{jet\,1} < 30.0$ GeV	$71 \pm 33^{+4}_{-20}$	± 2	$^{+4}_{-4}$

Table C.3: Single–differential cross–sections for the reactions $e^{\pm}p \to b\bar{b}+e'^{\pm}X$ and $e^{\pm}p \to c\bar{c}+e'^{\pm}X$ in terms of the transverse energy, $E_t^{jet\,1}$, of the highest energetic jet.

$\sqrt{s_{ep}} = 300$ GeV	$\frac{d\sigma_b}{d\eta^{jet\,1}}$ [pb]	$\Delta_{\mathcal{L}}(\frac{d\sigma_b}{d\eta^{jet\,1}})$ [pb]	$\Delta_{E_t}(\frac{d\sigma_b}{d\eta^{jet\,1}})$ [pb]
$-1.0 \le \eta^{jet\,1} < -0.5$	$139 \pm 160^{+3}_{-5}$	± 3	$^{+0}_{-0}$
$-0.5 \le \eta^{jet\,1} < 0.0$	$420 \pm 119^{+8}_{-16}$	± 8	$^{+0}_{-1}$
$0.0 \le \eta^{jet\,1} < 0.8$	$255 \pm 112^{+5}_{-10}$	± 5	$^{+0}_{-0}$
$0.8 \le \eta^{jet\,1} < 2.5$	$177 \pm 57^{+3}_{-7}$	± 3	$^{+0}_{-0}$
$\sqrt{s_{ep}} = 318$ GeV	$\frac{d\sigma_b}{d\eta^{jet\,1}}$ [pb]	$\Delta_{\mathcal{L}}(\frac{d\sigma_b}{d\eta^{jet\,1}})$ [pb]	$\Delta_{E_t}(\frac{d\sigma_b}{d\eta^{jet\,1}})$ [pb]
$-1.0 \le \eta^{jet\,1} < -0.5$	$139 \pm 160^{+3}_{-12}$	± 3	$^{+2}_{-3}$
$-0.5 \le \eta^{jet\,1} < 0.0$	$420 \pm 119^{+10}_{-36}$	± 9	$^{+7}_{-10}$
$0.0 \le \eta^{jet\,1} < 0.8$	$255 \pm 112^{+6}_{-22}$	± 6	$^{+4}_{-6}$
$0.8 \le \eta^{jet\,1} < 2.5$	$177 \pm 57^{+4}_{-15}$	± 4	$^{+3}_{-4}$
$\sqrt{s_{ep}} = 300$ GeV	$\frac{d\sigma_c}{d\eta^{jet\,1}}$ [pb]	$\Delta_{\mathcal{L}}(\frac{d\sigma_c}{d\eta^{jet\,1}})$ [pb]	$\Delta_{E_t}(\frac{d\sigma_c}{d\eta^{jet\,1}})$ [pb]
$-1.0 \le \eta^{jet\,1} < -0.5$	$1916 \pm 1179^{+152}_{-459}$	± 34	$^{+147}_{-80}$
$-0.5 \le \eta^{jet\,1} < 0.0$	$2039 \pm 799^{+162}_{-488}$	± 37	$^{+157}_{-85}$
$0.0 \le \eta^{jet\,1} < 0.8$	$3446 \pm 853^{+273}_{-825}$	± 62	$^{+265}_{-144}$
$0.8 \le \eta^{jet\,1} < 2.5$	$917 \pm 533^{+73}_{-220}$	± 17	$^{+71}_{-38}$
$\sqrt{s_{ep}} = 318$ GeV	$\frac{d\sigma_c}{d\eta^{jet\,1}}$ [pb]	$\Delta_{\mathcal{L}}(\frac{d\sigma_c}{d\eta^{jet\,1}})$ [pb]	$\Delta_{E_t}(\frac{d\sigma_c}{d\eta^{jet\,1}})$ [pb]
$-1.0 \le \eta^{jet\,1} < -0.5$	$1916 \pm 1179^{+107}_{-551}$	± 43	$^{+97}_{-115}$
$-0.5 \le \eta^{jet\,1} < 0.0$	$2039 \pm 799^{+114}_{-586}$	± 46	$^{+103}_{-122}$
$0.0 \le \eta^{jet\,1} < 0.8$	$3446 \pm 853^{+193}_{-991}$	± 78	$^{+174}_{-207}$
$0.8 \le \eta^{jet\,1} < 2.5$	$917 \pm 533^{+51}_{-264}$	± 21	$^{+46}_{-55}$

Table C.4: Single–differential cross–sections for the reactions $e^{\pm}p \to b\bar{b}+e'^{\pm}X$ and $e^{\pm}p \to c\bar{c}+e'^{\pm}X$ in terms of the pseudo–rapidity, $\eta^{jet\,1}$, of the highest energetic jet.

$\sqrt{s_{ep}} = 300$ GeV	$\frac{d\sigma_b}{dE_t^{jet\,2}}$ [pb/GeV]	$\Delta_{\mathcal{L}}(\frac{d\sigma_b}{dE_t^{jet\,2}})$ [pb/GeV]	$\Delta_{E_t}(\frac{d\sigma_b}{dE_t^{jet\,2}})$ [pb/GeV]
$6.0 \le E_t^{jet\,2} < 7.5$ GeV	$218 \pm 58^{+4}_{-8}$	± 4	$^{+0}_{-0}$
$7.5 \le E_t^{jet\,2} < 10.0$ GeV	$111 \pm 32^{+2}_{-4}$	± 2	$^{+0}_{-0}$
$10.0 \le E_t^{jet\,2} < 13.5$ GeV	$33 \pm 16^{+1}_{-1}$	± 1	$^{+0}_{-0}$
$13.5 \le E_t^{jet\,2} < 25.0$ GeV	$0 \pm 4^{+0}_{-0}$	± 0	$^{+0}_{-0}$
$\sqrt{s_{ep}} = 318$ GeV	$\frac{d\sigma_b}{dE_t^{jet\,2}}$ [pb/GeV]	$\Delta_{\mathcal{L}}(\frac{d\sigma_b}{dE_t^{jet\,2}})$ [pb/GeV]	$\Delta_{E_t}(\frac{d\sigma_b}{dE_t^{jet\,2}})$ [pb/GeV]
$6.0 \le E_t^{jet\,2} < 7.5$ GeV	$218 \pm 58^{+5}_{-18}$	± 5	$^{+4}_{-5}$
$7.5 \le E_t^{jet\,2} < 10.0$ GeV	$111 \pm 32^{+3}_{-9}$	± 2	$^{+2}_{-3}$
$10.0 \le E_t^{jet\,2} < 13.5$ GeV	$33 \pm 16^{+1}_{-3}$	± 1	$^{+1}_{-1}$
$13.5 \le E_t^{jet\,2} < 25.0$ GeV	$0 \pm 4^{+0}_{-0}$	± 0	$^{+0}_{-0}$
$\sqrt{s_{ep}} = 300$ GeV	$\frac{d\sigma_c}{dE_t^{jet\,2}}$ [pb/GeV]	$\Delta_{\mathcal{L}}(\frac{d\sigma_c}{dE_t^{jet\,2}})$ [pb/GeV]	$\Delta_{E_t}(\frac{d\sigma_c}{dE_t^{jet\,2}})$ [pb/GeV]
$6.0 \le E_t^{jet\,2} < 7.5$ GeV	$1353 \pm 552^{+107}_{-324}$	± 24	$^{+104}_{-57}$
$7.5 \le E_t^{jet\,2} < 10.0$ GeV	$1062 \pm 240^{+84}_{-254}$	± 19	$^{+82}_{-45}$
$10.0 \le E_t^{jet\,2} < 13.5$ GeV	$320 \pm 117^{+25}_{-77}$	± 6	$^{+25}_{-13}$
$13.5 \le E_t^{jet\,2} < 25.0$ GeV	$62 \pm 24^{+5}_{-15}$	± 1	$^{+5}_{-3}$
$\sqrt{s_{ep}} = 318$ GeV	$\frac{d\sigma_c}{dE_t^{jet\,2}}$ [pb/GeV]	$\Delta_{\mathcal{L}}(\frac{d\sigma_c}{dE_t^{jet\,2}})$ [pb/GeV]	$\Delta_{E_t}(\frac{d\sigma_c}{dE_t^{jet\,2}})$ [pb/GeV]
$6.0 \le E_t^{jet\,2} < 7.5$ GeV	$1353 \pm 552^{+76}_{-389}$	± 30	$^{+68}_{-81}$
$7.5 \le E_t^{jet\,2} < 10.0$ GeV	$1062 \pm 240^{+59}_{-305}$	± 24	$^{+54}_{-64}$
$10.0 \le E_t^{jet\,2} < 13.5$ GeV	$320 \pm 117^{+18}_{-92}$	± 7	$^{+16}_{-19}$
$13.5 \le E_t^{jet\,2} < 25.0$ GeV	$62 \pm 24^{+3}_{-18}$	± 1	$^{+3}_{-4}$

Table C.5: Single–differential cross–sections for the reactions $e^{\pm}p \to b\bar{b}+e'^{\pm}X$ and $e^{\pm}p \to c\bar{c}+e'^{\pm}X$ in terms of the transverse energy, $E_t^{jet\,2}$, of the second highest energetic jet.

$\sqrt{s_{ep}} = 300\,\text{GeV}$	$\frac{d\sigma_b}{d\eta^{jet\,2}}$ [pb]	$\Delta_{\mathcal{L}}(\frac{d\sigma_b}{d\eta^{jet\,2}})$ [pb]	$\Delta_{E_t}(\frac{d\sigma_b}{d\eta^{jet\,2}})$ [pb]
$-1.0 \le \eta^{jet\,2} < -0.5$	$299 \pm 98^{+5}_{-11}$	± 5	$^{+0}_{-0}$
$-0.5 \le \eta^{jet\,2} < 0.0$	$206 \pm 92^{+4}_{-8}$	± 4	$^{+0}_{-0}$
$0.0 \le \eta^{jet\,2} < 0.8$	$284 \pm 100^{+5}_{-11}$	± 5	$^{+0}_{-0}$
$0.8 \le \eta^{jet\,2} < 2.5$	$189 \pm 85^{+3}_{-7}$	± 3	$^{+0}_{-0}$
$\sqrt{s_{ep}} = 318\,\text{GeV}$	$\frac{d\sigma_b}{d\eta^{jet\,2}}$ [pb]	$\Delta_{\mathcal{L}}(\frac{d\sigma_b}{d\eta^{jet\,2}})$ [pb]	$\Delta_{E_t}(\frac{d\sigma_b}{d\eta^{jet\,2}})$ [pb]
$-1.0 \le \eta^{jet\,2} < -0.5$	$299 \pm 98^{+7}_{-25}$	± 7	$^{+5}_{-7}$
$-0.5 \le \eta^{jet\,2} < 0.0$	$206 \pm 92^{+5}_{-17}$	± 5	$^{+4}_{-5}$
$0.0 \le \eta^{jet\,2} < 0.8$	$284 \pm 100^{+7}_{-24}$	± 6	$^{+5}_{-7}$
$0.8 \le \eta^{jet\,2} < 2.5$	$189 \pm 85^{+4}_{-16}$	± 4	$^{+3}_{-5}$
$\sqrt{s_{ep}} = 300\,\text{GeV}$	$\frac{d\sigma_c}{d\eta^{jet\,2}}$ [pb]	$\Delta_{\mathcal{L}}(\frac{d\sigma_c}{d\eta^{jet\,2}})$ [pb]	$\Delta_{E_t}(\frac{d\sigma_c}{d\eta^{jet\,2}})$ [pb]
$-1.0 \le \eta^{jet\,2} < -0.5$	$1910 \pm 737^{+151}_{-458}$	± 34	$^{+147}_{-80}$
$-0.5 \le \eta^{jet\,2} < 0.0$	$1765 \pm 722^{+140}_{-423}$	± 32	$^{+136}_{-74}$
$0.0 \le \eta^{jet\,2} < 0.8$	$2196 \pm 822^{+174}_{-526}$	± 40	$^{+169}_{-92}$
$0.8 \le \eta^{jet\,2} < 2.5$	$2131 \pm 643^{+169}_{-510}$	± 38	$^{+164}_{-89}$
$\sqrt{s_{ep}} = 318\,\text{GeV}$	$\frac{d\sigma_c}{d\eta^{jet\,2}}$ [pb]	$\Delta_{\mathcal{L}}(\frac{d\sigma_c}{d\eta^{jet\,2}})$ [pb]	$\Delta_{E_t}(\frac{d\sigma_c}{d\eta^{jet\,2}})$ [pb]
$-1.0 \le \eta^{jet\,2} < -0.5$	$1910 \pm 737^{+107}_{-549}$	± 43	$^{+96}_{-115}$
$-0.5 \le \eta^{jet\,2} < 0.0$	$1765 \pm 722^{+99}_{-507}$	± 40	$^{+89}_{-106}$
$0.0 \le \eta^{jet\,2} < 0.8$	$2196 \pm 822^{+123}_{-631}$	± 49	$^{+111}_{-132}$
$0.8 \le \eta^{jet\,2} < 2.5$	$2131 \pm 643^{+119}_{-612}$	± 48	$^{+108}_{-128}$

Table C.6: Single–differential cross–sections for the reactions $e^{\pm}p \to b\bar{b}+e'^{\pm}X$ and $e^{\pm}p \to c\bar{c}+e'^{\pm}X$ in terms of the pseudo–rapidity, $\eta^{jet\,2}$, of the second highest energetic jet.

$\sqrt{s_{ep}} = 300\,\text{GeV}$	$\frac{d\sigma_b}{dE_t^{e-jet}}$ [pb/GeV]	$\Delta_{\mathcal{L}}(\frac{d\sigma_b}{dE_t^{e-jet}})$ [pb/GeV]	$\Delta_{E_t}(\frac{d\sigma_b}{dE_t^{e-jet}})$ [pb/GeV]
$6.0 \le E_t^{e-jet} < 7.5\,\text{GeV}$	$21 \pm 8^{+0}_{-1}$	± 0	$^{+0}_{-0}$
$7.5 \le E_t^{e-jet} < 10.0\,\text{GeV}$	$13 \pm 4^{+0}_{-1}$	± 0	$^{+0}_{-0}$
$10.0 \le E_t^{e-jet} < 13.5\,\text{GeV}$	$8 \pm 3^{+0}_{-0}$	± 0	$^{+0}_{-0}$
$13.5 \le E_t^{e-jet} < 25.0\,\text{GeV}$	$2 \pm 1^{+0}_{-0}$	± 0	$^{+0}_{-0}$
$\sqrt{s_{ep}} = 318\,\text{GeV}$	$\frac{d\sigma_b}{dE_t^{e-jet}}$ [pb/GeV]	$\Delta_{\mathcal{L}}(\frac{d\sigma_b}{dE_t^{e-jet}})$ [pb/GeV]	$\Delta_{E_t}(\frac{d\sigma_b}{dE_t^{e-jet}})$ [pb/GeV]
$6.0 \le E_t^{e-jet} < 7.5\,\text{GeV}$	$21 \pm 8^{+0}_{-2}$	± 0	$^{+0}_{-1}$
$7.5 \le E_t^{e-jet} < 10.0\,\text{GeV}$	$13 \pm 4^{+0}_{-1}$	± 0	$^{+0}_{-0}$
$10.0 \le E_t^{e-jet} < 13.5\,\text{GeV}$	$8 \pm 3^{+0}_{-1}$	± 0	$^{+0}_{-0}$
$13.5 \le E_t^{e-jet} < 25.0\,\text{GeV}$	$2 \pm 1^{+0}_{-0}$	± 0	$^{+0}_{-0}$
$\sqrt{s_{ep}} = 300\,\text{GeV}$	$\frac{d\sigma_c}{dE_t^{e-jet}}$ [pb/GeV]	$\Delta_{\mathcal{L}}(\frac{d\sigma_c}{dE_t^{e-jet}})$ [pb/GeV]	$\Delta_{E_t}(\frac{d\sigma_c}{dE_t^{e-jet}})$ [pb/GeV]
$6.0 \le E_t^{e-jet} < 7.5\,\text{GeV}$	$45 \pm 17^{+4}_{-11}$	± 1	$^{+3}_{-2}$
$7.5 \le E_t^{e-jet} < 10.0\,\text{GeV}$	$40 \pm 11^{+3}_{-9}$	± 1	$^{+3}_{-2}$
$10.0 \le E_t^{e-jet} < 13.5\,\text{GeV}$	$15 \pm 8^{+1}_{-3}$	± 0	$^{+1}_{-1}$
$13.5 \le E_t^{e-jet} < 25.0\,\text{GeV}$	$1 \pm 2^{+0}_{-0}$	± 0	$^{+0}_{-0}$
$\sqrt{s_{ep}} = 318\,\text{GeV}$	$\frac{d\sigma_c}{dE_t^{e-jet}}$ [pb/GeV]	$\Delta_{\mathcal{L}}(\frac{d\sigma_c}{dE_t^{e-jet}})$ [pb/GeV]	$\Delta_{E_t}(\frac{d\sigma_c}{dE_t^{e-jet}})$ [pb/GeV]
$6.0 \le E_t^{e-jet} < 7.5\,\text{GeV}$	$45 \pm 17^{+3}_{-13}$	± 1	$^{+2}_{-3}$
$7.5 \le E_t^{e-jet} < 10.0\,\text{GeV}$	$40 \pm 11^{+2}_{-11}$	± 1	$^{+2}_{-2}$
$10.0 \le E_t^{e-jet} < 13.5\,\text{GeV}$	$15 \pm 8^{+1}_{-4}$	± 0	$^{+1}_{-1}$
$13.5 \le E_t^{e-jet} < 25.0\,\text{GeV}$	$1 \pm 2^{+0}_{-0}$	± 0	$^{+0}_{-0}$

Table C.7: Single–differential cross–sections for the reactions $e^{\pm}p \to b\bar{b}+e'^{\pm}X$ and $e^{\pm}p \to c\bar{c}+e'^{\pm}X$ in terms of the transverse energy, E_t^{e-jet}, of the electron associated jet.

$\sqrt{s_{ep}} = 300$ GeV	$\frac{d\sigma_b}{d\eta^{e-jet}}$ [pb]	$\Delta_{\mathcal{L}}(\frac{d\sigma_b}{d\eta^{e-jet}})$ [pb]	$\Delta_{E_t}(\frac{d\sigma_b}{d\eta^{e-jet}})$ [pb]
$-1.0 \le \eta^{e-jet} < -0.5$	$25 \pm 10^{+0}_{-1}$	± 0	$^{+0}_{-0}$
$-0.5 \le \eta^{e-jet} < 0.0$	$48 \pm 15^{+1}_{-2}$	± 1	$^{+0}_{-0}$
$0.0 \le \eta^{e-jet} < 0.8$	$37 \pm 22^{+1}_{-1}$	± 1	$^{+0}_{-0}$
$0.8 \le \eta^{e-jet} < 2.5$	$51 \pm 24^{+1}_{-2}$	± 1	$^{+0}_{-0}$
$\sqrt{s_{ep}} = 318$ GeV	$\frac{d\sigma_b}{d\eta^{e-jet}}$ [pb]	$\Delta_{\mathcal{L}}(\frac{d\sigma_b}{d\eta^{e-jet}})$ [pb]	$\Delta_{E_t}(\frac{d\sigma_b}{d\eta^{e-jet}})$ [pb]
$-1.0 \le \eta^{e-jet} < -0.5$	$25 \pm 10^{+1}_{-2}$	± 1	$^{+0}_{-1}$
$-0.5 \le \eta^{e-jet} < 0.0$	$48 \pm 15^{+1}_{-4}$	± 1	$^{+1}_{-1}$
$0.0 \le \eta^{e-jet} < 0.8$	$37 \pm 22^{+1}_{-3}$	± 1	$^{+1}_{-1}$
$0.8 \le \eta^{e-jet} < 2.5$	$51 \pm 24^{+1}_{-4}$	± 1	$^{+1}_{-1}$
$\sqrt{s_{ep}} = 300$ GeV	$\frac{d\sigma_c}{d\eta^{e-jet}}$ [pb]	$\Delta_{\mathcal{L}}(\frac{d\sigma_c}{d\eta^{e-jet}})$ [pb]	$\Delta_{E_t}(\frac{d\sigma_c}{d\eta^{e-jet}})$ [pb]
$-1.0 \le \eta^{e-jet} < -0.5$	$126 \pm 39^{+10}_{-30}$	± 2	$^{+10}_{-5}$
$-0.5 \le \eta^{e-jet} < 0.0$	$135 \pm 40^{+11}_{-32}$	± 2	$^{+10}_{-6}$
$0.0 \le \eta^{e-jet} < 0.8$	$196 \pm 58^{+16}_{-47}$	± 4	$^{+15}_{-8}$
$0.8 \le \eta^{e-jet} < 2.5$	$25 \pm 51^{+2}_{-6}$	± 0	$^{+2}_{-1}$
$\sqrt{s_{ep}} = 318$ GeV	$\frac{d\sigma_c}{d\eta^{e-jet}}$ [pb]	$\Delta_{\mathcal{L}}(\frac{d\sigma_c}{d\eta^{e-jet}})$ [pb]	$\Delta_{E_t}(\frac{d\sigma_c}{d\eta^{e-jet}})$ [pb]
$-1.0 \le \eta^{e-jet} < -0.5$	$126 \pm 39^{+7}_{-36}$	± 3	$^{+6}_{-8}$
$-0.5 \le \eta^{e-jet} < 0.0$	$135 \pm 40^{+8}_{-39}$	± 3	$^{+7}_{-8}$
$0.0 \le \eta^{e-jet} < 0.8$	$196 \pm 58^{+11}_{-56}$	± 4	$^{+10}_{-12}$
$0.8 \le \eta^{e-jet} < 2.5$	$25 \pm 51^{+1}_{-7}$	± 1	$^{+1}_{-1}$

Table C.8: Single–differential cross–sections for the reactions $e^{\pm}p \to b\bar{b}+e'^{\pm}X$ and $e^{\pm}p \to c\bar{c}+e'^{\pm}X$ in terms of the pseudo–rapidity, η^{e-jet}, of the electron associated jet.

$\sqrt{s_{ep}} = 300$ GeV	$\frac{d\sigma_b}{dx_\gamma}$ [pb]	$\Delta_{\mathcal{L}}(\frac{d\sigma_b}{dx_\gamma})$ [pb]	$\Delta_{E_t}(\frac{d\sigma_b}{dx_\gamma})$ [pb]
$0.0 \le x_\gamma < 0.5$	$416 \pm 211^{+8}_{-16}$	± 7	$^{+0}_{-1}$
$0.5 \le x_\gamma < 0.8$	$869 \pm 336^{+16}_{-33}$	± 16	$^{+0}_{-1}$
$0.8 \le x_\gamma < 0.9$	$2422 \pm 593^{+44}_{-93}$	± 44	$^{+0}_{-4}$
$0.9 \le x_\gamma < 1.0$	$632 \pm 242^{+11}_{-24}$	± 11	$^{+0}_{-1}$
$\sqrt{s_{ep}} = 318$ GeV	$\frac{d\sigma_b}{dx_\gamma}$ [pb]	$\Delta_{\mathcal{L}}(\frac{d\sigma_b}{dx_\gamma})$ [pb]	$\Delta_{E_t}(\frac{d\sigma_b}{dx_\gamma})$ [pb]
$0.0 \le x_\gamma < 0.5$	$416 \pm 211^{+10}_{-35}$	± 9	$^{+7}_{-10}$
$0.5 \le x_\gamma < 0.8$	$869 \pm 336^{+20}_{-74}$	± 20	$^{+15}_{-21}$
$0.8 \le x_\gamma < 0.9$	$2422 \pm 593^{+57}_{-205}$	± 55	$^{+42}_{-58}$
$0.9 \le x_\gamma < 1.0$	$632 \pm 242^{+15}_{-54}$	± 14	$^{+11}_{-15}$
$\sqrt{s_{ep}} = 300$ GeV	$\frac{d\sigma_b}{dx_\gamma}$ [pb]	$\Delta_{\mathcal{L}}(\frac{d\sigma_b}{dx_\gamma})$ [pb]	$\Delta_{E_t}(\frac{d\sigma_b}{dx_\gamma})$ [pb]
$0.0 \le x_\gamma < 0.5$	$2091 \pm 2129^{+166}_{-501}$	± 38	$^{+161}_{-88}$
$0.5 \le x_\gamma < 0.8$	$9947 \pm 2438^{+788}_{-2383}$	± 179	$^{+766}_{-417}$
$0.8 \le x_\gamma < 0.9$	$10547 \pm 4289^{+836}_{-2527}$	± 190	$^{+812}_{-442}$
$0.9 \le x_\gamma < 1.0$	$11278 \pm 2547^{+894}_{-2702}$	± 203	$^{+868}_{-473}$
$\sqrt{s_{ep}} = 318$ GeV	$\frac{d\sigma_b}{dx_\gamma}$ [pb]	$\Delta_{\mathcal{L}}(\frac{d\sigma_b}{dx_\gamma})$ [pb]	$\Delta_{E_t}(\frac{d\sigma_b}{dx_\gamma})$ [pb]
$0.0 \le x_\gamma < 0.5$	$2091 \pm 2129^{+117}_{-601}$	± 47	$^{+106}_{-125}$
$0.5 \le x_\gamma < 0.8$	$9947 \pm 2438^{+556}_{-2859}$	± 224	$^{+502}_{-597}$
$0.8 \le x_\gamma < 0.9$	$10547 \pm 4289^{+590}_{-3032}$	± 237	$^{+532}_{-633}$
$0.9 \le x_\gamma < 1.0$	$11278 \pm 2547^{+630}_{-3242}$	± 254	$^{+569}_{-676}$

Table C.9: Single–differential cross–sections for the reactions $e^{\pm}p \to b\bar{b}+e'^{\pm}X$ and $e^{\pm}p \to c\bar{c}+e'^{\pm}X$ in terms of x_γ.

$\sqrt{s_{ep}} = 300$ GeV	$\frac{d\sigma_b}{d\log x_p}$ [pb]	$\Delta_{\mathcal{L}}(\frac{d\sigma_b}{d\log x_p})$ [pb]	$\Delta_{E_t}(\frac{d\sigma_b}{d\log x_p})$ [pb]
$-2.5 \le \log x_p < -1.9$	$329 \pm 89^{+6}_{-13}$	± 6	$^{+0}_{-1}$
$-1.9 \le \log x_p < -1.5$	$818 \pm 225^{+15}_{-31}$	± 15	$^{+0}_{-1}$
$-1.5 \le \log x_p < -1.1$	$491 \pm 269^{+9}_{-19}$	± 9	$^{+0}_{-1}$
$-1.1 \le \log x_p < -0.5$	$301 \pm 147^{+5}_{-12}$	± 5	$^{+0}_{-0}$
$\sqrt{s_{ep}} = 318$ GeV	$\frac{d\sigma_b}{d\log x_p}$ [pb]	$\Delta_{\mathcal{L}}(\frac{d\sigma_b}{d\log x_p})$ [pb]	$\Delta_{E_t}(\frac{d\sigma_b}{d\log x_p})$ [pb]
$-2.5 \le \log x_p < -1.9$	$329 \pm 89^{+8}_{-28}$	± 7	$^{+6}_{-8}$
$-1.9 \le \log x_p < -1.5$	$818 \pm 225^{+19}_{-69}$	± 18	$^{+14}_{-20}$
$-1.5 \le \log x_p < -1.1$	$491 \pm 269^{+11}_{-42}$	± 11	$^{+8}_{-12}$
$-1.1 \le \log x_p < -0.5$	$301 \pm 147^{+7}_{-26}$	± 7	$^{+5}_{-7}$
$\sqrt{s_{ep}} = 300$ GeV	$\frac{d\sigma_b}{d\log x_p}$ [pb]	$\Delta_{\mathcal{L}}(\frac{d\sigma_b}{d\log x_p})$ [pb]	$\Delta_{E_t}(\frac{d\sigma_b}{d\log x_p})$ [pb]
$-2.5 \le \log x_p < -1.9$	$1048 \pm 621^{+83}_{-251}$	± 19	$^{+81}_{-44}$
$-1.9 \le \log x_p < -1.5$	$8333 \pm 1930^{+660}_{-1996}$	± 150	$^{+641}_{-349}$
$-1.5 \le \log x_p < -1.1$	$5183 \pm 2796^{+411}_{-1242}$	± 93	$^{+399}_{-217}$
$-1.1 \le \log x_p < -0.5$	$789 \pm 945^{+63}_{-189}$	± 14	$^{+61}_{-33}$
$\sqrt{s_{ep}} = 318$ GeV	$\frac{d\sigma_b}{d\log x_p}$ [pb]	$\Delta_{\mathcal{L}}(\frac{d\sigma_b}{d\log x_p})$ [pb]	$\Delta_{E_t}(\frac{d\sigma_b}{d\log x_p})$ [pb]
$-2.5 \le \log x_p < -1.9$	$1048 \pm 621^{+59}_{-301}$	± 24	$^{+53}_{-63}$
$-1.9 \le \log x_p < -1.5$	$8333 \pm 1930^{+466}_{-2395}$	± 187	$^{+421}_{-500}$
$-1.5 \le \log x_p < -1.1$	$5183 \pm 2796^{+290}_{-1490}$	± 117	$^{+262}_{-311}$
$-1.1 \le \log x_p < -0.5$	$789 \pm 945^{+44}_{-227}$	± 18	$^{+40}_{-47}$

Table C.10: Single–differential cross–sections for the reactions $e^{\pm}p \to b\bar{b}+e'^{\pm}X$ and $e^{\pm}p \to c\bar{c}+e'^{\pm}X$ in terms of x_p.

$\sqrt{s_{ep}} = 300$ GeV	$\frac{d\sigma_b}{dy}$ [pb]	$\Delta_{\mathcal{L}}(\frac{d\sigma_b}{dy})$ [pb]	$\Delta_{E_t}(\frac{d\sigma_b}{dy})$ [pb]
$0.2 \le y < 0.3$	$2048 \pm 522^{+37}_{-79}$	± 37	$^{+0}_{-3}$
$0.3 \le y < 0.4$	$2143 \pm 849^{+39}_{-82}$	± 39	$^{+0}_{-3}$
$0.4 \le y < 0.6$	$1190 \pm 437^{+21}_{-46}$	± 21	$^{+0}_{-2}$
$0.6 \le y < 0.8$	$914 \pm 431^{+16}_{-35}$	± 16	$^{+0}_{-1}$
$\sqrt{s_{ep}} = 318$ GeV	$\frac{d\sigma_b}{dy}$ [pb]	$\Delta_{\mathcal{L}}(\frac{d\sigma_b}{dy})$ [pb]	$\Delta_{E_t}(\frac{d\sigma_b}{dy})$ [pb]
$0.2 \le y < 0.3$	$2048 \pm 522^{+48}_{-173}$	± 46	$^{+35}_{-49}$
$0.3 \le y < 0.4$	$2143 \pm 849^{+50}_{-181}$	± 48	$^{+37}_{-51}$
$0.4 \le y < 0.6$	$1190 \pm 437^{+28}_{-101}$	± 27	$^{+21}_{-28}$
$0.6 \le y < 0.8$	$914 \pm 431^{+21}_{-77}$	± 21	$^{+16}_{-22}$
$\sqrt{s_{ep}} = 300$ GeV	$\frac{d\sigma_b}{dy}$ [pb]	$\Delta_{\mathcal{L}}(\frac{d\sigma_b}{dy})$ [pb]	$\Delta_{E_t}(\frac{d\sigma_b}{dy})$ [pb]
$0.2 \le y < 0.3$	$16993 \pm 5218^{+1347}_{-4071}$	± 306	$^{+1308}_{-712}$
$0.3 \le y < 0.4$	$10915 \pm 5836^{+865}_{-2615}$	± 196	$^{+840}_{-458}$
$0.4 \le y < 0.6$	$6586 \pm 3411^{+522}_{-1578}$	± 119	$^{+507}_{-276}$
$0.6 \le y < 0.8$	$12382 \pm 3633^{+981}_{-2966}$	± 223	$^{+953}_{-519}$
$\sqrt{s_{ep}} = 318$ GeV	$\frac{d\sigma_b}{dy}$ [pb]	$\Delta_{\mathcal{L}}(\frac{d\sigma_b}{dy})$ [pb]	$\Delta_{E_t}(\frac{d\sigma_b}{dy})$ [pb]
$0.2 \le y < 0.3$	$16993 \pm 5218^{+950}_{-4885}$	± 382	$^{+858}_{-1019}$
$0.3 \le y < 0.4$	$10915 \pm 5836^{+610}_{-3138}$	± 246	$^{+551}_{-655}$
$0.4 \le y < 0.6$	$6586 \pm 3411^{+368}_{-1893}$	± 148	$^{+332}_{-395}$
$0.6 \le y < 0.8$	$12382 \pm 3633^{+692}_{-3559}$	± 279	$^{+625}_{-743}$

Table C.11: Single–differential cross–sections for the reactions $e^{\pm}p \to b\bar{b}+e'^{\pm}X$ and $e^{\pm}p \to c\bar{c}+e'^{\pm}X$ in terms of y.

$\sqrt{s_{ep}} = 300\,\text{GeV}$	$\frac{d\sigma_b}{dN_{jet}}$ [pb]	$\Delta_{\mathcal{L}}(\frac{d\sigma_b}{dN_{jet}})$ [pb]	$\Delta_{E_t}(\frac{d\sigma_b}{dN_{jet}})$ [pb]
$N_{jet} = 2$	$18.0 \pm 3.6^{+0.3}_{-0.7}$	± 0.3	$^{+0.0}_{--0.0}$
$N_{jet} = 3$	$7.7 \pm 3.0^{+0.1}_{-0.3}$	± 0.1	$^{+0.0}_{--0.0}$
$N_{jet} = 4$	$2.7 \pm 2.2^{+0.0}_{-0.1}$	± 0.0	$^{+0.0}_{--0.0}$
$N_{jet} = 5$	$0.1 \pm 2.7^{+0.0}_{-0.0}$	± 0.0	$^{+0.0}_{--0.0}$
$\sqrt{s_{ep}} = 318\,\text{GeV}$	$\frac{d\sigma_b}{dN_{jet}}$ [pb]	$\Delta_{\mathcal{L}}(\frac{d\sigma_b}{dN_{jet}})$ [pb]	$\Delta_{E_t}(\frac{d\sigma_b}{dN_{jet}})$ [pb]
$N_{jet} = 2$	$18.0 \pm 3.6^{+0.4}_{-1.5}$	± 0.4	$^{+0.3}_{-0.4}$
$N_{jet} = 3$	$7.7 \pm 3.0^{+0.2}_{-0.7}$	± 0.2	$^{+0.1}_{-0.2}$
$N_{jet} = 4$	$2.7 \pm 2.2^{+0.1}_{-0.2}$	± 0.1	$^{+0.0}_{-0.1}$
$N_{jet} = 5$	$0.1 \pm 2.7^{+0.0}_{-0.0}$	± 0.0	$^{+0.0}_{-0.0}$
$\sqrt{s_{ep}} = 300\,\text{GeV}$	$\frac{d\sigma_b}{dN_{jet}}$ [pb]	$\Delta_{\mathcal{L}}(\frac{d\sigma_b}{dN_{jet}})$ [pb]	$\Delta_{E_t}(\frac{d\sigma_b}{dN_{jet}})$ [pb]
$N_{jet} = 2$	$50.3 \pm 8.5^{+4.0}_{-12.0}$	± 0.9	$^{+3.9}_{-2.1}$
$N_{jet} = 3$	$11.5 \pm 6.8^{+0.9}_{-2.8}$	± 0.2	$^{+0.9}_{-0.5}$
$N_{jet} = 4$	$0.0 \pm 2.0^{+0.0}_{-0.0}$	± 0.0	$^{+0.0}_{-0.0}$
$N_{jet} = 5$	$0.0 \pm 1.1^{+0.0}_{-0.0}$	± 0.0	$^{+0.0}_{-0.0}$
$\sqrt{s_{ep}} = 318\,\text{GeV}$	$\frac{d\sigma_b}{dN_{jet}}$ [pb]	$\Delta_{\mathcal{L}}(\frac{d\sigma_b}{dN_{jet}})$ [pb]	$\Delta_{E_t}(\frac{d\sigma_b}{dN_{jet}})$ [pb]
$N_{jet} = 2$	$50.3 \pm 8.5^{+2.8}_{-14.5}$	± 1.1	$^{+2.5}_{-3.0}$
$N_{jet} = 3$	$11.5 \pm 6.8^{+0.8}_{-3.3}$	± 0.3	$^{+0.6}_{-0.7}$
$N_{jet} = 4$	$0.0 \pm 2.0^{+0.0}_{-0.0}$	± 0.0	$^{+0.0}_{-0.0}$
$N_{jet} = 5$	$0.0 \pm 1.1^{+0.0}_{-0.0}$	± 0.0	$^{+0.0}_{-0.0}$

Table C.12: Single–differential cross–sections for the reactions $e^{\pm}p \to b\bar{b}+e'^{\pm}X$ and $e^{\pm}p \to c\bar{c}+e'^{\pm}X$ in terms of the number of jets per event, N_{jet}.

Appendix D

Cross–Section Figures

D.1 Beauty Production

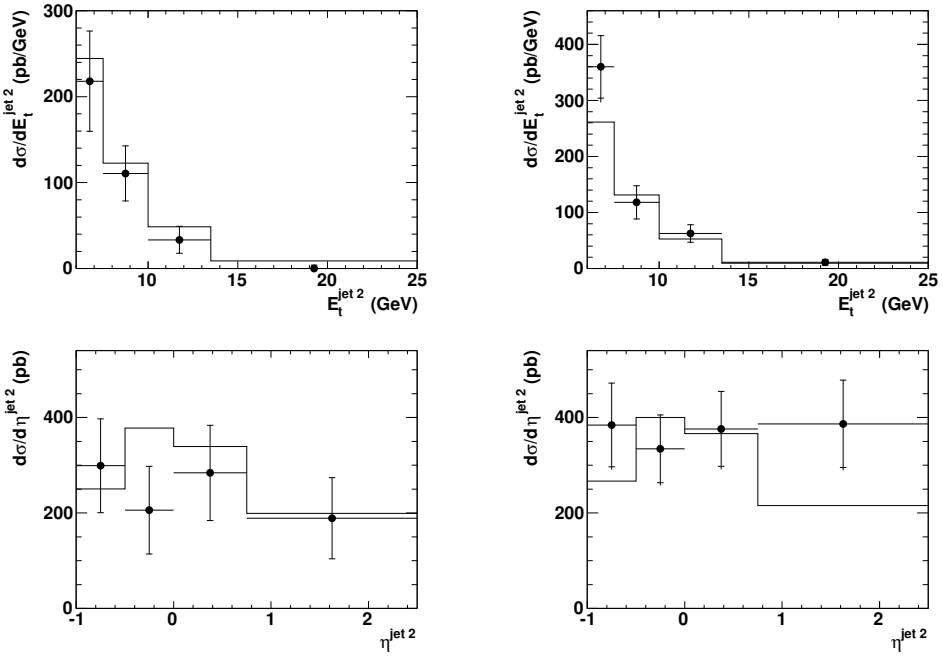

(a) $\sqrt{s_{\mathrm{ep}}} = 300\,\mathrm{GeV}$ (b) $\sqrt{s_{\mathrm{ep}}} = 318\,\mathrm{GeV}$

Figure D.1: Cross–section dependence for beauty production as a function of the transverse energy, $E_{\mathrm{t}}^{\mathrm{jet}\,2}$, and the pseudo–rapidity, $\eta^{\mathrm{jet}\,2}$, of the second most energetic jet in each event for centre–of–mass energies, $\sqrt{s_{\mathrm{ep}}} = 300\,\mathrm{GeV}$ (a) and $\sqrt{s_{\mathrm{ep}}} = 318\,\mathrm{GeV}$ (b). The measured cross–sections are depicted by the black dots, while the histograms represent the PYTHIA prediction, scaled by a factor of 1.75.

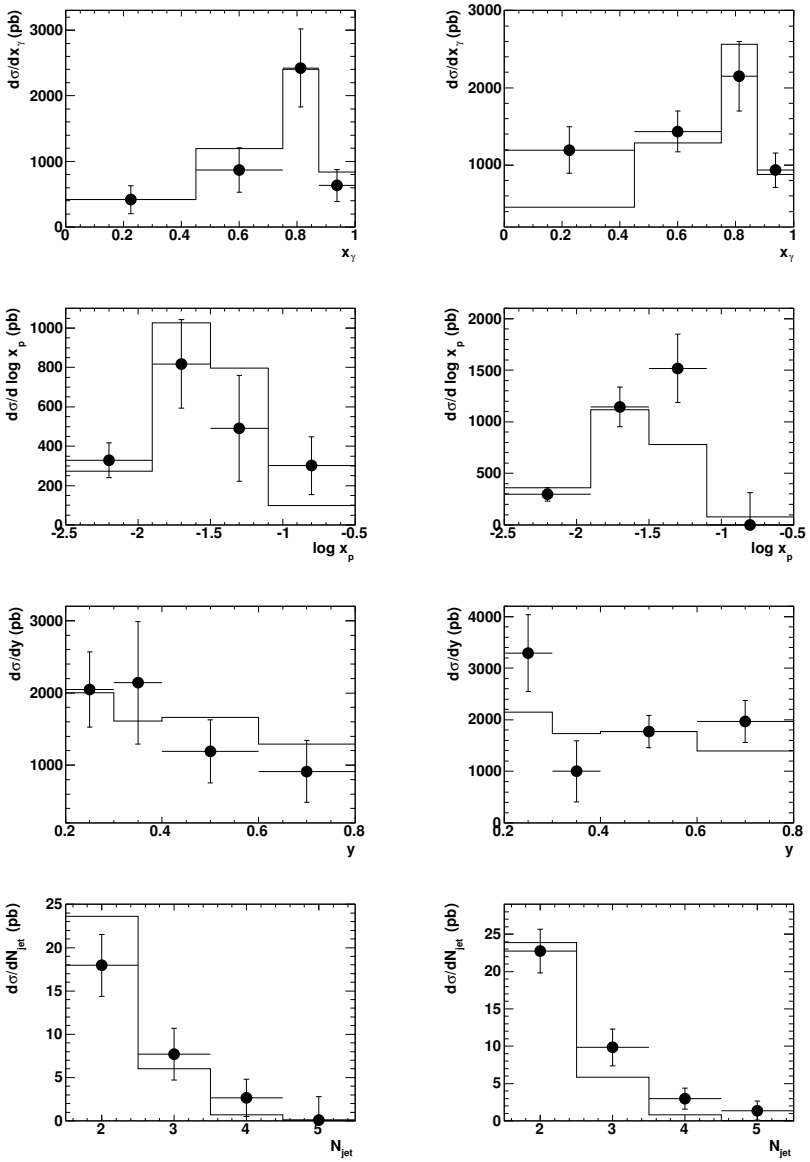

(a) $\sqrt{s_{\mathrm{ep}}} = 300\,\mathrm{GeV}$ (b) $\sqrt{s_{\mathrm{ep}}} = 318\,\mathrm{GeV}$

Figure D.2: Differential cross–sections for $\mathrm{b\bar{b}}$ production in terms of the kinematic variables x_γ, x_p, y and the number of jets per event, N_jet, for centre–of–mass energies, $\sqrt{s_{\mathrm{ep}}} = 300\,\mathrm{GeV}$ (a) and $\sqrt{s_{\mathrm{ep}}} = 318\,\mathrm{GeV}$ (b). The measured cross–sections are depicted by the black dots, while the histograms represent the PYTHIA prediction, scaled by a factor of 1.75.

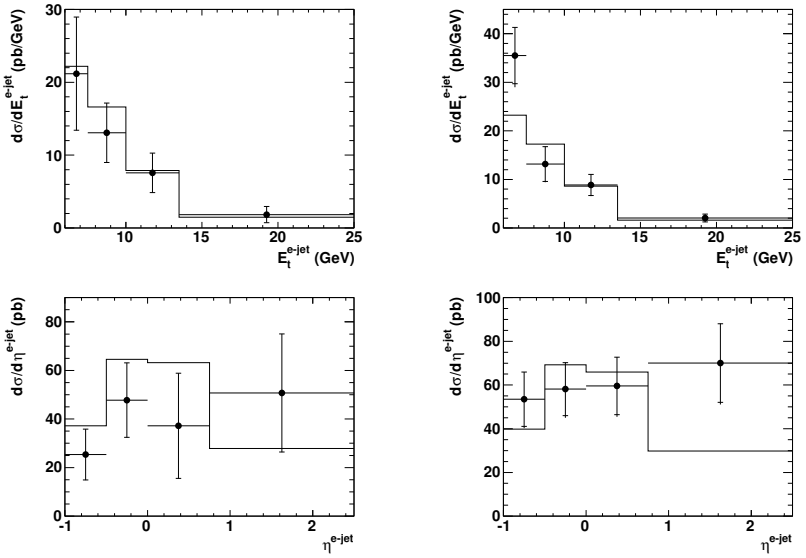

(a) $\sqrt{s_{\mathrm{ep}}} = 300\,\mathrm{GeV}$ (b) $\sqrt{s_{\mathrm{ep}}} = 318\,\mathrm{GeV}$

Figure D.3: Cross–section dependence for beauty production as a function of the transverse energy, $E_{\mathrm{t}}^{\mathrm{e-jet}}$, and the pseudo–rapidity, $\eta^{\mathrm{e-jet}}$, of the electron associated jet for centre–of–mass energies, $\sqrt{s_{\mathrm{ep}}} = 300\,\mathrm{GeV}$ (a) and $\sqrt{s_{\mathrm{ep}}} = 318\,\mathrm{GeV}$ (b). The measured cross–sections are depicted by the black dots, while the histograms represent the PYTHIA prediction, scaled by a factor of 1.75.

D.2 Charm Production

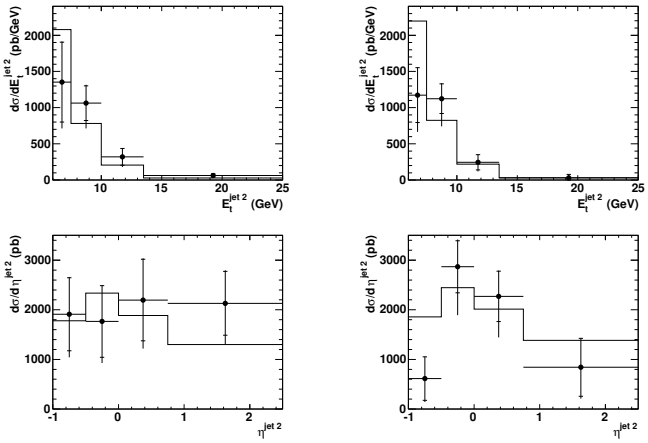

(a) $\sqrt{s_{\mathrm{ep}}} = 300\,\mathrm{GeV}$ (b) $\sqrt{s_{\mathrm{ep}}} = 318\,\mathrm{GeV}$

Figure D.4: Cross–section dependence for charm production as a function of the transverse energy, $E_{\mathrm{t}}^{\mathrm{jet\,2}}$, and the pseudo–rapidity, $\eta^{\mathrm{jet\,2}}$, of the second most energetic jet in each event for centre–of–mass energies, $\sqrt{s_{\mathrm{ep}}} = 300\,\mathrm{GeV}$ (a) and $\sqrt{s_{\mathrm{ep}}} = 318\,\mathrm{GeV}$ (b). The measured cross–sections are depicted by the black dots, while the histograms represent the PYTHIA prediction, scaled by a factor of 1.35.

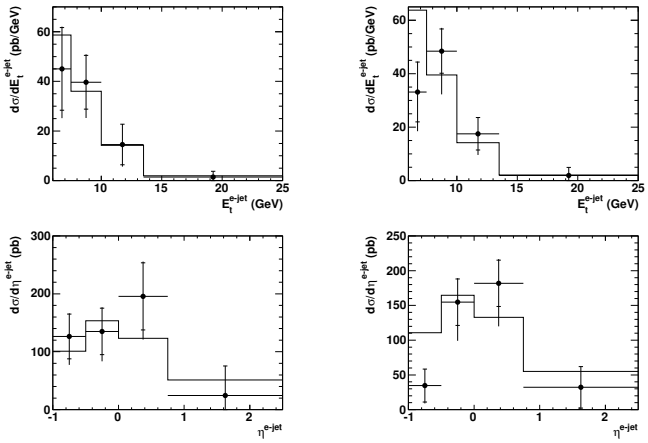

(a) $\sqrt{s_{\mathrm{ep}}} = 300\,\mathrm{GeV}$ (b) $\sqrt{s_{\mathrm{ep}}} = 318\,\mathrm{GeV}$

Figure D.5: Cross–section dependence for charm production as a function of the transverse energy, $E_{\mathrm{t}}^{\mathrm{e\text{–}jet}}$, and the pseudo–rapidity, $\eta^{\mathrm{e\text{–}jet}}$, of the electron associated jet for centre–of–mass energies, $\sqrt{s_{\mathrm{ep}}} = 300\,\mathrm{GeV}$ (a) and $\sqrt{s_{\mathrm{ep}}} = 318\,\mathrm{GeV}$ (b). The measured cross–sections are depicted by the black dots, while the histograms represent the PYTHIA prediction, scaled by a factor of 1.35.

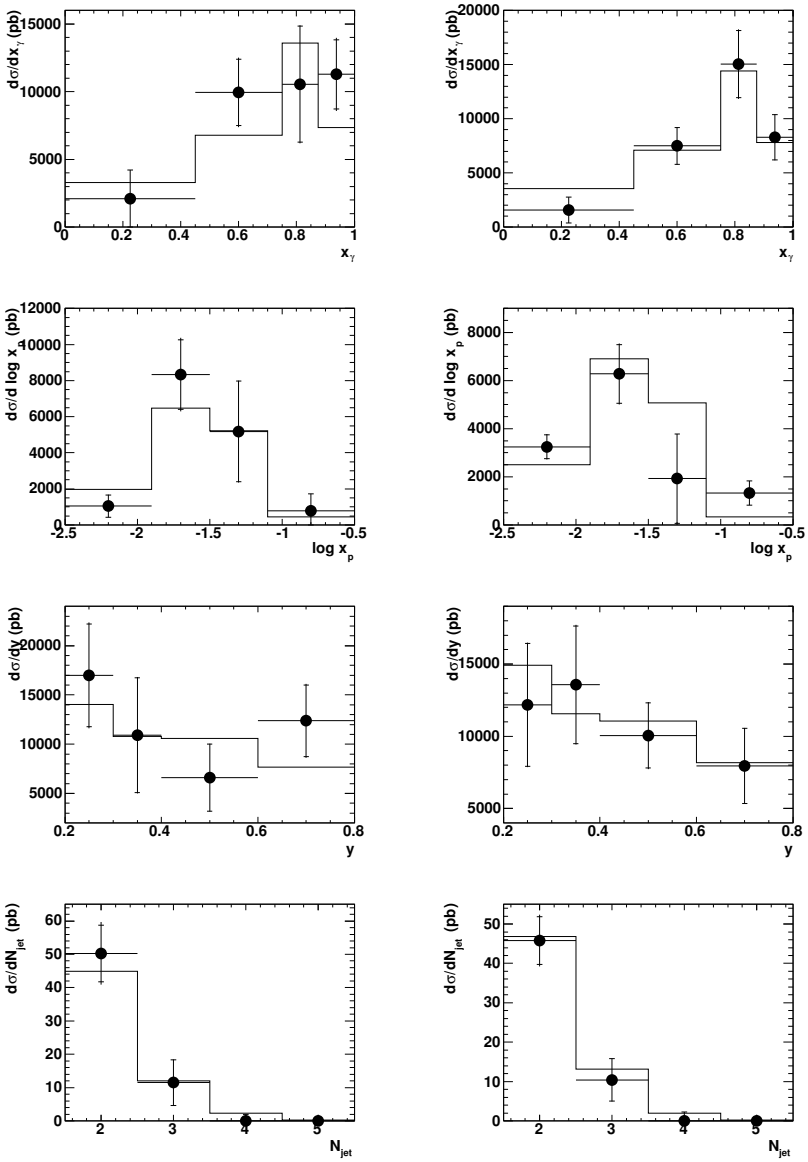

(a) $\sqrt{s_{ep}} = 300\,\text{GeV}$ (b) $\sqrt{s_{ep}} = 318\,\text{GeV}$

Figure D.6: Differential cross–sections for $c\bar{c}$ production in terms of the kinematic variables x_γ, x_p, y and the number of jets per event, N_{jet}, for centre–of–mass energies, $\sqrt{s_{ep}} = 300\,\text{GeV}$ (a) and $\sqrt{s_{ep}} = 318\,\text{GeV}$ (b). The measured cross–sections are depicted by the black dots, while the histograms represent the PYTHIA prediction, scaled by a factor of 1.35.

D.3 FMNR Comparisons

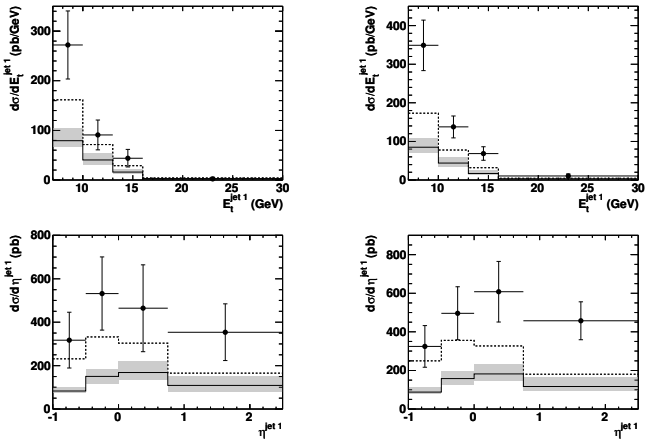

(a) $\sqrt{s_{\mathrm{ep}}} = 300\,\mathrm{GeV}$ (b) $\sqrt{s_{\mathrm{ep}}} = 318\,\mathrm{GeV}$

Figure D.7: FMNR comparison for beauty production as a function of the transverse energy, $E_{\mathrm{t}}^{\mathrm{jet}\,1}$, and the pseudo–rapidity, $\eta^{\mathrm{jet}\,1}$, of the most energetic jet in each event for centre–of–mass energies, $\sqrt{s_{\mathrm{ep}}} = 300\,\mathrm{GeV}$ (a) and $\sqrt{s_{\mathrm{ep}}} = 318\,\mathrm{GeV}$ (b). The measured cross–sections are depicted by the black dots, while the shaded bands represents the FMNR prediction. The PYTHIA predictions are also shown (dotted lines).

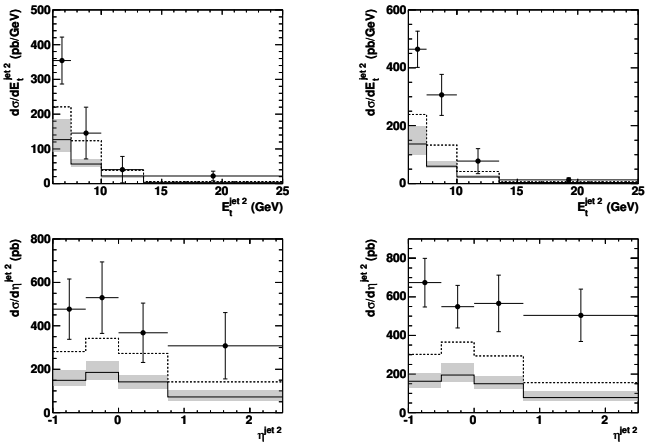

(a) $\sqrt{s_{\mathrm{ep}}} = 300\,\mathrm{GeV}$ (b) $\sqrt{s_{\mathrm{ep}}} = 318\,\mathrm{GeV}$

Figure D.8: FMNR comparison for beauty production as a function of the transverse energy, $E_{\mathrm{t}}^{\mathrm{jet}\,2}$, and the pseudo–rapidity, $\eta^{\mathrm{jet}\,2}$, of the second most energetic jet in each event for centre–of–mass energies, $\sqrt{s_{\mathrm{ep}}} = 300\,\mathrm{GeV}$ (a) and $\sqrt{s_{\mathrm{ep}}} = 318\,\mathrm{GeV}$ (b). The measured cross–sections are depicted by the black dots, while the shaded bands represents the FMNR prediction. The PYTHIA predictions are also shown (dotted lines).

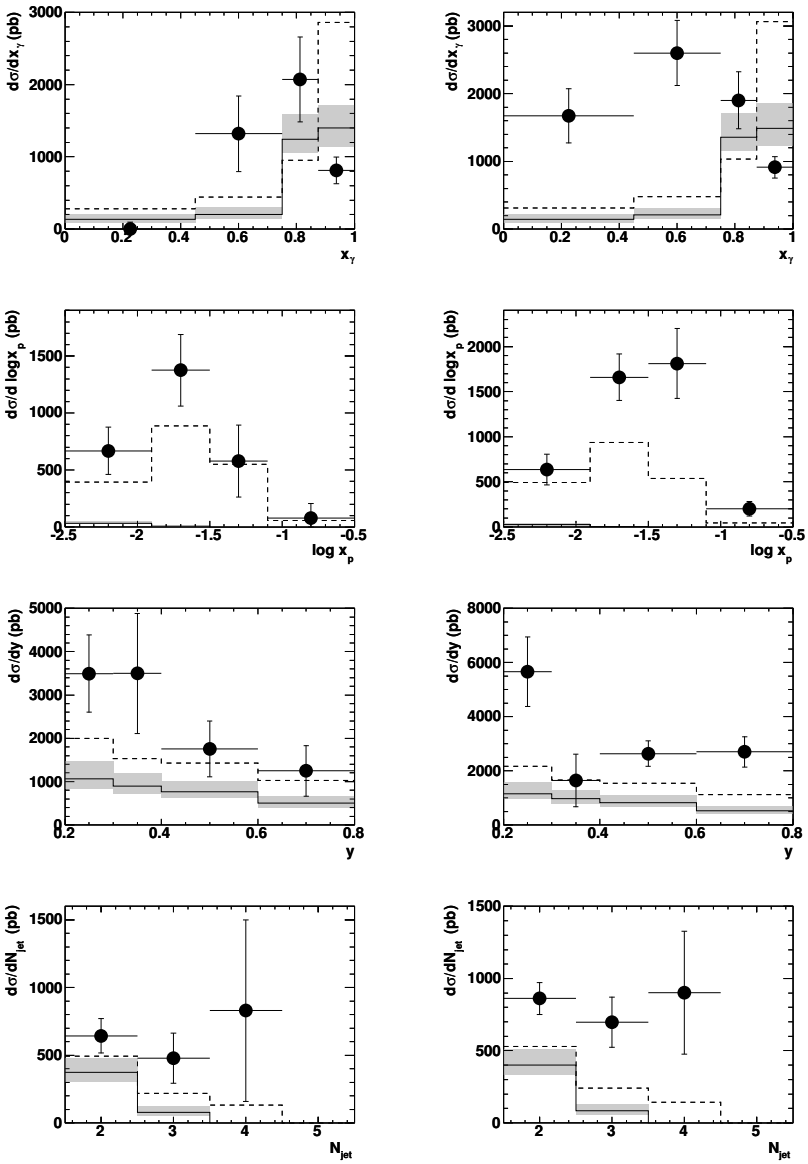

(a) $\sqrt{s_{ep}}$ = 300 GeV (b) $\sqrt{s_{ep}}$ = 318 GeV

Figure D.9: FMNR comparison for beauty production as a function of the kinematic variables x_γ, x_p, y and N_{jet} in events with centre–of–mass energies, $\sqrt{s_{ep}} = 300$ GeV (a) and $\sqrt{s_{ep}} = 318$ GeV (b). The measured cross–sections are depicted by the black dots, while the shaded bands represents the FMNR prediction. The PYTHIA predictions are also shown (dotted lines).

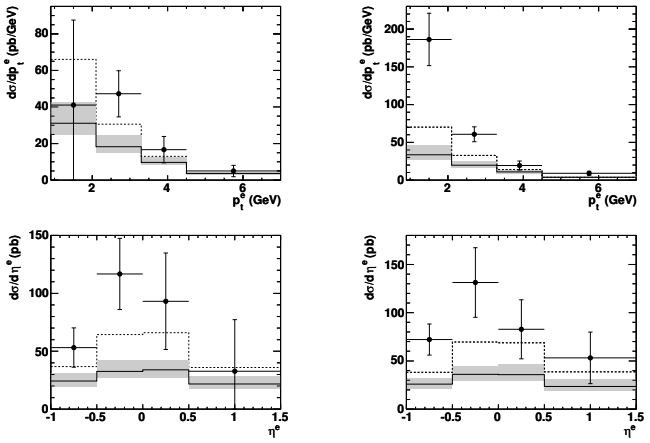

(a) $\sqrt{s_{ep}} = 300\,\text{GeV}$ (b) $\sqrt{s_{ep}} = 318\,\text{GeV}$

Figure D.10: FMNR comparison for beauty production as a function of the transverse momentum, p_t^e, and the pseudo–rapidity, η^e, of electron from semi–leptonic B decays for centre–of–mass energies, $\sqrt{s_{ep}} = 300\,\text{GeV}$ (a) and $\sqrt{s_{ep}} = 318\,\text{GeV}$ (b). The measured cross–sections are depicted by the black dots, while the shaded bands represents the FMNR predictions. The PYTHIA prediction is also shown (dotted lines).

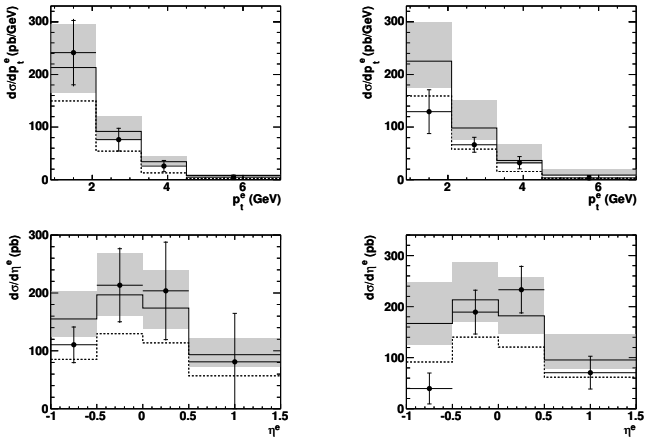

(a) $\sqrt{s_{ep}} = 300\,\text{GeV}$ (b) $\sqrt{s_{ep}} = 318\,\text{GeV}$

Figure D.11: FMNR comparison for charm production as a function of the transverse momentum, p_t^e, and the pseudo–rapidity, η^e, of electron from semi–leptonic charm decays for centre–of–mass energies, $\sqrt{s_{ep}} = 300\,\text{GeV}$ (a) and $\sqrt{s_{ep}} = 318\,\text{GeV}$ (b). The measured cross–sections are depicted by the black dots, while the shaded bands represents the FMNR predictions. The PYTHIA prediction is also shown (dotted lines).

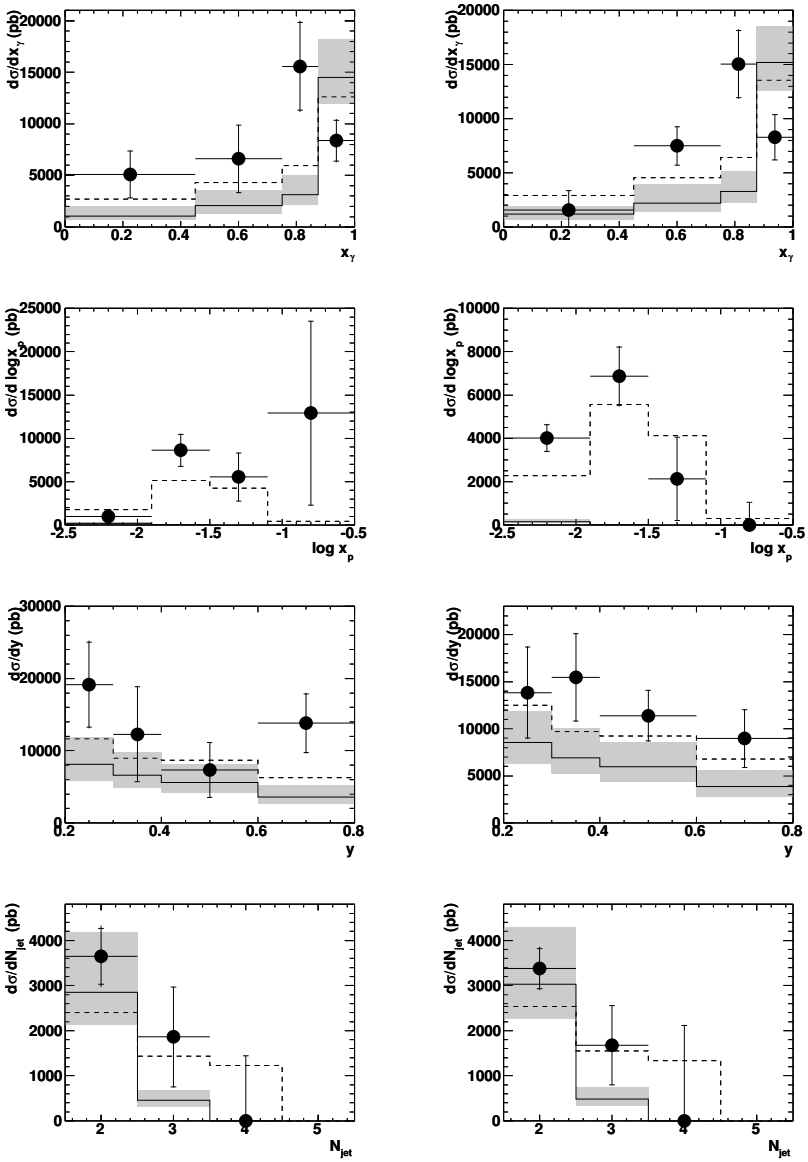

(a) $\sqrt{s_{ep}} = 300\,\text{GeV}$ (b) $\sqrt{s_{ep}} = 318\,\text{GeV}$

Figure D.12: FMNR comparison for charm production as a function of the kinematic variables x_γ, x_p, y and N_{jet} in events with centre–of–mass energies, $\sqrt{s_{ep}} = 300\,\text{GeV}$ (a) and $\sqrt{s_{ep}} = 318\,\text{GeV}$ (b). The measured cross–sections are depicted by the black dots, while the shaded bands represents the FMNR prediction. The PYTHIA predictions are also shown (dotted lines).

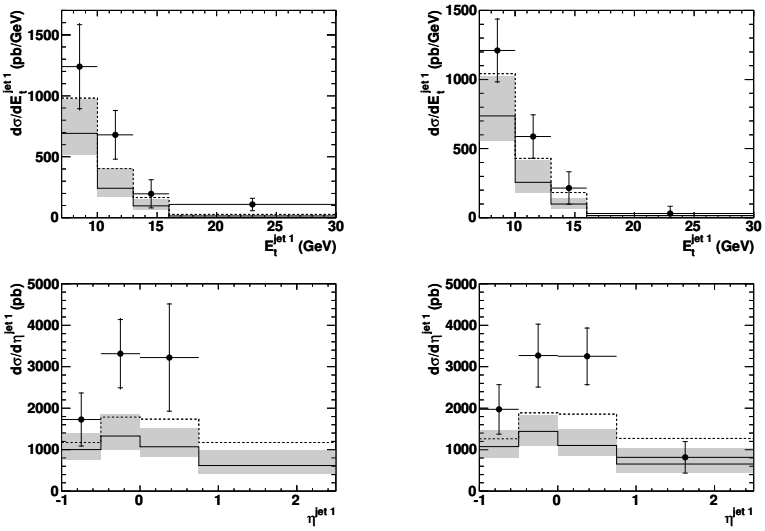

(a) $\sqrt{s_{ep}} = 300\,\text{GeV}$ (b) $\sqrt{s_{ep}} = 318\,\text{GeV}$

Figure D.13: FMNR comparison for charm production as a function of the transverse energy, $E_t^{\text{jet}\,1}$, and the pseudo–rapidity, $\eta^{\text{jet}\,1}$, of the most energetic jet in each event for centre–of–mass energies, $\sqrt{s_{ep}} = 300\,\text{GeV}$ (a) and $\sqrt{s_{ep}} = 318\,\text{GeV}$ (b). The measured cross–sections are depicted by the black dots, while the shaded bands represents the FMNR prediction. The PYTHIA predictions are also shown (dotted lines).

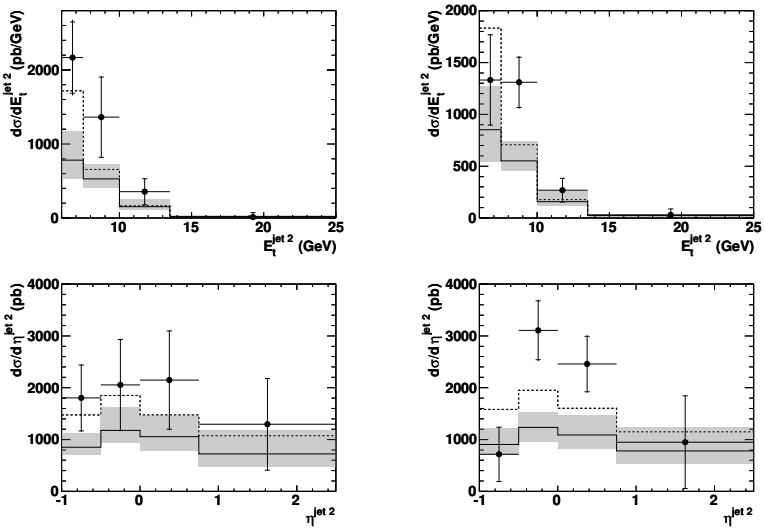

(a) $\sqrt{s_{ep}} = 300\,\text{GeV}$ (b) $\sqrt{s_{ep}} = 318\,\text{GeV}$

Figure D.14: FMNR comparison for charm production as a function of the transverse energy, $E_t^{\text{jet}\,2}$, and the pseudo–rapidity, $\eta^{\text{jet}\,2}$, of the second most energetic jet in each event for centre–of–mass energies, $\sqrt{s_{ep}} = 300\,\text{GeV}$ (a) and $\sqrt{s_{ep}} = 318\,\text{GeV}$ (b). The measured cross–sections are depicted by the black dots, while the shaded bands represents the FMNR prediction. The PYTHIA predictions are also shown (dotted lines).

Appendix E

Zeus Event Visualisation

At the end of the HERA-I running period the question arose what to do about the event display. The newly built detector components had to be added, and also the old event display, LAZE [Dor91], had to be ported to LINUX, since the so far supported old workstations were no longer available. The monolithic architecture of LAZE made changes difficult, and also some of the necessary program libraries were not supported anymore.[1] Therefore the development of a new, object–oriented event display, ZEVIS, was started. Since the development of the prototype and main sections of the first stable release was part of this thesis, a short overview about this project is given here. The code is implemented in C++ and heavily based on the RooT framework [B+06], which is briefly discussed in Sec. F.2. More details of the ZEVIS project can be found in [K+03]. The new event display was also the origin of the Z++ framework, which is the subject of Appendix F.

E.1 Data Model

Two types of data exist: geometry data describing the detector configuration, and event data containing information about collision events. Both sets are split.

The detector geometry is represented by a nested structure containing nodes connecting three–dimensional graphics primitives. Some examples are shown in Fig. E.1. In addition for some parts of the geometry two–dimensional representations are stored to be used in special projections. This is because in some cases, the two–dimensional projections cannot be derived from the three–dimensional representations in a consistent way. The geometry data is usually loaded once during the initialising phase of the program and stays in memory.

[1] In addition the LAZE program was very unstable and quite slow.

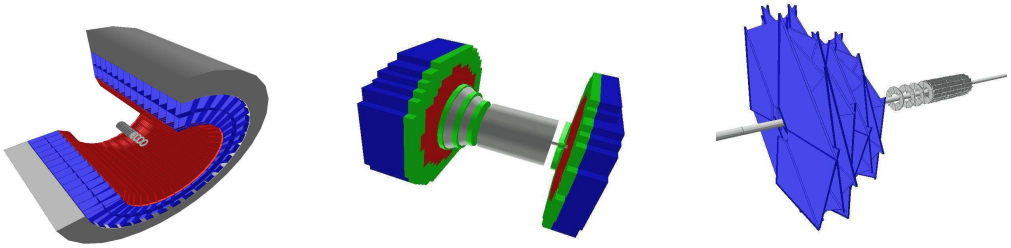

(a) Barrel calorimeter and micro–vertex detector

(b) F/RCAL, CTD and Forward Detector

(c) Straw–Tube Trackers, beam-pipe and MVD

Figure E.1: Examples of three–dimensional views of the detector geometry.

The event information is made of physical objects, like particle tracks, hits, energy deposits, as well as event header information, for instance run and event number, a date and time stamp, trigger information etc. The data is stored in a RooT event *tree* (*c. f.* Sec. F.2.3). The event classes are almost identical to the Z++ event classes, for more details see Sec. F.3.1. The main difference to these classes is the ability of the ZEVIS objects to be drawn.

E.2 Architecture

In contrast to the old LAZE program, which was able to run at a few specific machines at the DESY site only, the basic concept for the new event display is a client–server architecture. Here, the server provides the detector geometry and the event data, while the client displays the data, see Fig. E.2. The data is transferred in the form of RooT files via a standard HTTP–server. The RooT files are serialised objects in (platform–independent) text format. HTTP was chosen, because it penetrates most firewalls. Beside the necessary C++ code, the server side is implemented with the help of SHELL and PHP scripts.

Several server types exist:

Geometry server: Each client requests the detector geometry from the geometry server when started (*c. f.* Fig. E.3). The geometry server provides several detector configurations for different running periods. The server response is usually quick, well below one second. Instead of using a server, the clients are also able to load geometries locally for test purposes.

Single–event server: This is the most often used server for event data. With the help of the client the user requests particular collision events. The requests are received by event agents, which fetch the event from the ZEUS event database and convert it to a single–event RooT file (*z2root* program) which

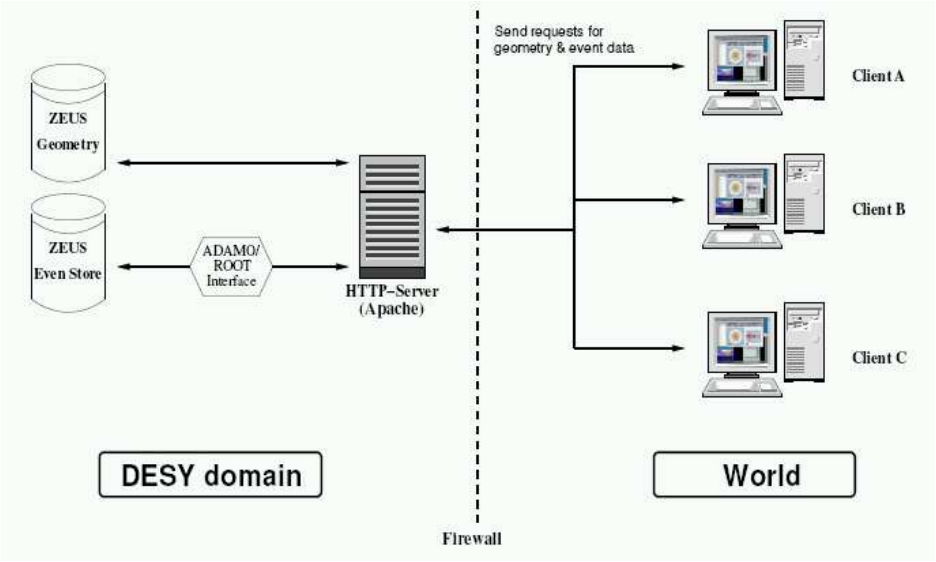

Figure E.2: ZEVIS clients from everywhere over the world can connect to the servers at DESY serving detector geometry and event data.

is forwarded to the client via an HTTP server (see Fig. E.4). The access to the ZEUS event database can be accelerated with the help of a tag database. The HTTP server handles also the client requests. These are put into a *fifo* file (first in, first out), which is watched by idle event agents. This simple mechanism guarantees an efficient processing of incoming requests. Stress tests have shown that even for numerous simultaneous requests the mean response time of the server is a few seconds only. This is further reduced if the events in question are in the cache.

Multi–event server: Sometimes it is useful to download a multi–event file (*e. g.* in case of pre-selected event lists etc.) and browse through the events off-line. The multi–event server (Fig. E.5) allows up to a hundred events in a row to be downloaded. The latency here is of the order of 10—30 s.

On-line server: An on-line event display gives additional information about the detector performance to the shift crew in the ZEUS control room. For this, events are copied from the ZEUS event stream with a rate of ~0.1 Hz. Since this data is in RAW–format it has to be processed on-line by the reconstruction program (ZEPHYR, see Sec. 2.2.4) in order to see more complex objects than hits. Afterwards the data is converted to ZEVIS/Root format and distributed by the server (Fig. E.6). Every standard ZEVIS client is able to connect with this server and display the events on-line. That means the on-line display is not restricted to the ZEUS control room; everybody can

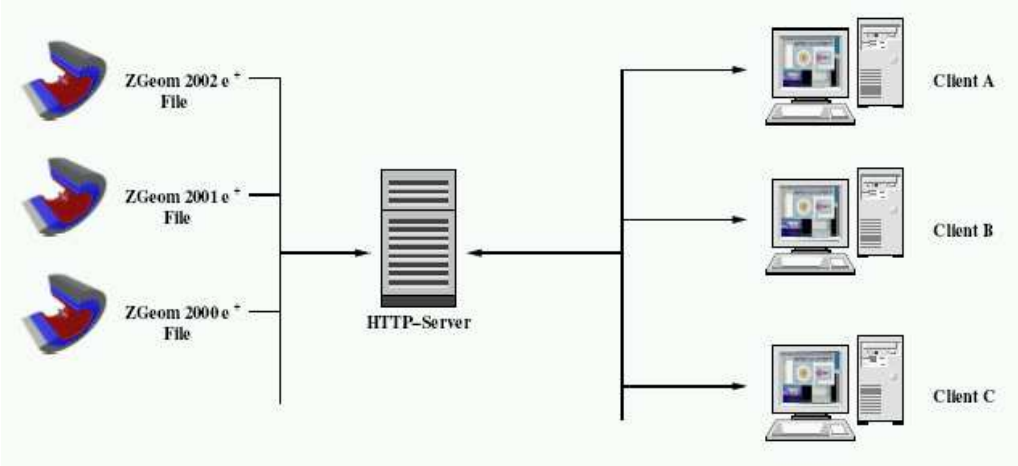

Figure E.3: ZEVIS geometry server. At start-up every client loads the detector geometry from the geometry server.

have a look at the current data taking.

E.3 The ZEVIS Client

The client is capable of displaying the detector geometry and event data. It mainly consists of a graphical user interface. The user can interactively request events from the server and display them in various formats. The client runs on every common UNIX platform as well as on LINUX, Mac OSX and Windows computers. For the three–dimensional rendering a faster graphics card might be useful.

Figure E.7 shows a screen–shot of the ZEVIS client. On the left one sees the event tree in case of multiple events loaded. The large canvas on the right displays the event header and two different views of the event. The client is able to show two and three–dimensional views of an event. Beside simple side views, the two–dimensional views are usually projections.[2] Most common are projections using the approximatively axial symmetry of the detector, *i. e.* the projection onto the *xy*–plane and the comprehensive *zr*–projection. Moving and zooming is possible as well as a fish–eye mode blowing up the inner regions. Three–dimensional views are possible either in a simple orthogonal wire–frame mode in the canvas, or, more exclusively, with the help of the x3d or OpenGL graphics libraries in an external viewer (*c. f.* Fig. E.1). These viewers provide hidden line and hidden surface removal algorithms as well as common shading models.[3] In addition more

[2] In a projection additive variables like energy deposits are *summed* along the projection axis.
[3] Filled objects only. Translucity is not (yet) possible.

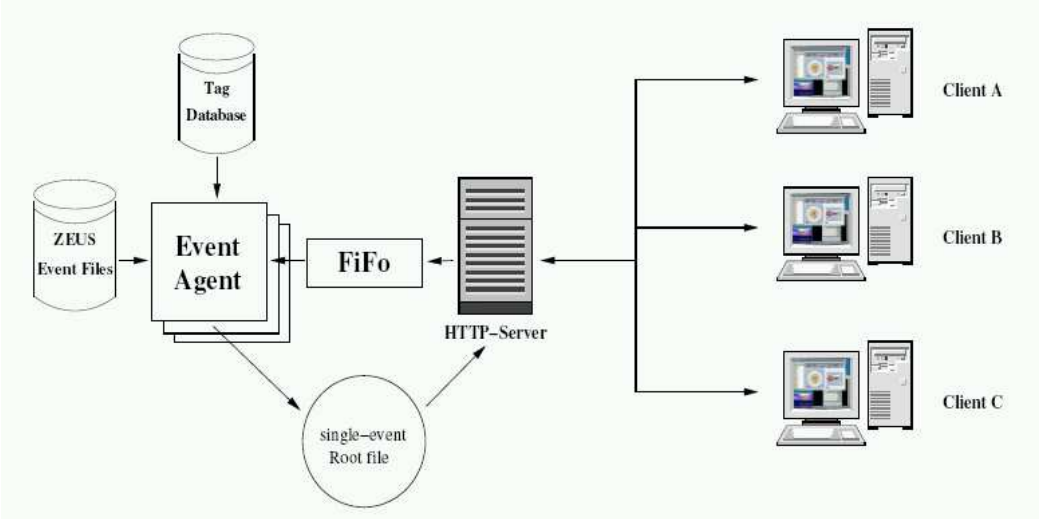

Figure E.4: ZEVIS single–event server. Multiple clients can request single collision events from the server.

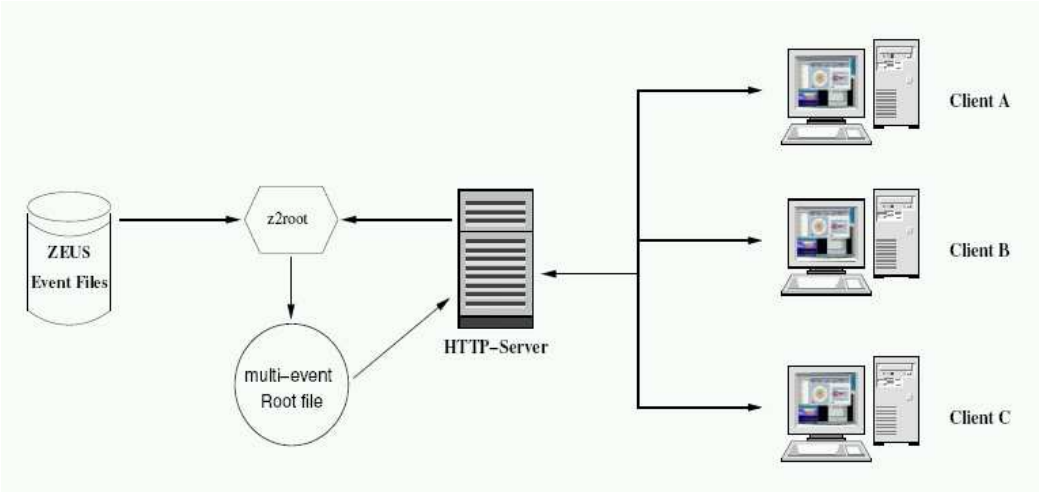

Figure E.5: ZEVIS multi–event server. In addition to the single–event mode users can download multiple events for off-line analysis.

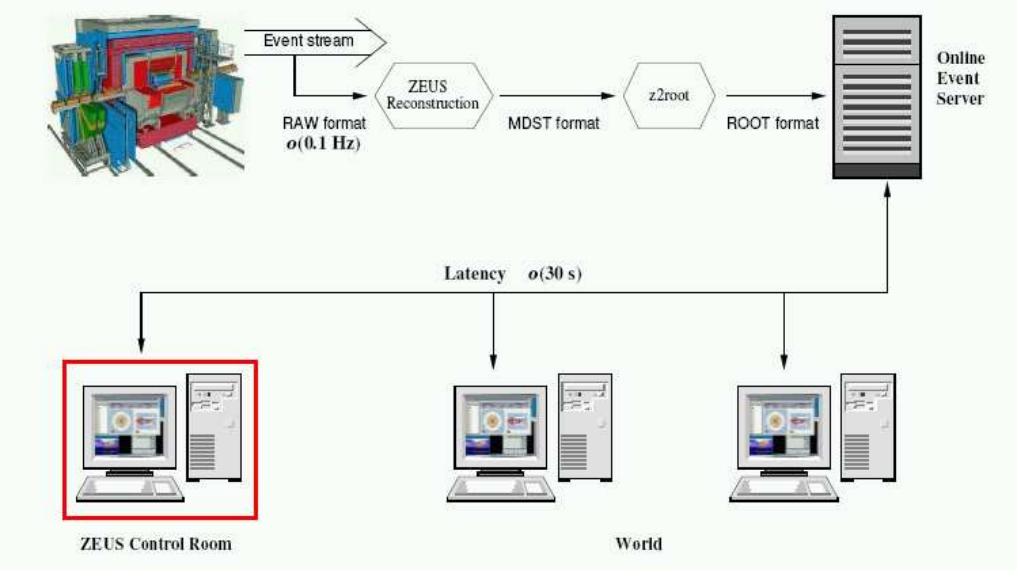

Figure E.6: ZEVIS on-line server. Access to on-line events is possible from everywhere.

special views are included, for instance the distribution of the energy deposits in the $\eta\phi$–plane, which is most important when studying jets. The graphical user interface provides several controls to change the way of displaying the information. Parts of the detector geometry or the event information can be hidden. The user is also able to pick graphical objects with the mouse in order to change their graphics attributes or retrieve textual information about them.

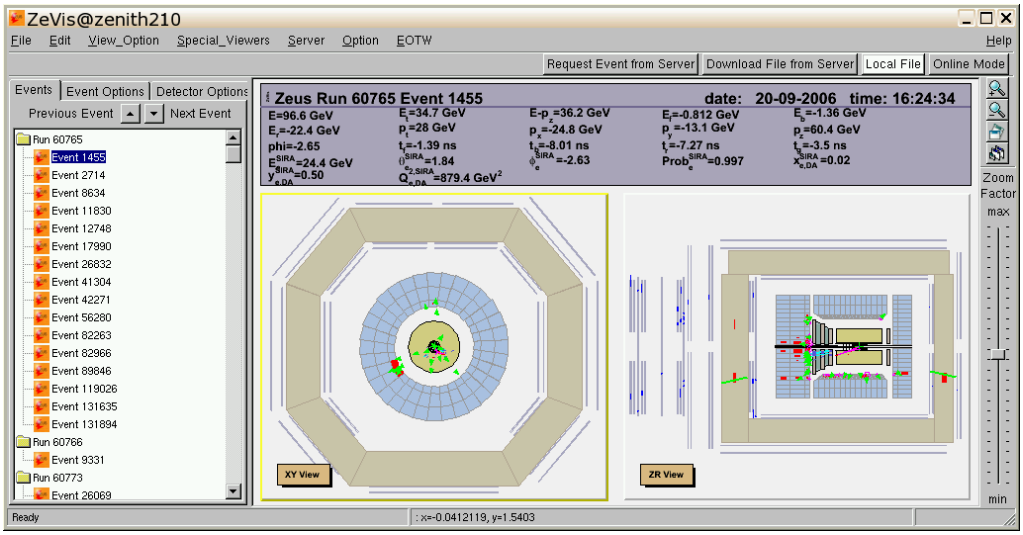

Figure E.7: Screen–shot of the ZEVIS client.

Appendix F

Z++ — An Analysis Framework for ZEUS

The daily routine of an high energy physicist consists mainly of programming within large computer systems. In fact the biggest part of the work is the development of appropriate software for data acquisitation, simulation, reconstruction and analysis. Also in this thesis, an essential part of the work was the development of a modern and efficient analysis framework for the ZEUS experiment. This section highlights the basic aspects of this framework.[1]

Already in the mid–nineties it was clear that the systems used for data analysis so far like PAW and also the corresponding data structures ZEBRA or HBOOK could not be used any further. Due to reasons of clarity and maintenance those systems, mostly written in FORTRAN and based upon nearly 20 year old program libraries, are not applicable for future high energy physics experiments like the LHC which will supersede by far all of the present experiments in the amount of data and complexity.[2] A solution is offered by the use of object–oriented programming languages, in particular C++.[3]

The framework described here is fully object–oriented and heavily based on

[1] A *framework* provides a whole infrastructure of functionality — class libraries in this case — for the user. The user in turn has less code to write because he should be able to use und re-use the majority of the code from the framework. Since code inherited from the framework has already been tested and integrated with the rest of the framework it should become more reliable and robust. Code re-use provides consistency and common capabilities between programs, no matter who writes them. Frameworks also make it easier to break programns into smaller pieces. In the end the user can concentrate on his particular problem domain. He does not have to be an expert in every field for many services are provided by the framework.

[2] It is estimated that the LHC will produce more than 1 Petabyte of data per year.

[3] Sometimes the language JAVA is also cited, but one has to admit that time–consuming operations never had been the purpose of this language. Furthermore the licence agreement of Sun Microsystems Inc. is vague at some points.

the RooT libraries (see Sec. F.2) and on the class libraries of the event display, ZEVIS, described in the previous Appendix. Its main feautures are outlined below (Section F.3).

F.1 Benefits of Object–Oriented Programming

An important insight of the seventies was that the success of a computer program depends strongly on the underlying data structure but not on the algorithms as people believed before. This and the growing understanding of modelling complex systems both artificial and in nature led to the object–oriented programming languages in the eighties. Their most important concepts shall be explained in more detail now. A good review on all concepts is found in [Wes99].

F.1.1 Abstraction and Encapsulation

Complex systems can often be separated into sub-systems showing both an internal (hidden) complexity (encapsulation) and external simplicity (abstraction). Those are the two basic rules of object–oriented programming. Abstraction provides code which is easy to read and to understand even in vast software projects. This is supported by encapsulation, because code sections are well separated (modularised). This is in particular helpful when working with a team of many developers. Not to mention the enormous advantage for the maintenance of the system due to the hidden complexity.

F.1.2 Inheritance, Virtual Functions and Polymorphism

Sometimes complex systems share simple ancestors with other systems. The evolution of simple general systems into more complex and specialised ones is part of the object–oriented model. This kind of inheritance saves the programmer a lot of code writing. Also, the abstraction level is pushed even further.

By declaring functions of inherited classes as *virtual* it is possible to apply functions with the same name but different meaning onto a heterogeneous mixture of objects. Think of propagating a bunch of charged and neutral tracks for instance. Such a concept is called *polymorphism*. It is heavily used in the RooT and in the Z++ framework.

F.2 RooT

The RooT framework [B+06] has been developed mainly for high energy physics computing. It comprises libraries for histogramming and graphing in one or more dimensions, curve fitting and minimisation of functions, statistical tools for data analsysis, matrix algebra, four–vector computations, standard mathematical functions, multivariate data analysis *i. e.* neural networks, image manipulation *e. g.* to analyse astronomical images, distributed computing, persistence and serialisation of objects, access to various databases, three–dimensional visualisation (geometry), creating files in various formats (like Postscript, PDF, JPEG, SVG, XML), reflection & introspection, interfacing Python and Ruby code in both directions, interfaces to event generators, TCP/IP connections, server/client processes , threading and much more. It can — and has been already — easily be extended to other domains. Applications to astrophysics, finance mathematics and life–sciences are reported. RooT is an open project published under the LGPL. Its development and release philosophy are in the tradition of [Ray00].

F.2.1 Ways of Running RooT

Opposite to the situation before the command language, the scripting language and the programming language of RooT are all C++ thanks to the builtin CINT C++ interpreter [G+02]. This interpreter allows for testing and fast prototyping of scripts because the time–consuming compile and link cycle drops. If more performance is needed the interactively developed scripts can be compiled using a common C++ compiler. Thus the user can easily add his own classes (mostly derived from existing RooT classes). These classes usually are bundled in shared images which can be used either interactively or in batch mode or made furthermore into a standalone executable.

F.2.2 Object Streams

The RooT system supports input/output of C++ objects from/to machine–independent files. Moreover, it is possible to send objects through a network via TCP/IP or HTTP protocol. Thus client–server aplications are easily to be made. Also, RooT allows for class/schema evolution. That means that RooT files can be read even if the corresponding class description has changed meanwhile (this might happen often during an evolution of a project). RooT files are internally compressed very efficiently.

F.2.3 Trees

In high energy physics thr requirements for storing event data are demanding due to the vast amount of data sets. The common way of storing event data had been data summary tapes (DST) mostly in form of ZEBRA [B+95] banks.[4] The advent of the HBOOK package [B+98c] made subsequent analyses much more efficient by introducing the ability to process only sub-sets of events which had not been possible so far. However, a major disadvantage of HBOOK was its lack of support for compound data structures. Only flat tables (ntuples) containing native data types and fixed–length arrays of them are allowed. The RooT system now provides facilities to cope with that problem. A *tree* can handle any collection of objects. Random seek and proccessing of sub-components are possible as well as persistent relations within an event.

F.2.4 Automated HTML Documentation Generation

Another nice feature of the RooT system is its capability to produce documentation in hypertext format for any class known to the system by parsing the class implementation.[5] The descriptional text is taken from comments in the source code provided by the developer. Thus detailed documentation for entire class libraries can be made with less effort. The HTML documentation consists of class descriptions, descriptions of the corresponding data members and member functions and inheritance maps. Even the source code is accessible.

F.3 Z++ Class Overview

The Z++ class libraries are all written in C++ and based upon the RooT framework. Thus they take all the advantages cited above. In addition they build an integrated system that means they cover everything needed for any ZEUS analysis. Even more, because of their open and abstract data structure they can be used for any kind of analysis or study at ZEUS. Extensions to data structures or functionality not yet in can be easily developed. The libraries are linked dynamically (shared) which is in many ways much more efficient than static linked libraries. Some basic characteristics are shown in Tab. F.1.

[4] At ZEUS the data is stored in ADAMO [F+93] which is based upon ZEBRA and supports an entity–relationship data model.

[5] Similar to the well–known documentation generator tool DOXYGEN.

No. of classes	~40
Lines of code	$\sim 10^5$
Developers	8—10
Development time	2—3 years
Language	C++
OS	LINUX, UNIX

Table F.1: Characteristics of the Z++ project (state of summer 2006).

F.3.1 Event Structure

HERA collision events are stored in a RooT tree in a fully object–oriented way. Every event inside the tree is an instance of the Z++ event class called `ZEvent`. As shown in Fig. F.1 the event object contains sub-objects like an event header (consisting of run and event number, all trigger bits, beam energies — and in case of MC — information about the event generator used, the simulated process etc.), kinematic information and lists of tracks, vertices, jets (at detector, hadron and parton level), energy flow objects, MC particles, electron and muon candidates etc. In addition, persistent relationships within the event like track–vertex relations exist. The event class and its descendants provides much functionality to ease the analysist's daily life.

F.3.2 EAZE Interface

As already pointed out in Sec. 2.2.4 ZEUS events are stored in MDST format after being reconstructed by the program ZEPHYR. For a physics analysis these data sets of many millions of events are strongly reduced by pre-selection cuts for further analysis. This is usually done by the program EAZE [Rya97] which allows the user to store the pre-selected events in a data format he likes (mostly HBOOK ntuples). Frequently the package ORANGE is used in combination with EAZE. This provides some more functionality often needed like jet finding or the application of calibration constants, systematic corrections etc. The Z++ libraries include an interface to the EAZE program for a conversion of the MDST and ORANGE data into the object–oriented format (see Fig. F.2). Event selection routines, *e. g.* for photoproduction or deep inelastic scattering, are provided as well as finders for particle decays like $D^* \to K\pi\pi$, $K^0_s \to \pi^+\pi^-$, $\Lambda^0 \to p\pi$ etc.

F.3.3 Tasks

The sub-sequent analysis usually is organised in *tasks* by which even complicated analyses can be clearly arranged. The tasks are organised in a folder–like envi-

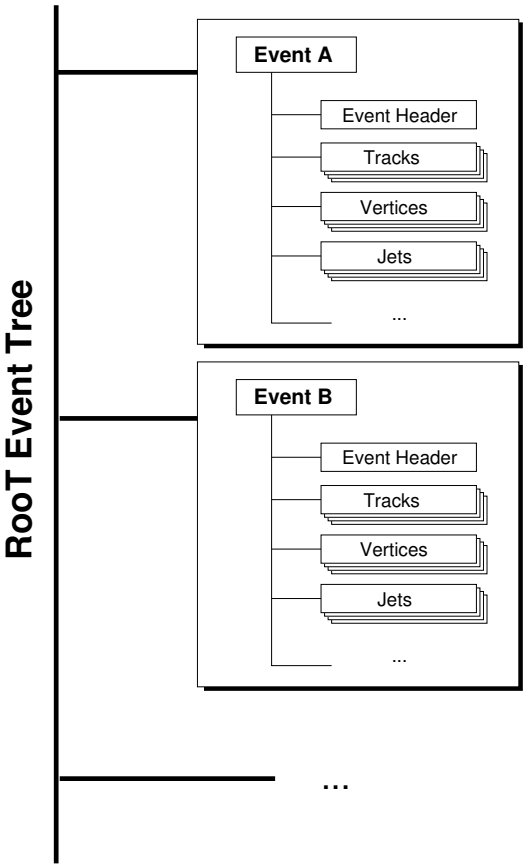

Figure F.1: Structure of the Z++ event tree. Each event object is mounted as super-branch to the RooT event tree. The event objects contains sub-objects like event header, lists of tracks, vertices, jets and many others. Since the structure is equal for all event instances most of the memory occupied by the event can be re-used when reading or writing the next event. The result is an tremendous increase in performance when processing a tree containing millions of events.

ronment. Things like the recursive execution of tasks, de-activating of specific tasks etc. is possible. The Z++ libraries provide classes for both the submission of EAZE jobs to the ZEUS batch facility and the often needed processing of a chain of event trees filling histograms, profiles etc.

F.3.4 Future Prospects

The main application of the Z++ framework so far has been the dE/dx calibration and the b $\rightarrow$ e analysis, but also D* measurements as well as tracking and alignment studies. Currently the framework is being extended for new aspects of the HERA-II data, *i. e.* improved tracking and vertexing information. This is part of recently started b $\rightarrow \mu$ analyses. Future plans are an interface to ntuple files produced by the ORANGE program as well as the integration with the ZEUS event display ZEVIS. More information about the Z++ project can be found at the Z++ webpage [Kin06].

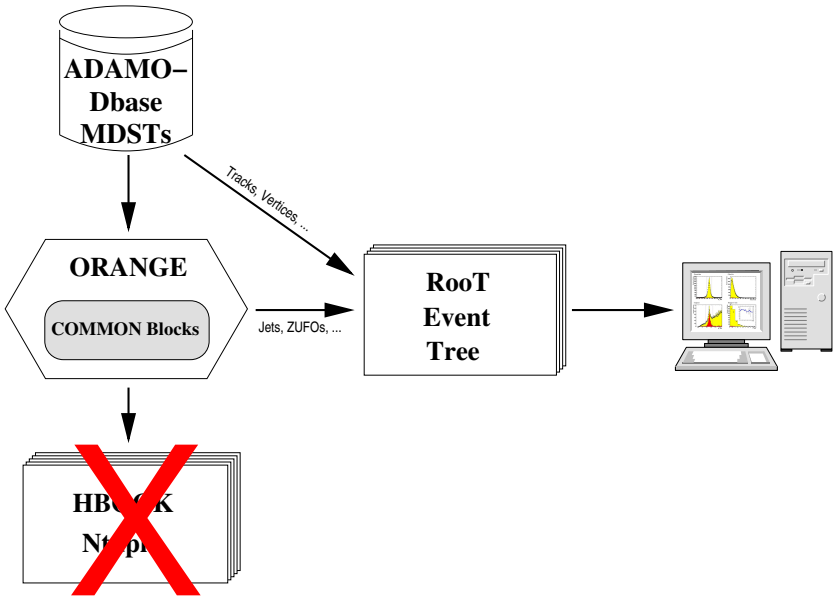

Figure F.2: Z++ analysis scheme. The MDST data is filtered and converted for furtheer analysis by the help of the EAZE and Orange programs to RooT event trees without the intermediate step of writing an Hbook ntuple.

Danksagung

Ich möchte mich bei all denjenigen bedanken, die zum Erfolg dieser Arbeit beigetragen haben.

Mein größter Dank gilt meinem Doktorvater Ian Brock, der mir nicht nur immer mit seiner Erfahrung und seinem Rat zur Seite stand, sondern mir auch jegliche Freiheiten bei der Durchführung meiner Projekte ließ. Gerade Letzteres half mir sehr, meine wissenschaftlichen Fähigkeiten zu entwickeln und gab mir Gelegenheit, neue Wege auszuprobieren.

Des weiteren geht ein großes Dankeschön an Markus Jüngst, der im Rahmen seiner Diplomarbeit und seiner beginnenden Promotion einen wesentlichen Beitrag zu dieser Arbeit geleistet hat, und an Detlef Bartsch, dessen detaillierte Dissertation zur Energieverlustmessung diese Analyse überhaupt erst ermöglicht hat. Detlef sei weiterhin für die kritische Durchsicht des Manuskriptes bedankt.

Ich danke dem „alten" FDET-Team Henning Schnurbusch, Jo Tandler, Peter Irrgang, Kai-Cristian Voss und Holger „Howie" Wessoleck für Unterstützung an der Konsole, die vielen ausschweifenden Diskussionen und die tolle Zeit in Hamburg. Arno Benen, intimer Kenner des Kalorimeters, sei herzlich für seine zahlreichen Maßnahmen zur Sozialisation gedankt. Roger Renner, der lange Zeit mit mir das Büro teilen mußte, danke ich für die herzliche Zusammenarbeit und seine Freundschaft. Kalle Glander bin ich sehr dankbar für viele Tipps und für die zahlreichen tiefgehenden und bisweilen sehr kritischen Diskussionen. Ursula Samson und Thomas Loddenkötter danke ich für die gute Zusammenarbeit. Letzterem sei zusammen mit Detlef und Julian Rautenberg für den unermüdlichen Einsatz bei der Administration des Computersystems gedankt.

Mein Dank geht aber auch an die jüngeren Mitglieder der Gruppe. Robert Zimmermann hat durch seine Diplomarbeit einen wichtigen Anteil geleistet, ebenso Melanie Lücker. Verena Schönberg, die mich durch ihr Erscheinen von vielen Pflichten entbunden hat, wird zusammen mit Markus und Ramoona Shehzadi diese Analyse fortsetzen. Dafür bin ich sehr dankbar. I would like to thank Michal Wlasenko for being such a nice guy. Daneben möchte ich mich auch bei den „old hands" Erwin Hilger und Ewald Paul für die geleisteten Mühen und die vielen Ratschläge bedanken. Special thanks to all co-workers in the heavy flavour group,

in particular to Massimo Corradi who provided many practical ideas for this work, and Michael Riveline who accompanied this analysis for a while. Mein Dank gilt auch dem ZEVIS-Team, ganz besonders Rainer Mankel und Olli Gutsche.

Der Universität Bonn und dem Deutschen Elektronensynchrotron DESY danke ich für die mehrjährige Unterstützung und Bereitstellung der Infrastruktur. Diese Arbeit wurde teilweise vom Bundesministerium für Bildung und Forschung finanziert.

Zum Schluß möchte ich mich ganz besonders bei meiner Freundin Ramona und meiner Familie bedanken, ohne deren Unterstützung diese Arbeit sicherlich unmöglich gewesen wäre.

List of Figures

List of Tables

Bibliography

[A+91a] ARGUS Collaboration, H. Albrecht et al. *Z. Phys.*, C52:353, 1991.

[A+91b] A. Andresen et al. Construction and beam test of the ZEUS forward and rear calorimeter. *Nucl. Instr. Methods*, A309:101–42, 1991.

[A+92a] ARGUS Collaboration, H. Albrecht et al. *Z. Phys.*, C54:1, 1992.

[A+92b] J. Andruszkòw et al. First measurements of HERA luminosity by ZEUS lumi monitor. Technical Report DESY-92-066, DESY, Hamburg, 1992.

[A+93] H1 Collaboration, I. Abe et al. *Nucl. Phys.*, B407:515, 1993.

[A+95a] H1 Collaboration, T. Ahmed et al. *Nucl. Phys.*, B445:195, 1995.

[A+95b] H1 Collaboration, S. Aid et al. *Z. Phys.*, C69:27, 1995.

[A+96a] OPAL Collaboration, K. Ackerstaff et al. *Z. Phys.*, C72:1, 1996.

[A+96b] H1 Collaboration, S. Aid et al. *Nucl. Phys.*, B472:32, 1996. http://arxiv.org/ps/hep-ex/9604005.

[A+98] OPAL Collaboration, K. Ackerstaff et al. *Eur. Phys. J.*, C1:439, 1998.

[A+99] H1 Collaboration, C. Adloff et al. Measurement of open beauty production at HERA. *Phys. Lett.*, B467:156–64, 1999. http://arxiv.org/ps/hep-ex/9909029.

[A+00a] D0 Collaboration, B. Abbott et al. The b-bbar production cross section and angular correlations in p-pbar collisions at sqrt(s) = 1.8 TeV. *Phys. Lett*, B487:264–72, 2000. // http://de.arxiv.org/ps/hep-ex/9905024.

[A+00b] DELPHI Collaboration, P. Abreu et al. *Eur. Phys. J.*, C12:209, 2000.

[A+02] BELLE Collaboration, K. Abe et al. Measurement of the inclusive semileptonic branching fraction of b mesons and $|v(cb)|$. *Phys. Lett.*, B547:181, 2002.
http://de.arxiv.org/pdf/hep-ex/0208033.

[A+03] BABAR Collaboration, B. Aubert et al. Measurement of the branching fraction for inclusive semi–leptonic b meson decays. *Phys. Rev.*, D67:311, 2003.
http://de.arxiv.org/pdf/hep-ex/0208018.

[A+05a] HERA-B Collaboration, I. Abt et al. Improved measurement of the b-bbar production cross section in 920 gev fixed-target proton-nucleus collisions. *Phys. Rev.*, D73, 2005.
http://arxiv.org/ps/hep-ex/0512030.

[A+05b] L3 Collaboration, P. Achard et al. Measurement of the cross section for open-beauty production in photon-photon collisions at LEP. *Phys. Lett.*, B619:71–81, 2005.
http://arxiv.org/ps/hep-ex/0507041.

[A+05c] H1 Collaboration, A. Aktas et al. Measurement of beauty production at HERA using events with muons and jets. *Eur. Phys. J.*, C41:453–67, 2005.
http://arxiv.org/ps/hep-ex/0502010.

[A+06a] H1 Collaboration, A. Aktas et al. Measurement of charm and beauty dijet cross sections in photoproduction at HERA using the H1 vertex detector. *submitted to Eur. Phys. J.*, C, 2006.
http://arxiv.org/ps/hep-ex/0605016.

[A+06b] H1 Collaboration, A. Aktas et al. Measurement of $F_2^{c\bar{c}}$ and $F_2^{b\bar{b}}$ at low Q^2 and x using the H1 vertex detector at HERA. *Eur. Phys. J.*, C45:23–33, 2006.
http://arxiv.org/ps/hep-ex/0507081.

[AC80] W.W.M. Allison and J.H. Cobb. Relativistic charged particle identification by energy loss. *Annual Review in Nuclear & Particle Physics*, (30):253–98, 1980.

[Aco] CDF Collaboration, D. Acosta. Underlying event in hard interactions at the Fermilab Tevatron $p\bar{p}$ collider.

[Alt82] G. Altarelli. Partons in quantum chromodynamics. *Phys. Rep.*, 81:1, 1982.

[AP77] G. Altarelli and G. Parisi. *Nucl. Phys.*, B126:298, 1977.

[B+78] T.H. Bauer et al. *Rev. Mod. Phys.*, 50:261, 1978.

[B+79] T.H. Bauer et al. *Rev. Mod. Phys.*, 51:407, 1979.

[B+87] René Brun et al. *GEANT 3.13*. CERN, 1987. CERN DD/EE/84-1.

[B+88] CLEO Collaboration, D. Bortoletto et al. *Phys. Rev.*, D37:1719, 1988.

[B+93] J. Botts et al. Cteq parton distributions and flavour dependence of the sea quarks. *Phys. Lett.*, B304:159, 1993.

[B+95] René Brun et al. *ZEBRA — Overview of the ZEBRA System*. CERN, 1995. CERN program library — long write-up Q100 and Q101
`http://wwwasdoc.web.cern.ch/wwwasdoc/psdir/zebra.ps.gz`.

[B+97] J. Binnewies et al. *Z. Phys.*, C76:677, 1997.

[B+98a] ZEUS Collaboration,J. Breitweg et al. *The European Physical Journal*, C1:109–22, 1998.

[B+98b] C.B. Brooks et al. Development of the ZEUS central tracking detector. *Nucl. Instr. Methods*, A283:477–83, 1998.

[B+98c] René Brun et al. *HBOOK — Statistical Analysis and Histogramming, Reference Manual*. CERN, 1998. CERN program library — long write-up Y250
`http://wwwasdoc.web.cern.ch/wwwasdoc/psdir/hbook.ps.gz`.

[B+99] ZEUS Collaboration, J. Breitweg et al. Measurement of inclusive D*+-D*+- and associated dijet cross sections in photoproduction at HERA. *The European Physical Journal*, C6(1):67–83, 1999.

[B+00] ALEPH Collaboration, R. Barate et al. *Eur. Pjys. J.*, C16:597, 2000.

[B+01] ZEUS Collaboration, Jason Breitweg et al. Measurement of open beauty production in photoproduction at HERA. *The European Physical Journal*, C 18(4):625–37, January 2001.
`http://www-zeus.desy.de/zeus_papers/ZEUS_PAPERS/DESY-00-166.ps.gz`.

[B+06] René Brun et al. *The ROOT System Homepage*. CERN, 1995—2006. http://root.cern.ch.

[BA83] B. Söderberg B. Anderson, G. Gustafson. *Z. Phys.*, C20:317, 1983.

[Bar00] Roger Barlow. *SLUO Lectures on Statistics and Numerical Methods in HEP: Lecture 5: Systematic Errors*. Manchester University, August 2000.
http://www.hep.man.ac.uk/u/roger/sluo5.ps.

[Bar02] Roger Barlow. Systematic errors: Facts and fictions. 2002.
http://de.arxiv.org/ps/hep-ex/0207026.

[Bar06] Detlef Bartsch. Systematic corrections of energy loss measurements with the CTD. Internal note, ZEUS, Hamburg, 2006. In preparation.

[Bar07] Detlef Bartsch. PhD thesis, Bonn University, 2007. IR-2007-05.

[BB33] Bethe and Bloch. Energieverlust durch Ionisation. *Zeitschrift für Physik*, 1933.

[BB64] W.H. Barkas and M.J. Berger. Tables of energy losses and ranges of heavy charged particles. In *Studies in Penetration of Charged Particles in Matter*, number 39 in Nuclear Science Series, pages 103–72. National Academy of Sciences-National Research Council, 1964. NAS-NRC Publication Nº1133, NASA-SP-3013.

[BB93] Roger Barlow and Christine Beeston. Fitting using finite monte carlo samples. *Computer Physics Communications*, (77):219–28, 1993.

[BC84] Steve Baker and Robert D. Cousins. Clarification of the use of chi-square and likelihood functions in fits of histograms. *Nuclear Instruments and Methods in Physics Research*, (221):437–42, 1984.

[Beh05] Olaf Behnke. *Production of Charm and Beauty Quarks at HERA*. Habilitationsschrift, Heidelberg University, October 2005.

[Ber93] B. Bernstein. *Nucl. Instr. Methods*, A336:23, 1993.

[Bet30] H. Bethe. Zur Theorie des Durchgangs schneller Korpuskularstrahlen durch Materie. *Ann. Physik*, 5:325–400, 1930.

[BFH+97] D.S. Bailey, B. Foster, G.P. Heath, et al. The designand performance of the ZEUS central tracking detector *z*–by–timing system. *Nucl. Instr. Metods*, A396:320–49, 1997. http://arxiv.org/abs/hep-ex/9707032.

[BH34] H. Bethe and W. Heitler. On stopping of fast particles and the creation of positive electrons. *Proc. Roy. Soc.*, A146:83–112, 1934.

[Bha38] H.J. Bhabha. On the penetrating component of cosmic radiation. *Proc. R. Soc. London*, A164:257–94, 1938.

[BHP+86] J.A. Blissett, D.K. Hasell, A.G. Parham, et al. Development of a tapered cell drift chamber II : Operation of high magnetic fields and different gas pressures. *Nucl. Instr. Methods*, A245:291–98, 1986.

[Bjö69] J. Björken. *Phys. Rev.*, 179:1547, 1969.

[BK05] W.H. Bragg and R. Kleeman. On the α particles of radium, and their loss of range in passing through various atoms and molecules. *Philos. Mag.*, (10):318–40, 1905.

[BKK95] J. Binnewies, B.A. Kniehl, and G. Kramer. *Phys. Rev.*, D52:4947, 1995.

[BL78] Ya. Balitsky and L. Lipatov. *Sov. J. Nucl. Phys.*, 28:822, 1978.

[Blo05] Ingo Bloch. *Measurement of Beauty Production from Dimuon Events at HERA/ZEUS*. PhD thesis, Universität Hamburg, November 2005. http://www-library.desy.de/preparch/desy/thesis/desy-thesis-05-034.ps.gz.

[BP69] J. Björken and D. Paschos. *Phys. Rev.*, 185:1475, 1969.

[BR93] Walter Blum and Luigi Rolandi. *Particle Detection with Drift Chambers*. Springer, 1993.

[Bru04] Graziano Bruni. P/pion separation using the ZEUS calorimeter. Internal note 04-018, ZEUS, Hamburg, September 2004. http://www-zeus.desy.de/ZEUS_ONLY/zeus_notes/ZEUS_NOTES/ZEUS-04-018.pdf.

[BS89] A.C. Bawa and W.J. Stirling. *J. Phys.*, G(15):1339, 1989.

[BW87] Ch. Berger and W. Wagner. *Phys. Rep.*, 146:1, 1987.

[C+84] TPC/2γ Collaboration, M.P. Cain et al. *Phys. Lett.*, 147B:232, 1984.

[C+97] M. Cacciari et al. *Phys. Rev.*, D55:2736, 1997.

[C+01] ZEUS Collaboration, S. Chekanov et al. Measurement of the photon-proton total cross section at a center-of-mass energy of 209 gev at hera. *Nucl. Phys.*, B627:3–28, 2001.

[C+03] ZEUS Collaboration, S. Chekanov et al. Dijet angular distributions in photoproduction of charm at HERA. *Phys. Lett.*, B565:87–101, 2003.

[C+04a] ZEUS Collaboration, S. Chekanov et al. Bottom photoproduction measured using decays into muons in dijet events in ep collisions at $\sqrt{s}$ = 318 GeV. *Physical Review*, D(70):012008, 2004. http://www-zeus.desy.de/zeus_papers/ZEUS_PAPERS/DESY-03-212.ps.

[C+04b] ZEUS Collaboration, S. Chekanov et al. Evidence for a narrow baryonic state decaying to K0s-(anti)proton in deep inelastic scattering at HERA. *Phys. Lett.*, B591:7–22, 2004.

[C+04c] ZEUS Collaboration, S. Chekanov et al. Measurement of beauty production in deep inelastic scattering at HERA. *Physics Letters*, B(599):173–89, October 2004. http://www-zeus.desy.de/zeus_papers/ZEUS_PAPERS/DESY-04-070.ps.

[C+04d] ZEUS Collaboration, S. Chekanov et al. Measurement of D*+- production in deep inelastic e+p scattering at HERA. *Phys. Rev.*, D69, 2004.

[CDSW93] S. Catani, Y.L. Dokshitzer, M.H. Seymour, and B.R. Webber. *Nucl. Phys.*, B406:187, 1993.

[CDW92] S. Catani, Y.L. Dokshitzer, and B.R. Webber. *Phys. Lett.*, B285:291, 1992.

[CE76] V.A. Chechin and V.K. Ermilova. The ionization–loss distribution at very samll absorber thicknesses. *Nucl. Instr. Methods*, 136:551, 1976.

[CG96] M. Caccariari and M. Greco. *Zeits. f. Phys.*, C69:459, 1996.

[CGM+92] A. Caldwell, I. Gialas, S. Mishra, et al. Design and implementation of a high precision readout system for the ZEUS calorimeter. *Nucl. Instr. Methods*, A321:356–64, 1992.

[CSS89] J.C. Collins, D.E. Soper, and G. Sterman. In A.H. Mueller, editor, *Perturbative Quantum Chromodynamics*, Singapore, 1989. World Scientific.

[CT04] Massimo Corradi and Monica Turcato. Beauty production in dijet events. Technical Report 04-005, ZEUS, Hamburg, 2004. `http://www-zeus.desy.de/ZEUS_ONLY/zeus_notes/ZEUS_NOTES/ZEUS-04-005.ps`.

[D+93] ZEUS Collaboration, M. Derrick et al. *Phys. Lett.*, B316:412, 1993.

[D+94a] ZEUS Collaboration, M. Derrick et al. *Z. Phys.*, C63:391, 1994.

[D+94b] ZEUS Collaboration, M. Derrick et al. *Phys. Lett.*, B322:287, 1994.

[D+95a] ZEUS Collaboration, M. Derrick et al. *Phys. Lett.*, 349B:225, 1995. Charm photoproduction.

[D+95b] ZEUS Collaboration, M. Derrick et al. *Phys. Lett.*, 346B:399, 1995. Average Q^2 in untagged photoproduction events.

[D+96] ZEUS Collaboration, M. Derrick et al. Dijet angular distributions in resolved and direct photoproduction at HERA. *Phys. Lett.*, B384:401–13, 1996.

[Dep99] Olaf Deppe. *Measurement of $D^{*\pm}$ Electroproduction at HERA*. PhD thesis, Universität Hamburg, 1999. `http://www-library.desy.de/preparch/desy/thesis/desy-thesis-00-006.ps.gz`.

[Deu] Deutsches Elektronensynchrotron Hamburg. HERA — A proposal for a large electron proton colliding beam facility at DESY. Technical report.

[DGH+91] M. Derrick, D. Gacek, N. Hill, et al. Design and construction of the ZEUS barrel calorimeter. *Nucl. Instr. Methods*, A309:77–100, 1991.

[DL92] A. Donnachie and P.V. Landshoff. *Phys. Lett.*, B(296):227, 1992.

[Doc77] Y.L. Dockshitzer. *Sov. Phys. JETP*, 46:641, 1977.

[Dor91] W. Dorth. LAE, logical access to ZEUS events. Internal note 91-069, ZEUS, Hamburg, 1991.

[EGM+79] R.K. Ellis, H. Georgi, M. Machacek, H.D. Politzer, and G.G. Ross. *Nucl. Phys.*, B(152):285, 1979.

[Erd97] Martin Erdmann. *The Partonic Structure of the Photon*, volume 138 of *Tracts in Modern Physics*. Springer, 1997.

[ES93] S.D. Ellis and D.E. Soper. *Phys. Rev.*, D48:3160, 1993.

[F+93] S.M. Fisher et al. *ADAMO entity–relationship programming system: Reference Manual*. CERN Programming Techniques Group, ECP Division, 1993.
http://adamo.web.cern.ch/Adamo/ADAMO_ENTRY.html.

[F+95] S. Frixione et al. *Nucl. Phys.*, B454:2, 1995.

[Fer40] E. Fermi. The inoization loss of energy in gases and condensed materials. *Phys. Rev.*, 57:485, 1940.

[Fey69] R. Feynman. *Phys. Rev. Lett.*, 23:1415, 1969.

[FM97] S. Frixione and M.L. Mangano. Heavy quark jets in hadronic collisions. *Nucl. Phys.*, B483:321, 1997.
http://de.arxiv.org/ps/hep-ph/9605270.

[FMNR94] S. Frixione, M.L. Mangano, P. Nason, and G. Ridolfi. *Nucl. Phys.*, B412:225, 1994.

[FMNR95] S. Frixione, M.L. Mangano, P. Nason, and G. Ridolfi. *Phys. Lett.*, B348:633, 1995.
http://de.arxiv.org/pdf/hep-ph/9412348.

[FMNR98] Stefano Frixione, Michelangelo L. Mangano, Paolo Nason, and Giovanni Ridolfi. Heavy-quark production. *Adv.Ser.Direct.High Energy Phys.*, 15:609–706, 1998.
http://de.arxiv.org/pdf/hep-ph/9702287.

[FMS+94] B. Foster, J. Malos, D.H. Saxon, et al. The design and construction of the ZEUS central tracking detector. *Nucl. Instrum. Methods*, A338:254–83, 1994.

[G+02] Masahuro Goto et al. *The* CINT *C/C++ Interpreter*, 2002. `http://root.cern.ch/root/Cint.html`.

[GL72] V. Gribov and L. Lipatov. *Sov. J. Nucl. Phys.*, 15:438, 1972.

[Gla61] S.L. Glashow. *Nucl. Phys.*, 22:579, 1961.

[GRV92] M. Glück, E. Reya, and A. Vogt. *Phys. Rev.*, D46:1973, 1992.

[GS88] K. Gather and D.H. Saxon. Axes, units, conventions. Internal note 88-012, ZEUS, Hamburg, 1988.

[Gut05] Oliver Gutsche. *Measurement of Beauty Quark Cross Sections in Photoproduction with the ZEUS Experiment at the Electron-Proton Collider HERA*. PhD thesis, Universität Hamburg, 2005. `http://www-zeus.desy.de/~gutsche/thesis/thesis.pdf`.

[H+92] J. Huth et al. In E.L. Berger, editor, *1990 DPF Summer study on High Energy Physics*, page 134, Colorado, 1992. Snowmass, World Scientific Singapore.

[Har98] G.F. Hartner. VCTRAK briefing: Program and math. Internal note 98-058, ZEUS, Hamburg, August 1998. `http://www-zeus.desy.de/ZEUS_ONLY/zeus_notes/ZEUS_NOTES/ZEUS-98-058.ps`.

[Hil86] E. Hilger. ZEUS coordinate system. Internal note 86-017, ZEUS, Hamburg, 1986.

[HIL+97] G.F. Hartner, Y. Iga, J.B. Lane, N.A. McCubbin, and M. Wing. VCTRAK (3.07/04): Offline output information. Internal note 97-064, ZEUS, Hamburg, September 1997. `http://www-zeus.desy.de/ZEUS_ONLY/zeus_notes/ZEUS_NOTES/ZEUS-97-064.ps`.

[Hoy95] Peter Hoyer. In *Workshop on Deep Inelastic Scattering and QCD*, NORDITA-95-65-P, Paris, France, 1995.

[HS95] B.W. Harris and J. Smith. *Nulc. Phys.*, B452:109, 1995. `http://arxiv.org/ps/hep-ph/9503484`.

[HWMN+99] Richard Hall-Wilton, Norman McCubbin, P. Nylander, Marc Sutton, and Matthew Wing. The CTD tracking resolution. Internal note 99-024, ZEUS, Hamburg, May 1999. `http://www-zeus.desy.de/ZEUS_ONLY/zeus_notes/ZEUS_NOTES/ZEUS-99-024.ps`.

[Irr04] Peter Irrgang. *Measurement of* $D^{*\pm}$ *production at low* Q^2 *with the beam–pipe calorimeter of ZEUS at HERA*. PhD thesis, Bonn University, 2004.

[JB79] F. Jaquet and A. Blondel. In *Proceedings of the study of an ep facility for Europe*, page 391, 1979. DESY–79/48.

[JLL+73] D. Jeanne, P. Lazeyras, I. Lehraus, et al. High energy particle identification using multilayer proportional counters. *Nucl. Instr. Methods*, 111:287–300, 1973.

[Jün05] Markus Jüngst. *Elektronidentifikation mit dem ZEUS-Detektor und Bestimmung des Beauty-Produktionsquerschnitts*. Diplom thesis, Bonn University, November 2005. BONN–IB–2005-15.

[K+97] B.A. Kniehl et al. *Z. Phys.*, C76:689, 1997.

[K+03] Oliver Maria Kind et al. A root-based client-server event display for the zeus experiment. La Jolla, California, March 2003. Computing in High Energy and Nuclear Physics.
`http://de.arxiv.org/pdf/hep-ex/0305095`.

[Kin06] Oliver Maria Kind. Z++ — An object–oriented analysis framework for ZEUS. Technical report, ZEUS, 2004–2006.
`http://www-zeus.desy.de/~kind/zplusplus/intro.html`.

[KKS95] M. Klasen, G. Kramer, and S.G. Salesch. *Z. Phys.*, C(68):113, 1995.

[KLF76] E. Kuraev, L. Lipatov, and V. Fadin. *Phys. Rev. Lett.*, 44:443, 1976.

[KLF77] E. Kuraev, L. Lipatov, and V. Fadin. *Phys. Rev Lett.*, 45:199, 1977.

[Kol84] H. Kolanoski. *Two Photon Physics at Electron–Positron Storage Rings*, volume 105 of *Springer Tracts in Mod. Phys.* Springer, Heidelberg, 1984.

[Krü92] J. Krüger. Habilitationschrift, DESY, 1992. F35-92-02.

[KZ88] H. Kolanoski and P. Zerwas. *High Energy Electron–Positron Physics*. DESY-87-175. World Scientific, Singapore, 1988.

[Lan44] L.D. Landau. On the energy loss of fast particles by ionization. *J. Phys. USSR*, (8):201, 1944.

[Lev92] A. Levy. Photoproduction at hera. In *DESY Academic Training Program*. 1992.

[Lip75] L.N. Lipatov. *Sov. J. Nucl. Phys.*, 20:96, 1975.

[LP82] Elliot Leader and Enrico Predazzi. *An Introduction to Gauge Theories and the New Physics*. Cambridge University Press, 1982.

[Lüd01] Stefan Lüders. *A measurement of the beauty production cross section via* $B \to J/\psi X$ *at HERA*. PhD thesis, ETH Zürich, October 2001. ETH No. 14480. ETHZ-IPP internal report 2001-10. `http://www-h1.desy.de/psfiles/theses/h1th-250.ps`.

[LZ06] A.V. Lipatov and N. Zotov. Unintegrated gluon distributions in $D^{*\pm}$ and dijet associated photoproduction at HERA. *Eur. Phys. J.*, C47:543, 2006. `http://arxiv.org/ps/hep-ph/0512013`.

[Man04] Michelangelo L. Mangano. The saga of bottom production in proton-antiproton collisions. Hadron Collider Physics Workshop, East Lansing, MI, June 2004. `http://de.arxiv.org/pdf/hep-ph/0411020`.

[MNR91] B. Mele, P. Nason, and G. Ridolfi. *Nucl. Phys.*, B357:409, 1991.

[MNR92] M.L. Mangano, P. Nason, and G. Ridolfi. *Nucl. Phys.*, B373:295, 1992.

[MNR93] M.L. Mangano, P. Nason, and G. Ridolfi. *Nucl. Phys.*, B405:507, 1993.

[MW84] G. Marchesini and B.R. Webber. *Nucl. Phys.*, B238:1, 1984.

[MW88] G. Marchesini and B.R. Webber. *Nucl. Phys.*, B310:461, 1988.

[MWA+92] G. Marchesini, B.R. Webber, G. Abbiendi, I.G. Knowles, M.H. Seymour, and L. Stanco. Herwig 5.9. *Comput. Phys. Commun.*, 67:465, 1992.

[Nac97] Jane M. Nachtman. *Search for Charginos at* $\sqrt{s}$ *= 161 and 172 GeVwith the ALEPH Detector*. PhD thesis, University of Wisconsin - Madison, 1997.

[Nis00] R. Nisius. The photon structure from deep inelastic electron photon scattering. *Phys. Rept.*, 332:165–317, 200. `http://de.arxiv.org/pdf/hep-ex/9912049`.

[NO99] P. Nason and C. Oleari. *Phys. Lett.*, B447:327, 1999.

[NO00] P. Nason and C. Oleari. A phenomenological study of heavy–quark fragmentation functions in electron–positron annihilation. *Nucl. Phys.*, B565:245, 2000.
http://de.arxiv.org/pdf/hep-ph/9903541.

[P+83] C. Peterson et al. *Phys. Rev.*, D27:105, 1983.

[Pau92] Ewald Paul. Multiparticle dynamics. DESY-92-026, page 267, Wuhan, China, 1992.

[PB93] H. Plothow-Besch. *Comp. Phys. Commun.*, 75:396, 1993.

[PTVF92] William H. Press, Saul A. Teukolsky, William T. Vetterling, and Brian P. Flannery. *Numerical Recipes in C*. Cambridge University Press, second edition, 1992.

[PZ94] K. Piotrzkowski and M. Zachara. Determination of the ZEUS luminosity in 1993. Internal note 94-167, ZEUS, Hamburg, 1994.

[PZ95] K. Piotrzkowski and M. Zachara. Determination of the ZEUS luminosity in 1994. Internal note 95-138, ZEUS, Hamburg, 1995.

[Ray00] Eric Steven Raymond. *The Cathedral and the Bazar*. 2000.
http://www.catb.org/~esr/writings/cathedral-bazaar/cathedral-bazaar/.

[Rya97] J.P. Ryan. The reference manual for the ZEUS scheme of modern software management. Internal note 97-046, ZEUS, Hamburg, 1997.
http://www-zeus.desy.de/ZEUS_ONLY/zeus_notes/ZEUS_NOTES/ZEUS-97-046.ps.

[S+89] W. Smith et al. The ZEUS trigger system. Internal note 89-084, ZEUS, Hamburg, 1989.

[S+02] Torbjörn Sjöstrand et al. *Pythia 6.2 – Physics and Manual*, 2002.
http://www.thep.lu.se/~torbjorn/pythia/pythia6206.pdf.

[Sal68] A. Salam. In N. Svartholm, editor, *Elementary Particle Physics*, page 367. Almquist and Wiksells, Stockholm, 1968.

[Sau77] F. Sauli. Principles of operation of multiwire proportional and drift chambers. Lectures given in the Academic Training Programme of CERN 1975–1976 77-09, CERN, 1977.

[SB82] S.M. Seltzer and M.J. Berger. Evaulation of the stopping power of elements and compounds for electrons and positrons. *Int. J. Appl. Radiation Isotope*, 33:1189, 1982.

[SB87] T. Sjöstrand and M. Bengston. *Comput. Phys. Comm.*, 43:367, 1987.

[SBS84] R.M. Sternheimer, M.J. Berger, and S.M. Seltzer. Density effect for the ionization loss of charged particles in various substances. *At. Data Nucl. Data Tables*, (30):261–71, 1984.

[Sey97] M.H. Seymour. Jet phenomenology. In *Proceedings of Les Rencontres de la Valee d'Acoste: Results and Perspectives in Particle Physics*, La Thuile, Italy, March 1997.
`http://de.arxiv.org/ps/hep-ph/9707349`.

[Sid95] D.G. Sideris. Simulation of the avalanche region of an anode wire in the ZEUS CTD. Internal note 95-076, ZEUS, Hamburg, 1995.

[SS93] G.A. Schuler and T. Sjöstrand. *Nucl. Phys.*, B407:539, 1993.

[SV97] R. Sinkus and T. Voss. Particle identification with neural netwroks using a rotational invariant momentum representation. *Nucl. Instr. Methods*, A391:360–68, 1997.

[SvZ87] T. Sjöstrand and M. van Zijl. *Phys. Rev.*, D36:2019, 1987.

[Tun01] N. Tuning. ZUFOs: hadronic final state reconstruction with calorimeter, tracking and backsplash correction. Internal note 01-021, ZEUS, 2001.
`http://www-zeus.desy.de/ZEUS_ONLY/zeus_notes/ZEUS_NOTES/ZEUS-01-021.ps`.

[Tur02] Monica Turcato. *Measurement of Beauty Photoproduction at HERA*. PhD thesis, Università degli studi di Padova, December 2002.
`http://www-library.desy.de/preparch/desy/thesis/desy-thesis-03-039.ps.gz`.

[Ueh54] E.A. Uehling. Penetration of heavy charged particles in matter. *Annu. Rev. Nucl. Sci.*, 4:315–50, 1954.

[Vac05] Monica Vacquez. Upcoming paper on charm into electron analysis. *Physics Review*, 2005.

[vdL93] H. van der Lugt. *The data acquisition and second level trigger system for the ZEUS calorimeter*. PhD thesis, University of Amsterdam, 1993.

[Ver98] W. Verkerke. *Measurement of Charm production in deep inelastic scattering*. PhD thesis, University of Amsterdam, 1998.

[VRFC82] J. Va'vra, L. Roberts, D. Freytag, and P. Clancey. Energy loss measurement in a jet chamber. SLAC-PUB 2882, Stanford Linear Accelerator Center, Stanford University, Stanford California, February 1982.

[vS00] A. López-Duran viani and S. Schlenstedt. Electron finder efficienciesand impurities. A comparison between SINISTRA, EM and EMNET. Internal note 99-077, ZEUS, Hamburg, 2000. `http://www-zeus.desy.de/ZEUS_ONLY/zeus_notes/ZEUS_NOTES/ZEUS-00-077.ps`.

[vW34] C.F. von Weizsäcker. *Z. Phys.*, 88:612, 1934.

[Wal95] P. Waloschek. HERA bulletin Nº4, 1995.

[Wei67] S. Weinberg. *Phys. Lett.*, 12:132, 1967.

[Wes99] Nick West. *The MINOS OO Companion*. Fermilab, 1999. `http://www-numi.fnal.gov/offline_software/srt_public_context/WebDocs/Companion/`.

[Wes02] Holger Wessoleck. *Messung der Wirkungsquerschnitte für den tiefinelastischen, inklusiven Prozess* $e^+p \rightarrow \overline{\nu}_e X$ *an der Speicherring-Anlage HERA mit ZEUS-Daten aus den Jahren 1999 und 2000*. PhD thesis, Universität Bonn, 2002. BONN-IR-2002-02.

[Wig87] L.W. Wiggers. Monte Carlo study of dead–time in the ZEUS DAQ system. Internal note 87-056, ZEUS, Hamburg, 1987.

[Wii91] B. Wiik. HERA status. In W. Buchmüller and G. Ingelman, editors, *Physics at HERA*, volume 1, pages 1–16, Hamburg, 1991. DESY.

[Wil35] E.J. Williams. *Kgl. Vidensk. Selskab. Mat.-Fiz. Medd.*, N4(13), 1935.

[Win99] Matthew Wing. *The Study of Heavy Quark Production in High E_T Photoproduction at HERA using the ZEUS Detector*. PhD thesis, University College London, 1999. http://www.hep.ucl.ac.uk/theses/mw.ps.gz.

[Win02] Matthew Wing. Setting the jet energy scale for the ZEUS calorimeter. In *10th International Conference on Calorimetry in High Energy Physics*, Pasadena, 2002. CALTECH. http://de.arxiv.org/ps/hep-ex/0206036.

[Wit77] E. Witten. *Nucl. Phys.*, B120:189, 1977.

[Y+06] W.-M. Yao et al. Review of Particle Physics. *Journal of Physics G*, 33:1+, 2006. http://pdg.lbl.gov.

[ZEU93] ZEUS Collaboration. *The ZEUS detector status report*. DESY, Hamburg, February 1993.

[ZEU04] ZEUS and H1 Collaboration. *Preprint*, hep-ex/0406036, 2004. http://arxiv.org/abs/hep-ex/0406036.

[ZEU06] ZEUS Collaboration. The ZEUS evtake and lumi page, 2006. http://www-zeus.desy.de/physics/lumi/.

[Zim07] Robert Zimmermann. Diplom thesis, Bonn University, 2007. In preparation.